

**SURFACE SEGREGATION ON Co-Rh  
AND OXIDATION OF Ni-Co ALLOYS**

**By**

**KEITH ANTHONY ELLISON, B.Eng**

**A Thesis**

**Submitted to the School of Graduate Studies  
in Partial Fulfillment of the Requirements**

**for the Degree  
Doctor of Philosophy**

**McMaster University**

**(c) Copyright by Keith Anthony Ellison, June 1990**

**SURFACE SEGREGATION ON Co-Rh  
AND OXIDATION OF Ni-Co ALLOYS**

DOCTOR OF PHILOSOPHY (1990)

McMASTER UNIVERSITY

(Materials Engineering)

Hamilton, Ontario

TITLE: Surface Segregation on Co-Rh and Oxidation of  
Ni-Co Alloys

AUTHOR: Keith Anthony Ellison, B.Eng (McMaster University)

SUPERVISORS: Professor W.W. Smeltzer  
Dr. P.R. Underhill  
Professor D.A. Thompson

NUMBER OF PAGES: xiii, 187

## ABSTRACT

Two model systems, Co-Rh and Ni-Co, were used to study surface segregation and oxidation phenomena on binary alloys.

Cobalt was found to sputter preferentially from five Co-Rh alloys ranging in composition from 19.3 to 84.7 at% Rh when irradiated by 4 keV Ar<sup>+</sup> ions. Surface segregation experiments on this system in the temperature range 623 to 1123 K showed that cobalt was enriched on the surface of a 84.7Rh alloy, while rhodium enrichment was determined for a 19.3Rh alloy. No conclusive segregation could be measured on the surface of a 47.8Rh alloy. The variation of surface concentration with temperature indicated enthalpy values of  $1 \pm 1 \text{ kJ mol}^{-1}$  and  $-3 \pm 7 \text{ kJ mol}^{-1}$  for the 19.3Rh and 84.7Rh alloys, respectively. Reasonable agreement was found between these measured enthalpy values and those calculated from the combined bond breaking and lattice strain models of surface segregation.

Oxidation experiments were performed on (110) Ni-3.86Co and Ni-4.0Co polycrystalline alloys at temperatures in the range 673 to 1073 K and a pressure of  $5 \times 10^{-3}$  Torr. The effects of surface pretreatment and orientation of the alloy surfaces were correlated to differences in oxide morphology and growth rates. Single crystal specimens which were chemically polished, annealed in vacuum and initially exposed to oxygen at room temperature showed a tendency to form (100) (NiCo)O || (110) Ni-3.86Co. These layers also exhibited the slowest growth rates and greater enrichment of CoO from the inner to outer oxide surfaces. Single crystal surfaces prepared by chemical polishing, annealing in vacuum and initial exposure to oxygen at the reaction temperatures developed additional oxide orientations parallel to the underlying alloys. Finally, the polycrystalline Ni-4.0Co specimens which were prepared by mechanical polishing followed by exposure to

room temperature oxygen developed polycrystalline oxide films. These types of structures were associated with higher rates of oxide growth and lower enrichments of CoO from the inner to the outer oxide surfaces.

The experimentally measured composition profiles were analysed according to the Wagner<sup>(6)</sup> model of oxidation, modified to include the effects of short circuit grain boundary diffusion. Effective alloy interdiffusion coefficients were calculated which showed that the rate of transport in the alloy zone beneath the growing oxide layer was enhanced relative to that expected solely on the basis of volume diffusion in this phase. The results were rationalized according to a dislocation model for the accomodation of plastic strain and vacancy annihilation in cation conducting scales<sup>(149)</sup>.

## ACKNOWLEDGEMENTS

The author wishes to express sincere thanks to Professor W.W. Smeltzer and Dr. P.R. Underhill for their advice and guidance throughout the course of this work. In addition, the interest shown by Dr. D.A. Thompson is greatly appreciated.

The help and advice of fellow graduate students, post doctoral fellows, research and technical personnel in the Department of Materials Science and Engineering and the Institute for Materials Research is also gratefully acknowledged. Thanks are due especially to Mssrs. F. Szostak and J. Garrett for their valuable technical assistance.

Drawings of the PHI 600 heating stage and sample holder were completed by the author's father, Mr. A. Ellison and also by Mr. D.S. Hodgson. Photographic and reproduction services were provided by Mssrs. T. Bryner, J. Whorwood and C. Butcher.

The author is indebted to the members of the Metallic Corrosion and Oxidation Section, Division of Chemistry, National Research Council of Canada for providing the basic design of the experimental apparatus used in the oxidation experiments. In particular, he wishes to thank Drs. R. Hussey and M.J. Graham. Funding for construction of the oxidation apparatus was provided in the form of an NSERC Equipment Grant to Professor Smeltzer.

I wish to acknowledge the financial support of the Department of Materials Science and Engineering, in the form of a graduate scholarship and teaching assistantship, and Alcan for the Alcan Postgraduate Fellowship Award.

Finally, and most importantly, I would like to thank my wife, Hania, for her loving support, patience and encouragement.

## TABLE OF CONTENTS

	Page
Chapter 1	1
INTRODUCTION	
Chapter 2	6
THEORY	
2.1	6
Introduction	
2.2	7
Surface Segregation on Binary Alloys	
2.2.1	7
Classical Thermodynamics and Quasichemical Models	
2.2.2	11
Monte Carlo and Electronic Calculations	
2.3	12
The Oxidation of Metals and Alloys	
2.3.1	13
The Oxidation of Pure Metals	
2.3.2	14
The Oxidation of Alloys	
2.3.3	15
The Diffusion Path Concept	
2.3.4	17
Single Phase Scale Formation on Noble Metal Alloys	
2.3.5	20
Formation of Solid Solution Scales	
2.3.6	27
Modifications to the Wagner Model	
2.3.7	28
Application of the Wagner Model to Experimental Investigations of the Oxidation of Binary Alloys	
2.3.8	29
Expected Range of Validity of the Wagner Model	
Chapter 3	32
LITERATURE REVIEW	
3.1	33
Introduction	
3.2	33
Properties of Co-Rh Alloys	
3.3	33
Properties of the Ni-Co System	
3.3.1	33
Structure, Thermodynamics and Diffusion	
3.3.2	36
Surface Thermodynamics	
3.4	38
Properties of the Ni-O System	
3.4.1	38
Crystal and Defect Structure	
3.4.2	40
Self-Diffusion of Ni and O in NiO	
3.4.3	45
Recent Developments in the Understanding of Grain Boundary Transport in NiO	
3.4.4	46
Oxidation Mechanisms and Kinetics	
3.5	51
The Properties of the Co-O System	
3.5.1	51
Structure, Thermodynamics and Diffusion	
3.5.2	53
Oxidation of Cobalt	
3.6	53
The Properties of the Ni-Co-O System	
3.6.1	53
Thermodynamics, Crystal and Defect Structure	
3.6.2	56
Diffusion Properties	
3.6.3	62
Oxidation of Ni-Co Alloys	

Chapter 4	<b>EXPERIMENTAL PROCEDURES</b>	66
	4.1 Introduction	66
	4.2 Sample Preparation	67
	4.2.1 Cobalt-Rhodium Alloys	67
	4.2.2 Single Crystal Nickel-Cobalt Alloy	70
	4.2.3 Polycrystal Nickel-Cobalt Alloy	72
	4.3 A Fast Entry Air-Lock-Compatible Hot Stage For the Collection of Auger Spectra at Elevated Temperatures	74
	4.4 Oxidation Apparatus and Procedures	77
	4.5 Specimen Characterization Techniques	82
	4.5.1 Secondary Electron Microscopy	82
	4.5.2 Auger Electron Microscopy	82
	4.5.3 Secondary Ion Microscopy	85
	4.5.4 Transmission Electron Microscopy	86
Chapter 5	<b>RESULTS AND DISCUSSION I SURFACE SEGREGATION ON COBALT-RHODIUM ALLOYS</b>	88
	5.1 Introduction	88
	5.2 Quantification of Auger Spectra and Selection of Standards for Co-Rh Alloys	88
	5.2.1 Auger Spectra for Cobalt and Rhodium	88
	5.2.2 Quantification of Auger Spectra From Co-Rh Alloys	91
	5.2.3 Selection of Standards for the Determination of Composition of Co-Rh Alloys from AES Peak Intensities: Preferential Sputtering on Co-Rh Alloys	93
	5.3 Surface Segregation on Co-Rh Alloys	100
Chapter 6	<b>RESULTS AND DISCUSSION II OXIDATION PROPERTIES OF NICKEL-COBALT ALLOYS BETWEEN 673 AND 1073 K</b>	114
	6.1 Introduction	114
	6.2 Oxidation of the Ni-3.86Co (110) Alloy: Hot-Bare Exposure	116
	6.3 Oxidation of the Ni-3.86Co (110) Alloy: Furnace-Raised Technique	125
	6.4 Oxidation Of The Ni-4Co Polycrystalline Alloy	132
	6.5 Discussion	143
	6.6 A Diffusion Model for the Growth of (Ni-Co)O Solid Solution Oxides by Combined Short Circuit Grain Boundary and Lattice Diffusion	150

Chapter 7

CONCLUSIONS

- 7.1 Surface Segregation on Co-Rh Alloys
- 7.2 Oxidation of Ni-Co Alloys

176  
177

REFERENCES

179

## LIST OF FIGURES

Figure		Page
2-1	The $\gamma^*$ versus $\sigma^*$ (surface tension ratio versus atomic size ratio) representation for the prediction of segregation on binary alloys <sup>(8)</sup> .	10
2-2	Schematic representation of the relationships between scale morphologies on binary alloys <sup>(22)</sup> .	16
2-3	Schematic phase diagram isotherm and equilibrium oxygen pressure-alloy diagram for noble metal alloys <sup>(4)</sup> .	18
2-4	Schematic phase diagram isotherms and equilibrium oxygen pressure-alloy diagram for a system in which the oxide and alloy phases are solid solutions <sup>(4)</sup> .	21
2-5	A two-dimensional cross-section through the alloy and oxide phases showing coordinate systems, schematic composition gradients and boundary values corresponding to the Wagner oxidation model.	22
2-6	Calculated and experimentally determined values for nickel composition as a function of normalized distance, $y$ , in (CoNi)O scale formed on Co-Ni alloys <sup>(34)</sup> .	30
3-1	The Co-Rh phase diagram <sup>(38)</sup> .	34
3-2	The Co-Ni phase diagram <sup>(41)</sup> .	35
3-3	Surface excess equilibrium diagram for Ni-Co alloys at 853 K <sup>(2)</sup> .	37
3-4	Measured lattice and grain boundary tracer diffusion coefficients of Ni, Co and O in NiO.	43
3-5	Arrhenius plots of parabolic oxidation constants at $P_{O_2} = 10^5$ Pa for NiO layer growth on polycrystalline, crystal faces and pre-oxidized polycrystalline nickel <sup>(69)</sup> .	48
3-6	Composition diagram of $Co_{1-x}O$ between 700°C and 1200°C showing its nonstoichiometry at several oxygen pressures <sup>(90)</sup> .	52
3-7	Parabolic rate constant measured for the growth of thick CoO films on Co in air <sup>(93)</sup> .	54
3-8	The effect of Ni concentration on the monoxide to monoxide + spinel transformation temperature in the Ni-Co-O system <sup>(89)</sup> .	57

3-9	Diffusion coefficients of $^{60}\text{Co}$ and $^{57}\text{Ni}$ in $(\text{NiCo})\text{O}$ crystals at 1445 and $1300^\circ\text{C}$ in air <sup>(102)</sup> .	59
3-10	Diffusion coefficients of $^{60}\text{Co}$ and $^{57}\text{Ni}$ in $\text{CoO}$ , $(\text{Ni}_{0.53}\text{Co}_{0.47})\text{O}$ and $\text{NiO}$ crystals as a function of temperature in air atmosphere <sup>(102)</sup> .	59
3-11	Parabolic scaling rates of $\text{Ni-Co}$ alloys exposed to 1 atm. $\text{O}_2$ at various temperatures as a function of composition <sup>(111)</sup> .	63
3-12	Master plots of $\text{CoO}$ mole fraction in $(\text{NiCo})\text{O}$ scales formed at $1200^\circ\text{C}$ in 1 atm. $\text{O}_2$ <sup>(111)</sup> .	63
3-13	Schematic presentations of oxidation behaviors of $\text{Ni-Co}$ alloys, showing the internal oxidation, $\text{Co}$ -depletion and phases of the oxide scale <sup>(111)</sup> .	65
4-1	Final back-reflection Laue pattern from the $\text{Ni-3.86Co}$ single crystal.	71
4-2	Electron channeling pattern from the $\text{Ni-3.86Co}$ $(110)$ single crystal alloy after the chemical polishing treatment.	71
4-3	An electron bombardment heating stage for the PHI 600 Scanning Auger Microprobe.	75
4-4	A fast entry, air-lock-compatible specimen holder for the electron bombardment heating stage.	76
4-5	A UHV-capable manometric assembly for the measurement of oxidation kinetics.	78
5-1	$\text{Co}$ Auger spectra.	89
5-2	$\text{Rh}$ Auger spectra.	90
5-3	Ratio of measured Auger peak-to-peak heights for scribed and sputtered $\text{Co-Rh}$ alloys.	95
5-4	Plot of Equation (5-2) to determine the average ratio of sputter yields, $Y_{\text{Rh}}/Y_{\text{Co}}$ for five $\text{Co-Rh}$ alloys.	97
5-5	The surface $\text{Rh}$ concentration, $X_{\text{Rh}}^{\text{s}}$ , for sputtered $\text{Co-Rh}$ alloys versus the bulk alloy composition.	98
5-6	The relative Auger intensity of the $\text{Co}$ 53eV peak versus bulk atomic percent $\text{Rh}$ from a bulk spectrum at room temperature and from surfaces equilibrated at high temperature.	101
5-7	The relative Auger intensity of the $\text{Rh}$ 298eV peak versus bulk atomic percent $\text{Rh}$ from a bulk spectrum at room temperature and from surfaces equilibrated at high temperature.	102
5-8	The relative Auger intensity of the $\text{Co}$ 773V peak versus bulk atomic percent $\text{Rh}$ from a bulk spectrum at room temperature and from surfaces equilibrated at high temperature.	103

5-9	The temperature dependence of the Auger peak intensities from the 19.3Rh alloy relative to those from a scratched surface at room temperature.	107
5-10	$\ln(X^S/1-X^S)$ versus $1/T$ plots for the 19.3Rh alloy.	108
5-11	$\ln(X^S/1-X^S)$ versus $1/T$ plots for the 84.7Rh alloy.	109
6-1	Parabolic plots of data from the oxidation of Ni-3.86Co (110) alloys by the hot-bare exposure technique.	117
6-2	Secondary electron images of Ni-3.86Co (110) specimens oxidized by the hot-bare technique at 673 K, $5 \times 10^{-3}$ Torr.	118
6-3	Secondary electron images of Ni-3.86Co (110) alloys oxidized by the hot-bare technique at $5 \times 10^{-3}$ Torr.	119
6-4	SIMS depth profiles of Ni-3.86Co (100) alloys after oxidation at 673 K, $5 \times 10^{-3}$ Torr.	121
6-5	Auger depth profile of a sample oxidized at 773 K, $5 \times 10^{-3}$ Torr by the hot-bare technique.	122
6-6	Transmission electron images of oxide films stripped from Ni-3.86Co (100) alloys oxidized at 673 K, $5 \times 10^{-3}$ Torr by the hot-bare technique.	123
6-7	Parabolic plots of data from the oxidation of Ni-3.86Co (110) alloys by the furnace-raised exposure technique.	126
6-8	Secondary electron micrographs of Ni-3.86Co (110) specimens oxidized at $5 \times 10^{-3}$ Torr by the furnace-raised technique.	127
6-9	TEM micrographs of stripped oxide films from furnace-raised samples.	130
6-10	Auger depth profiles of specimens oxidized by the furnace raised technique.	133
6-11	Parabolic plots of data from the oxidation of the Ni-4.0Co polycrystalline alloy at $5 \times 10^{-3}$ Torr by the furnace-raised technique.	137
6-12	Secondary electron micrographs of Ni-4Co polycrystalline specimens after oxidation at $5 \times 10^{-3}$ Torr.	138
6-13	TEM micrographs of oxide films stripped from polycrystalline Ni-4Co alloys.	139
6-14	Auger depth profiles of Ni-4Co polycrystalline specimens after oxidation at $5 \times 10^{-3}$ Torr.	141
6-15	Calculated and experimental composition profiles of specimens oxidized by the furnace-raised technique at $5 \times 10^{-3}$ Torr.	163

6-16	Calculated and experimental composition profiles of Ni-4.0Co polycrystals oxidized at $5 \times 10^{-3}$ Torr.	169
6-17	$D_{Co,eff}$ values derived from experimental data.	173

## LIST OF TABLES

Table		Page
3-1	Self-diffusion of Ni and O in NiO	41
3-2	Tracer diffusion of Co in NiO and Ni and Co in (NiCo)O.	61
4-1	Impurity contents of cobalt, 99.98% a/o pure, and rhodium, 99.97% a/o pure given as parts per million atomic.	69
4-2	Analysis of Co-Rh alloys in atomic % Rh.	69
4-3	Impurity contents of nickel rod (batch no. 08715) as supplied by Johnson Matthey Chemicals Limited given as parts per million by weight.	73
4-4	Impurity contents of Ni-5Co alloy as determined by glow discharge mass spectrometry (ppm by weight).	73
4-5	Uncertainty of pressure readings for an MKS Instruments 1mmHg type 315 differential sensor head.	81
4-6	Typical operating conditions used in AES measurements.	83
4-7	Typical operating conditions used in SIMS measurements.	86
5-1	Surface concentration changes calculated from signal intensity ratios ( $I_i^{sb}/I_i^b$ ) for the two alloys showing segregation.	106
5-2	Enthalpy and entropy of segregation values calculated from the slopes and intercepts of Figures (5-10) and (5-11).	106
5-3	Experimental and calculated surface tension values for Co and Rh.	113
6-1	Average grain diameters of stripped oxide films from polycrystalline Ni-4.0Co alloys measured from TEM BF images	143
6-2	Instantaneous parabolic rate constants for oxidation of (110)Ni-3.86Co and Ni-4.0Co polycrystalline alloys at $5 \times 10^{-3}$ Torr.	144
6-3	Calculated values of $D_{all}$ and $\rho$ based on analysis of experimental composition profiles in (NiCo)O films.	156
6-4	An evaluation of the parameter $\beta$ for polycrystalline (NiCo)O oxides based on a comparison of experimental and calculated $k_{p,eff}^*$ values.	161

## CHAPTER 1

### INTRODUCTION

An understanding of the chemical and physical properties of interfaces is essential in many areas of science and engineering, including biology, catalysis, corrosion, high temperature oxidation, and wear. Interfacial properties may be influenced by many factors such as the bulk composition, impurity segregation, oxidation, phase transformations and radiation damage, to name only a few. Clearly, the study of interfaces and near-surface phenomena (including thin films) covers a broad range of disciplines and interests.

Over the last two decades, progress in these areas has been aided immensely by the development of a host of surface analytical techniques. It is now routinely possible to examine the structure and composition of solid surfaces and films which may correspond to thicknesses of less than one atomic layer. One of the most widely used spectroscopies for the measurement of near surface composition is Auger electron spectroscopy, AES. With the aid of this and other techniques, researchers have made extensive investigations leading to an improved understanding of the chemical and physical properties of atomically clean metals and alloys as well as the earliest stages of the interaction of these surfaces with reactive atmospheres. In particular, there is now a substantial body of literature related to the thermodynamics and kinetics of adsorption or segregation at solid surfaces and

interfaces. This growing experimental database has led to increasingly detailed models which attempt to theoretically explain the observed segregation phenomena.

The thermodynamic principles of adsorption or segregation were set forth by Gibbs<sup>(1)</sup> over a century ago. Many authors have since proposed refinements to this theory which attempt to correlate the observed adsorption behaviour to other experimentally measurable parameters. Two principle intrinsic factors have generally been used to predict the constituent of a homogeneous binary alloy which will be enriched at the surface relative to the bulk. These are the differences in chemical bond strength and atomic size. However, there is less agreement about the the actual extent of segregation, which is mainly due to the relative importance assigned to each of these factors. Additionally, there are differences in the exact way in which the two driving forces are represented and in the choice of the most appropriate correlating physical property.

The surface segregation measurements comprising the first part of this thesis research were initiated on a model system, Co-Rh, as a further test of the current theories of segregation. These alloys were an interesting choice for experimental investigation because the two driving forces described earlier theoretically work in opposite directions for this system. This indicated that a changeover of the segregating species might occur depending on which element acted as the solute species. A review of the literature was conducted which failed to find any previous experimental work on the segregation behaviour of Co-Rh alloys.

Co-Ni alloys have also been the subject of surface segregation investigations, but for somewhat different reasons. Prior to the work of Hajcsar and coworkers<sup>(2,3)</sup> the few experimental data for this system had been contradictory regarding the nature and extent of the surface enrichment in this system. This situation was thought to be due to the fact that nickel and cobalt are very close in atomic size and

chemical binding energy, leading to very small predicted driving forces for segregation. In an attempt to resolve these differences and also to demonstrate the feasibility of using the most surface sensitive LVV Auger electron peaks as quantitative indicators of composition, further studies were conducted at McMaster University. In these investigations digital spectrum simulation techniques were also employed as a method of deconvoluting overlapping Auger transitions from the two elements, which is another reason that study of this system is difficult. Similar analysis techniques were used to study the Co-Rh alloys. The early stages of oxide nucleation and film formation are also of interest for the Co-Ni system, but experiments in this area were limited to the nucleation and growth stages of oxide islands at low oxygen pressures.

Another important surface-related phenomenon is that of corrosion, which in its broadest sense, refers to the chemical attack of a material by reaction with its environment. The basis of corrosion protection for most metals and alloys used at high temperatures is the formation of a protective oxide layer which significantly reduces the rate of further attack by acting as a barrier to the transport of reactants between the metal and the reactive environment. These transport properties are dependent on many physical and chemical properties of the oxide. It is therefore important to have as complete a physical and chemical description of the reaction layers as possible in order to fully understand the corrosion reaction.

The oxidation of alloys in various reactive atmospheres may result in a seemingly limitless number of oxide morphologies and reaction rates. However, by restricting their attention to simpler alloy systems in controlled atmospheres, researchers have attempted to classify the possible limiting cases which may naturally occur. The basic principles which are derived from this type of research may then be applied to the design of more complex engineering materials.

At elevated temperatures and oxygen partial pressures, Co-Rh and Ni-Co alloys can be expected to develop different steady state oxide scale morphologies. This prediction may be made upon consideration of the relative thermodynamic stabilities and diffusivities of components in each of the possible oxide phases. Co-Rh alloys are a particular example of a more general class of noble metal alloys. While the oxidation properties of this system have not been examined experimentally, their behaviour is expected to be similar to other single phase binary systems in which one component is selectively oxidized, while the other more noble component remains thermodynamically inert. Scale morphologies which may be produced in these systems have been reviewed by Whittle<sup>(4)</sup> and Smeltzer<sup>(5)</sup> along with models based upon ternary diffusion and solution thermodynamics which may account for the observed growth mechanisms.

The oxides of cobalt and nickel exhibit complete oxide solubility and hence represent the simplest of binary systems under conditions in which both components are oxidizable. The relative proportions of each species in a uniform external oxide scale are therefore determined by the relative oxidation potentials and diffusivities of each component in the two solid phases. A ternary diffusion model for this type of growth was first proposed by Wagner<sup>(6)</sup> in 1969. His theory was subsequently used to interpret the oxidation behaviour of a number of systems (including Ni-Co-O) displaying this type of growth morphology.

While there appears to be a sound theoretical basis for our understanding of these two limiting types of binary alloy oxidation, much more experimental data related to thermodynamic, diffusional and oxidation properties is presently available for the Ni-Co-O system than for the Co-Rh-O system. In order to extend and evaluate the potential application of these oxidation models at lower temperatures where alternative growth mechanisms may come into play, this independent data

becomes very important. Hence, the Ni-Co system was selected for further oxidation study in the latter part of this thesis. These experiments were intended to explore the thin film range of solid-solution oxide growth at intermediate temperatures. Until recently, very little experimental work has been done in this area.

At sufficiently high temperatures the transport of reactants through oxides of the transition metals and their alloys is primarily controlled by ambipolar diffusion of lattice point defects (i.e. vacancies and electronic defects) in the bulk oxide. However, at low or intermediate temperatures of up to approximately one-half of the oxide melting temperature, there is now sufficient evidence to conclude that diffusion through low activation sites, such as oxide grain boundaries is the main rate determining process. The growth rates of monophasic scales on zirconium, nickel and chromium have been quantitatively interpreted by mechanisms involving short-circuit diffusion where independently determined diffusion data were available<sup>(5)</sup>. Previous experimental work on solid solution oxides has been concentrated in the high temperature range (i.e. above 1000°C), so that these alternative diffusion mechanisms did not have a significant influence on the oxidation process. Recent published tracer diffusion data for the grain boundary transport of Ni, Co and O in NiO now make it feasible to include these types of diffusion processes in the analysis of low temperature (NiCo)O film growth. Oxidation experiments were therefore performed on Ni-Co alloys between 673 and 1073 K in order to investigate the kinetics, structural development and chemical composition of (NiCo)O solid solution oxides at intermediate temperatures.

## CHAPTER 2

### THEORY

#### 2.1 Introduction

The physical and chemical states of an alloy and its surface are determined by both internal and external driving forces which may come to bear on the system. In an ultra-high vacuum environment, the external influence of pressure and the possibility of a reaction with the surrounding medium are essentially removed, so that changes in the surface state are mainly governed by temperature and the composition of the bulk system. Under these conditions, and given sufficient time, a semi-infinite bulk alloy and its surface will reach some final equilibrium or steady state condition.

Introducing a reactive gas into the surrounding medium may alter this equilibrium state, due to chemical interactions between the surface of the alloy and the new environment. Very often, new phases form at the alloy-gas interface, and unless they are volatile, these reaction products may retard or inhibit further reaction between the alloy and gas. This is expected, since contact between the alloy and the environment is now limited by transport of reactive species through the intermediate layer.

The present chapter has been prepared in order to give an outline of the relevant theoretical models pertaining to surface segregation and oxidation of binary

alloy systems. This review is therefore divided into two main sections dealing first with segregation followed by a discussion of metal and alloy oxidation. For a more detailed description of these processes, the reader is referred more comprehensive works on segregation<sup>(7-9)</sup> and oxidation<sup>(10-14)</sup>.

## 2.2 Surface Segregation On Binary Alloys

### 2.2.1 Classical Thermodynamics and Quasichemical Models

The selective segregation of the constituent elements of alloys was first predicted thermodynamically by Gibbs more than a century ago<sup>(1)</sup>. However, substantial investigation of his predictions has only taken place in the last two decades with the development of ultrahigh vacuum (UHV) techniques and surface sensitive spectroscopies such as Auger electron spectroscopy (AES). In an attempt to compare the growing experimental database with the Gibbsian model, a number of approximations have been proposed, which usually attempt to relate the observed segregation to experimentally measurable parameters such as elemental surface tensions, heats of formation and elastic constants. In general, however, most of the current theories can be divided into two main categories, characterized by the specification of the force(s) driving the segregation; these are the "bond breaking" and "lattice strain" theories.

The bond breaking theories consider the difference in binding energy of the components in a binary alloy as the driving force for segregation. The element having the lowest bond energy will tend to be enriched at the surface so that an overall reduction in the surface free energy of the system is realized. Lattice strain theories predict segregation on the basis of size differences in the two components.

Solute elements with atomic radii considerably different from that of the solvent will have associated with them an elastic strain field which may be partially or completely released by moving the solute to a surface site. An excellent review of these models has been given by Kelley and Ponec<sup>(7)</sup>.

For a binary single phase solid solution alloy system, assuming that the segregation is confined to the monolayer of atoms closest to the surface, the concentration of element 1 at the surface,  $X_1^s$ , relative to that in the bulk,  $X_1^b$ , is given by

$$\frac{X_2^s}{X_1^s} = \frac{X_2^b}{X_1^b} \exp \left[ -\frac{\Delta G_{seg}}{RT} \right], \quad (2-1)$$

where  $\Delta G_{seg}$  is the molar free energy difference associated with the exchange of atoms of element 2 in the bulk with atoms of element 1 on the surface. In general,  $\Delta G_{seg}$  is written in terms of an enthalpy and entropy as

$$\Delta G_{seg} = \Delta H_{seg} - T\Delta S_{seg}, \quad (2-2)$$

where the entropy of mixing due to segregation can be determined entirely in terms of the grand canonical ensemble model of thermodynamics.

Within the bond breaking category, at the simplest level of approximation, called the ideal solution model, the heat of mixing for the alloy is assumed to be zero, so that  $\Delta H_{seg}$  is given by

$$\Delta H_{seg} = \frac{Z-Z^s}{Z} (\Delta H_2^{sub} - \Delta H_1^{sub}), \quad (2-3)$$

where  $Z^s$  is the coordination number of a surface atom,  $Z$ , the coordination number of a bulk atom and  $\Delta H_i^{sub}$  is the heat of formation of a gaseous atom from the element in its standard state. Alternatively, some authors use

$$\Delta H_{seg} = (\sigma_2 - \sigma_1)\alpha, \quad (2-4)$$

where  $\sigma_i$  is the solid surface tension of the pure element and  $\alpha$  is the molar surface

area. At the next higher level of approximation, the regular solution model, extra terms are added to  $\Delta H^{\text{seg}}$  to account for a finite heat of mixing.

In the "lattice strain" models  $\Delta H^{\text{seg}}$  is calculated on the basis of linear elasticity theory. Eshelby<sup>(15)</sup> has obtained the following expression for the elastic energy associated with a solute atom in terms of the shear modulus of the solvent:

$$E_{\text{el}} = (16/3)\pi G_1 r_1 (r_2 - r_1)^2, \quad (2-5)$$

where  $G_1$  is the shear modulus of the solvent and  $r_1$  and  $r_2$  are the solvent and solute radii, respectively. This energy is assumed in segregation models to be totally released when the solute atom is moved to the surface plane of atoms.

Neither the bond breaking models or the lattice strain theories alone agree with all of the experimentally observed segregation phenomena. As a result, more recent models have combined the two contributions in order to more accurately predict segregation. One such model is that of Abraham and Brundle<sup>(8)</sup>, whose approach is to minimize the total energy of a binary system (at 0 K) through atomic relaxation consistent with long-range, pairwise interactions between atoms. They introduce the concept of the  $\gamma^* - \sigma^*$  coordinate plane (Figure 2-1) divided into regions where solute segregation is or is not expected to occur.  $\gamma^*$  is the surface tension ratio and  $\sigma^*$  is the size ratio. From the calculations of the total system potential energy they derive a driving force,  $\Delta Q_{\Psi}$ , for a variety of bond strength and size ratios. The  $\Delta Q_{\Psi} = 0$  curve separates the regions of solute segregation or no solute segregation, the position of the curve depending on the choice of the interatomic potential used, which in this case was a Lennard-Jones 12:6 type.

Almost all binary alloys studied experimentally to the present come in two of the four quadrants of the  $\gamma^* - \sigma^*$  plane, as shown in Figure (2-1). These quadrants are

Figure (2-1)

The  $\gamma^*$  vs.  $\sigma^*$  (surface tension versus atomic size ratio) representation for the prediction of segregation on binary alloys. Solute enrichment is predicted if the ratios place an alloy below the zero energy curve. The positions of the Co-Rh and Rh-Co alloy points indicate that Rh segregation may occur on the former, while Co enrichment is expected on the latter. The other smaller and closed symbols are for experimental measurements of segregation in other binary alloys. (8)

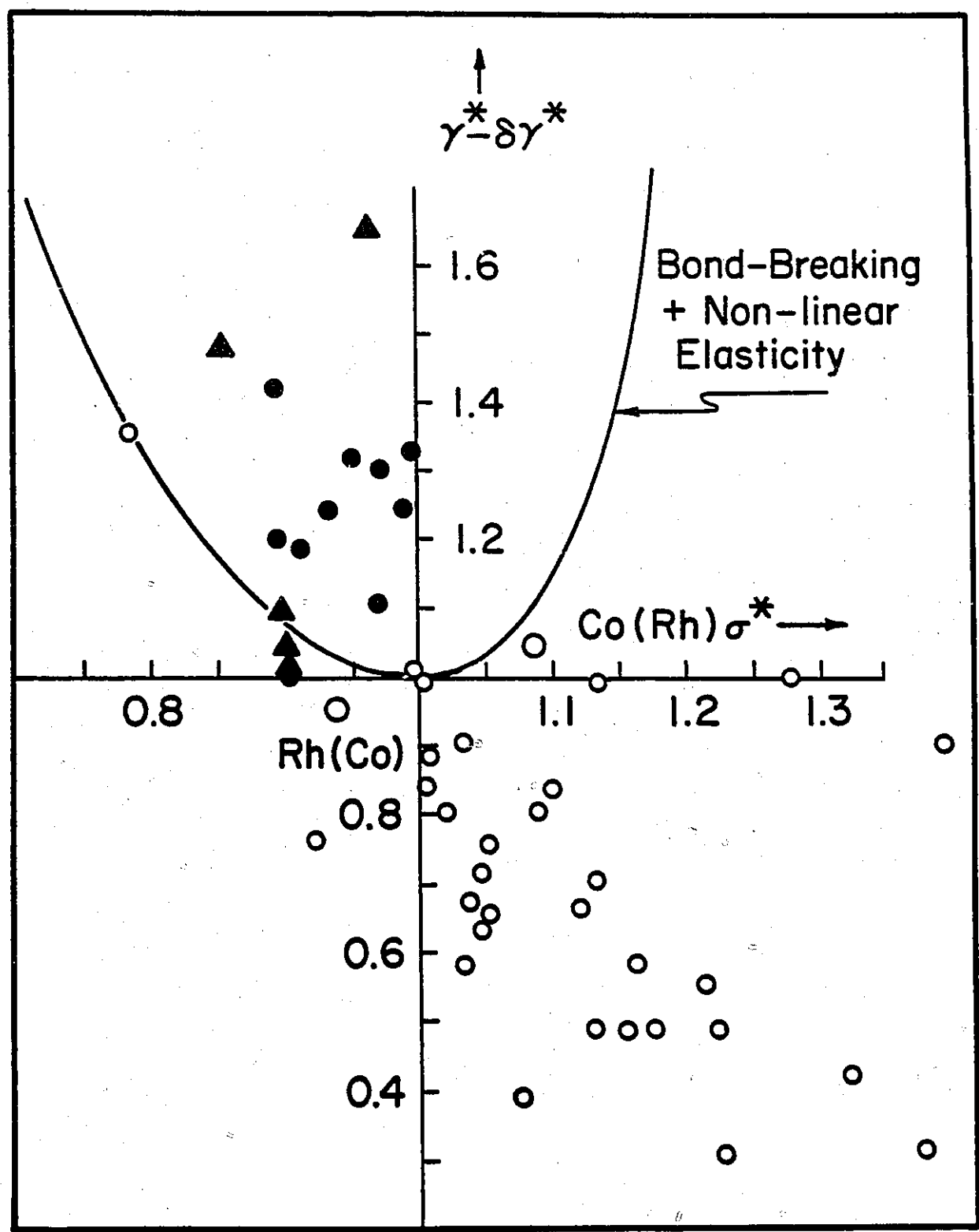


Fig. (2-1)

$$\begin{aligned} \gamma^* &\geq 1, \sigma^* \leq 1; \\ \gamma^* &\leq 1, \sigma^* \geq 1. \end{aligned}$$

In the first class no solute segregation was generally observed. In the second class the systems exhibited solute segregation. For cobalt–rhodium alloys, however, the theoretical points lie in the other two quadrants:

$$\begin{aligned} \gamma^* &> 1, \sigma^* > 1 \text{ [Co(Rh): } \gamma^* = 1.06, \sigma^* = 1.08\text{]}; \\ \gamma^* &< 1, \sigma^* < 1 \text{ [Rh(Co): } \gamma^* = 0.94, \sigma^* = 0.93\text{]}. \end{aligned}$$

This makes this system an interesting one to study since for rhodium rich alloys both bond breaking and strain energy considerations favour cobalt segregation because both the surface tension and size ratios are less than unity. For cobalt rich alloys, however, the values resulting from these two ratios still favour solute segregation which now predicts rhodium enrichment.

### 2.2.2 Monte Carlo and Electronic Calculations

More sophisticated computational and theoretical approaches have been applied to the prediction of surface segregation on binary alloys, based on Monte Carlo simulations and electron band filling.

Monte Carlo calculations<sup>(16–18)</sup> start with a random placement of the alloying elements in a crystal lattice. The crystal lattice configuration may correspond to a semi-infinite slab, a thin film, or a small particle. In any case, the initial atomic distribution is allowed to relax to its lowest energy state through repeated trial exchanges of randomly picked neighbouring atoms. For each step of the calculation, if the exchange of neighbouring atoms results in a decrease in the total energy of the system, then the new atomic configuration is adopted. To reach the final equilibrium state, these methods obviously require a large number of calculations.

Additional complexity may also be introduced by allowing for variations in bond energy between atoms, depending on the coordination number. The attractiveness of these techniques lies in their ability to predict atomic configurations explicitly. They have been used to not only predict the sense of segregation, but also to show how the variation in atomic concentration may change as a function of depth from the surface of the alloy.

Electron band energy models<sup>(19,20)</sup> seek to calculate the segregating component at the surface of an alloy based on the tight-binding approximation. First, the electron energy levels are predicted for a certain arrangement of atomic cores. These energy levels depend on the choice of the interatomic potentials used in the model. The available electrons are then allowed to fill these energy levels beginning with the lowest energy state. The final energy of the system is then determined and a surface segregation prediction is based on minimizing the internal energy with respect to composition in each plane for a fixed total number of atoms in the system. The results of Kerker and coworkers indicated that for  $n_A, n_B \leq 5$  and  $n_A < n_B$ , where  $n$  represents the number of  $d$  electrons per atom, enrichment of A atoms would occur. However, for  $n_A, n_B \geq 5$  and  $n_A < n_B$ , surface enrichment of B atoms on the surface was predicted.

### 2.3 The Oxidation Of Metals And Alloys

Most metals and alloys, when subjected to a gaseous oxidizing atmosphere at sufficiently high temperatures and pressures, spontaneously react to form intermediate layers of reaction products in the vicinity of the original solid/gas interface. Further reaction between the metal and its environment is usually controlled by diffusion of either the metal or oxidizing species through this

superficial zone. These transport rates depend on factors such as the oxide crystal structure, composition, lattice defects (vacancies, interstitials, dislocations, grain boundaries, etc.) phase distribution and scale morphology. If the properties of the oxide are sufficiently well known, the oxidation kinetics can often be predicted with reasonable accuracy from models based on solid state diffusion of reactants.

### 2.3.1 The Oxidation of Pure Metals

Wagner<sup>(21)</sup> has advanced a phenomenological theory to account for the parabolic scaling rates of single phase scales based upon ambipolar diffusion (charge transport with no net electrical current) of reactants. The independent migration of ions and electrons under the influence of an electrochemical potential gradient can be described by flux equations of the type

$$J_i = -C_i B_i \left[ \frac{d\mu_i}{dx} + q_i \frac{dV}{dx} \right] \quad (2-6)$$

where  $q_i$ ,  $C_i$  and  $B_i$  are the charge, concentration and mobility of species  $i$ . The first term in brackets represents the chemical potential gradient, while the second term corresponds to the electrical potential gradient. Wagner equated the total flux of positive and negative species and utilized the local equilibrium concept at interfaces to obtain an expression for the total flux of matter in the oxide scale. By equating the mobilities with conductivity and transport numbers this was expressed as

$$\bar{J} = \bar{J}_M + |\bar{J}_O| = \frac{1}{|z_O| F} (t_M + t_O) t_e K \frac{d\mu_O}{dx} \quad (2-7)$$

Here  $\bar{J}$  is the total flux of matter in equivalents per  $\text{cm}^2 \text{sec}$ ,  $z_O$  is the number of elementary charges on the oxygen ion ( $|z_O| = +2$ ),  $F$  is the Faraday constant,  $t_i$  are the transport numbers ( $t_M + t_O + t_e = 1$ ) and  $K$  is the conductivity. For a scale which

is a metal conducting semiconductor,  $t_e=1$ . Integrating (2-7) over the scale thickness,  $X$ , under the assumption that only the metal ions are mobile leads to

$$\bar{J} = \frac{RT}{|z_O| F^2 X} \int_{a_O}^{a_O''} t_M K da_O \quad (2-8)$$

where the oxygen chemical potential is now expressed as an activity,  $a_O$ . The single and double superscripts refer to the alloy-scale and scale-gas interfaces, respectively. Conductivity may be expressed in terms of the self diffusion coefficients, leading to an expression for the parabolic scaling rate.

$$k_r(\text{eq/cm}^2) = \bar{C}_{\text{eq}} \int_{a_O}^{a_O''} \frac{z_M}{|z_O|} D_M da_O \quad (2-9)$$

where  $\bar{C}_{\text{eq}}$  is the average concentration of metal or oxygen per unit volume ( $\text{eq/cm}^3$ ) and  $D_M$  is the metal ion self-diffusion coefficient.

This theory has been used to interpret the reaction kinetics of a number of transition metals which form a single-phase oxide scale at elevated temperatures. In cases where deviations from an exact parabolic relationship have been observed, the scales often exhibited structural features which were associated with alternative transport mechanisms. Furthermore, the diffusion of reactants may be complicated by the presence of more than one type of lattice defect.

### 2.3.2 The Oxidation of Alloys

The various scale morphologies and growth mechanisms arising from the oxidation of multicomponent alloys at elevated temperatures are of such diversity that it is worthwhile to consider the simplest limiting cases observed for certain groups of binary alloys. The general principles derived from this type of research

have been used in the design of alloys intended for high temperature engineering applications.

Summaries of binary alloy oxidation and sulfidation behaviour have been prepared in which the steady state phase distributions and elemental composition profiles were shown on schematic two-dimensional cross-sections through the oxide and alloy. An example of this type of representation is given in Figure (2-2) from a survey by Bastow and coworkers<sup>(22)</sup>. The growth of these reaction products may be described by ternary thermodynamics and diffusion models. These models have been used to predict the conditions necessary for the development of certain limiting scale morphologies. Alternatively, ternary diffusion processes in multiphase systems may be conveniently represented on an isothermal A-B-O phase diagram using the concept of diffusion paths. In the following sections two types of binary alloy oxidation will be discussed. These are the selective oxidation of one component of noble metal alloys and the formation of solid solution oxide scales, which are the growth mechanisms of relevance to alloys such as Co-Rh and Ni-Co.

### 2.3.3 The Diffusion Path Concept

Diffusion composition paths are a useful and compact way of representing ternary diffusion behaviour arising from the oxidation or sulfidation of binary alloys. They were first used by Rhines<sup>(23)</sup> as a means of predicting the sequence of oxide phases which developed on copper alloys. Kirkaldy and Brown<sup>(24)</sup> later developed a set of theorems related to the construction of these paths on ternary isothermal diagrams. A review of these concepts as they apply to binary alloy oxidation and the Fe-Ni, Fe-Cr and Ni-Cr systems in particular was conducted by Dalvi and Coates<sup>(25)</sup>.

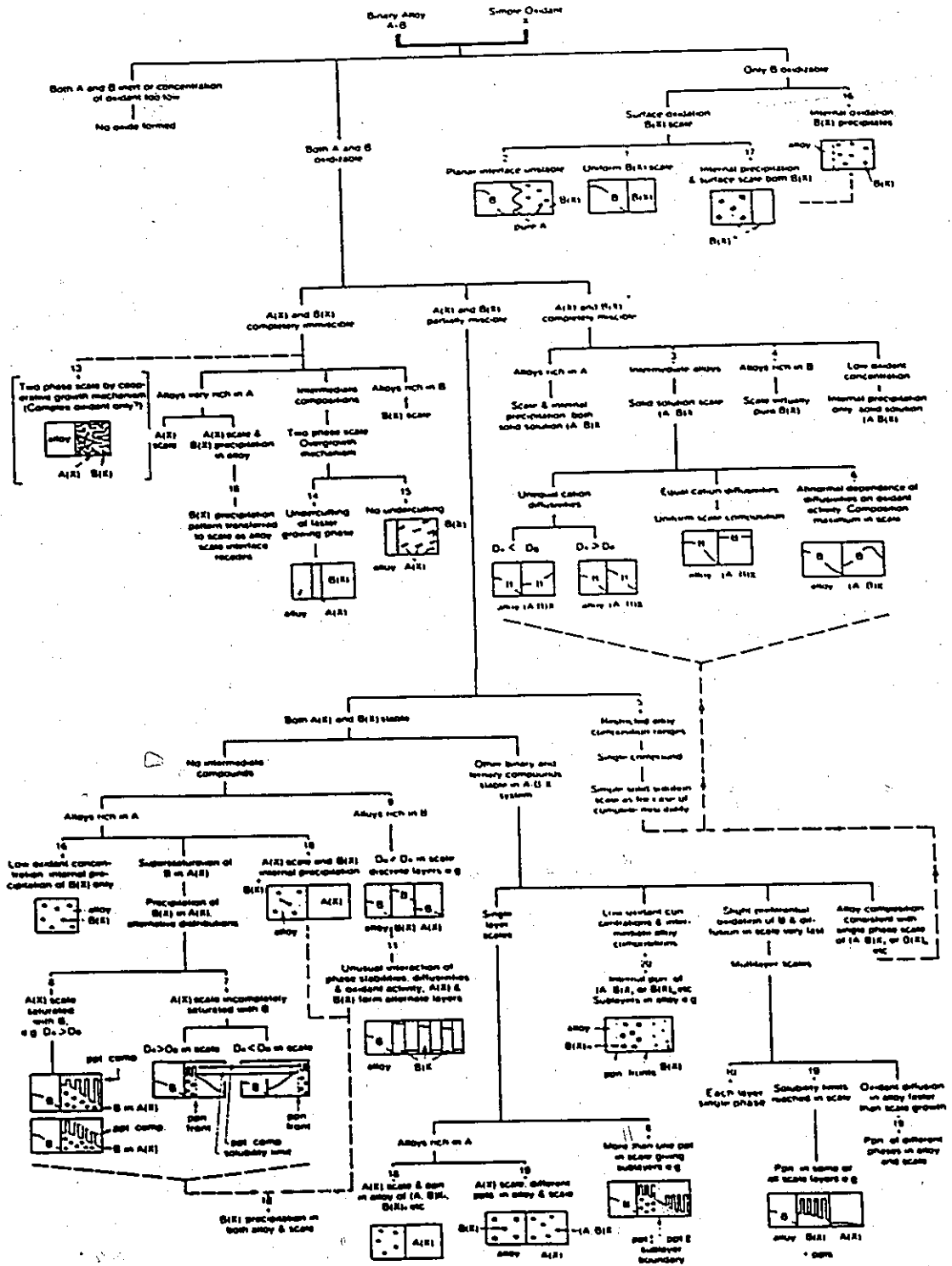


Figure (2-2)

Schematic representation of the relationships between scale morphologies on binary alloys. (22)

Using this method, the locus of compositions is traced out through the sequence of phases extending from the unoxidised bulk alloy to the oxygen atmosphere. A virtual diffusion path is obtained from calculations based upon a given sequence of single phase layers having planar interfaces. This sequence of phases is assumed to exist under steady state conditions, such that the expressions for the composition for each species are independent of distance and time in the final  $(x/\sqrt{t})$  parametric formalism. The virtual path may be unstable (i.e. may penetrate across tie line in a two phase field), corresponding to a zone of supersaturation which could develop interfacial instabilities and/or a zone of internal precipitation. In these cases the actual diffusion path would differ from the virtual path to reflect these processes. Examples of the diffusion path representation are given in the following discussions of limiting types of binary alloy oxidation.

#### 2.3.4 Single Phase Scale Formation on Noble Metal Alloys

A schematic illustration of scale formation on noble metal alloys is shown in Figure (2-3). In addition, typical diffusion paths have been placed on the ternary phase and alloy- $P_{O_2}$  diagrams corresponding to the four morphological developments. In all cases component B is selectively oxidized to form the single phase oxide BO which is present as (a) a complete external layer, (b) an external layer containing undissolved particles of pure A, (c) an internal precipitation zone of BO beneath an external BO scale or (d) only internal particles of BO.

The main parameters governing the development of a particular morphology are the bulk alloy composition, oxygen solubility and diffusion in the alloy phase. Wagner<sup>(26)</sup> has advanced a model for the critical solute concentration for the transition from internal to exclusive external scale formation. Assuming that the

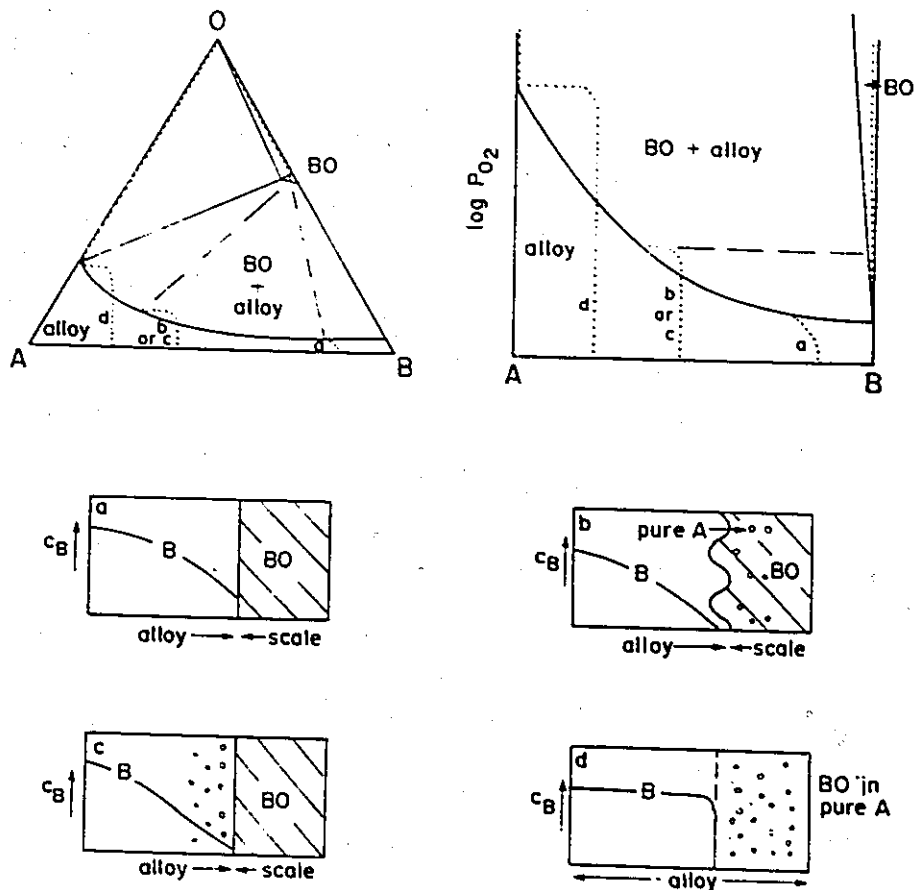


Figure (2-3) Schematic phase diagram isotherm and equilibrium oxygen pressure diagram for noble metal alloys showing typical diffusion paths and concentration profiles: (a) BO scale formation; (b) or (c) interfacial instability or internal oxidation; (d) internal oxidation (4).

alloy behaves as an ideal solution (i.e that metal and oxygen diffuse down their own concentration gradients with no ternary interactions), then the condition for exclusive external scale formation was expressed as

$$N_B^O \geq \frac{F(u) + (1/v)(D_O/D_{AB})^{1/2} u \pi^{1/2}}{1 + (1/v)(D_O/D_{AB})^{1/2} u \pi^{1/2}} \quad (2-10)$$

where  $N_B^O$  is the bulk concentration of B,  $D_{AB}$  and  $D_O$  are the interdiffusion coefficient and the oxygen diffusion coefficient in the alloy, respectively.  $u$  in this expression replaces  $\sqrt{k/2D_{AB}}$ , where  $k$  is a parabolic constant which describes the rate of recession of the alloy-oxide interface.  $F(u)$  is an auxiliary function defined by

$$F(u) = \sqrt{\pi} u \exp u^2 \operatorname{erfc} u \quad (2-11)$$

and  $v$  is the ratio of oxygen to metal in the oxide ( $BO_v$ ). The minimum content of B necessary to form an exclusive external scale is seen to increase with increasing O diffusivity in the alloy and decrease with a higher alloy interdiffusion coefficient.

This criterion has been modified by Smeltzer and Whittle<sup>(27)</sup> to include the effects of ternary thermodynamics and diffusion in the alloy phase. These authors have also shown that the onset of internal oxidation can be correlated to diffusion paths drawn on the ternary and alloy- $P_{O_2}$  phase diagrams. External scale formation alone occurs when the virtual diffusion path in the alloy phase contacts the oxygen solubility curve for the alloy. This is a case where the virtual and actual diffusion paths are coincident. External scale formation accompanied by internal oxidation or internal oxidation alone occur when the virtual diffusion path for the alloy cuts into and across the two-phase alloy/oxide field. These paths are representative of oxygen supersaturation and oxide precipitation and as a consequence, the virtual diffusion paths do not correspond to the actual diffusion paths. The actual diffusion paths will be shifted to reflect reduced concentrations of

B and O in the internal oxidation zone after precipitation and a steeper rise in the concentration of B to the bulk concentration value beyond this zone.

### 2.3.5 Formation of Solid Solution Oxide Scales

Schematic ternary and alloy-P<sub>O</sub><sub>2</sub> phase diagrams for a system in which both alloy and oxide exhibit complete solid solubility are shown in Figure (2-4). Diffusion paths representing alternative concentration profiles in the alloy and oxide phases are indicated for four limiting cases, where  $D_A$  and  $D_B$  now represent the diffusivities of A and B in the oxide phase. The distributions of A and B across the oxide are seen to be dependent upon their relative diffusivities.

The first comprehensive diffusion theory describing the growth of a ternary solid solution oxide upon a binary alloy was published by Wagner<sup>(6)</sup> in 1969. This theory describes the oxidation process in terms of a flux of cations, A and B, through the bulk oxide lattice from the alloy-scale interface to the scale-gas interface where they react with the nonmetal, X. Diffusion of the anionic species was assumed to occur at a much slower rate and was not included in the analysis. Wagner considered the oxide to be a single phase, uniform in thickness and free of any defects such as voids and cracks, while the underlying alloy was treated as a semi-infinite slab. The migration of reactants was presumed to occur strictly by ambipolar diffusion of each species and local thermodynamic equilibrium was assumed to exist within any given volume element of the scale. In general, the diffusion coefficients of A and B were expected to differ, giving rise to the possibility of composition gradients within the oxide and the alloy.

A schematic illustration of the Wagner model is shown in Figure (2-5). Diffusion profiles which develop in the alloy,  $N_B(\lambda)$ ; and in the oxide,  $\xi(y)$ , are

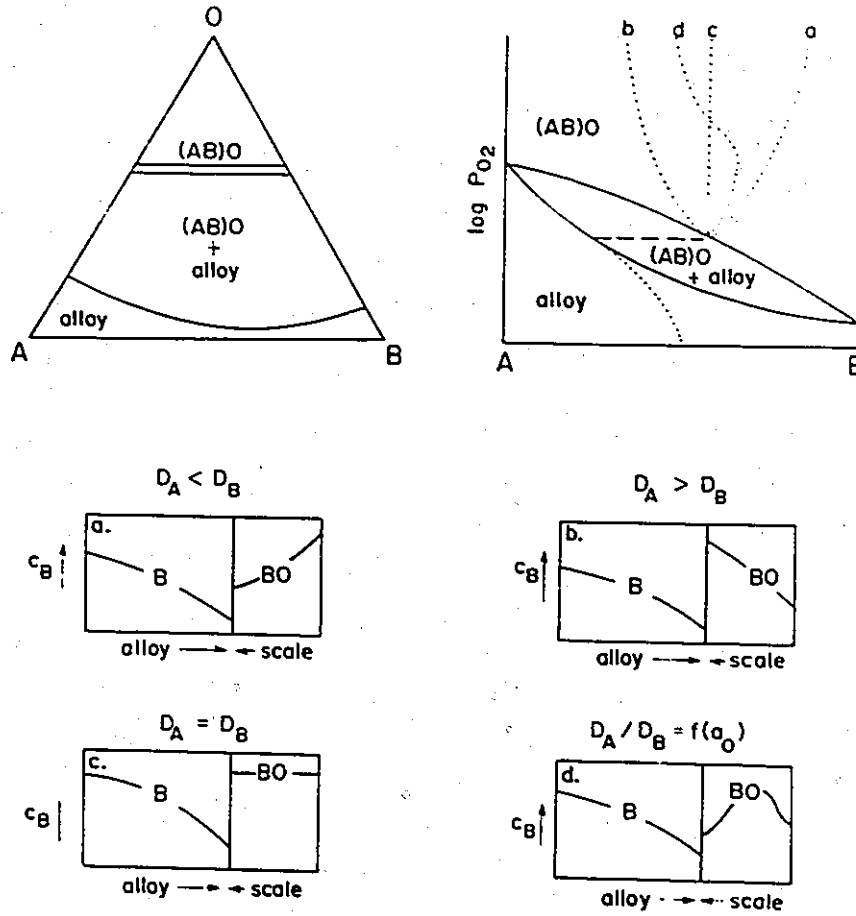


Figure (2-4) Schematic phase diagram isotherms and equilibrium oxygen pressure- alloy diagram for a system in which the oxide and alloy phases are solid solutions. Typical diffusion paths and composition profiles in the alloy-scale model are shown for different relative values of the metal diffusivities in the oxide phase (4).

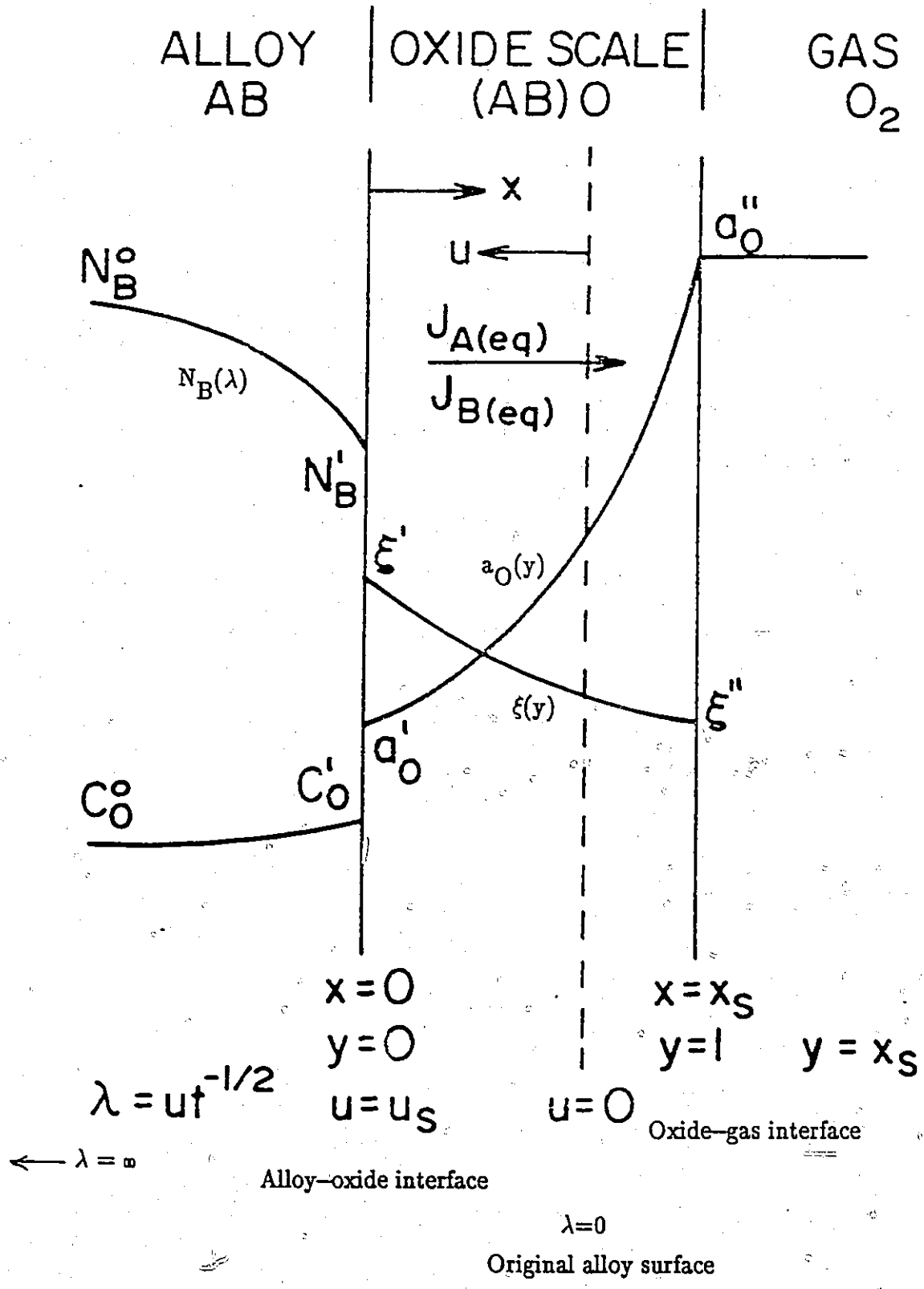


Fig. (2-5)

shown, along with the activity of oxygen,  $a_O(y)$ . The coordinate system for diffusion in the alloy has its origin at the original alloy surface,  $u=0$ . However, by replacing  $u$  with the parameter  $\lambda = u/t^{1/2}$ , the profile in this phase becomes time independent. Similarly, in the oxide scale, the coordinate  $x$ , representing distance from the alloy oxide interface, is replaced by  $y = x/x_s$ .

Using the above assumptions, Wagner derived two coupled equations which describe the flux of metal cations in the scale in terms of a fractional thickness,  $y$ , the parabolic rate constant,  $k$ , and the metal and oxygen activity gradients. The diffusion flux of B across the scale from Fick's first law is given in equivalents per unit cross section, per unit time, as

$$J_B = -\frac{D_B \xi}{V_{eq}} \frac{d \ln a_B}{dx} \quad (2-12)$$

where  $\xi$  is the mole fraction of BO and  $V_{eq}$  is the volume per equivalent of compounds AO and BO. When the activity of B is expressed in terms of activities of oxygen,  $a_x$ , and oxide,  $a_{BO}$ , this becomes

$$J_B = -\frac{D_B \xi}{V_{eq}} \left[ \frac{\partial \ln a_{BO}}{\partial \xi} \cdot \frac{\delta \xi}{\delta x} - \frac{Z_B}{Z_O} \cdot \frac{\partial \ln a_O}{\partial x} \right] \quad (2-13)$$

Here,  $Z_B$  and  $Z_O$  are the absolute valences of B and O respectively. A similar expression is derived for element A, which combined with (2-13), gives an expression for the rate of thickening of the scale:

$$(J_A + J_B) V_{eq} = \frac{dx_s}{dt} = \frac{k}{x_s} \quad (2-14)$$

where  $k$  is a parabolic scaling constant. Together with  $y = x/x_s$ , Wagner expressed the parabolic scaling rate as

$$D_A(1-\xi) \left[ \frac{\partial \ln a_{AO}}{\partial \xi} \cdot \frac{d\xi}{dy} + \frac{Z_A}{Z_O} \cdot \frac{d \ln a_O}{dy} \right] + D_B \xi \left[ \frac{\partial \ln a_{BO}}{\partial \xi} \cdot \frac{d\xi}{dy} + \frac{Z_B}{Z_O} \cdot \frac{d \ln a_O}{dy} \right] = k. \quad (2-15)$$

A second equation was derived by using Fick's second law to represent the mass balance in a given volume element of the mixed oxide:

$$y k \frac{d\xi}{dy} = \frac{d}{dy} \left[ D_B \xi \left[ \frac{\partial \ln a_{BO}}{\partial \xi} \cdot \frac{d\xi}{dy} + \frac{Z_B}{Z_O} \cdot \frac{d \ln a_O}{dy} \right] \right] \quad (2-16)$$

The distribution of element B in the alloy is also a solution of Fick's second law and was expressed in terms of  $\lambda$  as

$$\frac{d}{d\lambda} \left[ D_{\text{all}} \cdot \frac{dN_B}{d\lambda} \right] + \frac{1}{2} \lambda \frac{dN_B}{d\lambda} = 0; \quad \lambda = \frac{u}{\sqrt{t}} \quad (2-17)$$

where  $D_{\text{all}}$  is the alloy interdiffusion coefficient,  $N_B$  is the mole fraction of B and  $u$  is a coordinate of distance measured into the alloy from the original alloy surface position at  $t=0$ .

The boundary conditions necessary for the solution of these equations are the gas phase oxygen activity,  $a_O''$ , the bulk mole fraction of B in the alloy,  $N_B^0$ , and a relationship between the composition of the scale at the alloy-scale interface,  $\xi'$ , and the corresponding oxygen activity,  $a_O'$ , established by the oxide dissociation reaction.

There are also two auxiliary boundary equations which arise from a consideration of the mass balances at the alloy-scale and scale-gas interfaces. Whittle and coworkers<sup>(28)</sup> have shown that the boundary condition at the alloy-scale interface can be derived based on a knowledge of only compositions in the scale. These authors begin with the average content of BO in the scale, which they expressed as

$$\xi_{av} = (1/x_s) \int_0^{x_s} \xi dx = \int_0^1 \xi dy \quad (2-18)$$

Now the scale is considered to increase in thickness by an incremental value,  $dx_s$ , during which time,  $dt$ , the number of equivalents of BO per unit cross section which accumulate in the scale is equated to the number diffusing away from the interface into the scale:

$$\frac{dx_s \xi_{av}}{V_{eq}} = [J_B]_{x=0} \cdot dt \quad (2-19)$$

Substituting for  $J_B$ (eq) from equation (2-13) gives

$$\frac{dx_s \xi_{av}}{V_{eq}} = \left[ \frac{D_B \xi}{V_{eq}} \cdot \left[ \frac{\partial \ln a_{BO}}{\partial \xi} \cdot \frac{\delta \xi}{\delta x} - \frac{Z_B}{Z_O} \cdot \frac{\partial \ln a_O}{\partial x} \right] \right]_{x=0} \cdot dt \quad (2-20)$$

Again, using  $y = x/x_s$  and  $x_s = (2kt)^{1/2}$  this becomes

$$k \xi_{av} = \left[ D_B \xi \left[ \frac{\partial \ln a_{BO}}{\partial \xi} \cdot \frac{d\xi}{dy} + \frac{Z_B}{Z_O} \cdot \frac{d \ln a_O}{dy} \right] \right]_{y=0} \quad (2-21)$$

substitution from equation (2-15) yields

$$\xi_{av} = \frac{\xi'}{pZ_A(1-\xi') + Z_B \xi'} \left[ Z_B + \frac{pD_B'(1-\xi')}{k} \right] \left[ Z_B \frac{\partial \ln a_{AO}}{\partial \xi} - Z_A \frac{\partial \ln a_{BO}}{\partial \xi} \right] \cdot \left[ \frac{d\xi}{dy} \right]_{y=0} \quad (2-22)$$

where  $p = D_A/D_B$ .

Whittle and coworkers make the following arguments to simplify this expression:

(1) The variation of  $\xi$  in the scale is principally determined by the differences in diffusivities of cations A and B. Very close to the alloy scale interface this difference has operated over such an insignificant distance that the gradient of the concentration profile,  $\left[ \frac{d\xi}{dy} \right]_{y=0}$ , will be negligibly small.

(2)  $\xi' < 1$  and  $p < 1$  for enrichment of B at the scale-gas interface.

(3)  $D_B'/k$  is very small, since  $a_o$  is very small at the alloy-scale interface.

Hence, the second term in brackets in Eq. (2-22) is small in comparison to  $Z_B$ , which simplifies the expression after re-arrangement to

$$\xi' \approx \frac{pZ_A \xi_{av}}{Z_B(1-\xi_{av}) + pZ_A \xi_{av}} \quad (2-23)$$

At the scale-gas interface, the arrival rate of B cations is related to the thickening rate of the scale by

$$[J_B]_{y=1} = \frac{\xi''}{V_{eq}} \frac{dx_s}{dt}$$

Again, using  $y = x/x_s$ ,  $x_s = (2kt)^{1/2}$  and Eq. (2-13) this becomes

$$k\xi'' = \left[ D_B \xi \left[ \frac{\delta \ln a_{BO}}{\delta \xi} \frac{d\xi}{dy} + \frac{Z_B}{Z_O} \frac{d \ln a_O}{dy} \right] \right]_{y=1} \quad (2-25)$$

which, upon substitution of (2-15) gives

$$\left[ \frac{d\xi}{dy} \right]_{y=1} = \frac{k}{D_B} \frac{\xi''(1-\xi'')(p-1)}{p} \quad (2-26)$$

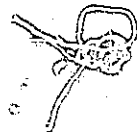
The solution of equation (2-17), which expresses the composition gradient of B in the alloy is given by

$$N_B = N_B' + (N_B^0 - N_B') \frac{\operatorname{erf}(\lambda/2\bar{D}_{all}^{1/2}) - \operatorname{erf}(\alpha/2\bar{D}_{all}^{1/2})}{\operatorname{erfc}(\alpha/2\bar{D}_{all}^{1/2})} \quad (2-27)$$

where  $\alpha = u_s du_s/dt$  is a parabolic rate constant in terms of the displacement of the alloy-scale interface.  $\alpha$  is related to  $k$  according to

$$(\alpha/k)^{1/2} = du_s/dx_s = (V_{all}/V_{eq}) [(1-\xi_{av})/Z_A + \xi_{av}/Z_B] \quad (2-28)$$

and  $V_{all}$  is the molar volume of the alloy. A definition of  $\xi_{av}$ , based on an alternative mass balance expression at the alloy-scale interface was given by Coates and Dalvi<sup>(29)</sup> as



$$\xi_{av} = \frac{1}{Z_B N_B' + Z_A (1 - N_B')} \left[ Z_B N_B' + Z_A Z_B \left[ \frac{2}{k} \right]^{1/2} \frac{V_{eq} \bar{D}_{all}}{V_{all}} \left[ \frac{dN_B'}{d\lambda} \right]_{\lambda = u_s t^{1/2}} \right] \quad (2-29)$$

Now, substituting (2-27) and (2-28) into (2-29) gives

$$\xi_{av} = \frac{1}{Z_B N_B' + Z_A (1 - N_B')} \left[ Z_B N_B' + \frac{Z_B Z_A}{F(\varphi)} \left[ \frac{1 - \xi_{av}}{Z_A} + \frac{\xi_{av}}{Z_B} \right] (N_B^0 - N_B') \right] \quad (2-30)$$

where  $\varphi$  represents the ratio  $(\alpha/2\bar{D}_{all})^{1/2}$  and the auxiliary function

$$F(\varphi) = \pi^{1/2} \varphi \exp \varphi^2 \operatorname{erfc} \varphi \quad (2-31)$$

$$F(\varphi) = 1 - \frac{1}{2} \varphi^2 + \dots \text{ if } \varphi \gg 1 \quad (2-32)$$

Equation (2-30) may be re-arranged to give

$$\xi_{av} = \frac{Z_B [F(\varphi) N_B' + N_B^0 - N_B']}{F(\varphi) [Z_B N_B' + Z_A (1 - N_B')] + (Z_B - Z_A) (N_B^0 - N_B')} \quad (2-33)$$

When  $\bar{D}_{all} \rightarrow 0$ ,  $\varphi \rightarrow \infty$  and  $F(\varphi) \rightarrow 1$ . Thus, irrespective of the value of  $N_B'$ ,

$$\xi_{av} = \frac{Z_B N_B^0}{Z_A + (Z_B - Z_A) N_B^0} = N_B^0 \text{ for } Z_A = Z_B \quad (2-34)$$

In addition, when  $Z_A = Z_B$  then,

$$F(\varphi) = \frac{N_B^0 - N_B'}{\xi_{av} - N_B'} \quad (2-35)$$

### 2.3.6 Modifications to the Wagner Model

The only significant modifications to Wagner's original theory have been the consideration of oxygen diffusion into the alloy phase<sup>(29)</sup>, attempts to simplify the

expression for the average content of BO in the scale<sup>(28,29)</sup> and finally, inclusion of the effects of deviations in oxide stoichiometry<sup>(30)</sup>. Coates and Dalvi<sup>(29)</sup> extended Wagner's model to include the dissolution and transport of oxygen in the alloy phase resulting from dissociation of the oxide at the alloy-scale interface. This effect was not expected to result in significant changes in the parabolic scaling rate of a binary alloy, and none has been demonstrated experimentally. Coates and Dalvi<sup>(29)</sup> and later Whittle et al.<sup>(28)</sup> re-examined Wagner's integral expression for the average content of BO in the scale,  $\xi_{av}$ , in order to simplify the computational solution of his equations. The latter authors noted that such an expression should reduce to the condition that  $\xi_{av} = N_B^O$  when diffusion in the alloy is the slowest step, and advanced an equation for the limit at which this approximation is valid:

$$\gamma = \sqrt{\alpha/2D_{AB}} \geq 3 \quad (2-17)$$

where  $\alpha$  is the rate of recession of the alloy-oxide interface. Finally, Young and co-workers<sup>(30)</sup> included the effects of deviations from stoichiometry on the activities of the various oxide components in a re-working of the diffusion equations. They found that the effect on the calculated cation profiles was insignificant for the oxidation of a Co-10.9Ni alloy but noticed small changes for Co-5.8Fe and Co-10.1Fe alloys. This was attributed to the greater degree of nonstoichiometry in CoO-FeO mixed oxides. The effect on the calculated parabolic constants was negligible in both cases.

### 2.3.7 Application of The Wagner Model to Experimental Investigations of the Oxidation of Binary Alloys

Wagner's diffusion model has been tested on a number of alloy systems which form solid solution oxides. These investigations are mainly confined to monoxides

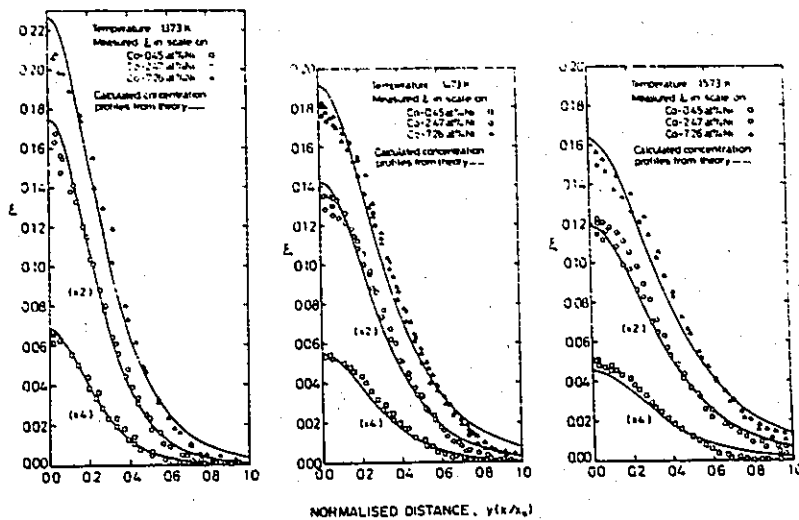
having the NaCl cubic lattice and have been reviewed in detail by various authors<sup>(31-33)</sup>. Results from the work of Narita et al.<sup>(34)</sup> can be used to illustrate the general approach used in these comparisons. These authors used independent measurements of the cation tracer diffusivities in Co-Ni-O solid solutions and solved the diffusion equations numerically. They determined the cation and oxygen activity profiles in the scale along with the parabolic scaling rates. Good agreement with the experimentally observed values was obtained as shown for example by the nickel composition profiles in Figure (2-6). For the NiO-CoO system, most authors use the assumption that the oxide behaves as an ideal solution in order to approximate various thermodynamic parameters. There is now a large body of experimental data related to the diffusional, defect and oxidation properties for this system which supports this approach. A review of this literature is presented in the following chapter.

### 2.3.8 Expected Range of Validity of the Wagner Model

Wagner's 1969 model for the growth of solid solution oxides contained a number of assumptions, explicit and implicit, which, upon closer inspection, should provide some indication of the expected range of validity of this analysis.

Wagner assumed that diffusion of reactants was occurring through the bulk lattice as a rate limiting step. This has been shown to be a poor approximation in many oxides containing a significant volume fraction of grain boundary or dislocation diffusion sites at temperatures below approximately one-half of the oxide melting temperature. The particular case of NiO growth will be dealt with in detail in section 3.4.3.

Another problem with the assumption that bulk oxide properties and equilibria



Figure(2-6) Calculated and experimentally determined values for nickel composition as a function of normalized distance,  $y$ , in  $(Co Ni)O$  scale formed on  $Co-Ni$  alloys containing 0.45, 2.44 and 7.26 at. % Ni under 1 atm oxygen pressure at 1373, 1473 and 1573 K (nickel compositions for the  $Co-0.45 Ni$  and the  $Co-2.47 Ni$  alloys were plotted by multiplying two and four times their original values, respectively)

(35)

will dominate during scale growth arises at sufficiently small values of film thickness. Transport by ambipolar diffusion requires that charge migration occur under the condition of local electroneutrality. This is not a valid approximation near the surface dipole region of an ionic crystal where an adsorbed surface charged species resides with a space-charge region of opposite polarity extending into the oxide. The extent of this space-charge region is analogous to the Debye-Huckel screening length for the potential distribution in dilute solutions of strong electrolytes and is characterized by the following parameter<sup>(35)</sup>

$$\kappa = \left[ \frac{ekT}{e^2 n} \right]^{1/2} \quad (2-18)$$

which has the units of length. This relationship indicates that the width of the space-charge region is proportional to the inverse of the square-root of the total concentration of electrically charged species,  $n$ . The assumption of charge neutrality is only valid if the oxide thickness is much larger than the Debye length. For single crystals of NiO, Atkinson<sup>(36)</sup> has estimated that the Debye length is of the order of 100 Å for a charge defect concentration of  $10^{-6}$  per mole at 500° C. If the oxide were to contain charged impurities or intrinsic defect concentrations which were larger near internal line defects such as dislocations or grain boundaries, then the effective Debye length could be considerably reduced from this value.

## CHAPTER 3

### LITERATURE REVIEW

#### 3.1 Introduction

This chapter reviews the available and appropriate data on the Co-Rh, Ni-Co, Ni-O and Co-O binary systems and the Ni-Co-O ternary system. The data available for the Co-Rh system is fairly limited in relation to the Ni-Co system. There have been no previous investigations of surface segregation on Co-Rh alloys. Recent experimental work on segregation in the Ni-Co system is reviewed as background both to Chapters 5 and 6.

For the oxidation of Ni-Co alloys, reviews are presented of data in the related binary systems, Ni-O and Co-O as precursors to the ternary Ni-Co-O case. The literature dealing with nickel oxidation is far more extensive than for cobalt since nickel forms a single oxide which is stable over a wide range of temperatures and pressures. This system has therefore been investigated as a model system to test and extend the Wagner theory of metallic oxidation. The thermodynamic, structural and diffusion properties relevant to this type of comparison are given along with the oxidation data.

Ni-Co alloys have been used to investigate the formation of solid solution oxides on binary alloys at high temperatures. A review of work in this field along with the results of models based upon ambipolar diffusion of reactants are

presented.

### 3.2 Properties of Co-Rh Alloys

$\alpha$ -Co and Rh form a continuous series of solid solutions. Koster and Horn<sup>(37)</sup> have used microscopic and lattice-parametric investigations to determine the temperature effect of alloying on the allotropic change in cobalt (Figure (3-1)). The temperature of the start of the diffusionless transformations (f.c.c.  $\alpha \rightarrow$  c.p.h.  $\epsilon'$  and  $\epsilon' \rightarrow \alpha$ ) was observed to be higher for heating than for cooling. Lattice parameter changes showed an essentially linear variation with composition. Stone<sup>(39)</sup> noted a possible transformation below room temperature for Rh-rich alloys (13 to 20% Co) based on hardness changes measured following quenching cycles in water, liquid nitrogen and liquid helium. Mit'ko and coworkers<sup>(40)</sup> measured the surface tension and density of Rh-Co alloys at temperatures up to 2200° C. At 2000° C they noted a small negative deviation of the surface tension isotherm from the ideal curve and a small positive deviation of the mole volume isotherm from an additive straight line. The liquidus curve was also determined more accurately than in the earlier investigation and has been added to the phase diagram, Figure (3-1).

### 3.3 Properties of the Ni-Co System

#### 3.3.1 Structure, Thermodynamics and Diffusion

Co and Ni also exhibit complete solid solubility in the  $\alpha$  phase, as shown in Figure (3-2). As in the Co-Rh system, the  $\alpha$  and  $\epsilon$  phase boundary is not well established because of difficulties in reaching equilibrium at low temperatures. Heat of mixing and activity data in both the liquid and solid phases have been reviewed

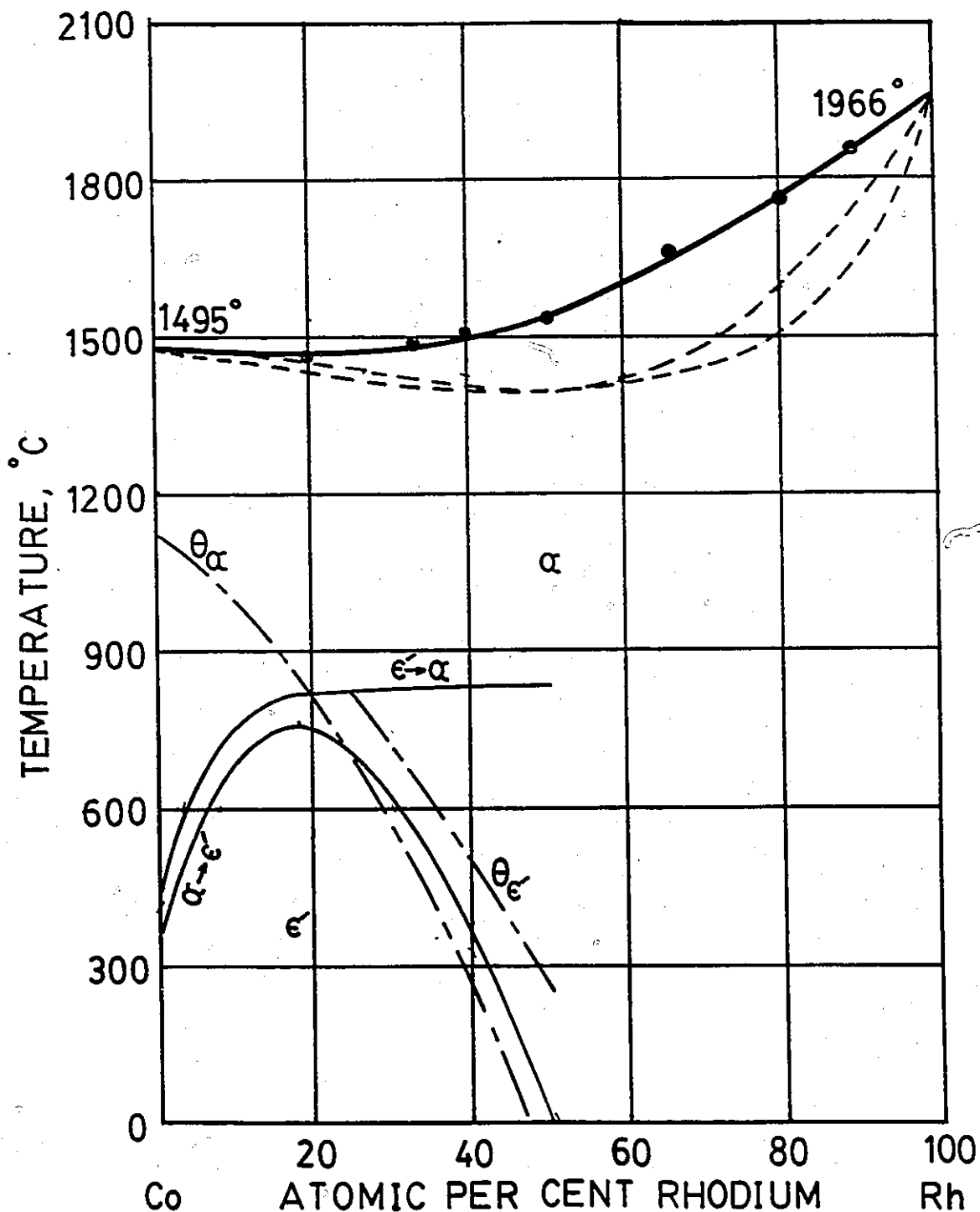


Figure (3-1). The Co-Rh phase diagram, redrawn from Hansen<sup>(38)</sup>. Phase and magnetic transformation curves are shown for heating and cooling<sup>(37)</sup>. Liquidus data are from Mit'ko and coworkers<sup>(40)</sup>. Dashed liquidus and solidus curves were hypothetical<sup>(37)</sup>.

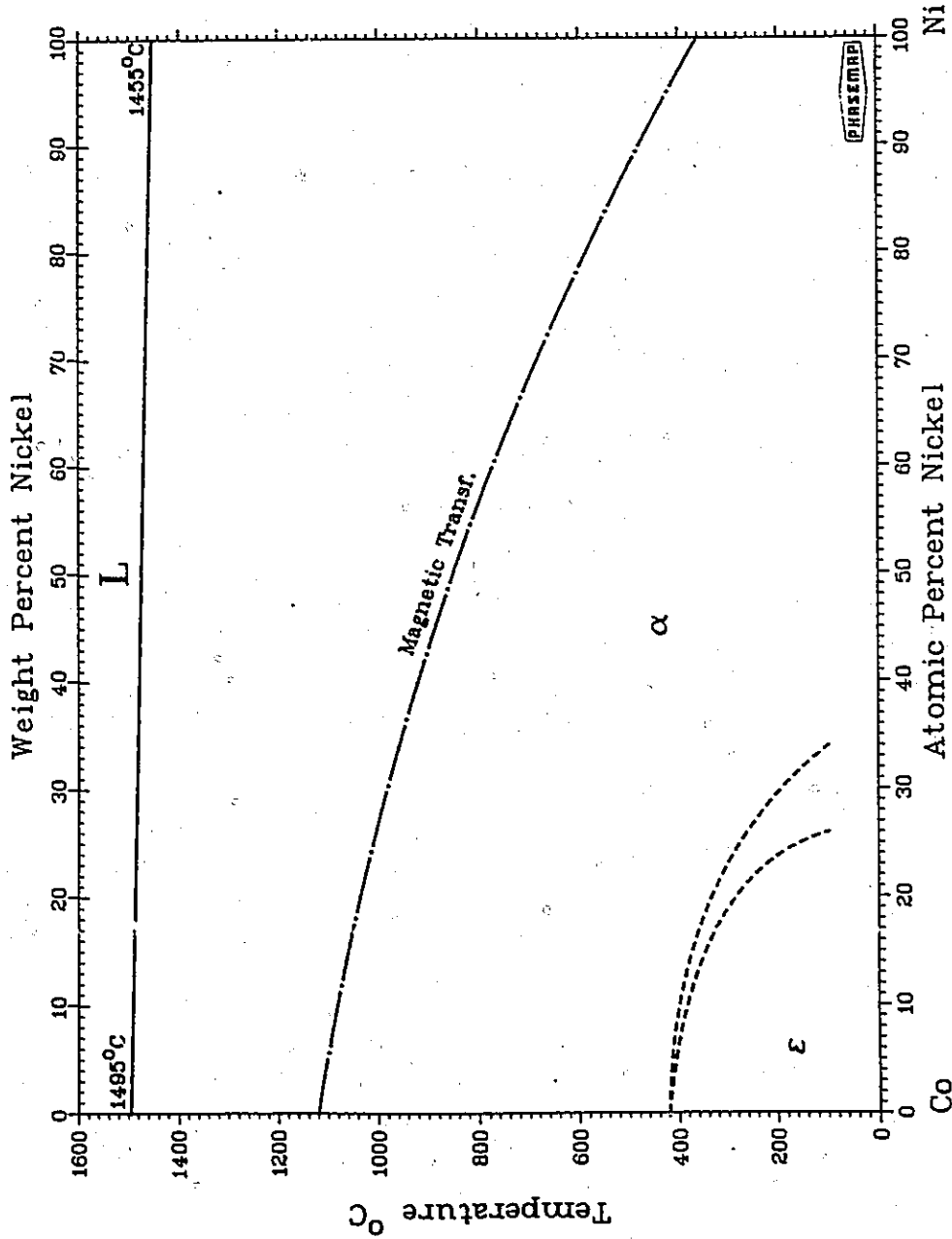


Figure (3-2). The Co-Ni phase diagram, from Nishizawa and Ishida (41)

by Nishizawa and Ishida<sup>(41)</sup>. These show slightly negative deviations from Raoult's law, positive heats of mixing and negative excess free energies, and indicate that the solution thermodynamics of this system are close to ideal. Tracer diffusion measurements have been made across the entire composition range in Ni-Co alloys and have been tabulated by Askill<sup>(42)</sup>.

### 3.3.2 Surface Thermodynamics

The surface composition of Ni-Co alloys at 853 K has been studied by Hajcsar and coworkers using Auger electron spectroscopy<sup>(2,3)</sup>. Experiments with annealed and quenched polycrystals over the entire composition range indicated that nickel was enriched at the surface in all cases. The results of this study are shown in Figure (3-3). The surface excess was calculated based on two limiting approximations: the first being monolayer segregation only and the second representing a homogeneous composition over the analysed depth. The former correction leads to a larger calculated excess of nickel, as shown by the (x) symbols in Figure (3-3).

The temperature dependence of segregation on the alloys having bulk compositions of 50.0 and 56.0 a/o Ni were determined for different crystallographic orientations. The reported enthalpy and entropy values for these two alloys were:

a/oNi	(hkl)	$-\Delta H_{\text{seg}}^{\circ}$ (kJ/mol)	$-\Delta S_{\text{seg}}^{\circ}$ (J/mol·deg)
Bulk			
56.0	(111)	17.4±1.60	14.1±1.74
	(210)	7.3±0.94	3.1±0.79
50.0	(111)	17.8±1.08	11.3±1.09
	(100)	20.4±0.87	13.2±0.86
	(110)	14.9±1.54	7.9±1.59

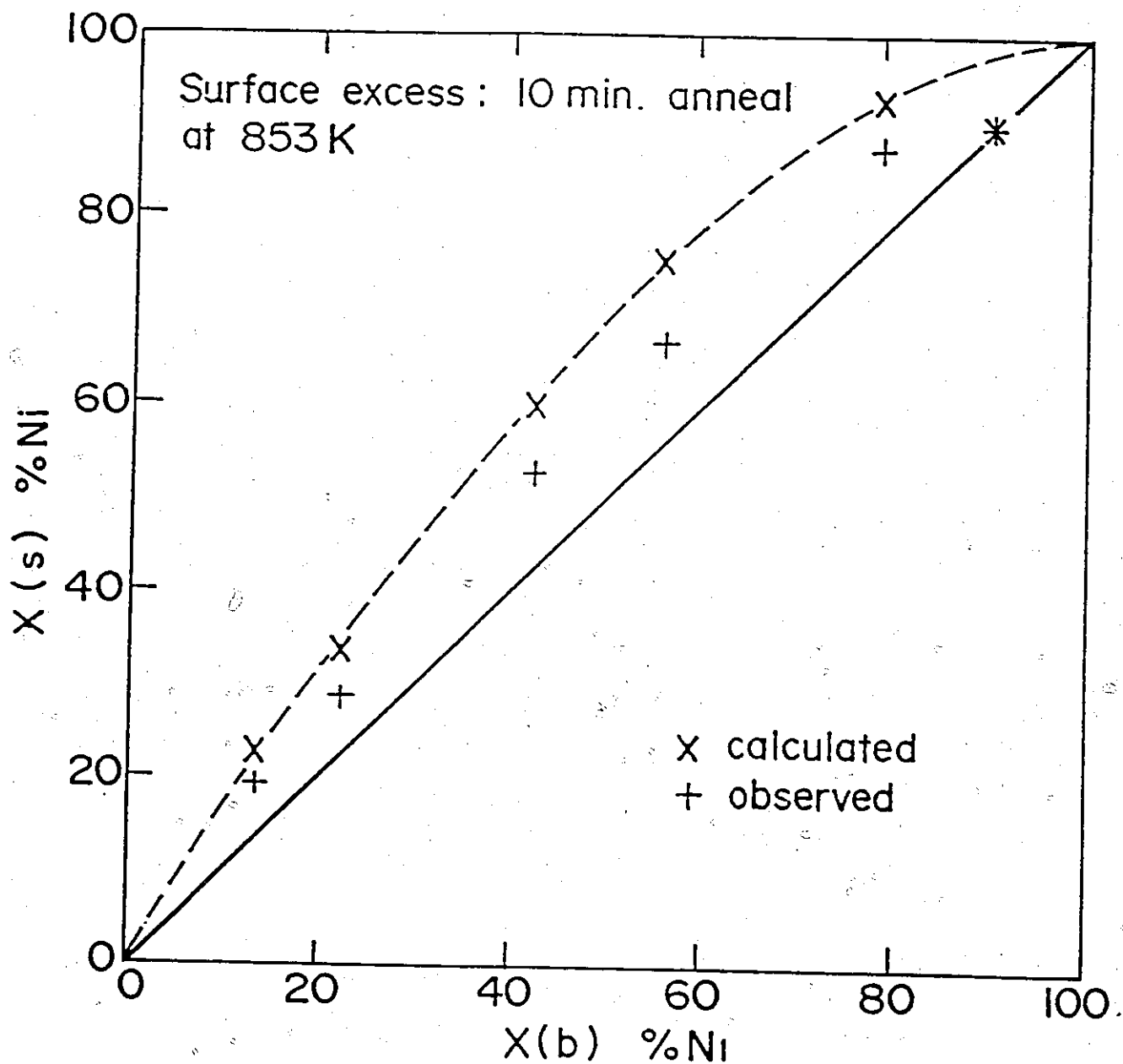


Figure (3-3)

Surface excess equilibrium diagram for Ni-Co alloys at 853 K. Spectra from the low energy (50-60 eV) Auger peaks were interpreted by assuming a homogeneous composition distribution (+) and monolayer segregation (x). The experimental sampling depth was approximately 1.5 monolayers. (2)

The experimental value for the (111) face was in reasonable agreement with a calculated value of  $-16.1 \pm 0.6$  kJ/mol for the 50.0 alloy using an embedded atom model<sup>(44)</sup>.

### 3.4 Properties of the Ni-O System

#### 3.4.1 Crystal and Defect Structure

$\text{Ni}_{1-y}\text{O}$  is a metal deficient, p-type intrinsic semiconductor with the NaCl structure and a wide range of stability. The anionic sublattice is considered to be practically undefected while the cationic sublattice contains concentrations of vacancies and electron holes which vary continuously with temperature and oxygen activity. The overall departure from stoichiometry, when compared to the other transition metal oxides with the same structure, is sufficiently small ( $y \approx 10^{-4}$  at  $1000^\circ\text{C}$  and 1 atm.  $\text{O}_2$ ) that significant interactions among defects may be neglected to a good approximation<sup>(45)</sup>. In view of these properties, NiO has been considered a model semiconductor and the subject of many experimental investigations which have attempted to correlate its electrical conductivity, diffusional and oxidation properties with predictions based on simple defect equilibria.

Using the notation of Kroger and Vink<sup>(46)</sup>, the formation of various types of cation vacancies in NiO can be expressed by the following reactions:



where, V represents a vacancy, O an oxygen atom, subscripts refer to sublattices

and superscripts to excess charge states: x, ', and '' are neutral, single and double negative charges, while h' is a singly charged positive electron hole. Considering only these three reactions neglects any contributions due to impurities or defect associates, in addition to other isolated point defects and electrons. The concentration of vacancies in NiO, expressed as a mole fraction with respect to the cationic sites of the perfect lattice, is therefore given as

$$\sum [V_{Ni}]_{NiO} = y = K^x a_O + \frac{K^x K'}{[h']} a_O + \frac{K^x K' K''}{[h']^2} a_O \quad (3-4)$$

where  $K^x$ ,  $K'$ , and  $K''$  are the equilibrium constants for the above reactions and  $a_O$  is the oxygen activity ( $a_O = P_{O_2}^{1/2}$ ). The concentration of positive holes,  $[h']$ , is determined by the electroneutrality condition,

$$[h'] = [V_{Ni}'] + 2[V_{Ni}''] \quad (3-5)$$

which, when expressed in terms of the above equilibrium constants, yields

$$[h']^3 - K^x K' [h'] a_O - 2K^x K' K'' a_O = 0 \quad (3-6)$$

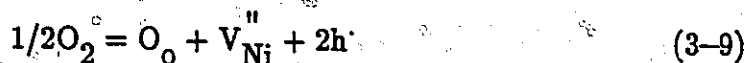
In the limiting case that the vacancies in NiO are predominantly singly charged, the overall reaction for the formation of cation vacancies would become



so that

$$[V_{Ni}'] = K^s (P_{O_2})^{1/4} \quad (3-8)$$

A second limiting case arises if the dominant defect type is a doubly charged cation vacancy, for which the overall reaction is



and

$$[V_{Ni}'] = K^d (P_{O_2})^{1/6} \quad (3-10)$$

Information concerning the values of  $y$  and the charge state of the nickel vacancies in  $Ni_{1-y}O$  is available from a number of original sources<sup>(47-52)</sup> and

reviews<sup>(53,54)</sup>. On the basis of these investigations it is not conclusively shown that one type of vacancy species is predominant over the entire oxide stability range. At temperatures above 900° C it appears necessary to consider the presence of all three types of metal vacancies in a detailed analysis of the experimental results. From the results of Osburn and Vest<sup>(51,52)</sup>, the equilibrium constants for the creation of vacancies of differing charge by the above reactions are found to be

$$K^x = 1.213 \times 10^{12} T^{-3} \exp \left[ \frac{-44.76(\text{kcal/mole})}{RT} \right] \quad (3-11)$$

$$K' = 3.60 \times 10^{-2} T^{3/2} \exp \left[ \frac{-2.21(\text{kcal/mole})}{RT} \right] \quad (3-12)$$

$$K'' = 9.0 \times 10^{-8} T^{3/2} \exp \left[ \frac{-8.83(\text{kcal/mole})}{RT} \right] \quad (3-13)$$

In addition, the presence and concentration of aliovalent impurities appears to have a significant effect on the overall nonstoichiometry, especially at low temperatures and oxygen activities where the intrinsic defect concentrations are very small.

### 3.4.2 Self-Diffusion of Ni and O in NiO

As a result of its defect structure, the self diffusion coefficient of nickel in NiO will be related to the vacancy and tracer diffusivities by a relationship of the form

$$D_{\text{Ni}} = D_{V_{\text{Ni}}} [V_{\text{Ni}}] = \frac{D^T}{f} \quad (3-14)$$

where  $D_{V_{\text{Ni}}}$  and  $[V_{\text{Ni}}]$  are the vacancy diffusion coefficient and the total vacancy concentration respectively,  $D^T$  is the tracer diffusion coefficient and  $f$  is a correlation factor determined by the crystallographic geometry and diffusion mechanism ( $f=0.78$  for vacancy diffusion in FCC structures). A number of investigations have been conducted using a variety of methods to experimentally determine the tracer diffusion coefficient of Ni isotopes in NiO. These investigations are summarized in Table (3-1) and some representative values are shown in the Arrhenius plot of Figure (3-4).

Table (3-1)

## Self Diffusion of Ni and O in NiO

Temperature range(°C)	Oxygen pressure	Method	Result (R in kcal/mol·deg)	Comments	Reference
740-1400	Air	Decline in surface activity ( <sup>63</sup> Ni)	$D_{Ni}^* = 1.7 \times 10^{-2} \exp \left[ \frac{-56 \pm 1.2}{RT} \right]$	SC, metal oxidation layers, sintered pellets(85% density)	(55)
1000-1400	Air	Decline in surface activity ( <sup>63</sup> Ni)	$D_{Ni}^* = 4.4 \times 10^{-4} \exp \left[ \frac{-44.2 \pm 3}{RT} \right]$	PC, SC	(56)
1000-1470	Air	Micro-sectioning ( <sup>63</sup> Ni)	$D_{Ni}^* = 1.83 \times 10^{-3} \exp \left[ \frac{-45.6 \pm 2}{RT} \right]$	SC	(57)
1190-1400	Air	Thermally growing NiO precoated with <sup>63</sup> Ni; sectioning	$D_{Ni}^* = 4.8 \times 10^{-4} \exp \left[ \frac{-48.4 \pm 2}{RT} \right]$		(58)
1182-1762	1 to 5x10 <sup>-7</sup> atm ( <sup>63</sup> Ni, <sup>57</sup> Ni)	Micro-sectioning	$D_{Ni}^* = (4.77 \pm 1.3) \times 10^{-2} \exp \left[ \frac{-60.8 \pm .6}{RT} \right]$ (1 atm O <sub>2</sub> )	$D_{Ni}^* \propto P_{O_2}^{1/n}$ ; n ≈ 0.16 at 1245° C n ≈ 0.20 at 1380° C	(59)

continued...

Table (3-1), continued Self Diffusion of Ni and O in NiO

Temperature range(°C)	Oxygen pressure	Method	Result (R in kcal/mol·deg)	Comments	Reference
522-1400	1 atm	RF sputtering,	$D_{Ni}^* = 2.2 \times 10^{-2} \exp \left[ \frac{-5.9}{RT} \right]$	Dislocation pipe	(60)
lattice		radioisotopes	$D_{Ni}^d = 0.26 \exp \left[ \frac{-4.6}{RT} \right]$	radius $\approx 10^{-7}$ cm	
522-800	1 atm,	RF sputtering	$D_{Ni}^{*b} = 3.0 \times 10^{-8} \exp \left[ \frac{-4.1}{RT} \right]$	Measurement gives product	(61)
dislocations	$10^{-11}$ atm (700° C)			of grain boundary width and diffusion coefficient	
1100-1600	150 Torr	SIMS, $^{18}O$	$D_O^* = 50 \exp \left[ \frac{-1.29}{RT} \right]$	SC; evaporation/condensation reaction considered in analysis of profiles.	(62)
1300-1550	$10^{-4}$ atm	SIMS, $^{18}O$	$D_O^*$ pressure dependence small at 1300° C, significant at 1550° C with a continuous increase between the two extremes. Oxygen vacancies and interstitials considered as minority defects. Same materials and analysis as above.		(63)
1100-1600	0.2 atm,	$^{18}O(\rho, \alpha)^{15}N$	$D_O^{*b} \approx D_{Ni}^{*1}$		(64)
	50% $^{18}O$	technique, RF sputtering			

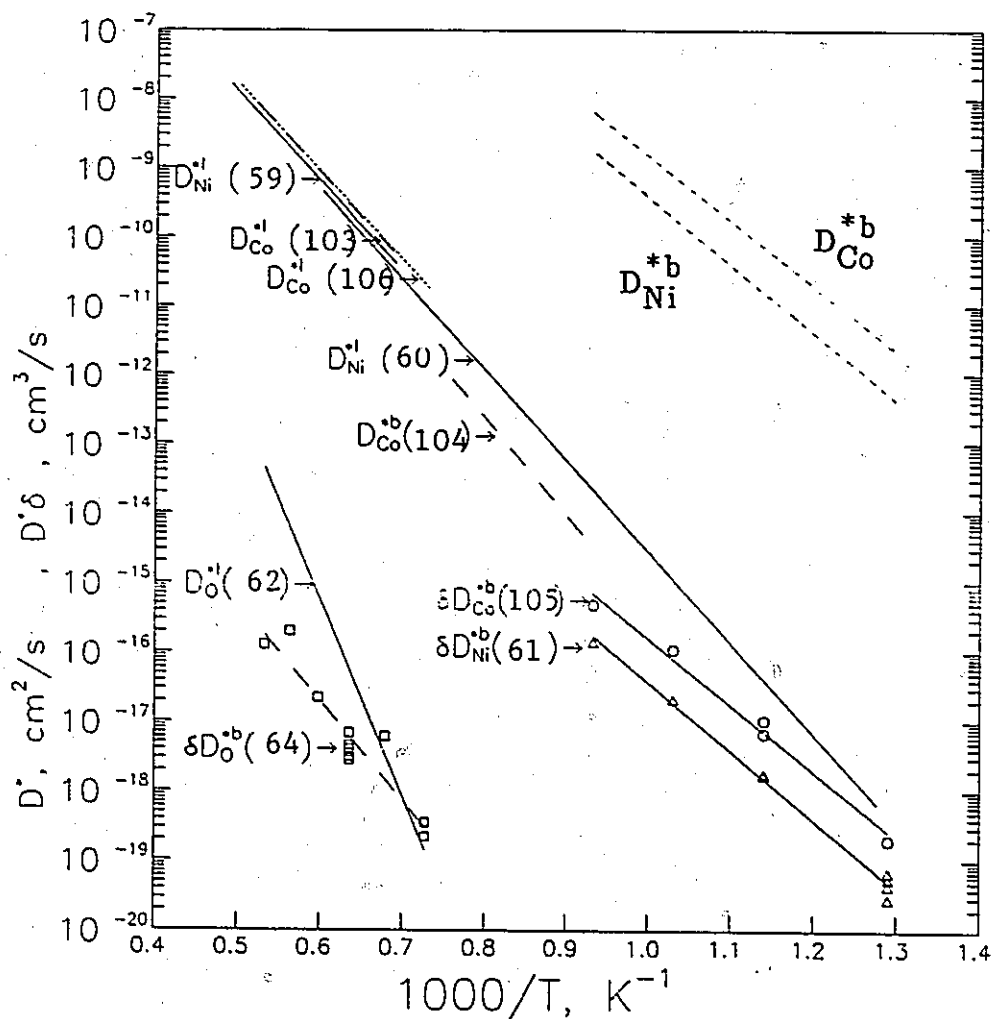


Figure (3-4)

Measured lattice and grain boundary tracer diffusion coefficients of Ni, Co and O in NiO. Grain boundary values are expressed as the product of the grain boundary width,  $\delta$ , and the grain boundary diffusion coefficient,  $D_{\text{Ni}}^{*b}$ . The values of nickel and cobalt grain boundary diffusion coefficients due to Atkinson and coworkers<sup>(61,105)</sup> have been multiplied by an assumed grain boundary width of 1 nm (upper right) in order to show direct comparisons to the lattice  $D_{\text{Ni}}^1$  values.

Initial studies<sup>(55-58)</sup> were conducted in air atmosphere and indicated that the activation energy for Ni diffusion was between 44.2 and 56 kcal/mole. Volpe and Reddy<sup>(59)</sup> made more comprehensive investigations over a range of temperatures and pressures. At an oxygen pressure of one atmosphere their experimental activation energy of 60.8 kcal/mole was higher than earlier published results. They also reported that the pressure dependence varied from approximately  $P_{O_2}^{1/4}$  at 1380° C to  $P_{O_2}^{1/6}$  at 1245° C. This was regarded as evidence that both singly and doubly charged vacancies were active in the transport of Ni in NiO.

The most recent results are those of Atkinson and Taylor<sup>(60,61)</sup> who used a sensitive radio-frequency sputtering technique in order to make measurements of Ni tracer diffusion in the lattice, along dislocations and grain boundaries in NiO. Their technique also allowed measurements to be made at much lower temperatures than in the earlier investigations. The activation energies for lattice (59 kcal/mole), dislocation (46 kcal/mole) and grain boundary (41 kcal/mole) diffusion differed significantly. Diffusion along dislocations was associated with low angle boundaries observed in the NiO specimens. The radius of the high diffusivity region in the vicinity of the dislocation "pipes" was estimated to be  $10^{-7}$  cm. This value was based on the observed spacing of the dislocations and the assumption that the total diffusion coefficient could be expressed as a sum of independent grain boundary and lattice diffusion coefficients (eq. (3-15)). The lattice contribution was approximated as being negligible relative to the dislocations. They believed that the vacancy concentration in these pipes was greater than, but proportional to the vacancy concentration in the bulk. The grain boundary diffusion measurements were expressed as the product of the grain boundary diffusion coefficient and the grain boundary width,  $D_{Ni}^b \delta$  (cm<sup>3</sup>/sec). The estimated grain boundary width,  $\delta$ ,

was  $7 \times 10^{-8}$  cm. An additional experiment at  $700^\circ$  C and  $P_{O_2} = 7 \times 10^{-6}$  atmospheres indicated that  $D_{Ni}^b \delta$  varied qualitatively the same way as the lattice diffusion coefficient. That is, the value  $D_{Ni}^b \delta$  was decreased by approximately one order of magnitude by lowering the oxygen pressure by a factor of approximately  $10^5$ . Again, this was regarded as evidence that diffusion along grain boundaries was occurring by a vacancy mechanism and that the vacancy concentration or mobility (or both) were increased at grain boundaries with respect to the oxide lattice.

Oxygen diffusion, being much slower than that of Ni in NiO, has only recently been studied using  $^{18}O$  tracer exchange and sensitive depth profiling techniques. Dubois and coworkers<sup>(62,63)</sup> have used SIMS to determine the tracer diffusion coefficient of  $^{18}O$  in NiO single crystals. They found that this value was 5–8 orders of magnitude smaller than that of Ni, as shown for comparison in Figure (3–4). The grain boundary diffusion of  $^{18}O$  has been studied in NiO specimens prepared in the same way as those used for the Ni grain boundary diffusion measurements<sup>(64)</sup>. The results of this investigation indicated that the grain boundary diffusion coefficient of oxygen is similar in magnitude to that of Ni diffusion in the lattice.

### 3.4.3 Recent Developments in the Understanding of Grain Boundary Transport in Nickel Oxide.

In contrast to the bulk transport properties diffusion along grain boundaries in NiO is poorly understood. Based on theoretical computer calculations of relaxed static grain boundary structures it is possible to predict qualitatively how diffusion properties may be affected, but further experimental evidence is required in this area. Using solid state theory for ionic solids Duffy and Tasker<sup>(65,66)</sup> have modeled the stable atomic configurations in coincidence tilt and twist boundaries in NiO. The results for the  $\langle 001 \rangle$  and  $\langle 011 \rangle$  tilt boundaries showed that the equilibrium structures could be viewed as linear dislocation arrays. These structures were

associated with dislocation "pipes" running parallel to the rotation axis which could lead to anisotropic diffusion properties in the boundary plane. For the pure [001] twist boundary, a stable configuration was created by introducing one Shottky defect per unit cell in the restructured boundary plane with a formation energy of  $-1.37$  eV. The symmetrical structure resulting in this case led the authors to surmise that any enhancement of diffusion would likely be an isotropic effect. In the case of pure tilt boundaries, some relaxed structures were fairly open (lower density) than corresponding metallic boundaries.

It can be seen that the boundaries considered by these authors were confined to a range of pure tilt or pure twist with a high periodicity. These may not be representative of the majority of boundaries found in a growing polycrystalline oxide, but they do begin to illustrate the types of structures which may be present in more complicated, random boundaries.

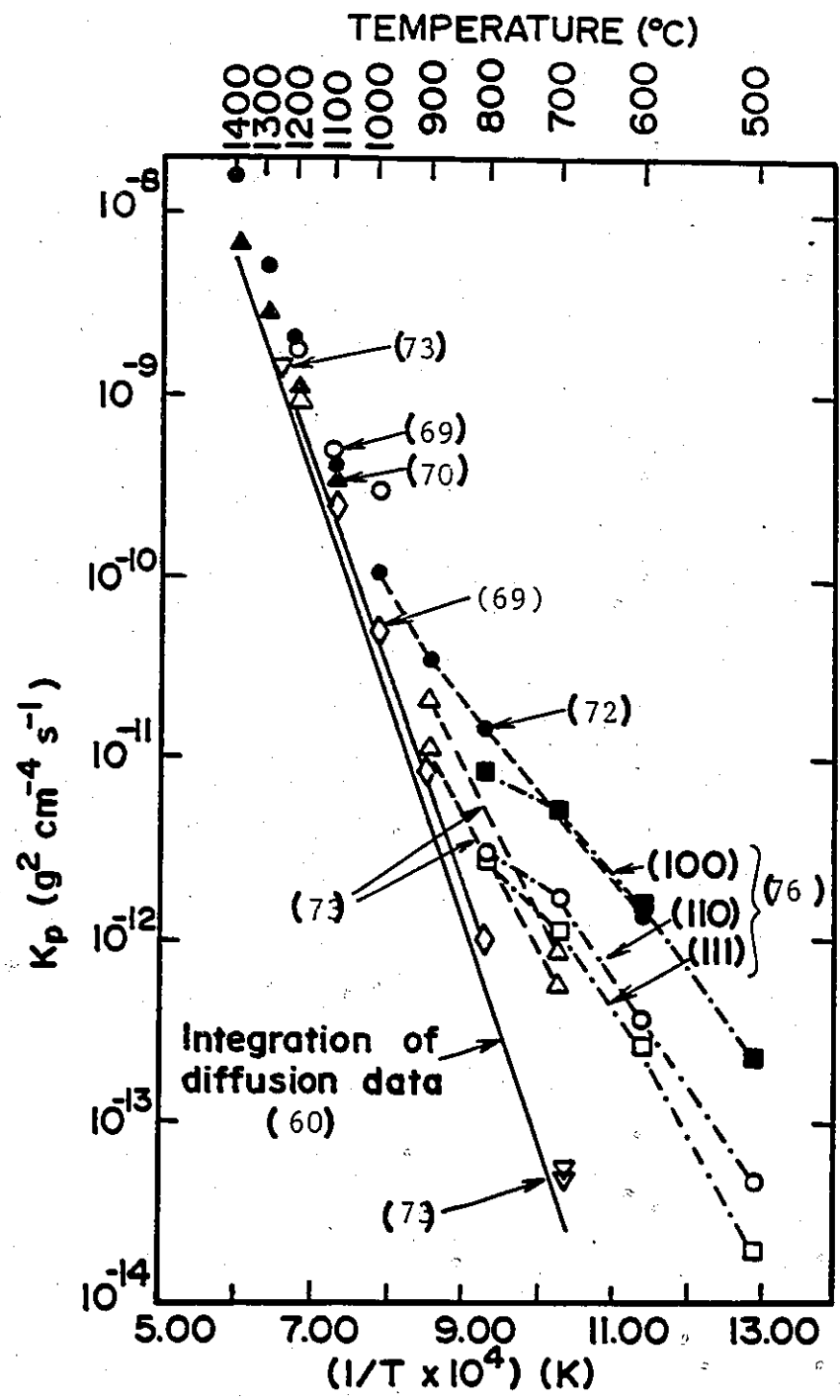
Recent high-resolution electron microscopic observations of symmetric tilt boundaries in NiO, similar to those described above, do not indicate the same degree of "openness" as predicted in the computer models<sup>(67)</sup>. They did however indicate a possible reduction in atomic density in the boundary plane as shown by Fresnel contrast effects<sup>(68)</sup>. Simulations of the observed images were based on reduced occupancy of individual lattice columns near the boundary and showed that such contrast could be produced by a vacancy content of  $\approx 25\%$ .

#### 3.4.4 Oxidation Mechanisms and Kinetics

The oxidation of nickel has been investigated over wide ranges of temperature and pressure. Above  $500^{\circ}$  C the growth of thick ( $> 1\mu\text{m}$ ) scales is controlled by diffusion of nickel from the metal to the scale gas interface and follows parabolic-type kinetics<sup>(69-81)</sup>. The Wagner theory<sup>(21)</sup> for the oxidation of metals has been successfully applied to this type of growth with modifications to include

diffusion of nickel along both lattice and low resistance grain boundary paths. Below 500<sup>o</sup> C, the earliest stages of oxygen adsorption, chemisorption and film formation have been observed at low pressures using controlled exposures of O<sub>2</sub><sup>(84-87)</sup>. Logarithmic kinetics have been associated with film growth for thicknesses up to 30 Å and temperatures in the range 25<sup>o</sup>-350<sup>o</sup> C<sup>(74)</sup>. The onset of parabolic growth behavior may take place at 350<sup>o</sup> C; the measured activation energies being similar to those for nickel diffusion in NiO grain boundaries.

Elrefaie et al.<sup>(69)</sup> have summarized the reported  $k_p$  values for NiO scales above 500<sup>o</sup> C, as shown in Figure (3-5). The variation in these measurements is thought to be associated with the use of Ni samples of varying purity (resulting in doping effects in NiO)<sup>(72,73)</sup>, surface preparation<sup>(69,73-75)</sup> and crystal orientation<sup>(73-77)</sup>. Above 1000<sup>o</sup>C the  $k_p$  data are in reasonable agreement with those calculated from Wagner's theory which considers transport of reactants by lattice point defects. The activation energies for oxidation are between 49 and 57 kcal/mole. Below 1000<sup>o</sup> C a change in slope of the Arrhenius plots is observed, and the measured  $k_p$  values are generally much larger than those calculated from Eq.(2-9) using self diffusion data for Ni in the NiO lattice (5-7 orders of magnitude difference at 500<sup>o</sup>C). There are two notable exceptions to this behavior. The first comes from optical observations of the thickening rate of NiO on individual nickel grains which formed a single-crystal overgrowth<sup>(73)</sup>. The second is due to Elrefaie et al.<sup>(69)</sup> who preoxidized nickel specimens at 1200<sup>o</sup> C which resulted in textured, large grained, columnar oxide scale structures, preventing a rapid rate of nickel diffusion along high angle grain boundaries. The  $k_p$  values determined in these latter investigations are nearly identical to those calculated from the Wagner model extended to temperatures as low as 700<sup>o</sup> C; all other data points fall above this curve.



Among the explanations advanced to account for such behavior are impurity doping of the oxide<sup>(72)</sup>, new oxide formation and "swelling" at NiO grain boundaries by rapid inward transport of oxygen along NiO grain boundaries supported by nickel diffusion through the lattice<sup>(78,79)</sup> and finally, outward diffusion of nickel along NiO grain boundaries<sup>(76,77,80,81)</sup>. Berry and Paidassi<sup>(72)</sup> considered that significant levels of aliovalent impurities (i.e. 20–200 ppm Fe) could alter the relative concentrations of the singly and doubly charged nickel vacancies, resulting in the observed change in slope of the Arrhenius plots. The lattice diffusion data for Ni in NiO of purity similar to that of samples used in oxidation experiments<sup>(60)</sup> does not support this argument. Rhines et al<sup>(78,79)</sup> suggested that the formation of new oxide upon boundaries in initially formed columnar NiO grains resulted in the generation of stresses parallel to the metal–oxide interface sufficient to alter the physical dimensions of their samples. This stress would be in addition to the stresses resulting from the geometric constraint of the constantly changing area of the metal–oxide interface. Rhines and coworkers postulated that the new oxide was formed by inward migration of oxygen along NiO boundaries, supported by nickel transport through the NiO lattice. While the data on diffusion in NiO show these diffusivities to be of similar magnitude, the relative grain boundary diffusivities of nickel and oxygen make this argument less reasonable than that proposed by Perrow, Smeltzer and Embury<sup>(80)</sup> who suggested that fast diffusion of Ni along oxide grain boundaries was the rate limiting factor in the growth of NiO scales below 1000° C.

Structural studies of thin oxide films formed at temperatures  $\leq 1/2$  the oxide melting temperature have revealed the presence of crystallite boundaries and dislocations which may act as low resistance diffusion paths for the transport of reactants. In the early stages of oxide growth these films may be epitaxially

oriented to the underlying metal, resulting in a variation in the number and types of boundaries for short-circuit diffusion<sup>(75,77,80,82)</sup>. For a given film orientation the average size of the oxide grains has been observed to increase with increasing oxidation time<sup>(77,80,81)</sup>. This increase has been associated with the processes of recrystallization and grain growth.

In order to include the effects of short-circuit diffusion in the transport equations for the growth of oxide layers, Smeltzer, Haering and Kirkaldy<sup>(83)</sup> have assigned an effective diffusion coefficient

$$D_{\text{eff}} = D^l(1-\phi) + D^b\phi \quad (3-15)$$

where  $D^l$  and  $D^b$  are the lattice and grain boundary diffusion coefficients and  $\phi$  is the fraction of sites associated with low resistance diffusion paths. This expression has been incorporated into Wagner's model for growth of an oxide layer to give the following modified parabolic oxidation rate equation<sup>(80)</sup>

$$X^2 = 2\Omega D^l \Delta c \int_0^t (1 + \frac{D^b}{D^l} \phi) dt = k_p \int_0^t (1 + \frac{D^b}{D^l} \phi) dt = k_{p,\text{eff}}(t) \quad (3-16)$$

Here,  $X$  is the layer thickness,  $\Omega$  is the volume of oxide formed by a diffusing particle,  $\Delta c$  is the concentration gradient across the oxide layer and  $k_{p,\text{eff}}$  is the effective parabolic rate constant. With increasing time, the value of  $\phi$  may decrease due to a decay of the numbers of grain boundary sites, as described above. In this case the value of  $k_{p,\text{eff}}$  would be expected to approach a limiting value at long times as the second term in brackets loses significance.

This analysis, in conjunction with a simple physical model for the changing oxide structure, was used to evaluate the relative lattice and grain boundary diffusion coefficients and activation energies in NiO<sup>(77,80)</sup>. In a later study, Atkinson and coworkers<sup>(81)</sup> used their radio-isotope tracer measurements of Ni diffusion in the NiO lattice and grain boundaries to compare calculated  $k_{p,\text{eff}}$

values to those obtained from an oxidation study. In this case, agreement was found between the observed and calculated parabolic constants when the measured and assumed grain diameters were of comparable dimensions.

### 3.5 The Properties of the Co—O System

#### 3.5.1 Structure, Thermodynamics and Diffusion

Cobalt has two oxides,  $\text{Co}_{1-\delta}\text{O}$  and  $\text{Co}_3\text{O}_4$ , which have stability ranges defined by the temperature and oxygen partial pressure.  $\text{Co}_{1-\delta}\text{O}$  has the same crystallographic structure (B1) as  $\text{Ni}_{1-\delta}\text{O}$  and is also cation deficient.  $\text{Co}_3\text{O}_4$  is stable at higher oxygen potentials and has a spinel structure. The equilibrium coexistence between these two phases is lowered by decreasing the oxygen activity, as shown in Figure (3-6) from Przybylski and Smeltzer<sup>(90)</sup>.

$\text{Co}_{1-\delta}\text{O}$  and  $\text{Ni}_{1-\delta}\text{O}$  have similar defect properties, however the total vacancy concentrations are higher for  $\text{Co}_{1-\delta}\text{O}$  than for  $\text{Ni}_{1-\delta}\text{O}$  at given values of temperature and pressure. Dieckmann<sup>(91)</sup> has analysed the available data on  $\text{Co}_{1-y}\text{O}$  nonstoichiometry, electrical conductivity and tracer diffusion and concluded that the degree of ionization could be expressed by the following equilibrium constants (as was done for  $\text{Ni}_{1-\delta}\text{O}$  in section 3.4.1):

$$K^x = 1.6 \times 10^{-2} \exp \left[ \frac{-6.21(\text{kcal/mole})}{RT} \right] \quad (3-17)$$

$$K' = 2.4 \exp \left[ \frac{-12.2(\text{kcal/mole})}{RT} \right] \quad (3-18)$$

$$\text{and } K'' = 0.17 \exp \left[ \frac{-17.2(\text{kcal/mole})}{RT} \right] \quad (3-19)$$

Doubly-charged vacancies prevail at low oxygen activities, while singly-charged vacancies predominate at high oxygen activities. However, the crossing between the two occurs at lower oxygen activities and temperatures for  $\text{Co}_{1-\delta}\text{O}$  than for  $\text{Ni}_{1-\delta}\text{O}$ .

Tracer diffusion measurements have been made as a function of temperature

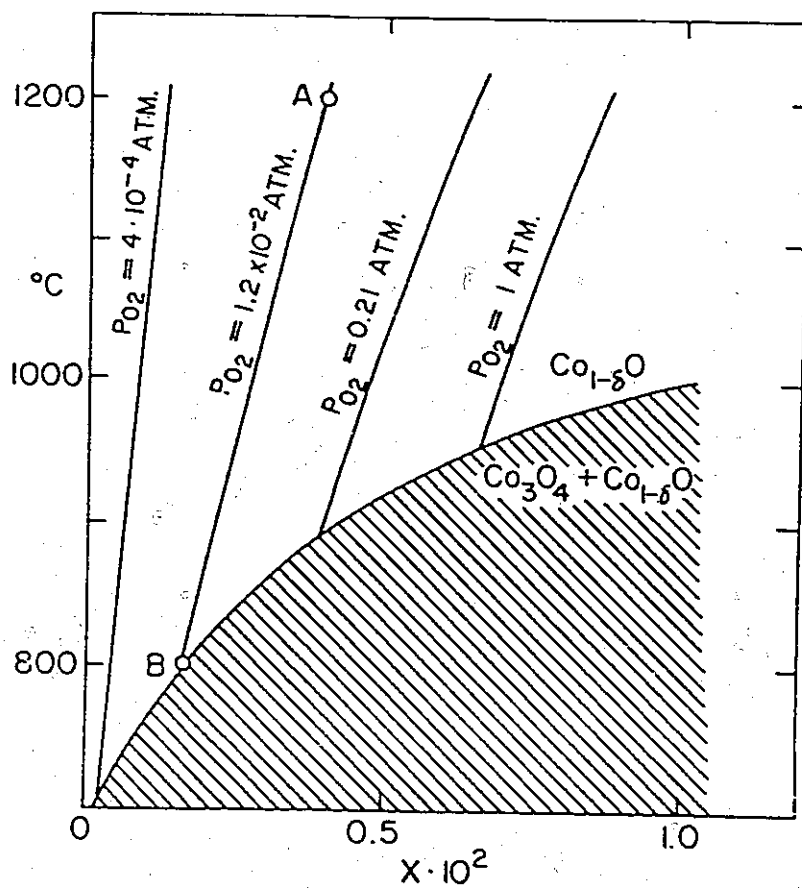


Figure (3-6)

Composition diagram of  $\text{Co}_{1-\delta}\text{O}$  between  $700^{\circ}$  and  $1200^{\circ}$  C showing its nonstoichiometry at several oxygen pressures. (90)

and pressure in  $\text{Co}_{1-\delta}\text{O}$ <sup>(92)</sup>. These results indicated that the diffusivities were proportional to a constant power of the oxygen partial pressure, but that this power varies from 0.35 to 0.27 over the temperature range 950° to 1350°C. This change was rationalized by assuming that the degree of ionization of the Co vacancies varied with temperature (as indicated by equations (3-17) to (3-19) above).

### 3.5.2 Oxidation of Cobalt

Single phase CoO scale growth on cobalt at temperatures above 1000°C has been analysed according to the Wagner theory of oxidation using current data for cobalt diffusion and defect concentrations in this oxide.  $k_p$  values for CoO growth are significantly higher than those of pure nickel, as shown in Figure (3-7) due to Atkinson<sup>(93)</sup>. Here, calculations of  $k_p$  (upper solid line) have been made using measured tracer diffusion coefficients for Co in CoO (lower solid line) and equation (2-9) approximated as  $k_p = 5.1D_{\text{Co}}^*$ . The agreement is seen to be within 5-20% of measured values. At lower oxygen activities, the pressure dependence of  $k_p$  changes from  $(a_{\text{O}_2})^{1/4}$  at 1300°C to  $(a_{\text{O}_2})^{1/3.3}$  at 950°C which has been correlated with an increased contribution to  $D_{\text{Co}}^*$  from uncharged cobalt vacancies.

## 3.6 The Properties of the Ni-Co-O System

### 3.6.1 Thermodynamics, Crystal and Defect Structure

At temperatures above 950° C and an oxygen pressure of one atmosphere, cobalt substitution into nickel oxide results in the formation of a continuous series of solid solution oxides of the type  $(\text{Ni}_{1-\xi}\text{Co}_\xi)_{1-y}\text{O}$  which are similar in structure and defect properties to the pure oxides  $\text{Ni}_{1-y}\text{O}$  and  $\text{Co}_{1-y}\text{O}$ . This situation arises due to the nearly equal cationic radii, similar valence states and free energies of formation of the component oxides. Zintl<sup>(100,101)</sup> has made extensive

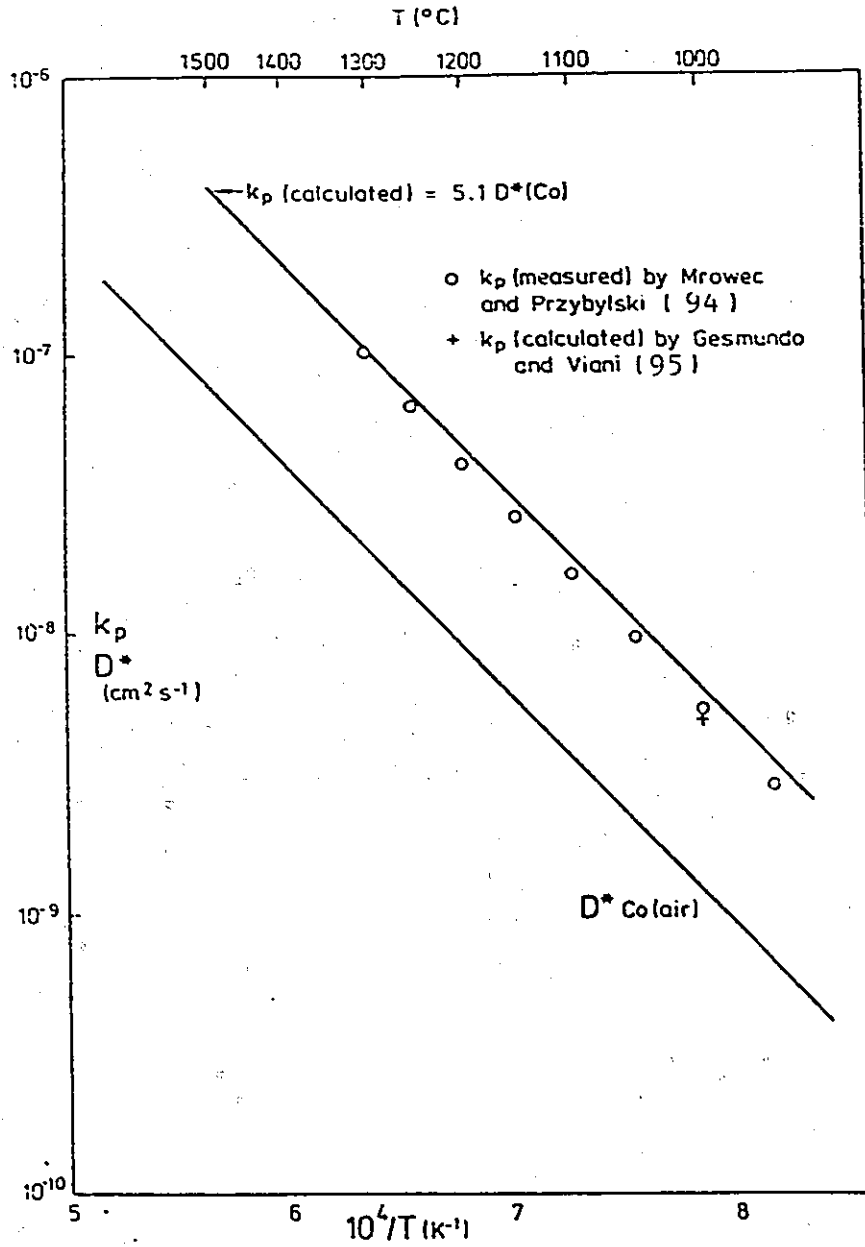


FIG.(3-7) Parabolic rate constant measured for the growth of thick CoO films on Co in air [ $a(\text{O}_2)=0.21$ ] compared with that calculated using Wagner's theory and the tracer diffusion coefficient for Co in CoO, or the concentration and mobility of Co vacancies in CoO (Gesmundo and Viani, 95 ). (93)

measurements of the defect structure of  $(\text{Ni}_{1-\xi}\text{Co}_\xi)_{1-y}\text{O}$  solid solutions at  $1000^\circ\text{C}$  and oxygen pressures ranging from 1 to  $10^{-4}$  atmospheres. His results indicated an almost linear dependence of the logarithm of the concentration of vacancies and specific conductivity on the oxide composition.

Torkar and Schneider<sup>(98)</sup> used EMF measurements at 1000 and 1300 K to investigate the thermodynamics of the NiO–CoO system. They noted slight deviations from ideal solution behavior:  $\Delta H_{\text{mix}} \cong 1$  kJ/mole for  $(\text{Ni}_{0.5}\text{Co}_{0.5})\text{O}$  at 1000 K. Using the thermodynamic activities determined from that investigation and a previous study of Ni–Co alloys<sup>(97)</sup>, Bergman and Ågren<sup>(96)</sup> used the regular solution model to predict the miscibility gap for the NiO–CoO pseudo-binary system. Their model included energetic contributions due to magnetic ordering below the Curie temperature and gave a maximum critical temperature of  $185^\circ\text{C}$ .

Tracer diffusion coefficients for Co and Ni were measured by Chen and Peterson<sup>(102,103)</sup> in  $(\text{Ni}_{1-\xi}\text{Co}_\xi)_{1-y}\text{O}$  crystals as a function of temperature and composition in air atmosphere. These diffusivities were also found to increase exponentially with an increase of the cation fraction of cobalt in the mixed oxides at constant temperature. The small deviations from an exact exponential relationship were included in their empirical expressions of  $D_{\text{Ni}}^*$  and  $D_{\text{Co}}^*$  by the use of a quadratic expression involving  $\xi$ .

The observed dependence of defect structure, electrical conductivity and diffusional parameters on composition in  $\text{Ni}_{1-y}\text{O} - \text{Co}_{1-y}\text{O}$  solid solutions has led previous authors to approximate the solution thermodynamics of this system to be ideal. Using this approximation, expressions such as the free energy of formation of the mixed oxides are given by linear relationships of the form

$$\Delta G^0[(\text{Ni}_{1-\xi}\text{Co}_\xi)_{1-y}\text{O}] = \Delta G^0(\text{Ni}_{1-y}\text{O})(1-\xi) + \Delta G^0(\text{Co}_{1-y}\text{O})\xi \quad (3-20)$$

where  $\Delta G^0(\text{Ni}_{1-y}\text{O})$  and  $\Delta G^0(\text{Co}_{1-y}\text{O})$  are the standard free energy changes for

the formation of the binary oxides. Similar expressions could be written for the formation of vacancies of varying charge in the mixed oxide solutions, where the free energy terms would now represent the free energies of formation of the appropriate type of vacancy in pure  $\text{Ni}_{1-y}\text{O}$  and  $\text{Co}_{1-y}\text{O}$ . These free energies are available from the general relationship between the free energy change of a reaction and the equilibrium constants for reactions of the type (3-1) to (3-3):

$$\Delta G_{V^z}^0[(\text{Ni}_{1-\xi}\text{Co}_\xi)_{1-y}\text{O}] = -RT \ln \bar{K}^z \quad (3-21)$$

where  $z$  is the charge state of a particular vacancy species, and the equilibrium constant  $\bar{K}^z$  for the mixed oxide is expressed in terms of  $\xi$  as

$$\bar{K}^z = K^z(\text{Ni}_{1-y}\text{O}) \left[ \frac{K^z(\text{Co}_{1-y}\text{O})}{K^z(\text{Ni}_{1-y}\text{O})} \right]^\xi \quad (3-22)$$

Only two investigations of phase equilibria in the Ni-Co-O system have been published. Robin<sup>(89)</sup>, investigated the effect of composition on the monoxide to monoxide + spinel transformation temperature. These results are reproduced in Figure (3-8). Kinoshita and coworkers<sup>(99)</sup> in a TEM study of (NiCo)O single crystals observed a possible phase separation at temperatures as high as 760°C. However, they were not able to identify the composition or structure of the small (10-50nm) precipitates.

### 3.6.2 Diffusion Properties

The available measurements of Co tracer diffusion in NiO and Ni and Co tracer diffusion in (NiCo)O crystals are summarized in Table (3-2), p 61.

Tracer diffusion coefficients of cobalt and nickel in (NiCo)O single crystals were determined by Chen and Peterson<sup>(102)</sup> over the temperature range 1122 - 1545°C in air atmosphere.  $D_{\text{Ni}}^*$  and  $D_{\text{Co}}^*$  are shown as functions of composition at

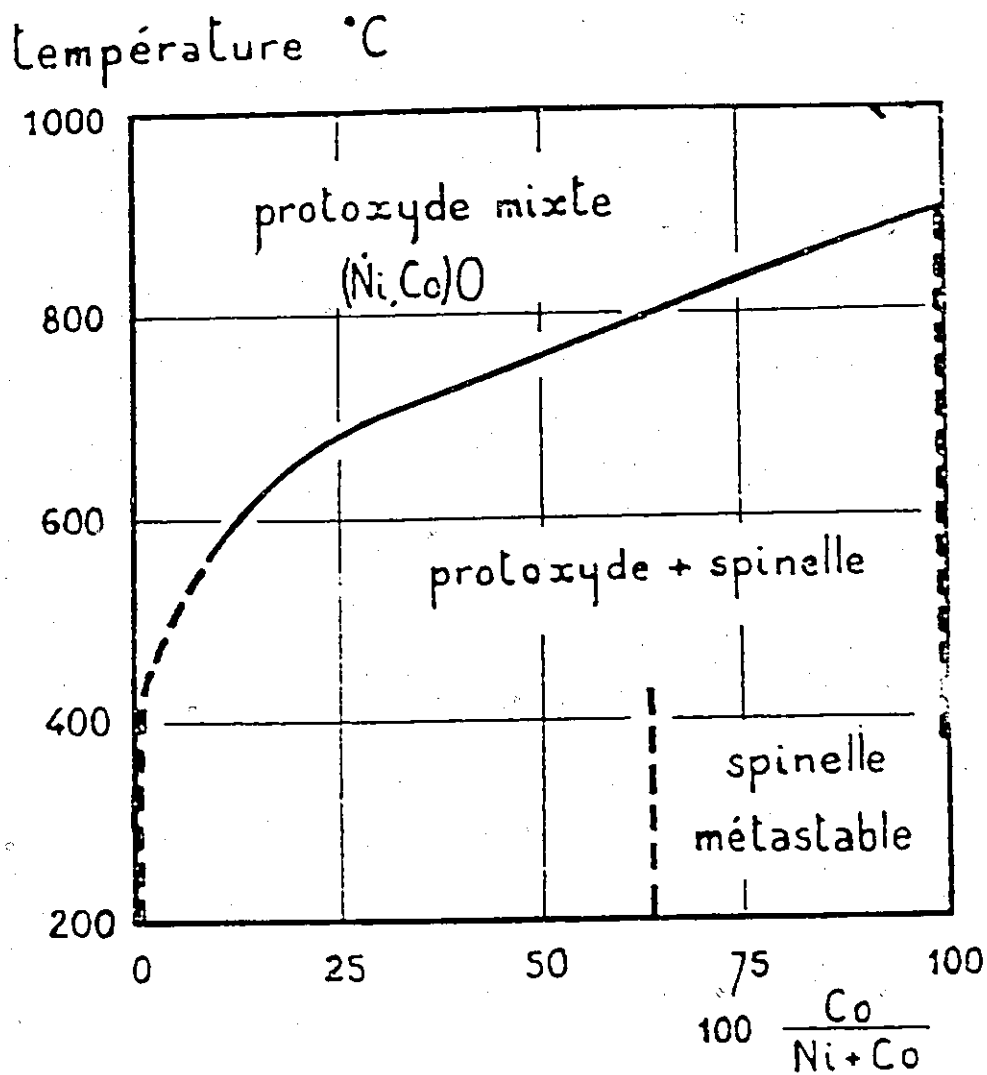


Figure (3-8)

Effect of Ni concentration on the monoxide to monoxide + spinel transformation temperature in the Ni-Co-O system determined from X-ray diffraction data<sup>(89)</sup>.

1445<sup>o</sup> and 1300<sup>o</sup>C in Figure (3-9). From this data it is seen that  $D_{Co}^*$  is approximately  $2D_{Ni}^*$  at all compositions. Additionally, there is a quasi-exponential increase in both  $D_{Co}^*$  and  $D_{Ni}^*$  with the cation mole fraction of cobalt in these solid solutions.  $D_{Co}^*$  increased slightly faster than  $D_{Ni}^*$  as a function of cobalt composition due to a difference in correlation effects for the diffusion of <sup>60</sup>Co and <sup>57</sup>Ni in the solid solutions.

Arrhenius plots of  $D_{Co}^*$  and  $D_{Ni}^*$  in NiO, (Ni<sub>0.53</sub>Co<sub>0.47</sub>)O and CoO are given in Figure (3-10). In all cases the temperature dependence of  $D^*$  could be expressed as  $D^* = D^{*o} \exp(-Q/RT)$ . The composition dependence of the activation energies were expressed by second order polynomials with respect to  $\xi$  as

$$D_{Co}^* = D_{Co}^{*o} \exp[F_{Co}\xi + G_{Co}\xi^2] \quad (3-23)$$

$$\text{and } D_{Ni}^* = D_{Ni}^{*o} \exp[F_{Ni}\xi + G_{Ni}\xi^2] \quad (3-24)$$

The empirical constants  $F_{Co}$ ,  $G_{Co}$ ,  $F_{Ni}$  and  $G_{Ni}$  were determined at 1200, 1300 and 1445<sup>o</sup>C and were found to be essentially independent of temperature. The values  $D_{Co}^{*o}$  and  $D_{Ni}^{*o}$  represent the tracer diffusion coefficients in the pure component oxides.

Tracer diffusion measurements of <sup>55</sup>Co and <sup>60</sup>Co in NiO were made by Chen and Peterson<sup>(103)</sup> over the temperature range 1179-1649<sup>o</sup>C. The temperature dependence of the cobalt diffusivity in air was expressed as

$$D_{Co} = (9.12 \pm 0.58) \times 10^{-3} \exp(-54160 \pm 460/RT) \quad (3-25)$$

where the activation energy is expressed in cal/mole.

Chen and Peterson<sup>(104)</sup> and Atkinson and Taylor<sup>(105)</sup> have measured the diffusion of Co radioisotopes along high angle grain boundaries in NiO (see Figure(3-4)). The results of the former authors in the temperature range 806 - 1043<sup>o</sup>C indicated that the activation energy for Co diffusion along NiO grain boundaries was almost identical to that for lattice diffusion. The cobalt diffusion

Figure (3-9)

Diffusion coefficients of  $^{60}\text{Co}$  and  $^{57}\text{Ni}$  in  $(\text{NiCo})\text{O}$  crystals at 1445 and 1300° C in air. (102)

Figure (3-10)

Diffusion coefficients of  $^{60}\text{Co}$  and  $^{57}\text{Ni}$  in  $\text{CoO}$ ,  $(\text{Ni}_{0.53}\text{Co}_{0.47})\text{O}$  and  $\text{NiO}$  crystals as a function of temperature in air atmosphere. (102)

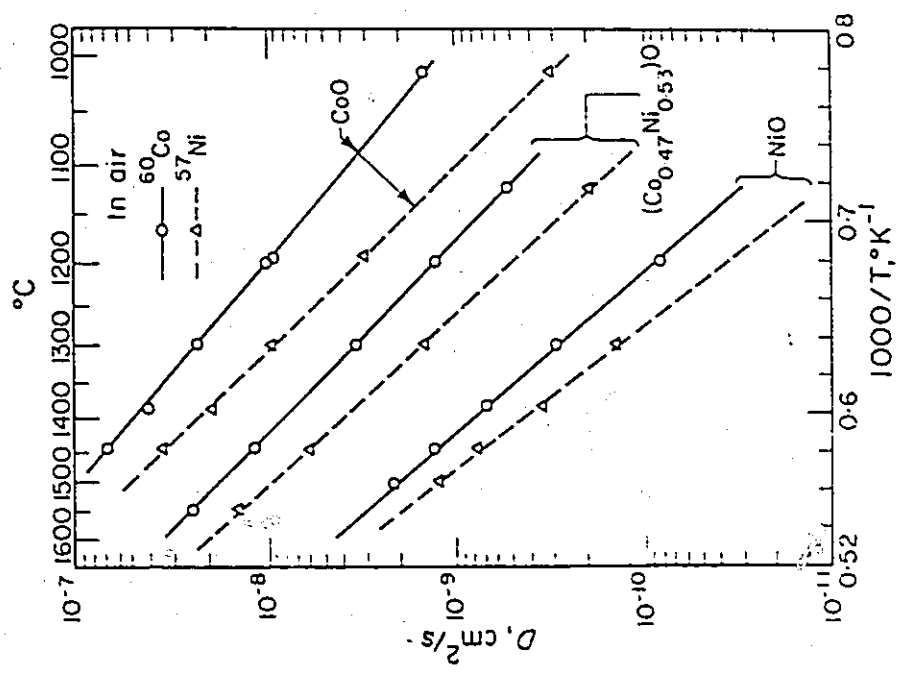


Fig. (3-10)

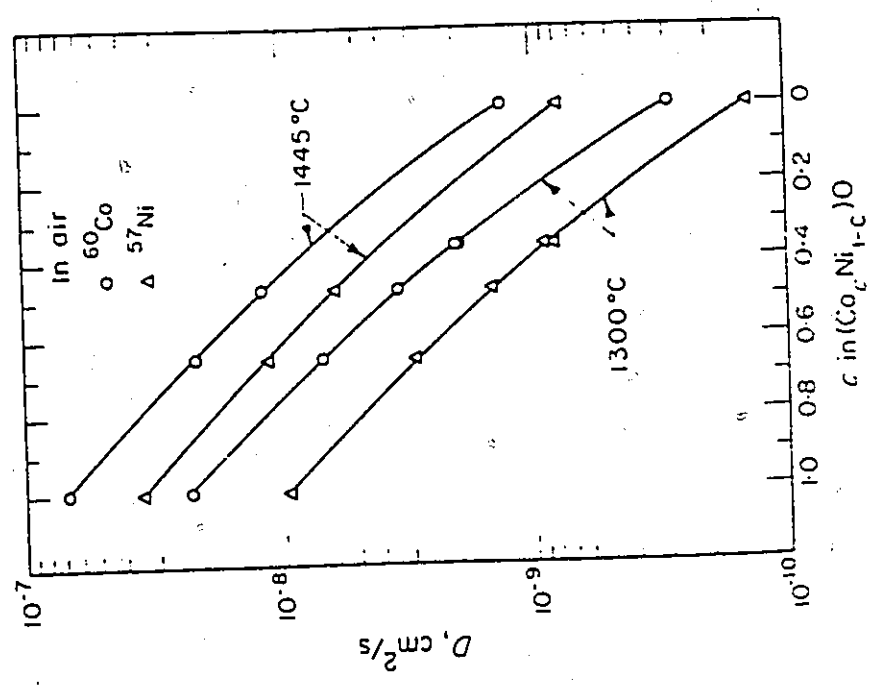


Fig. (3-9)

parameter was also a factor 30 greater than that of Ni along NiO grain boundaries, with no measurable pressure dependence over the range 0.21 to  $1.3 \times 10^{-6}$  atm  $O_2$ . Atkinson and Taylor later obtained values for  $\alpha D_{Co}^b \delta$  in NiO for  $p_{O_2} = 1$  atm and  $500^\circ < T < 800^\circ C$ , where  $\alpha$  is a partition coefficient (segregation coefficient) of the solute between the boundary and the lattice ( $\alpha = 1$  for self diffusion). Their results showed that the activation energies for cobalt and nickel grain boundary diffusion were the same within the experimental error and that the cobalt diffusivity was approximately three times faster than than the nickel diffusivity. In contrast to the results of Chen and Peterson, Atkinson and Taylor also observed a dependence of  $\alpha D_{Co}^b \delta$  on pressure at  $700^\circ C$ . Decreasing the pressure of oxygen by a factor  $10^{11}$  resulted in a decrease in  $\alpha D_{Co}^b \delta$  from  $1.1 \times 10^{-16}$  to  $1.2 \times 10^{-18}$ . The experimental data points for Co tracer diffusion in NiO in the lattice and along grain boundaries are shown in Figure (3-4).

Table (3-2)  
Tracer Diffusion of Co in NiO and Ni and Co in (NiCo)O

Temperature range(°C)	Oxygen pressure	Method	Result (R in kcal/mol·deg)	Comments	Reference
1179-1649	Air	Tracer sectioning technique	$D_{Co}^* = (9.12 \pm 0.58) \times 10^{-3} \exp \left[ \frac{-54.16 \pm 0.46}{RT} \right]$	SC, Co and Ni diffusivities enhanced by addition of Co in solid solution	(103)
800-1700	Air	Non-radioactive (<1%) Co EMPA, SIMS	$D_{Co}^* = 3.7 \times 10^{-2} \exp \left[ \frac{-58.1 \pm 0.7}{RT} \right]$		(106)
802-1043	Air	<sup>60</sup> Co, serial sectioning	Enhanced diffusion of Co in NiO gb's rel. to lattice	T dependence of $D_{Co}^*$ same as for $D_{Co}^*$ . Not $\alpha$ $P_{O_2}$ .	(104)
522-800	$1, 10^{-11}$ atm	RF sputtering, <sup>57</sup> Co	$\alpha D_{Co}^* \delta \approx 3 D_{Ni}^* \delta$	Activation energy same as for $D_{Ni}^* \delta$	(105)
1122-1545	Air	Sectioning	$D_{Ni}^* = D_{Ni}^{*0} \exp[F_{Ni} \xi + G_{Ni} \xi^2]$ $D_{Co}^* = D_{Co}^{*0} \exp[F_{Co} \xi + G_{Co} \xi^2]$	SC, $F_{Ni}$ , $G_{Ni}$ , $F_{Co}$ , $G_{Co}$ det'd at 1200, 1300, 1445°C	(102)

### 3.6.3 Oxidation of Ni-Co Alloys

The growth kinetics, structure, morphology and cation distributions have been determined by several investigators<sup>(107-117)</sup> for thermally growing oxide layers on Ni-Co alloys. These oxides have been observed to follow parabolic kinetics over the temperature range 800<sup>o</sup>-1400<sup>o</sup> C in air atmosphere. Cation distributions in thermally growing (NiCo)O layers have been shown to exhibit cobalt enrichment near the outer oxide surface and depletion near the metal-oxide interface. The main focus of the most recent studies was to accurately determine the parabolic scaling constants and cation concentration profiles (eg. by electron microprobe analysis) in order to compare experimental observations to those predicted from Wagner's ternary diffusion model for the growth of solid solution oxide scales on binary alloys.

The parabolic scaling rates of Ni-Co alloys were determined by Frederick et al<sup>(108)</sup> and Nishida et al<sup>(111)</sup>. The results of the latter investigation are shown in Figure (3-11). These reaction rates decreased exponentially with nickel content in the oxide scale. Internal oxidation and depletion of cobalt in the alloy substrate were found in nickel-rich alloys accompanied by cobalt enrichment in the oxide scales. The deviation from an exact exponential decrease in  $k_p$  with nickel concentration was attributed to the internal oxidation reaction.

A master plot of CoO concentration profiles vs. normalized distance in the external (NiCo)O scales at 1200<sup>o</sup>C was prepared by these same authors as shown in Figure(3-12). Co and Ni were concentrated near the scale-gas and alloy-scale interfaces respectively. These concentration profiles correspond to steady state growth and hence fall on a master curve when plotted vs.  $x/\sqrt{t}$ . A further example of cation concentration profiles in (NiCo)O scales determined by EMPA was given in Figure (2-7), due to Nishida and coworkers<sup>(111)</sup>. Here the Wagner model has been

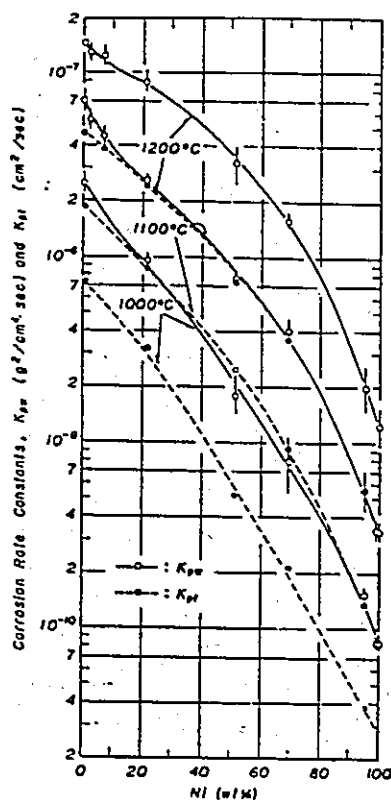


Figure (3-11) Parabolic scaling rates of Ni-Co alloys exposed to 1 atm.  $O_2$  at various temperatures as a function of composition. <sup>(111)</sup>

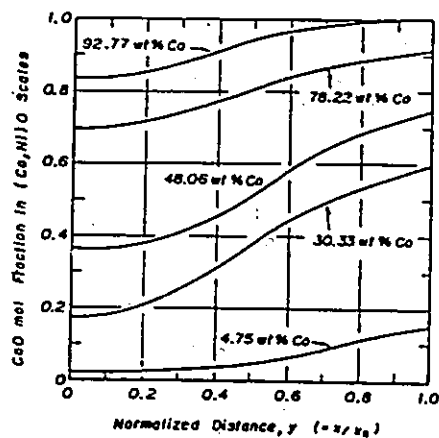


Figure (3-12) Master plots of CoO mole fraction in (NiCo)O scales formed at  $1200^\circ C$  in 1 atm.  $O_2$ . <sup>(111)</sup>

used to calculate composition profiles using Chen and Peterson's diffusion data<sup>(102)</sup>.

Based on a review of the available data, Nishida et al<sup>(111)</sup> compiled a schematic oxide map shown in Figure(3-13) which indicates the observed oxidation behavior as a function of temperature and composition. It may be seen that for high Co alloys,  $\text{Co}_3\text{O}_4$  layers are formed in the scale. The field indicating Co depletion and internal oxidation is shifted towards the Ni rich side of the plot but apparently does not extend below  $800^\circ\text{C}$ . based on the available data.

There have been initial attempts to measure cation concentrations in thin ( $\leq 500 \text{ \AA}$ ) films using AES and ion microprobes<sup>(112-114)</sup>, however these studies have not been connected with any attempt to understand the transport mechanisms or film structures in the intermediate temperature range.

There are no systematic studies of the orientation dependence or surface pretreatment effects on the parabolic scaling rate. There is no accurate kinetic data for oxidation in this system at temperatures  $\leq 500^\circ\text{C}$ . The initial uptake of oxygen<sup>(115)</sup> and the formation of oxide islands<sup>(116)</sup> has been observed using Auger spectroscopy.

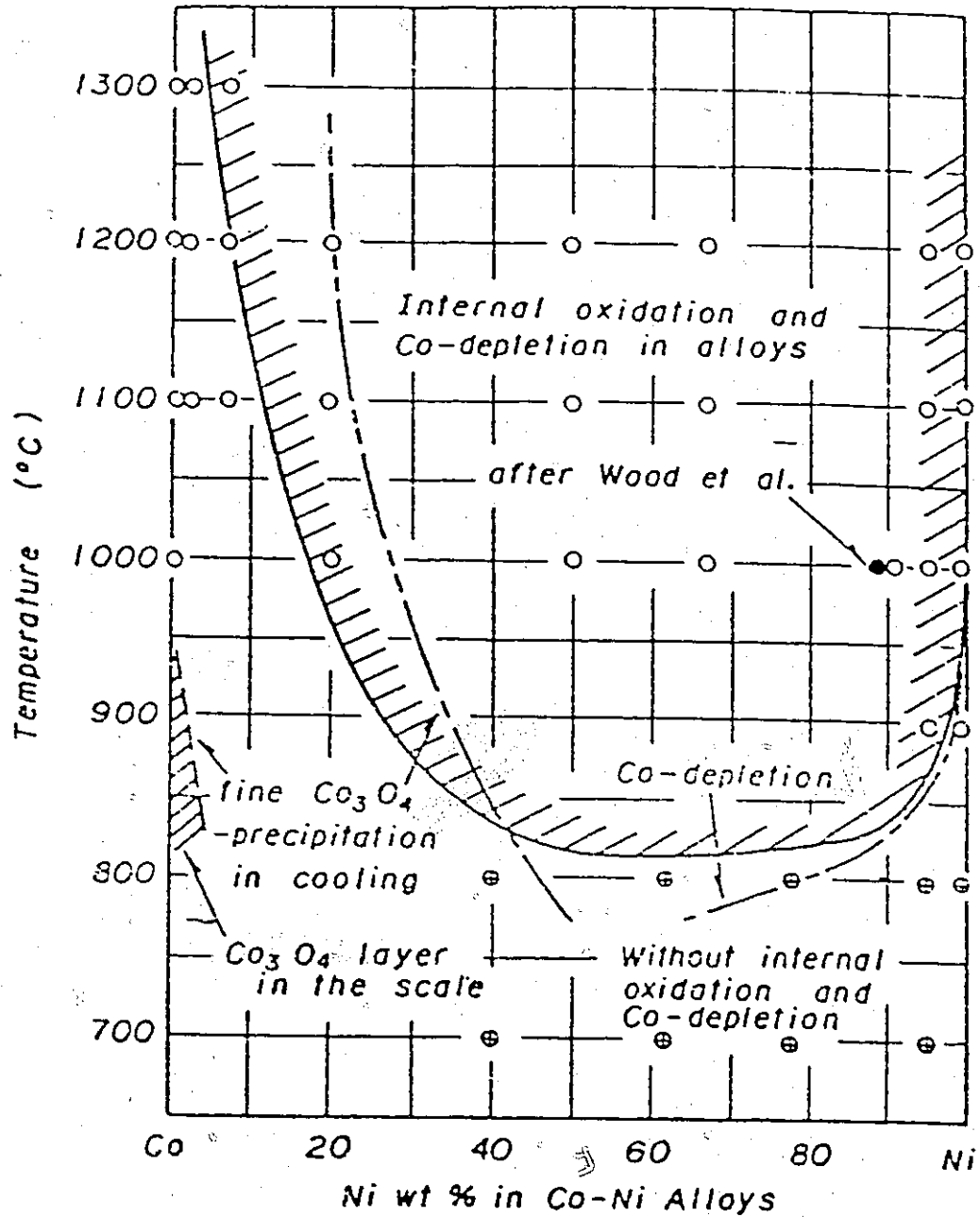


Figure (3-13)

Schematic presentations of oxidation behaviors of Ni-Co alloys, showing the internal oxidation, Co-depletion and phases of the oxide scale. (111)

## CHAPTER 4

### EXPERIMENTAL PROCEDURES

#### 4.1 Introduction

This chapter deals with the preparation of specimens, the design and testing of a heating stage for the scanning Auger microprobe, an ultrahigh vacuum manometric assembly for the determination of oxidation kinetics, and electron and ion microprobe analysis methods.

In the study of equilibrium surface segregation it is usually desirable to obtain Auger spectra while holding samples at high temperature. An alternative and in many cases easier approach has been to use spectra from samples which were heated and quenched *in situ*. The difficulty with the second method is that at sufficiently high temperatures, the surface may have time to relax during cooling which can lead to an incorrect assesment of segregation<sup>(117)</sup>.

The heating module available from the manufacturer of the PHI 600 Scanning Auger Microprobe uses a resistive heating element to heat both the sample holder and stage. This arrangement allows spectra to be taken at temperature, but limits the maximum attainable temperature to approximately 873 K. Furthermore, since the thermocouple is embedded in the stage there is some uncertainty as to how accurately it represents the temperature of the top surface of the sample being analysed. In order to achieve sample temperatures of over 1273 K and to attach

thermocouples directly to the sample surface, an improved electron bombardment heating stage was designed. This unit was compatible with the fast entry airlock system of the PHI 600 and was optimised to ensure containment of the heating electrons so that they did not contribute a significant background in the Auger spectra.

The oxidation kinetics of Ni-Co alloys in the temperature range 673–1073K were determined using a manometric system having ultra-high vacuum capabilities. This unit was based on a design used by workers in the Division of Chemistry, National Research Council of Canada<sup>(74)</sup>. During experiments, a high accuracy differential capacitance manometer was used to follow the uptake of oxygen by the samples as a function of time. This system was better suited to the measurement of thin film oxidation kinetics than a conventional microbalance assembly which had been used in earlier oxidation experiments. The microbalance suffered from electronic noise effects which on blank runs corresponded to average deviations of approximately  $\pm 80 \mu\text{g}$ . In contrast to this, the manometric system was capable of resolving oxygen uptakes corresponding to only a few monolayers surface coverage.

Finally, a number of analytical techniques, including SEM, TEM, Auger and SIMS were used to characterize the specimens from the surface segregation and oxidation experiments. A summary of the operating parameters and methodology for obtaining the results is presented for these instruments.

## 4.2 Sample Preparation

### 4.2.1 Cobalt-Rhodium Alloys

The Co-Rh alloys were prepared from weighed samples of pure rhodium and cobalt. The rhodium, in powder form, was pressed into pellets which were cast into boules in the water-cooled hearth of a monoarc furnace. The furnace was first evacuated to less than  $10^{-5}$  Torr before being back-filled with 0.5 atm argon. The

Co was received in the form of a 3 mm diameter rod which was cut to the desired length, then cleaned in acetone and methanol prior to alloying. After a final weighing the Co rod and the Rh boule were placed into the monoarc furnace and melted together to form an alloy. Each alloy button was turned and remelted at least 5 times to promote homogeneity of the final casting. The samples were weighed after alloying to determine their weight loss and place error limits on the final composition. The impurity contents of the pure cobalt and from the rhodium boule are given in Table (4-1). Each casting was etched in hot aqua regia to remove the surface contaminants and then given a homogenizing anneal for 48 hours in an evacuated ( $<10^{-6}$  Torr) quartz tube at 1423 K.

The castings were cut into 1 mm thick disks on a high speed wafering saw, giving an average diameter of 7 mm. These specimens were then mechanically polished down to a 1  $\mu$ m diamond finish using kerosene as lubricant. Prior to mounting for AES analysis the samples were cleaned ultrasonically in trichloroethylene followed by acetone and methanol.

Table (4-1)

Impurity contents of cobalt, 99.98% a/o pure, and rhodium,  
99.97% a/o pure given as parts per million atomic

	Element(ppma)									
	C	N	O	Na	Mg	Al	Si	P	S	Cl
Cobalt	18.	13.	90.	0.5	3.	4.	26	0.8	14.	9.
Rhodium	18.	15.	14.	0.1	.03	1.	39.	0.6	3.0	0.2
	K	Ca	Sc	Ti	V	Cr	Mn	Fe	Ni	Cu
	Cobalt	0.8	10.	—	.03	.01	.04	.08	6.	6.
Rhodium	1.	—	.02	4.	0.2	5.	4.	39.	3.	55.
	Zn	Ge	As	Br	Rb	Sr	Y	Zr	Mo	Ru
	Cobalt	5.	0.8	2.	0.1	.01	0.3	0.1	0.7	0.2
Rhodium	—	—	0.5	—	—	—	1.	—	55.	33.
	Rh	Ag	In	Sn	Sb	Te	I	Cs	La	Ba
	Cobalt	2.	7.	0.5	0.4	0.1	0.3	.08	.008	—
Rhodium	maj	—	0.7	0.4	2.	—	—	—	0.7	—
	W	Ir	Au	Pb	Bi					
	Cobalt	—	—	13.	1.	.02				
Rhodium	2.	25.	1.	—	—					

Table (4-2)

Analysis of Co-Rh alloys in atomic % Rh \*

Alloy #	1	2	3	4	5
Composition	19.3±.1	41.3±.1	47.8±.1	55.1±.1	84.7±.5

\* as determined by weight measurements

#### 4.2.2 Single Crystal Nickel-Cobalt Alloy

The nickel-cobalt single crystal alloy, having a nominal composition of 5 atomic percent, was prepared by the Monocrystals Company, Cleveland, Ohio from materials supplied by Johnson Matthey Chemicals Limited. The cobalt was from the same source used for the cobalt-rhodium alloys. The batch analysis supplied by Johnson Matthey for the nickel rod is shown in Table (4-3). The single crystal, 1.4 cm in dia. and 11.2 cm long was prepared using the Bridgeman technique in an alumina crucible. An impurity analysis by glow discharge mass spectrometry was kindly supplied by the Division of Chemistry, National Research Council of Canada. This analysis is shown in Table (4-4) and indicates a purity comparable to the Ni samples used to measure diffusion properties of Ni and Co in NiO<sup>(60,61)</sup>. The actual composition of this alloy was determined to be Ni-(3.86±0.03)Co by emission spectroscopy.

A Laue back reflection X-ray taken from one end of the crystal revealed that the ingot axis was 3.5 to 4° off the <110> direction. A final Laue orientation to within 0.5° of the <110> was achieved by using a sample-to-film distance of 5 cm, as shown in Figure (4-1). The crystal was held and positioned accurately in the cutting process by transferring the entire sample and goniometer assembly to the bed of the sectioning saw. Slices 1 mm thick were cut from the crystal, cleaned using trichloroethylene and acetone and stored in a dessicator for later use.

Specimens for the oxidation experiments were prepared by polishing on all sides through a series of silicon carbide papers (200, 320, 400 and 600 grit) using water as lubricant. Final mechanical polishing was carried out on cloths impregnated with  $6 \times 10^{-6}$  m and then  $1 \times 10^{-6}$  m diamond paste with kerosene as the lubricant. The specimens were then cleaned using trichloroethylene and



Figure (4-1)

Final Laue back-reflection pattern of the Ni-3.86 Co single crystal. The incident beam is parallel to [011]. Molybdenum source, 50 KeV, 12  $\mu$ A, 2.5 hr. exposure, 5 cm specimen-to-film distance.

Figure (4-2)

Electron channeling pattern from the Ni-3.86Co (110) single crystal surface after the chemical polishing treatment<sup>(121)</sup>. 30 KeV, low mag., scanning defocussed beam. The pattern is produced from a thin region at the surface of the crystal corresponding to no more than two extinction distances<sup>(122)</sup>. For 30 KeV electrons in Ni, this corresponds to thicknesses from 140 Å for the (111) reflection to 730 Å for the (420) reflection<sup>(123)</sup>. The distortion in this pattern is probably due to a slight bending of the crystal which occurred during the mechanical polishing process.

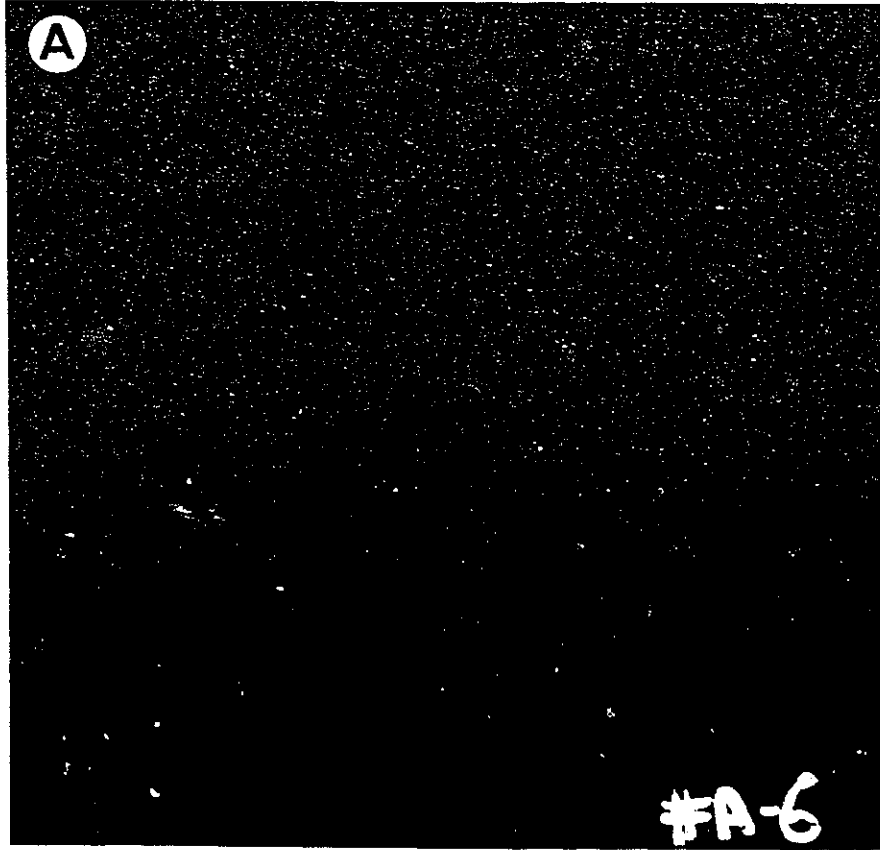


Fig.(4-1)



Fig.(4-2)

acetone.

The cold-worked surface layers were removed by trying several of the electropolishing and chemical polishing solutions which are published in the literature<sup>(118-121)</sup>. Of the former methods the best results were obtained using a 60 percent sulfuric acid solution chilled in an ice bath. A current density of 0.5-0.7 A/cm<sup>2</sup> at 2.5 V for 1 min resulted in the least amount of pitting while removing all traces of the mechanical polish when viewed in the light microscope. However, surface pitting could not be completely eradicated using this technique so methods of chemically polishing the specimens were investigated. The best results were obtained using a solution due to Fox<sup>(121)</sup> consisting of 65 ml acetic acid, 35 ml nitric acid and 0.5 ml hydrochloric acid at room temperature. By immersing specimens in 300 ml of this solution for a total of 5 min. the cold worked layer was completely removed, leaving a smooth, pit free surface. Evidence of the relatively undeformed surface condition is shown by the <110> electron channeling pattern in Figure (4-2).

#### 4.2.3 Polycrystal Nickel-Cobalt Alloy

A polycrystalline nickel-cobalt alloy, having a nominal composition of 5 atomic percent cobalt, was prepared using the same arc melting apparatus and procedures as described in 4.2.1. The starting materials were from the same source as the Ni and Co used to prepare the single crystal alloy. The alloy was cast into the form of a rod, approximately 1 cm in diameter and 4 cm in length. This rod was subsequently sealed in an evacuated ( $10^{-6}$  Torr) quartz tube and annealed at 1473 K for 10 hours. 0.1 cm thick specimens were cut from this ingot on a high speed SiC wafering saw using kerosene as lubricant. These samples were

Table (4-3)

Impurity contents of nickel rod (batch No. 08715) as supplied by Johnson Matthey Chemicals Limited given as parts per million by weight.

Element	Fe	Al	Ca	Cr	Cu	Mg	Si	Ag
Concentration	3	<1	<1	<1	<1	<1	<1	<1

Table (4-4)

Impurity contents of Ni-5Co alloy as determined by glow discharge mass spectrometry (ppm by weight).

Element	B	C	N	O	F	Na	Mg	Al	Si	P	S
ppm	0.2	47	0.6	25	<.04	0.2	0.3	42	90	.09	3
Element	Cl	K	Ca	Ti	V	Cr	Mn	Fe	Co	Ni	Cu
ppm	0.2	0.1	1	0.3	0.7	0.5	0.5	44	maj	maj	4
Element	Zn	Ga	Ge		As	Se	Y	Zr	Nb	Mo	Ag
ppm	0.9	.2	<.02		<.01	<.07	.03	.2	.7	.07	.09
Element	Cd	In		Sn	Sb	Te		Ba	Hf		W
ppm	0.5	<.003		<.08	0.2	<.01		<.02	<.04		0.2
Element	Pt	Au	Hg		Tl	Pb	Bi		Th		U
ppm	0.1	<.02	<.02		<.02	0.2	<.01		<.001		<.001

mechanically polished using the same steps as for the single crystal alloys. No further chemical or electrochemical steps were used. The actual composition of this alloy was Ni-(4.0±0.1)Co by the emission spectroscopy technique.

### 4.3 A Fast Entry Air-Lock-Compatible Hot Stage For the Collection of Auger Spectra at Elevated Temperatures

In order to obtain the most accurate surface composition data for the alloys used in this investigation, a heating stage was designed and tested for the "PHI 600 Scanning Auger Microprobe" manufactured by Perkin-Elmer. An electron bombardment heating source was chosen in order to minimize the power requirements, yet allow samples to be heated *in situ* to temperatures of up to 1273 K. The stage and sample holder are shown in Figures (4-3) and (4-4).

Some important aspects of the stage design are illustrated in the cut-away view of Figure (4-3). A tungsten hairpin filament was located in the center of the assembly and electrically isolated from the rest of the stage. The filament was held at a positive potential of up to 1200 volts while the top portion of the stage was grounded. The beam was focussed by creating a cross-over point as it passed through a Wehnelt aperture. The exact positioning of the filament, aperture size, and Wehnelt potential were optimized during testing in order to achieve the best focus and maximize the current delivered to the sample. The beam diameter was checked visually by placing a phosphour-coated glass<sup>(124)</sup> on top of the sample holder. Thermocouple connections to the transferable sample holder were provided by spot welding the chromel and alumel wires to the back of the retaining spring clips.

The sample holder is shown in Figure (4-4). The two halves were built around a central insulating ceramic ring. Thermocouple connections were made by spot welding chromel and alumel wires to the bottom rim of the holder which then made contact with the stage spring clips. These connections were continued to the top of the holder where smaller diameter (0.003 in.) thermocouples could be directly



Figure (4-3)

An electron bombardment heating stage for the PHI 600 Scanning Auger Microprobe: (a) cut-away view showing filament and aperture positions, (b) assembled stage ready for insertion into the U.H.V. chamber.

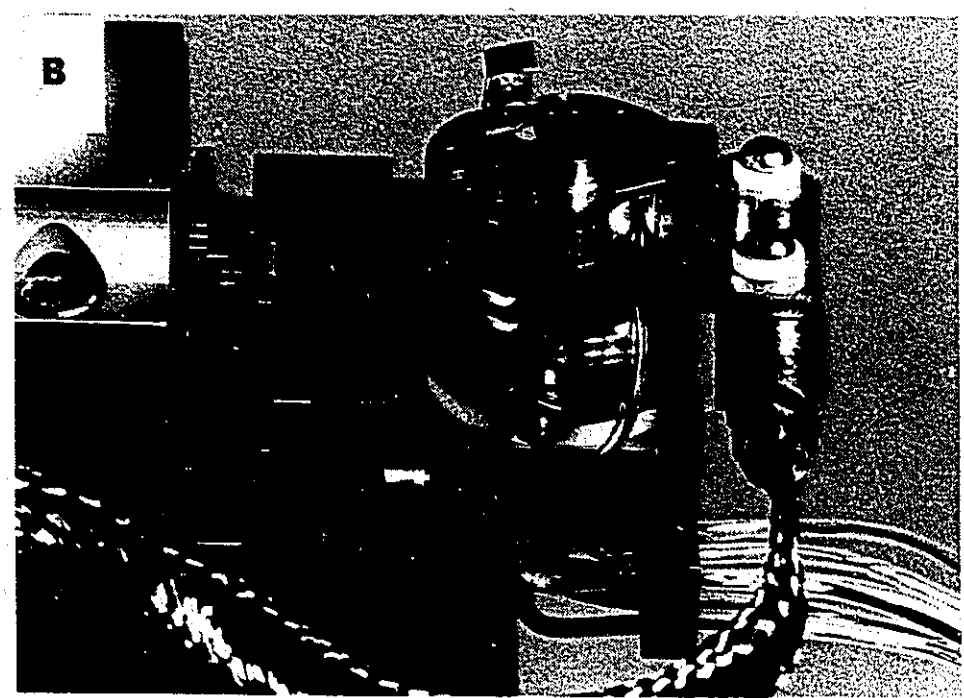
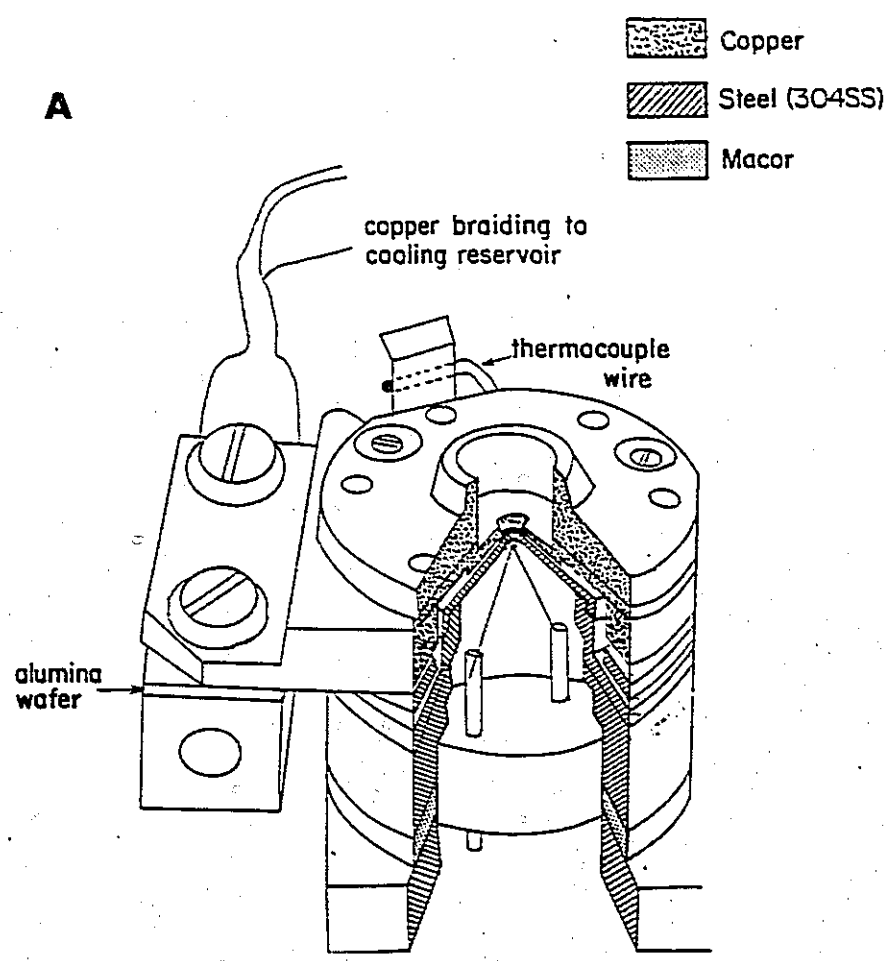


Fig. (4-3)

Figure (4-4)

A fast entry, air-lock-compatible specimen holder for the electron bombardment heating stage: (a) cut-away view showing inner grounded and outer thermocouple sections, (b) sample holder with Co-Rh alloy and chromel-alumel thermocouples in place.

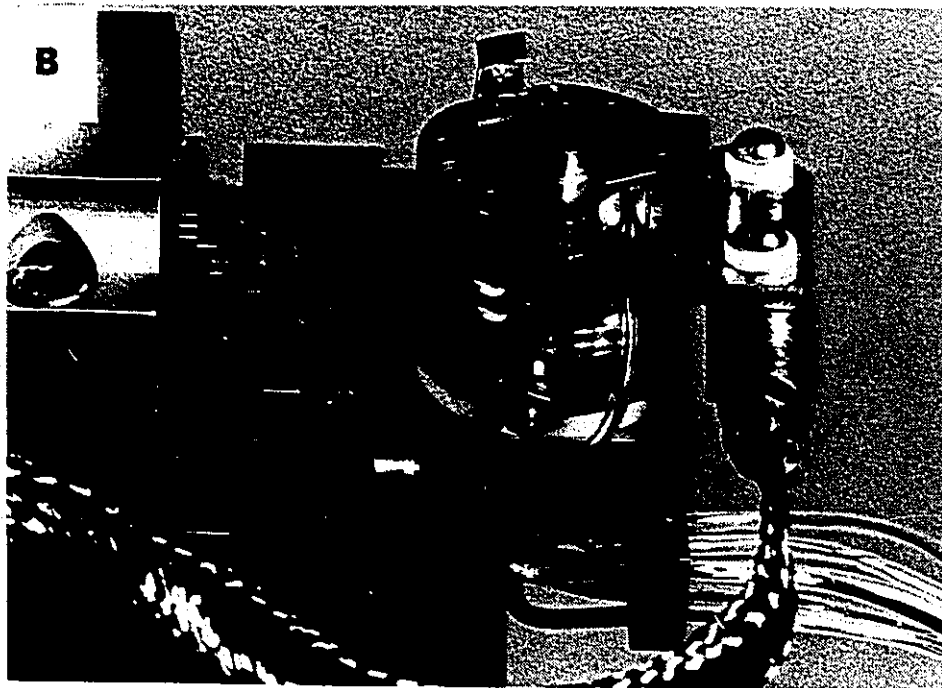
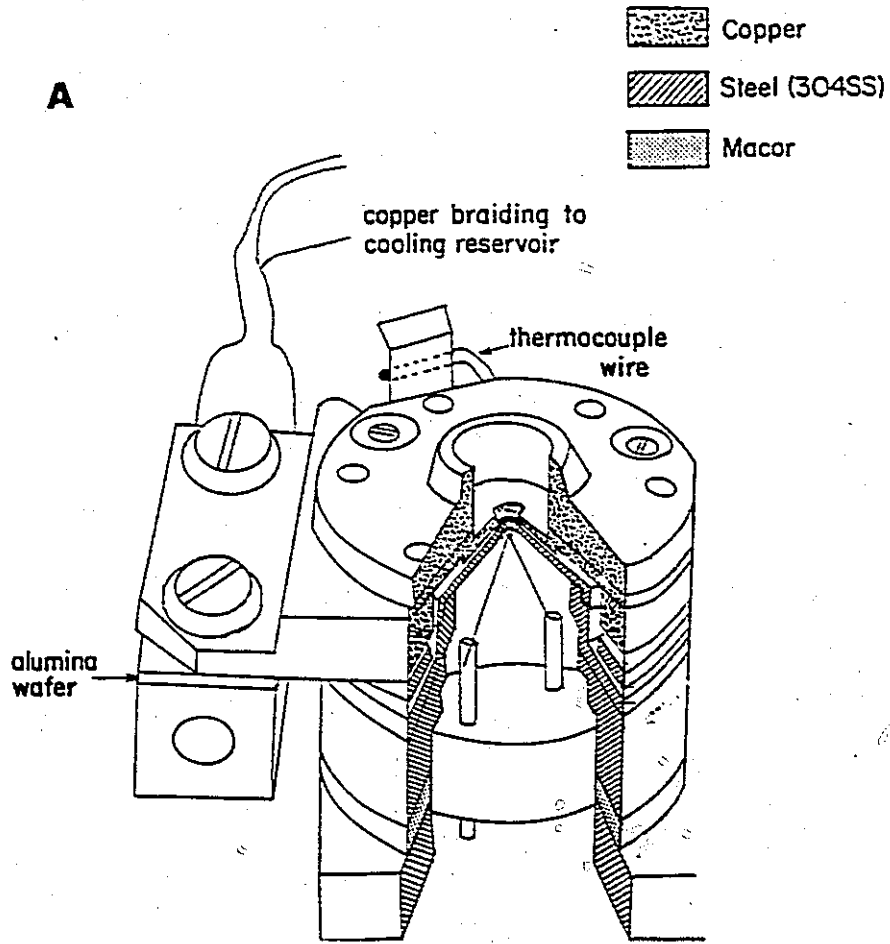


Fig. (4-3)

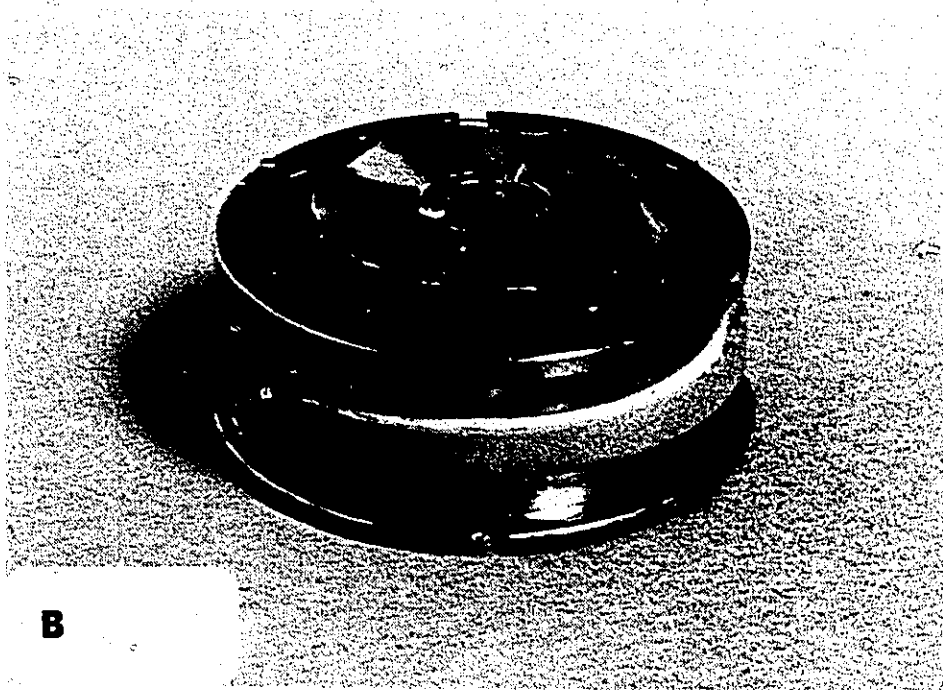
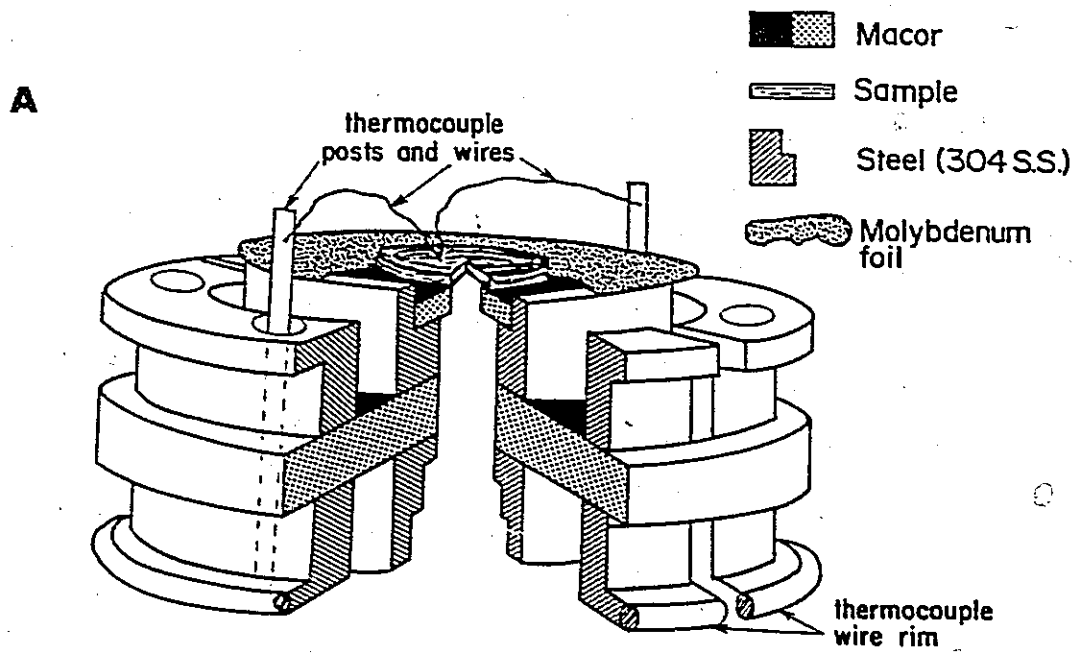


Fig.(4-4)

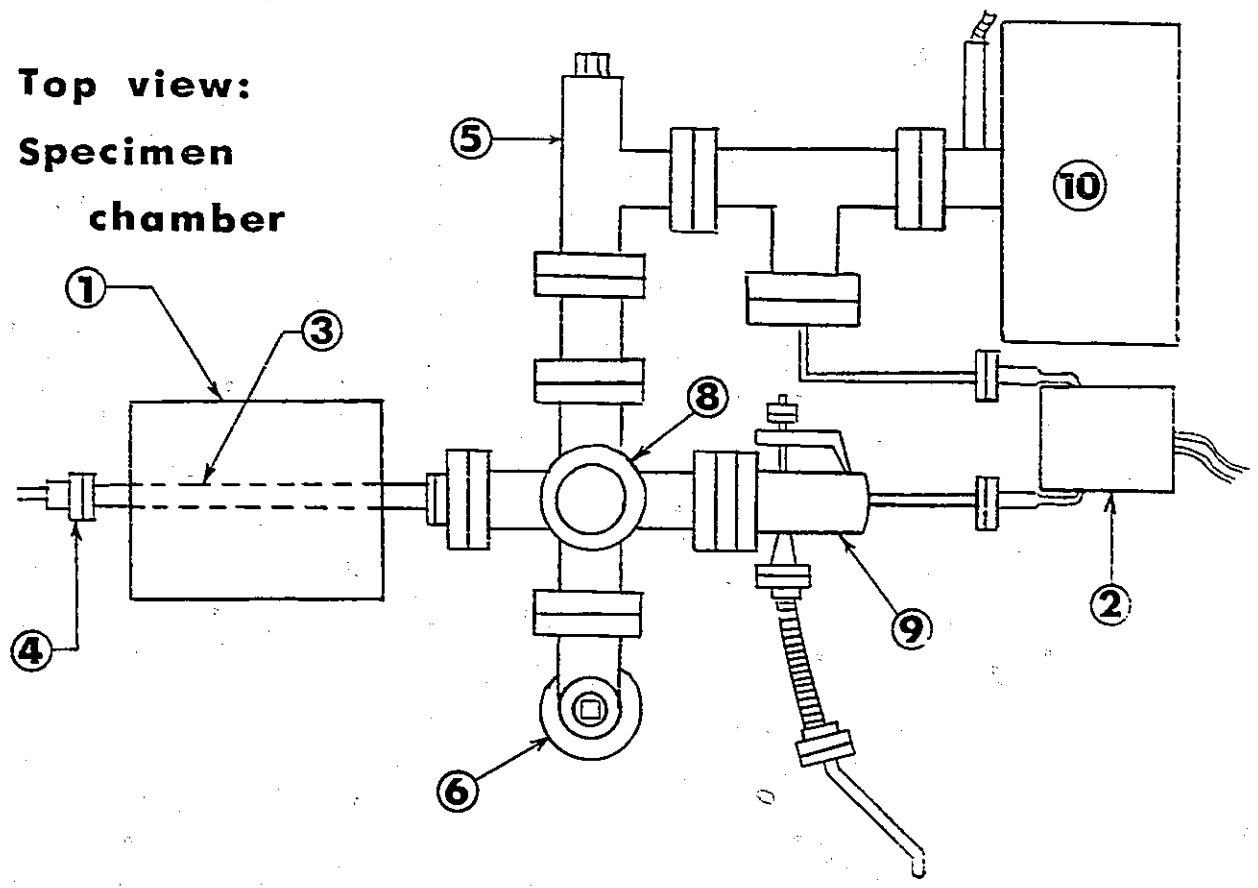
attached to the sample surface. The central portion of the holder acted as a ground connection and support for the disc-shaped sample. Leakage current from the electron heating source was minimized by placing the sample, held by three tungsten wires, on top of a ceramic insulating ring designed to close the gap between the sample and the holder. In addition, a molybdenum foil ring was placed above the sample as a final barrier between the holder and energy analyser. Using this configuration the count rate due to the heating electrons was less than 0.1% of the count rate due to the primary electron beam.

The accuracy of the thermocouple readings was checked by observing the melting points of three metals, Pb; 600.5 K, Al; 933.4 K and Ge; 1210.4 K. In each case, the observed melting points were within  $\pm 5$  K of the actual values.

#### 4.4 Oxidation Apparatus and Procedures

Oxidation kinetics of the Ni-Co alloys at temperatures in the range 473–1073 K were determined using a manometric apparatus capable of measuring oxygen uptakes much less than could be determined by microbalance techniques. This ultrahigh vacuum manometric apparatus was based upon a design utilized successfully by workers at the National Research Council of Canada<sup>(74)</sup> for investigations of the oxidation properties of Ni, Fe and stainless steel. An illustration of the apparatus is shown in Figure (4-5). Base pressures in the range  $10^{-9}$  to  $10^{-10}$  Torr were achieved by the use of a Balzers TPU 050 50 l/s turbomolecular pump and a Varian 20 l/s ion pump. This capability was necessary in order to ensure that pressure changes due to leakage of gas into the system during an experiment were insignificant compared to those changes resulting from uptake of gas by the samples. Additionally, annealing the nickel-cobalt alloys in a UHV environment resulted in atomically clean, gas-free metallic surfaces which

**Top view:  
Specimen  
chamber**



**Side view:  
Gas manifold**

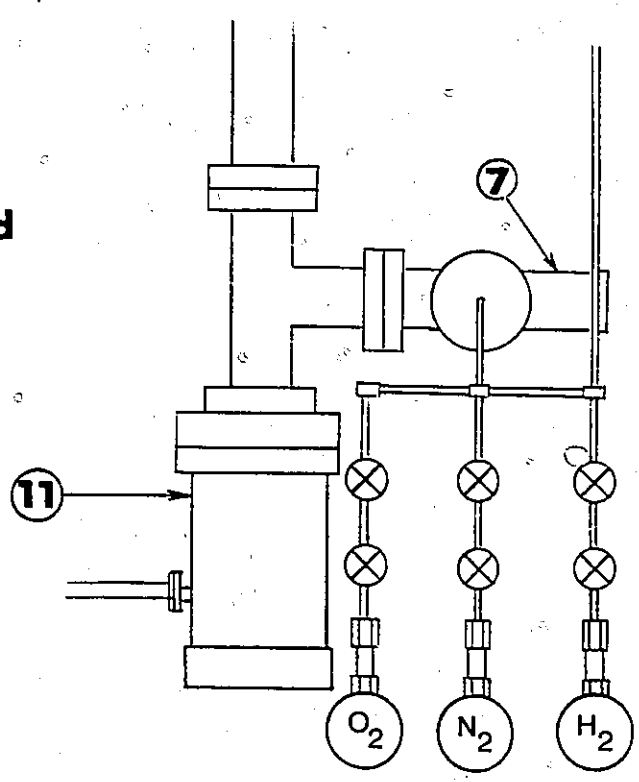
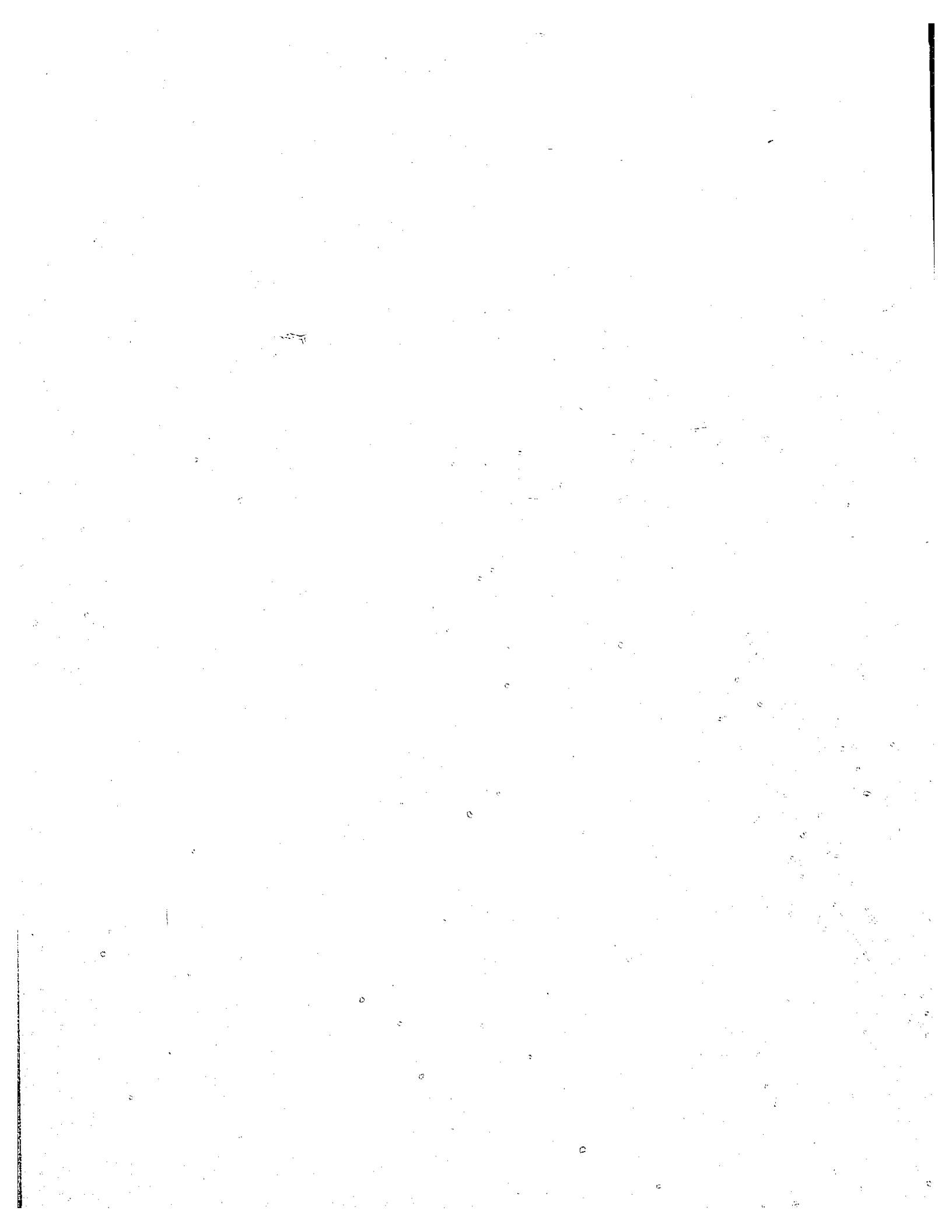


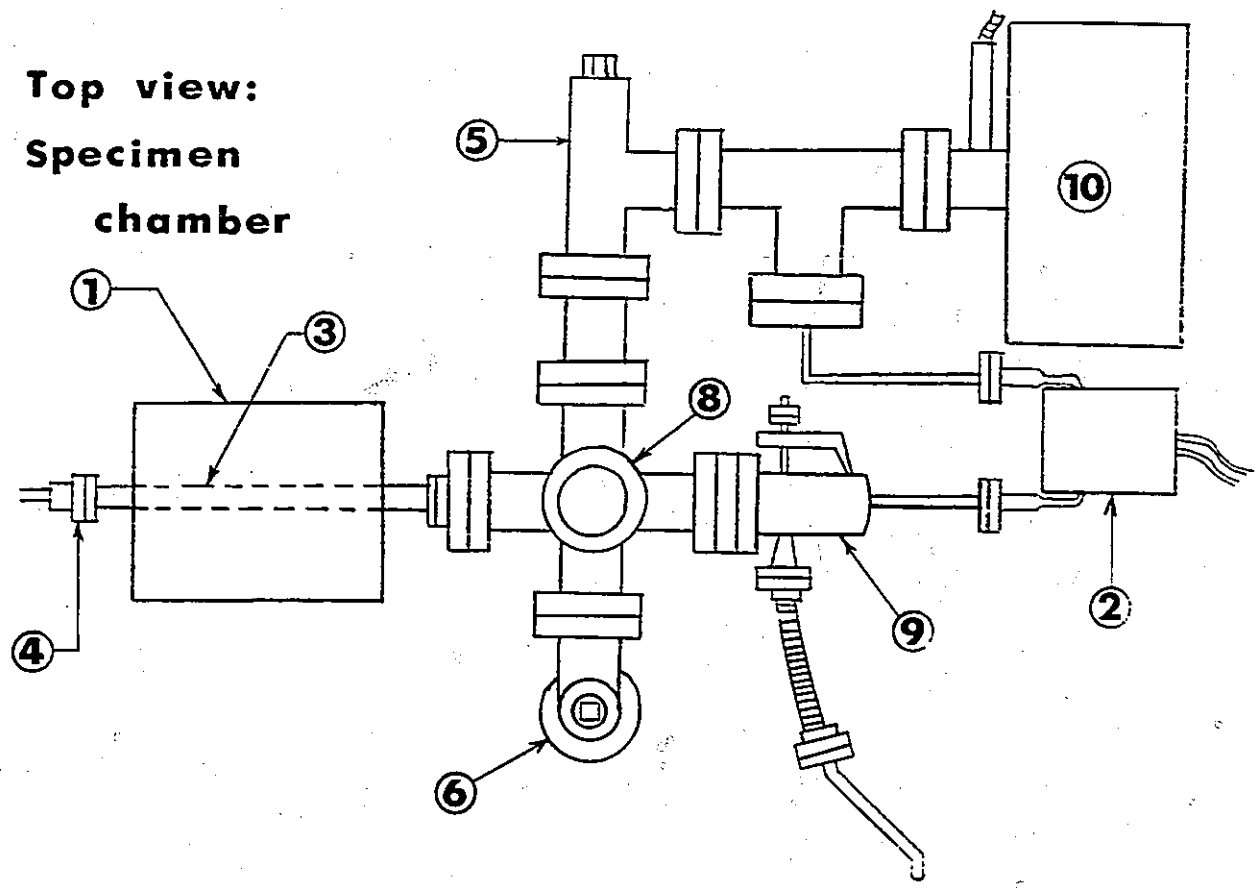
Fig (4-5)

Figure (4-5)

A U.H.V.-capable manometric assembly for the measurement of oxidation kinetics: 1. quartz lamp infra-red heating chamber, 2. differential capacitance manometer, 3. specimen chamber (quartz), 4. Pt-Pt13%Rh thermocouple feed-through, 5,6,7. U.H.V. valves, 8. ion gauge, 9. U.H.V. leak valve, 10. ion pump and 11. turbo-molecular pump.



**Top view:  
Specimen  
chamber**



**Side view:  
Gas manifold**

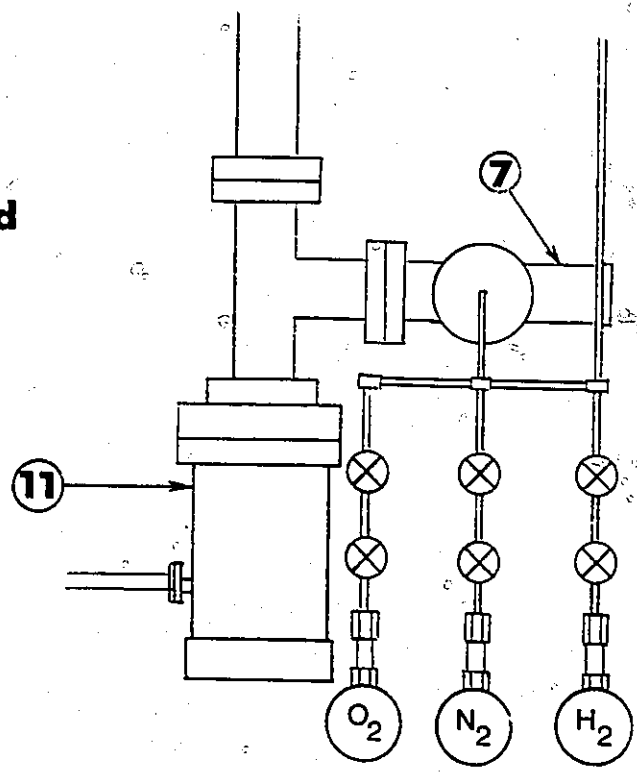


Fig (4-5)

could be maintained for periods of up to several hours prior to oxygen exposure. Samples were mounted on Pt-Pt13%Rh thermocouples and heated by infrared radiation from a quad elliptical heating chamber (Research Inc. Model E4-02). The quartz lamps were powered by a Halmar Electronics, Inc. Series LZFI SCR controller with a Thermo Electric Series 900 digital temperature controller and monitor. The reaction kinetics were determined by an MKS Instruments Inc., type 315 high accuracy differential capacitance manometer designed to operate in the range  $10^{-6}$  to 1 Torr. The manometer sensor head was stabilized at 323 K by a heater shell thus reducing uncertainties due to thermal fluctuations. The digital outputs from the capacitance gauge controller (MKS Instruments Inc. Type 270B) were used as inputs to an interface circuit for an IBM PC/XT compatible computer. Time and pressure readings taken during an experiment were stored in the computer for later analysis. The interface was also used to admit additional oxygen to the system through a Balzers UDV 035 gas dosing valve under the control of a stepper motor circuit. Automatic gas dosing made it possible to leave the system unattended during prolonged exposures of up to 50 hours.

The uncertainty of the pressure readings is expressed as the sum of errors due to non-linearity, hysteresis, inaccuracies resulting from temperature changes and non-repeatability of sensor measurements<sup>(125,126)</sup>. The overall system uncertainty for the above type of sensor is expressed as a percent of reading and is shown in Table (4-5). In the present investigation most experiments were conducted at a pressure of  $5 \times 10^{-3}$  Torr. The uncertainty in these pressure readings is therefore in the range of 0.5%.

A typical experiment involved placing a sample into the system after which the assembly was pumped down and "baked out" at 443 K for 12 hours. When the

system had cooled after bakeout, the pressure was usually in the  $10^{-9}$  to  $10^{-10}$  Torr range. The Ni-Co alloys were given a 5 hour, 873 K anneal at this pressure in order to remove the remaining thin oxide layer present due to chemical polishing and exposure to the lab atmosphere<sup>(127)</sup>. Following the anneal the sample was cooled and 1 Torr of oxygen was admitted for 1-2 hours to saturate the walls of the reaction chamber. This uptake was monitored using the capacitance gauge to determine when saturation was complete. The remaining oxide on the sample surface could be removed by briefly pumping the system down below  $10^{-9}$  Torr followed by a 5 min. anneal at 873 K. Experiments were then conducted by exposing a sample to oxygen by either of two methods; the hot-bare or furnace-raised techniques.

Hot-bare oxidations were performed on samples free of prior oxide. Following the last UHV anneal described above the sample was cooled to the desired temperature after which oxygen was admitted to start the experiment. Furnace-raised experiments were initiated by cooling the annealed samples to room temperature, at which time oxygen was admitted and the sample temperature was slowly increased at a rate of approximately  $100^{\circ}$  C per minute to its final value. This nomenclature is adopted from the work of Graham et al<sup>(74)</sup> who used similar techniques to study the effects of surface preparation on the oxidation of pure nickel. The effect of these starting procedures is discussed in Chapter 6.

The measurement volume of the manometric system was adjusted according to the rate of uptake by the sample. At low temperatures, when the rate of consumption was low, a measurement volume of  $666 \pm 7$  ml was chosen which corresponded to a reservoir of  $5.74 \pm 0.06 \mu\text{g O}_2$  at  $5 \times 10^{-3}$  Torr. The use of this smaller volume increased the sensitivity of the kinetic readings. At higher temperatures, the more rapid pressure decreases created the need for more frequent

dosing of gas into the system, so a larger volume was added to make a total of  $1598 \pm 8$  ml, or  $13.76 \pm 0.07 \mu\text{g O}_2$ . In order to place these quantities in perspective, it is to be noted that an uptake of  $1 \mu\text{g O}_2/\text{cm}^2$  on pure nickel corresponds to an average film thickness of 6.2 nm of NiO.

Table (4-5)

Uncertainty of pressure readings for an MKS Instruments  
1 mmHg type 315 differential sensor head<sup>(125,126)</sup>.

Pressure reading at:	Total uncertainty in Torr <sup>*</sup>	Total uncertainty as a percent of reading
Full Scale(FS) (1 Torr)	$2.51 \times 10^{-3}$	0.25%
10 % FS ( $10^{-1}$ Torr)	$2.55 \times 10^{-4}$	0.26%
1 % FS ( $10^{-2}$ Torr)	$3.00 \times 10^{-5}$	0.30%
0.1 % FS ( $10^{-3}$ Torr)	$7.5 \times 10^{-6}$	0.75%
0.01 % FS ( $10^{-4}$ Torr)	$5.25 \times 10^{-6}$	5.25%
0.001 % FS ( $10^{-5}$ Torr)	$5.03 \times 10^{-6}$	50.3%

\* Includes non-linearity, hysteresis, non-repeatability (0.25% reading), resolution ( $1 \times 10^{-6}$  Torr), zero temperature coefficient (0.0004%FS), and span temperature coefficient (0.0003% reading).

## 4.5 Specimen Characterization Techniques

### 4.5.1 Secondary Electron Microscopy

The morphological features of the oxide films were examined in the Phillips model 515 scanning electron microscope (SEM). Samples were placed on aluminum stubs using silver dag and coated with a thin evaporated gold layer to improve conduction at the surface and prevent charging. Furthermore, the surface crystallinity of the single crystal Ni-Co alloys was checked using electron channeling patterns, as illustrated in Figure (4-2).

### 4.5.2 Auger Electron Spectroscopy

Surface segregation on the cobalt-rhodium alloys and composition vs. depth profiles for (NiCo)O films were determined using the Perkin Elmer "PHI 600 Scanning Auger Microprobe", equipped with a single-pass cylindrical mirror analyser (CMA) and the heating stage described above. A summary of typical parameters used for AES analysis and ion sputtering is presented in Table (4-6). The methods used to quantify the Auger data were based on linear least-squares fitting of the spectra in the  $N(E) \cdot E$  mode<sup>(128)</sup> using standards obtained either from pure elements or from alloy surfaces corresponding to the bulk composition obtained by scratching the surface of the alloy with a diamond scribing tool inside the analysis chamber. The latter method has the advantage of avoiding the need to apply matrix-dependent backscatter correction factors.

For the analysis of surface segregation, the area analysed was confined to a single grain. In order to do so it was necessary to compensate for stage drift during heating by observing the secondary electron image and making manual adjustments

Table (4-6)

## Typical Operating Conditions Used in AES Measurements

	Electron Beam	Ion Beam
Incident Beam Energy	5 keV	4 keV
Beam Current	0.2-1 $\mu$ A	1-2 $\mu$ A
Beam Diameter	100-300 nm	200 $\mu$ m
Rastered Area	50x50 $\mu$ m <sup>2</sup>	2x2 mm <sup>2</sup>
Ion Species	—	<sup>16</sup> O <sup>-</sup> , <sup>40</sup> Ar <sup>+</sup> , <sup>131</sup> Xe <sup>+</sup>
	When Sputtering	Not Sputtering
Chamber pressure range in Torr	10 <sup>-8</sup>	10 <sup>-10</sup>
Beam incidence ( $\perp$ to surface):		
e <sup>-</sup> beam	45 <sup>o</sup>	90 <sup>o</sup>
ion beam	45 <sup>o</sup>	—
Method of recording data:		N(E)·E vs. E
Spectrometer resolution:		0.3
CMA scan rate:		0.5 V/step
Analyser output for quantitative analysis:		
	pulse counting (800-1000 kilocounts/s)	

to the stage position or beam deflection. The equilibrium segregation experiments were conducted by first raising the sample temperature to approximately 673 K and allowing the system to reach thermal equilibrium. The sample was then sputtered clean and raised to the desired temperature over a period of approximately 60 seconds. While waiting for the surface to reach an equilibrium composition, the Co and Rh Auger signals were monitored. The sample was also checked for the appearance of other elements, such as C, O and S. If no contamination was occurring, the sample temperature was changed, typically by 50-100<sup>o</sup> C and the sample allowed to equilibrate again. The time to reach equilibrium was dependent on temperature and ranged from approximately 30 to 5 min at 623 and

1123 K, respectively. The process of changing the temperature, waiting for equilibrium to be established and then recording a spectrum was continued until surface contamination could be detected, whereupon the sample was cooled to approximately 673 K and sputtered briefly before restarting this process. 673 K was chosen as the maximum temperature for sputtering due to the risk of introducing long-range compositional changes at higher temperatures created by preferential sputtering and diffusion of the alloying components.

The maximum temperature for each alloy was limited by the vapour pressure of Co, which is  $5 \times 10^{-9}$  Torr at 1173 K. At higher temperatures one would not achieve true equilibrium, but rather a dynamic equilibrium between evaporation and diffusion. A further difficulty at temperatures above 973 K was the cosegregation of sulfur which was present in the bulk at ppm levels (Table (4-1)). In order to deal with this effect, the sample was heated to approximately 1073 K for 20 minutes followed by a brief sputtering treatment to remove the impurity. By repeating this procedure several times it was possible to develop a sulfur-depleted zone below the alloy surface, such that no sulfur was detectable in the times required to equilibrate the samples.

In order to obtain approximate equilibration times, the samples were sputtered at high temperature in order to induce Co depletion by the processes described above and similar to effects observed by other investigators<sup>(129)</sup>. After sputtering the Co and Rh signals were monitored as they asymptotically returned to their equilibrium values. At 1273 K the time required for this to occur was approximately 10 minutes. Since the perturbation introduced by this method was substantially deeper than that expected to arise from surface segregation or sputtering at lower temperatures, it was believed that allowing the sample to equilibrate for the times reported above at 623 and 1123 K would allow for

equilibrium to be reestablished after each temperature change in the segregation experiments.

#### 4.5.3 Secondary Ion Mass Spectroscopy

Some secondary ion mass spectroscopy (SIMS) measurements were used to complement the AES depth profiling of the (NiCo)O films. A Cameca IMS-3f ion microscope at the Surface Science Western, University of Western Ontario was used in the early stages of the oxidation investigation. Additional measurements were made using a Physical Electronics Inc. Model SIMS 1 which was temporarily added to the PHI 600 analysis chamber. Typical conditions used in these instruments are given in Table (4-7).

Table (4-7)  
 Typical Operating Conditions Used in SIMS Measurements

	Cameca IMS-3f	PHI SIMS 1
Beam Energy	10.4-12.4 KeV	4 KeV
Beam Current	100 nA(O <sub>2</sub> <sup>+</sup> ), 2-25 nA(Cs <sup>+</sup> )	1-2 μA
Beam Diameter	50 μm	200 μm
Rastered Area	250x250 μm <sup>2</sup>	2x2 mm <sup>2</sup>
Ion Species	O <sub>2</sub> <sup>+</sup> , Cs <sup>+</sup>	Ar <sup>+</sup> , Xe <sup>+</sup>
Raster/Optical Gating:	150x150 μm <sup>2</sup>	50-80%
Positive/Negative Ion Detection:	Pos.	Pos.

#### 4.5.4 Transmission Electron Microscopy

The structure of the thin oxide layers was investigated using transmission electron microscopy (TEM) in the bright field (BF), dark field (DF), and selected area diffraction (SAD) modes. This work was completed using the Phillips 400 model TEM at McMaster University. Information about the crystallinity and orientation of the oxides was obtained by removing the films from the alloy substrates and mounting them on 3 mm copper TEM grids. The film stripping technique using an iodine methanol solution was the same as that used by Khoi<sup>(127)</sup>, however it was found necessary to give structural stability to the very thin oxides ( $\leq 50$  nm) with a temporary plastic support layer as described by Dye et al.<sup>(130)</sup>. A supply of the chlorinated rubber compound Alloprene, grade R-20 manufactured by Imperial Chemical Industries Ltd. (CIL) was kindly donated for this purpose by Stanchem, Mississauga, Ontario. The alloprene was applied by

dipping the samples in a 1% solution in chloroform which resulted in the formation of a thin (0.05 mm), transparent coating which was highly resistant to the iodine solution used to dissolve the underlying alloy. The plastic support was removed after the oxides were floated onto the TEM grids by dissolution in chloroform solution.

## CHAPTER 5

### RESULTS AND DISCUSSION I

#### SURFACE SEGREGATION ON COBALT-RHODIUM ALLOYS

##### 5.1 Introduction

The results of the surface segregation measurements on cobalt-rhodium alloys are presented. First, the method of quantifying the Auger data is discussed, along with investigations into the possible use of various standards, including the pure elements, sputtered and scribed alloys. Results of the segregation measurements are presented for three alloys (19.3, 47.8 and 84.7 at% Rh) in the temperature range 623–1123 K using AES. Cobalt segregation occurred on the Co-84.7Rh alloy with a heat of segregation of  $-3.7 \pm 7 \text{ kJ mol}^{-1}$ , while rhodium enrichment was observed on the Co-19.3Rh alloy with a heat of segregation of  $1 \pm 1 \text{ kJ mol}^{-1}$ . No variation from the bulk composition could be conclusively demonstrated on the surface of the Co-47.8Rh alloy. There is good quantitative agreement between these results and the combined bond breaking and lattice strain theories of segregation.

##### 5.2 Quantification of Auger Spectra and Selection of Standards for Co-Rh Alloys.

###### 5.2.1 Auger Spectra for Cobalt and Rhodium

Pure element spectra for Co and Rh are shown in Figures (5-1) and (5-2), respectively. These spectra were obtained from polished specimens after sputtering



Figure (5-1)

Cobalt elemental spectra indicating (a) the LMM triplet between 600-800 eV and (b) low energy valence band transition between 40-60 eV.

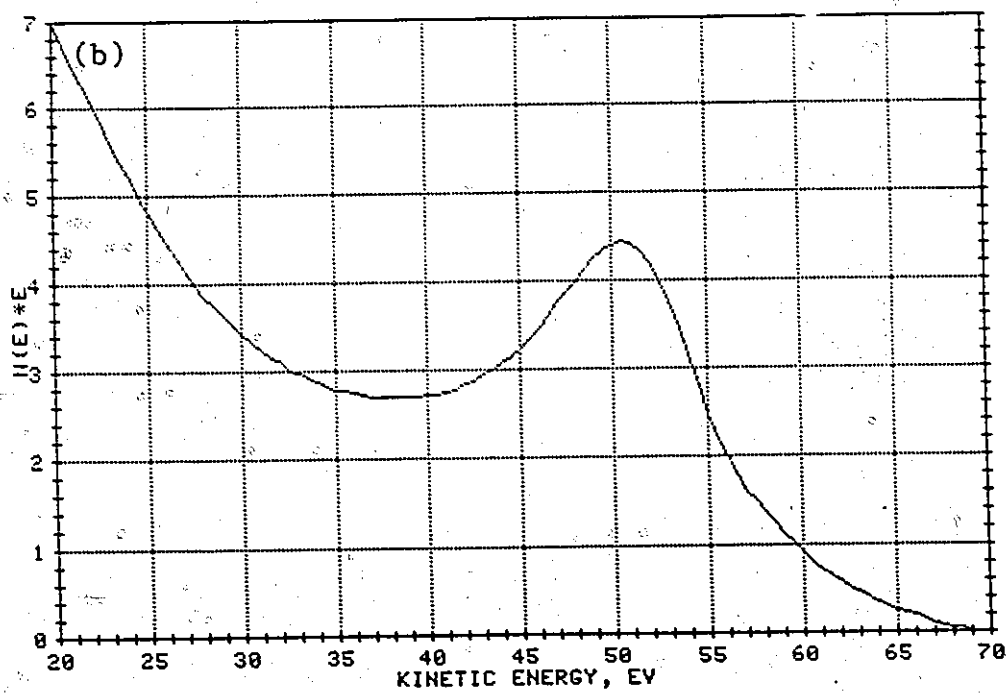
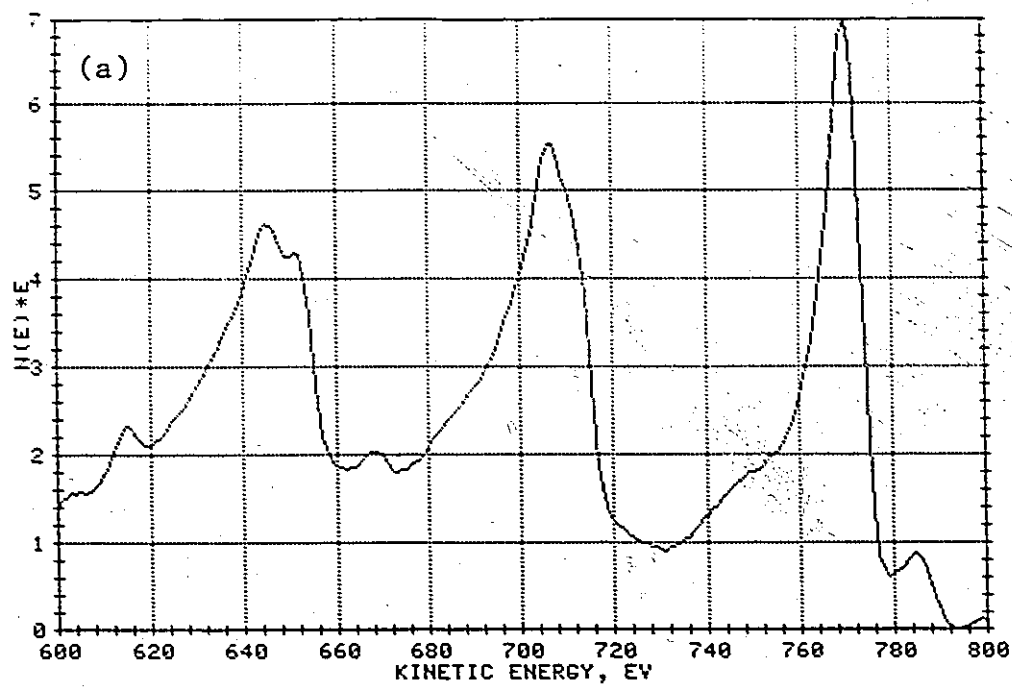


Fig.(5-1)

Figure (5-2)

Rhodium elemental spectra indicating (a) the MNN peaks in the range 200-310 eV and (b) low energy valence band transition between 30-45 eV.

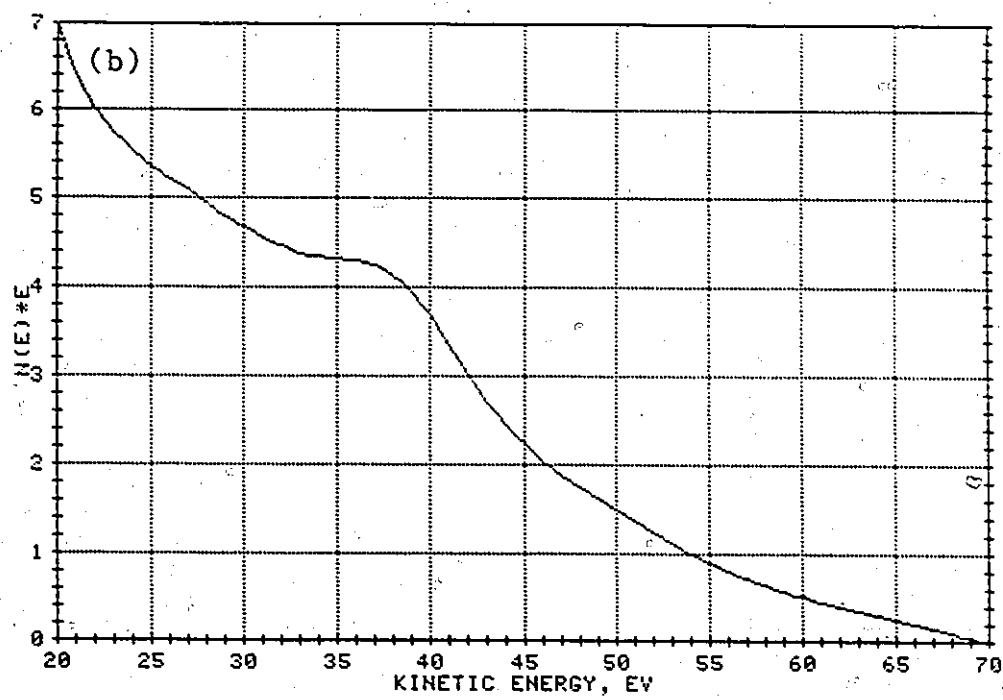
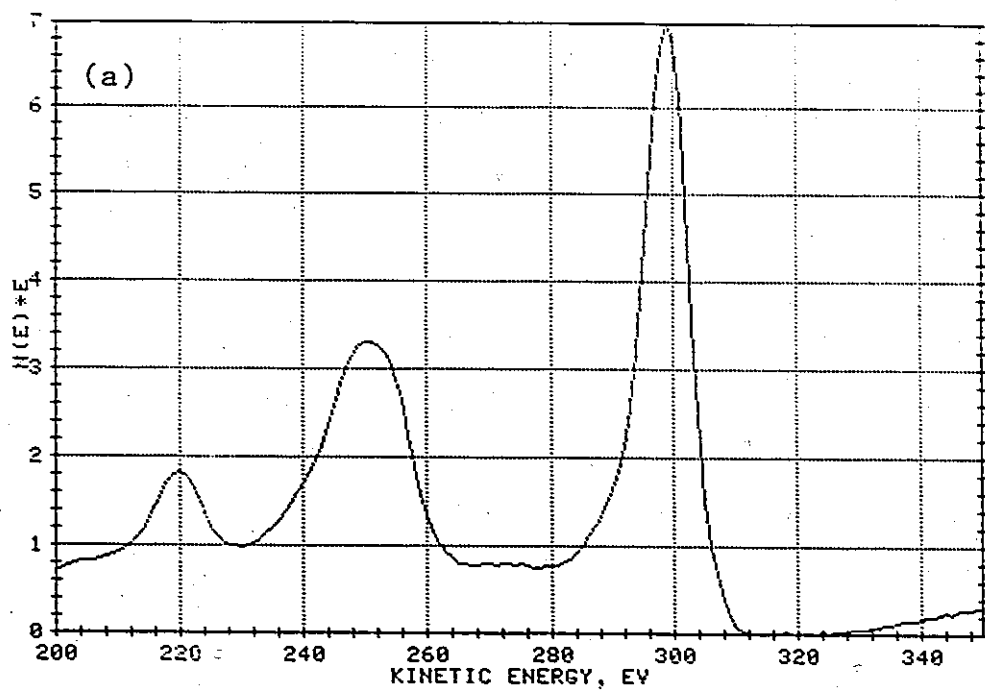


Fig. (5-2)

to remove surface impurities using the analysis conditions given in Table (4-6). For cobalt, a 3d transition metal, the principal Auger feature is the LMM triplet at energies between 600-800 eV. Rhodium is a member of the second transition series, and its main Auger features are the MNN peaks in the range 200-310 eV. Both elements have low energy valence band transitions: these are referred to in the following discussion as the Co 53 eV and Rh 40 eV peaks. There is no significant overlap of features in the spectra for these two pure elements, indicating that an evaluation of the peak intensities should not be hindered by this possibility. When attempting to quantify Auger data one must be aware of the relative escape lengths of Auger electrons. The low energy valence peaks are the most surface sensitive, having escape lengths of approximately one monolayer<sup>(131)</sup>. The Rh 298 eV and Co 773 eV peaks, which were also used in this analysis, have escape lengths of approximately 3.5 and 6 monolayers, respectively. The higher energy peaks therefore contain chemical composition information from deeper inside the samples.

### 5.2.2 Quantification of Auger Spectra From Co-Rh Alloys

The first step in the quantification of Auger data is to obtain, in an accurate and reproducible way, a measure of the elemental Auger peak intensities. As can be seen from Figures (5-1) and (5-2), peaks of interest in Auger spectra are superimposed on a large and sloping background. This background is mainly due to back-scattered primary electrons, but also includes inelastically scattered Auger and "true" secondary electrons. The backscattered contribution to the Auger signal is largely responsible for the matrix dependence of the efficiency of Auger production which must be considered when attempting to quantify Auger signal intensities. Early investigators of AES were therefore favourable to the use of phase sensitive detection techniques so that collected spectra appeared in differential form

with the peaks appearing as sharp swings on a fairly smooth background. This also made quantitative measurement of Auger signals convenient, since intensities could be obtained directly as the peak-to-peak height in the resultant spectrum. Most of the newer spectrometers, however, (including the PHI 600) record spectra in the direct or  $E \cdot N(E)$  mode by utilizing improved signal-to-noise measurement techniques and digital signal processing to make the small peaks more visible. The most common technique for intensity measurement following this is to numerically differentiate the spectrum and obtain peak-to-peak heights as before. The popularity of this approach resides in its speed and the fact that tabulated sensitivity factors and reference spectra are readily available from manufacturers and literature sources.

Difficulties with the above techniques have been cited by several authors<sup>(128,131-134)</sup> who have drawn attention to the possible variations in peak-to-peak height with modulation voltage and analyzer resolution, degradation of the signal-to-noise ratio by numerical transformations, and finally changes in peak shape due to the chemical environment. The general conclusion upon consideration of these effects has been that it is better to measure peak intensities (i.e. leave spectra) in the  $E \cdot N(E)$  form, if possible. In order to accomplish this, a linear least-squares fitting program has been developed<sup>(128)</sup> which allows a spectrum in  $E \cdot N(E)$  form to be simulated using standard spectra which have compositions similar to that of the unknown. This technique has several advantages over other methods. It does not involve background stripping, instead allowing both the peak and its inelastically scattered tail to be modeled. This means that improved fits should be obtained if standards are used which have a similar composition over the escape depth of the Auger electrons. Additionally, it makes deconvolution of overlapping peaks possible, as in the case of Co-Ni alloys, which

are the subject of the following chapter. The intensities of the unknown and standard were always normalized using the ratio of the background counts at the same energy at a position above the peak in the energy spectrum. This approach is similar to that of Langeron and coworkers<sup>(134)</sup> who used peak to background ratios in order to obtain peak intensity values which were largely independent of such extrinsic factors as the primary beam intensity, multiplier gain, collection angle, beam deflection and focusing. The insensitivity of this ratio to incident beam angle also means that the effects of surface topography can also be effectively eliminated by its use<sup>(131)</sup>.

### 5.2.3 Selection of Standards for the Determination of Composition of Co-Rh Alloys from AES Peak intensities: Preferential Sputtering on Co-Rh Alloys.

Having identified a method of determining relative peak intensities from AES spectra, the selection of appropriate standards is of paramount importance when attempting to convert these measurements into compositional information. For the case of a binary alloy, the simplest approach is to use elemental spectra. For a homogeneous alloy, the normalized ratio of the elemental peak intensities is expected to be equal to the atomic fraction of that element in the bulk, if matrix effects (including inelastic mean free path, electron backscattering factors and atomic densities) are the same for the alloy and component elements. This approximation is reasonably valid for alloys of Co and Ni for which the ratio of the above parameters is essentially unity, but not for Co and Rh. A more accurate method, which circumvents the need to apply correction factors for matrix effects is to use a bulk alloy standard whose composition is similar to that of the unknown surface. In order to do this, one must have a way of producing atomically clean surfaces with compositions equal to those of the bulk standards *in situ*. Sputtering using low energy (KeV) ions would be useful for this purpose, except in the case

where preferential sputtering of either alloy component occurs. For alloys whose constituent elements have significantly different chemical binding energies and atomic masses, a modification of surface chemistry by this process is often observed. A more reliable method is to use a stainless steel or diamond scribing tool inside the UHV chamber<sup>(135,136)</sup>.

The difference in the use of these two techniques is illustrated in Figure (5-3), where the ratio of Rh and Co Auger peak-to-peak heights (APPH) is given for the five alloys prepared for this investigation. The numerically differentiated spectra were used in this instance to give only relative compositions; absolute determinations of composition were not attempted using the linear least squares technique. The sputtered surfaces were obtained by using 4 KeV Ar<sup>+</sup> ions at 70° incidence, relative to the surface normal, at 298 K. The alloys were sputtered for 5-10 minutes until no further change in APPH was observed. In every case the sputtered surfaces showed an enrichment of Rh relative to the scribed alloys. The relative change in the signals, Rh(298)/Co(53) and Rh(298)/Co(773), does not appear to depend on the energy of the Auger transitions used in these measurements. This may be an indication that the change in surface composition is uniform over the escape depth of the electrons used. A further check of this observation can be made by calculating the range of 4 KeV Ar<sup>+</sup> ions in Co and Rh targets (see below).

Under steady-state sputtering conditions, the surface composition of a binary alloy may vary from the bulk according to a relation of the form

$$\frac{X_A^s}{X_B^s} = \frac{Y_B}{Y_A} \cdot \frac{X_A^b}{X_B^b} \quad (5-1)$$

where  $X_i^s$  and  $X_i^b$  refer to the surface and bulk atom fractions of element  $i$ , and the  $Y_i$  are the component sputtering yields (number of atoms out per incoming ion).

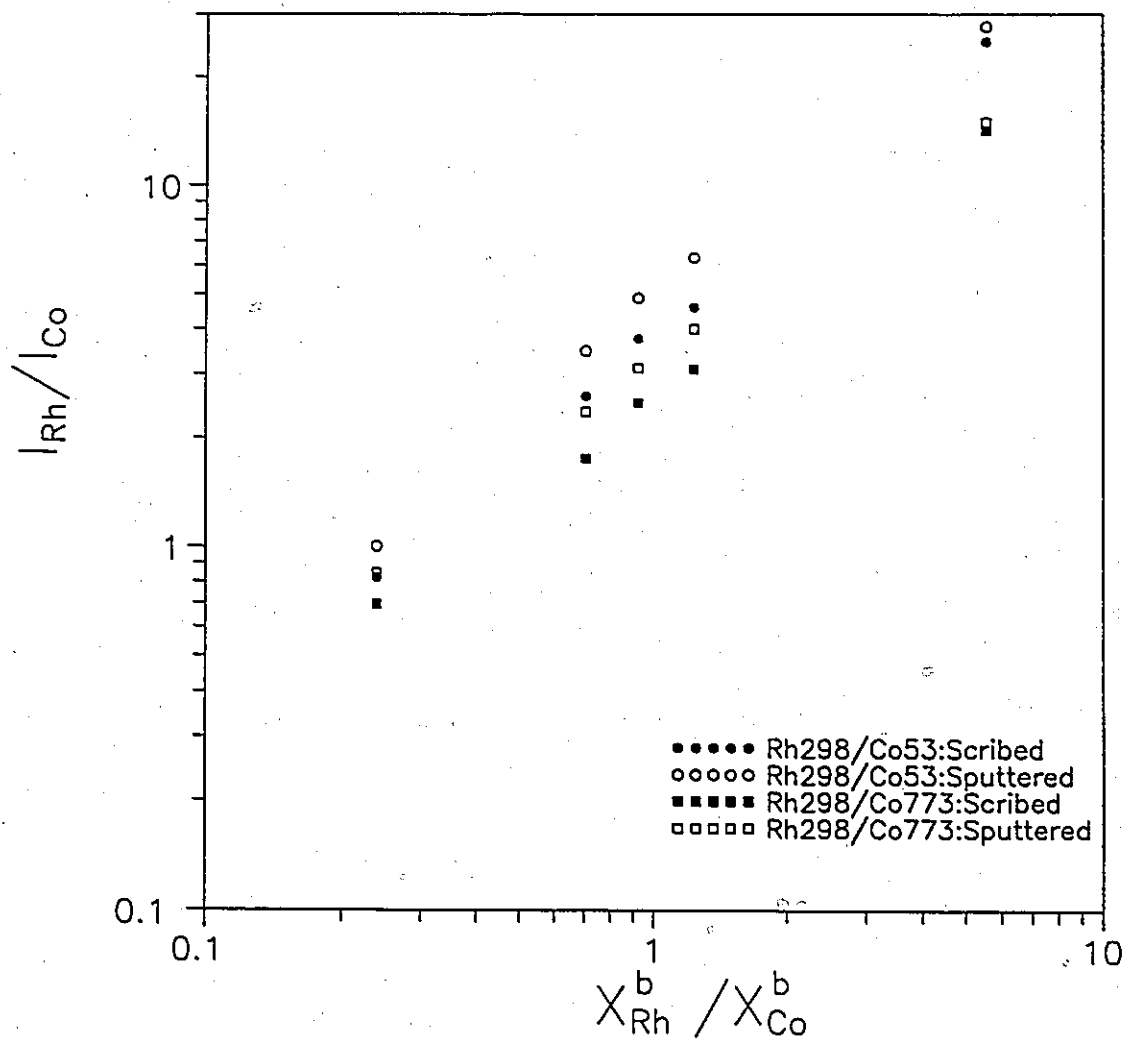


Figure (5-3). Ratio of measured Auger peak-to-peak heights (APPH) for scribed (solid symbols) and sputtered (open symbols) Co-Rh alloys. Sputtered surfaces were produced by 4 KeV Ar<sup>+</sup> at 70° incidence.

Rearranging this expression, the surface composition of one element can be written as

$$X_A^s = \left[ 1 + \frac{Y_A}{Y_B} \frac{X_B^b}{X_A^b} \right]^{-1} \quad (5-2)$$

and a plot of  $[(X_A^s)^{-1} - 1]$  vs  $(X_B^b/X_A^b)$  should yield a straight line with slope equal to  $Y_A/Y_B$ . This treatment also assumes that the relative sputtering yields do not depend on composition, and that the altered surface composition is uniform over the depth of analysis. Conversion of the signal intensity ratios from the sputtered alloys into surface compositions is achieved by using the scribed spectra to obtain the corresponding ratios for the bulk alloy. The surface composition of rhodium can then be determined as

$$X_{Rh}^{s pu} = \frac{A}{1-A} \quad (5-3)$$

where  $A = (X_{Rh}^b/X_{Co}^b) \cdot (I_{Rh}^{s pu}/I_{Rh}^{s cr}) \cdot (I_{Co}^{s cr}/I_{Co}^{s pu})$ . These values are plotted according to Equation (5-2) in Figure (5-4), which gives an average ratio of sputter yields for the five alloys of  $Y_{Rh}/Y_{Co} = 0.83 \pm 0.03$ , using a linear least-squares fit. This value has been used to calculate the surface composition of Rh according to (5-1) in figure (5-5). Also shown are the experimental points, not all of which lie on the curve calculated using this simple model.

At the next higher level of approximation, the sputter yields of the two components may be allowed some composition dependence. Kelly<sup>(137)</sup> has advanced a model for preferential sputtering of binary alloys which attempts to include the effects of mass differences, surface binding energies and relative abundance of the two alloy components. His expression for the ratio of sputtered species is given as

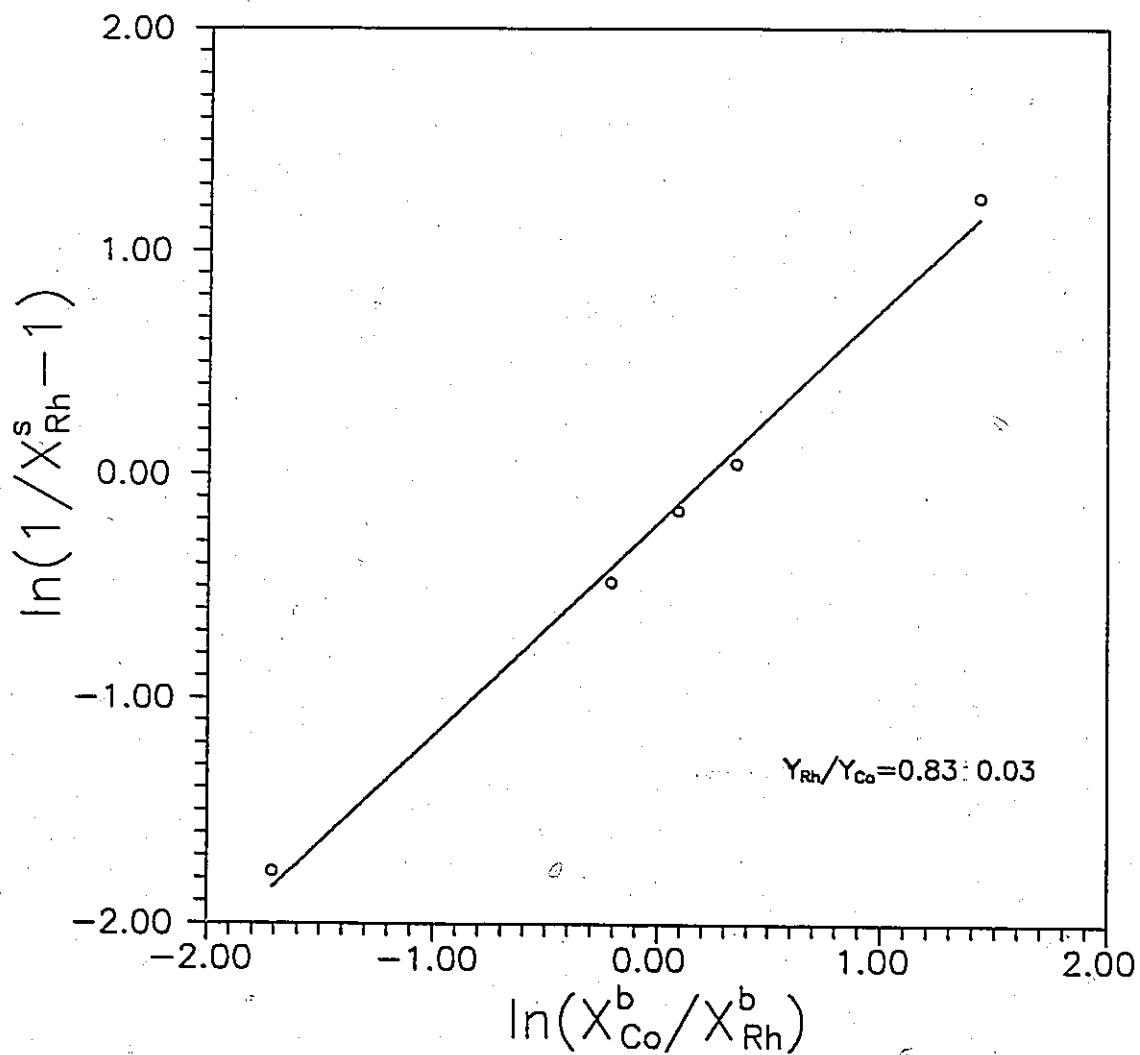


Figure (5-4). Plot of Equation (5-2) to determine the average ratio of sputter yields,  $Y_{Rh}/Y_{Co}$ , for five Co-Rh alloys.

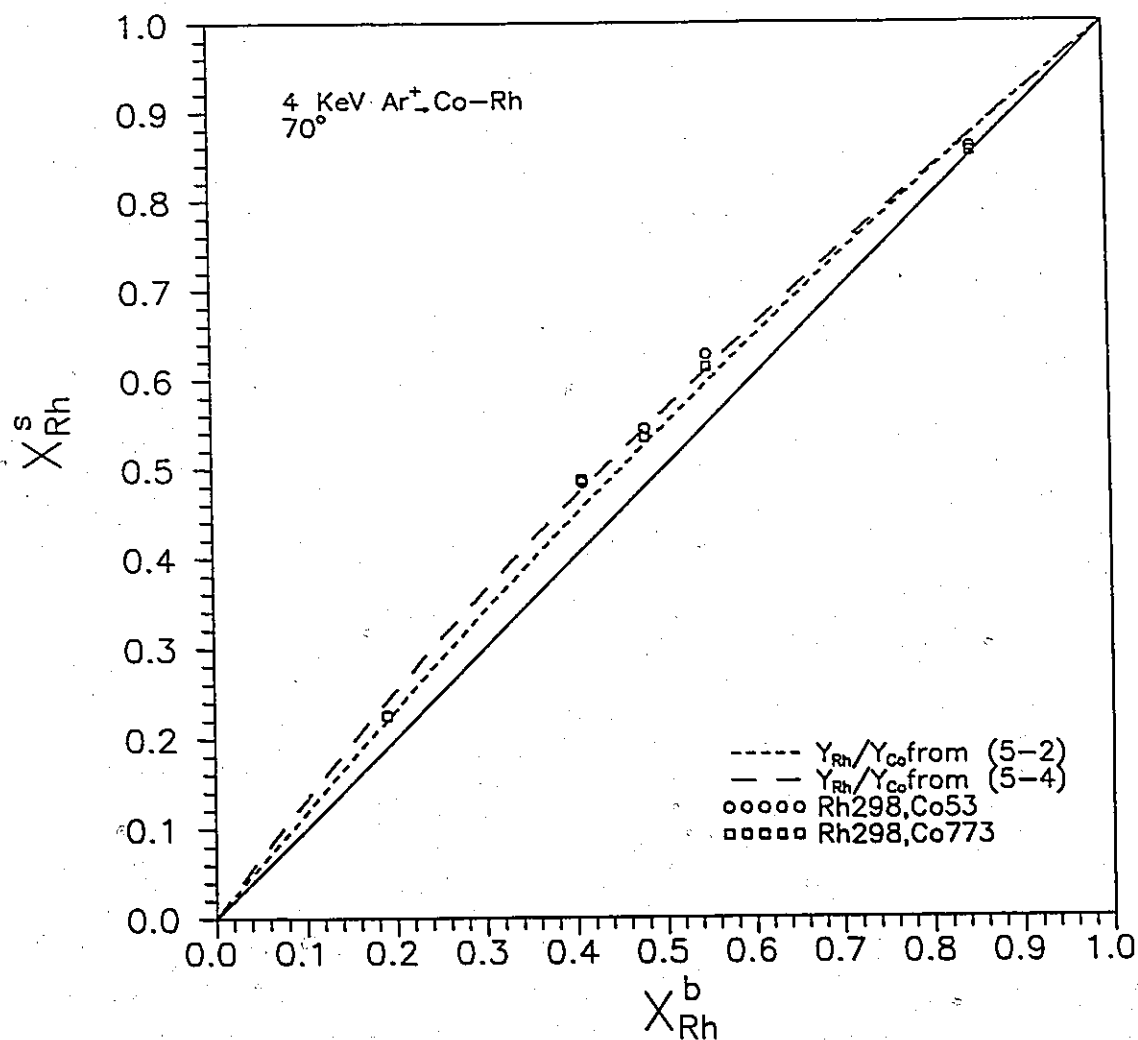


Figure (5-5). The surface Rh concentration,  $X_{Rh}^s$ , for sputtered Co-Rh alloys plotted as a function of the bulk composition.  $X_{Rh}^s$  was calculated from the sputtered ratios (Rh298/Co53 and Rh298/Co773) using the scribed alloys as bulk standards. In the absence of preferential sputtering the data would fall on the solid line. The dashed curves correspond to surface composition calculations using Equations (5-2) and (5-4) to obtain the ratio of sputter yields,  $Y_{Rh}/Y_{Co}$ .

$$\frac{Y_A}{Y_B} = \frac{X_A U_B}{X_B U_A} \cdot \frac{X_A + X_B \gamma_{AB}}{X_B + X_A \gamma_{AB}} \quad (5-4)$$

where  $U_i$  are the surface binding energies (estimated from the heats of sublimation  $\approx$  heats of vapourization) and  $\gamma_{AB}$  is a maximum energy transfer parameter for a head-on collision:

$$\gamma_{AB} = 4M_A M_B / (M_A + M_B)^2 \quad (5-5)$$

Equation (5-4) indicates that the target becomes enriched in the less abundant component, rather than the heavier component. The surface binding energy term again predicts enrichment of the less volatile component. A calculation of surface enrichment from this model is shown in Figure (5-5) and indicates closer agreement to the experimental data.

Finally, the range of  $\text{Ar}^+$  in Co and Rh has been estimated from the nuclear energy loss for these target-ion combinations. Details of Lindhard's theory have been reviewed by Feldman and Mayer<sup>(138)</sup> and are used to make the following analysis. The range of a low energy projectile ion in a target is estimated from the nuclear energy loss,  $NS_n(E_0)$ , according to

$$R = E_0 / (dE/dX)_n \quad (5-6)$$

where  $E_0$  is the ion energy and  $(dE/dX)_n = NS_n(E_0)$ . The nuclear energy loss may be expressed as

$$NS_n = N \frac{\pi^2}{2} Z_1 Z_2 e^2 a \frac{M_1}{M_1 + M_2} (\text{ev}/\text{\AA}) \quad (5-7)$$

which is energy independent in this expression due to the form chosen for the screening potential  $(1/r^2)$ .  $N$  is the atomic density,  $Z_i$  and  $M_i$  are the atomic numbers and masses and  $a$  is the Thomas-Fermi screening radius for the collision:

$$a = \frac{0.885a_0}{(Z_1^{1/2} + Z_2^{1/2})^{2/3}} \quad (5-8)$$

$a_0$  is the Bohr radius (0.53 Å). For Ar in Co and Rh  $dE/dX|_n \cong 124$  and  $150$  eV/Å, respectively. Ion range values were then calculated to be  $\cong 32.3$  and  $26.7$  Å for Co and Rh. The projected range will be somewhat less than these values due to collisions in the surface and after correcting for the angle of incidence used in these experiments ( $70^\circ$ ). It is still reasonable to expect, however, that over the depths analyzed in the Auger measurements there will be significant mixing which would tend to produce a homogeneous composition at the surfaces of the alloys.

### 5.3 Surface Segregation on Co-Rh Alloys

Due to the preferential sputtering observed for the Co-Rh alloys, the segregation measurements were compared to either the pure element spectra or to the scratch test results. Furthermore, the use of sputtering at temperatures above which bulk thermal diffusion could occur produced a macroscopic depletion of cobalt beneath the surface of the alloys. Thus, in order to reduce the annealing time necessary to achieve equilibrium between the surface and the bulk all alloys were cooled before being sputter cleaned, as reported in the Experimental Methods. Figures (5-6)-(5-8) show the intensities of the Co 53 eV, Rh 298 eV and Co 773 eV peaks relative to those obtained from the pure elements, plotted against the Rh bulk atom fraction. Included are data for both scribed alloys and alloys equilibrated at high temperature. The deviation of the measured intensity ratios from the bulk atom fraction for the scratched alloys is attributed to composition-dependent matrix effects. Comparing these ratios to those of the three alloys at temperatures between 890 and 948 K shows that cobalt is enriched on the surface of the 84.7Rh alloy, while rhodium enrichment is observed on the surface of the 19.3Rh alloy. In both cases, consistency amongst three Auger peaks was obtained. For the 19.3Rh and 41.3Rh alloys the three peaks were those referred to in the previous text. On

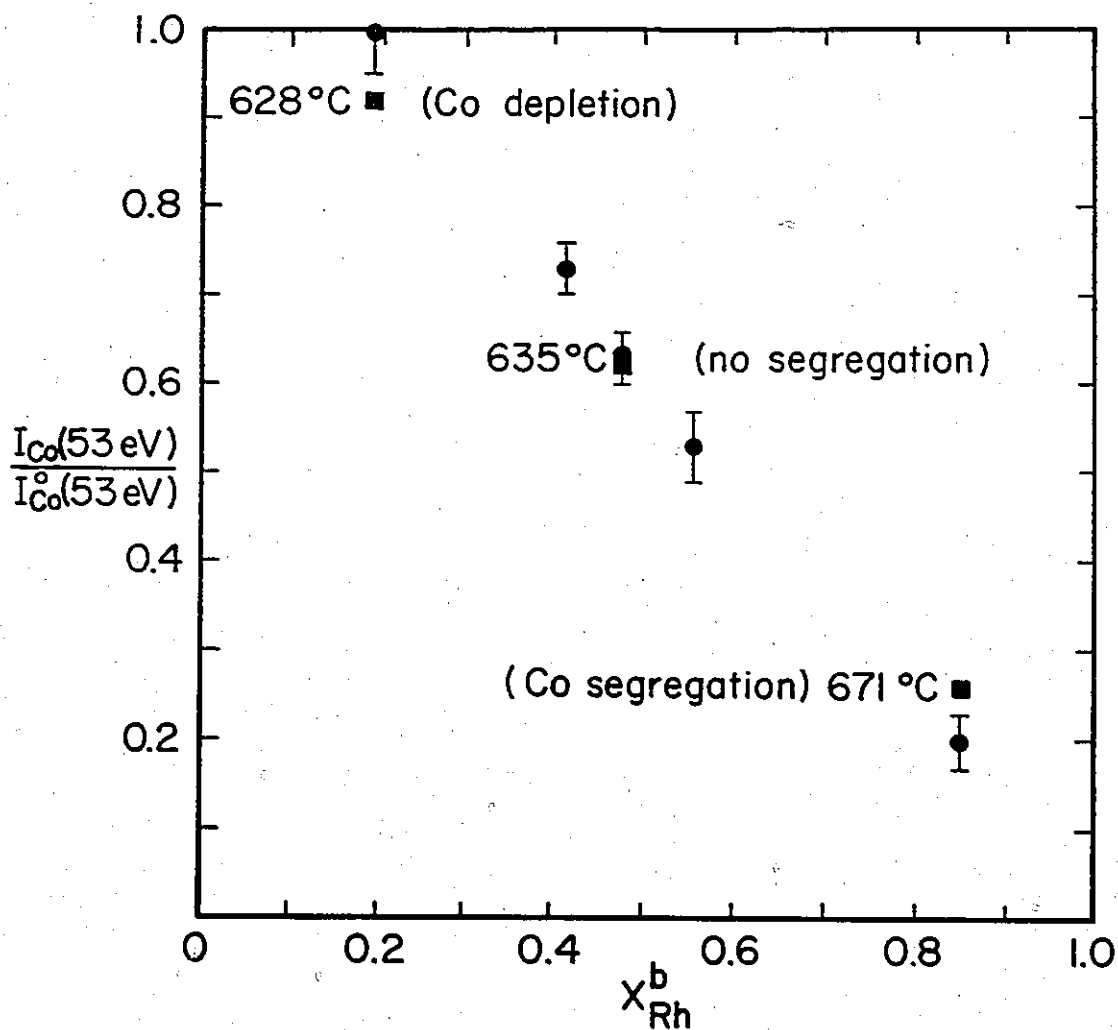


Fig.(5-6) The relative Auger intensity of the Co 53eV peak vs. bulk atomic percent Rh from a bulk spectrum at room temperature (●) and from surfaces equilibrated at high temperature (■).

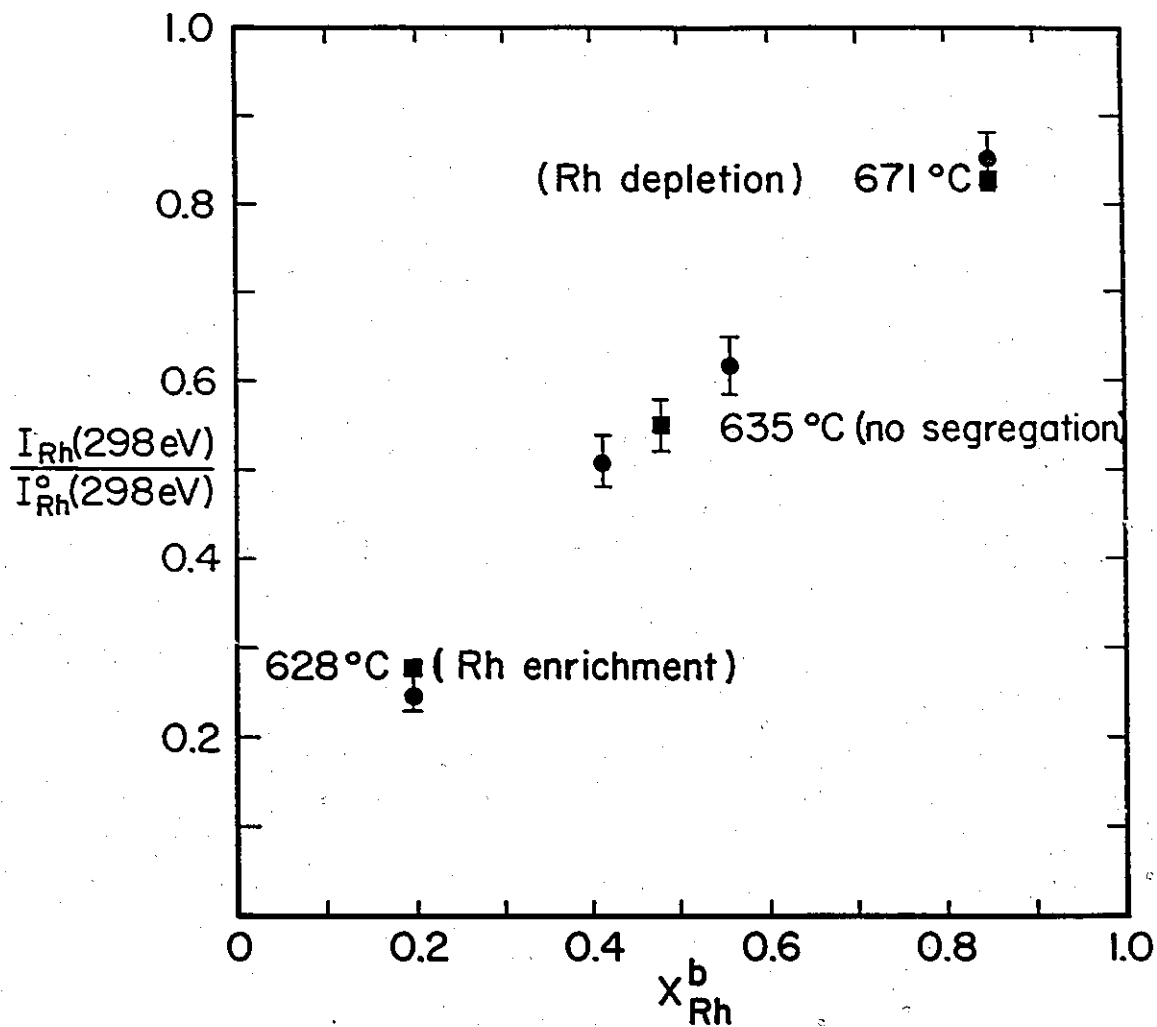


Fig. (5-7) The relative Auger intensity of the Rh 298eV peak vs. bulk atomic percent Rh from a bulk spectrum at room temperature (●) and from surfaces equilibrated at high temperature (■).

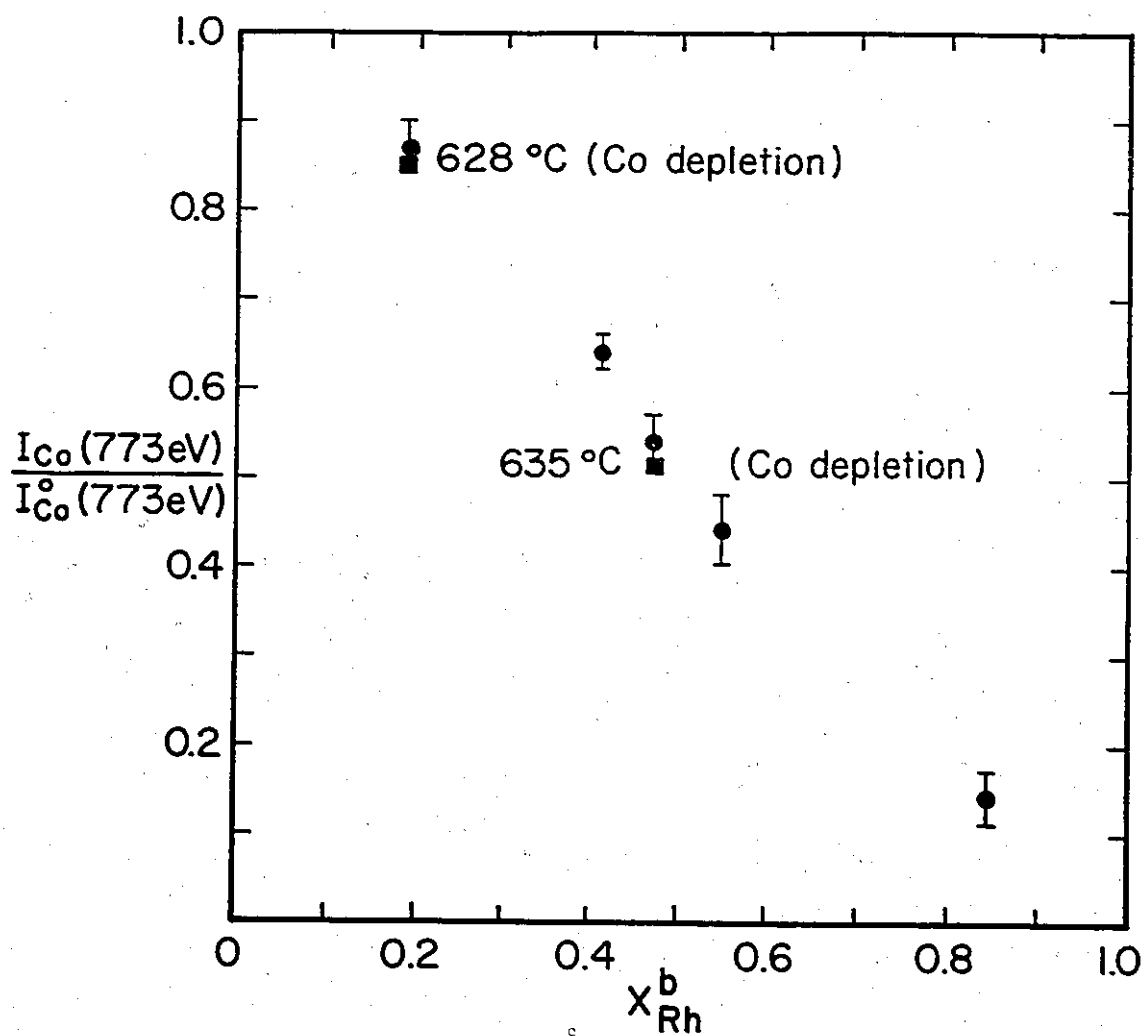


Fig.(5-8) The relative Auger intensity of the Co 773eV peak vs. bulk atomic percent Rh from a bulk spectrum at room temperature (●) and from surfaces equilibrated at high temperature (■).

the 84.7Rh alloy the Co 773 eV peak was not collected in the segregation measurements due to its very poor signal-to-noise ratio. A third measurement of segregation was obtained for this alloy by using the Rh 40 eV peak instead. This peak was not used for any of the other alloys because it is situated just below the Co 53 eV peak and was obscured by the inelastically scattered Auger electron tail of the neighbouring peak.

For the 47.8Rh alloy the segregation of either cobalt or rhodium was not conclusively demonstrated by these measurements. The Co 53 eV and Rh 298 eV peaks show no segregation within the experimental uncertainty, while the Co 773 eV peak (which is the least surface sensitive) shows a slight Co depletion.

In order to convert the measured Auger intensities into changes in surface composition it is necessary to make some assumptions about the depth distribution of the two species. This necessity arises due to the differing escape lengths of the Auger electrons, discussed earlier. Using the monolayer model of segregation it is possible to derive an expression such that the Auger intensity,  $I_i^{s,b}$ , from an alloy with a molar surface concentration  $X_i^s$  and bulk concentration  $X_i^b$  relative to the intensity corresponding to the bulk composition throughout,  $I_i^b$ , is given by

$$\frac{I_i^{s,b}}{I_i^b} = 1 + \frac{\Delta X_i^s}{X_i^b} \left\{ 1 - \exp[-d/(\lambda \cos \theta)] \right\} \quad (5-9)$$

$\Delta X_i^s$  is the change in the molar surface composition of element i, d is the plane spacing perpendicular to the surface,  $\lambda$  is the escape length or attenuation length of the Auger electrons perpendicular to the surface, and  $\theta$  is the angle the electron analyzer makes with the surface normal. The value of d clearly depends on both crystal orientation and composition. For pure Rh the values range from 2.2 Å for the [111] direction to 1.9 Å for the [100] direction. For pure Co the value is 2.04 Å for the [1000] direction. The exact orientation of the grains analyzed in each of

these experiments was not determined, hence an average of 2.1 Å was used as the layer spacing in the calculations. The values of  $\lambda$  are also not well known. The empirical formula of Seah and Dench<sup>(131)</sup> for metallic materials gives approximate values of 3.4 Å for the Co 53 eV peak, 7.3 Å for the Rh 298 eV peak and 11.8 Å for the Co 773 eV peak.

The least-squares fitting routine was used to obtain  $(I_i^{s,b}/I_i^b)$  values by fitting the various peaks obtained at high temperature to those obtained from the scribed surfaces at room temperature. By using three different Auger peaks with different escape lengths it was possible to use the above expression to check the internal consistency of the measurements under the monolayer approximation. The results of these calculations are shown in Table (5-1). As the data shows, the segregation effect on the alloys studied is very small.

The variation of surface composition with temperature was also investigated for this system. Figure (5-9) shows an example of the various Auger intensities taken at high temperature plotted versus temperature. Within the experimental uncertainty there was very little temperature dependence of the surface composition for any of the three alloys studied. Plotting  $\ln[X^s/(1-X^s)]$  vs  $1/T$  as seen from the form of eq. (2-1) should yield a straight line with a slope equal to  $\Delta H_{seg}/R$ . The intercept at  $T=0$  yields a constant containing the entropy of segregation. When the data are plotted in this way the results are those shown in Figures (5-10) and (5-11) for the two alloys exhibiting segregation. From the least-squares fitting of a straight line through each set of data the enthalpies and entropies of segregation were obtained from the slope and intercept values. These are shown in Table (5-2).

Several interesting results are apparent from these data. First, it would appear that there is a change in the segregating species with composition which clearly implies that pure "bond breaking" models cannot be adequate for describing this

Table (5-1)

Surface concentration changes calculated from signal intensity ratios ( $I_i^{sb}/I_i^b$ ) for the two alloys showing segregation.

Alloy (atomic percent)	$\Delta X_i^s$ (atomic percent)			
	Rh 40 eV	Co 53 eV	Rh 298 eV	Co 773 eV
Co - 19.3 Rh (628°C)	---	-0.09	+0.07	-0.04
Co - 84.7 Rh (671°C)	-0.22	+0.07	-0.08	---

Table (5-2)

Enthalpy and entropy of segregation values calculated from the slopes and intercepts of Figs (5-10) and (5-11).

Alloy (atomic percent)	Rh 40 eV	Co 53 eV	Rh 298 eV	Co 773 eV	Average <sup>a</sup>
Co - 19.3 Rh $\Delta H_{seg}$ (kJ. mol <sup>-1</sup> )	---	0.9±1.6	2.7±0.7	0.7±1.1	1.4±1.1
$\Delta S_{seg}$ (J. mol <sup>-1</sup> .K <sup>-1</sup> )	---	6.1±2.2	6.7±1.0	3.3±1.5	5.4±1.8
Co - 84.7 Rh $\Delta H_{seg}$ (kJ. mol <sup>-1</sup> )	-4.5±7.9	-2.1±6.2	1.3±1.9*	---	-3.3±7.0
$\Delta S_{seg}$ (J. mol <sup>-1</sup> .K <sup>-1</sup> )	5.0±7.6	0.3±5.9	8.6±1.8*	---	2.7±3.3

\*The enthalpies and entropies of segregation for the Rh 298eV peak were not included in the average values for this alloy since this peak is not as surface sensitive as the two lower energy peaks.

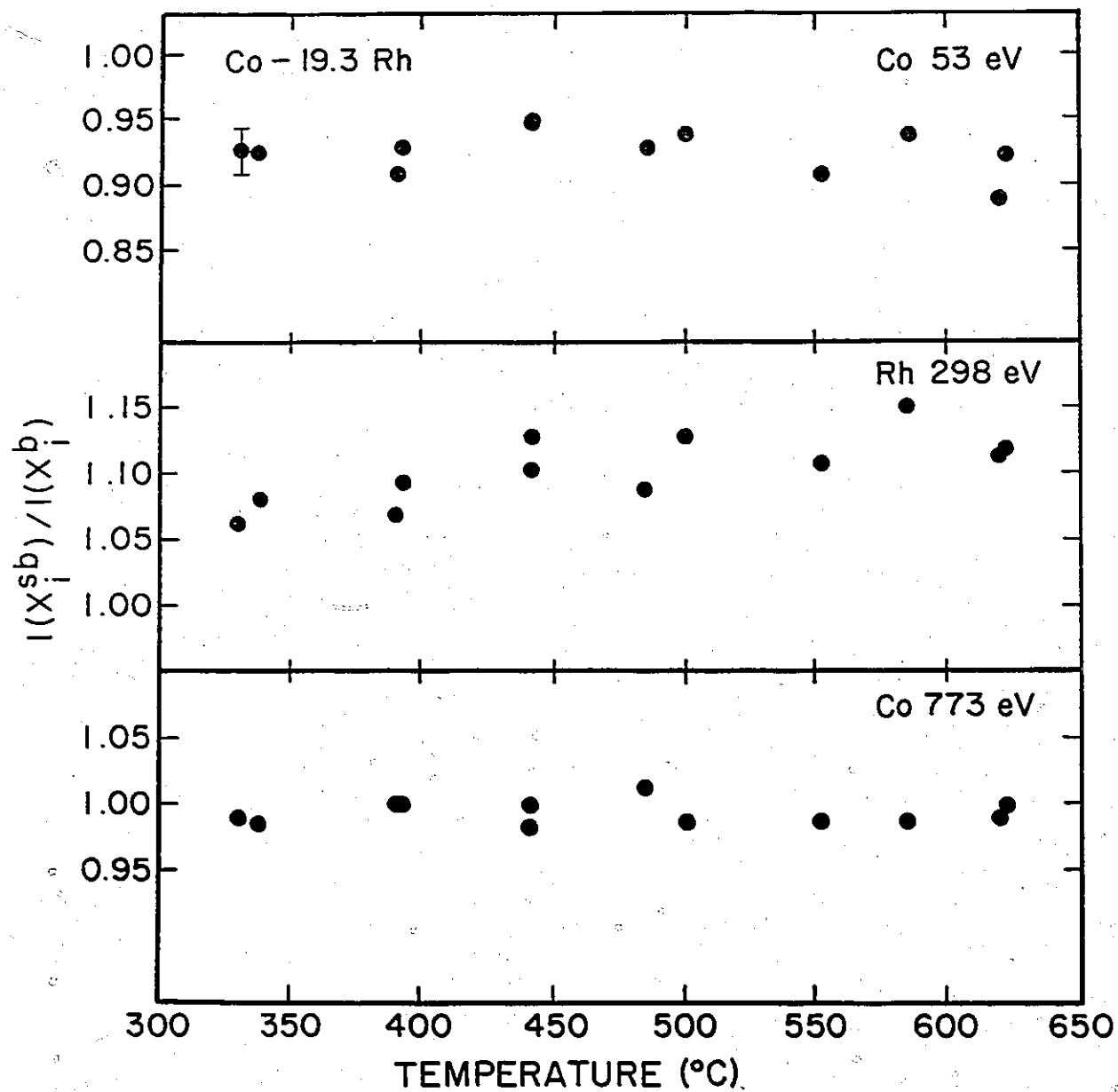


Fig. (5-9) The temperature dependence of the Auger peak intensities from the 19.3Rh alloy relative to those from a scratched surface at room temperature.

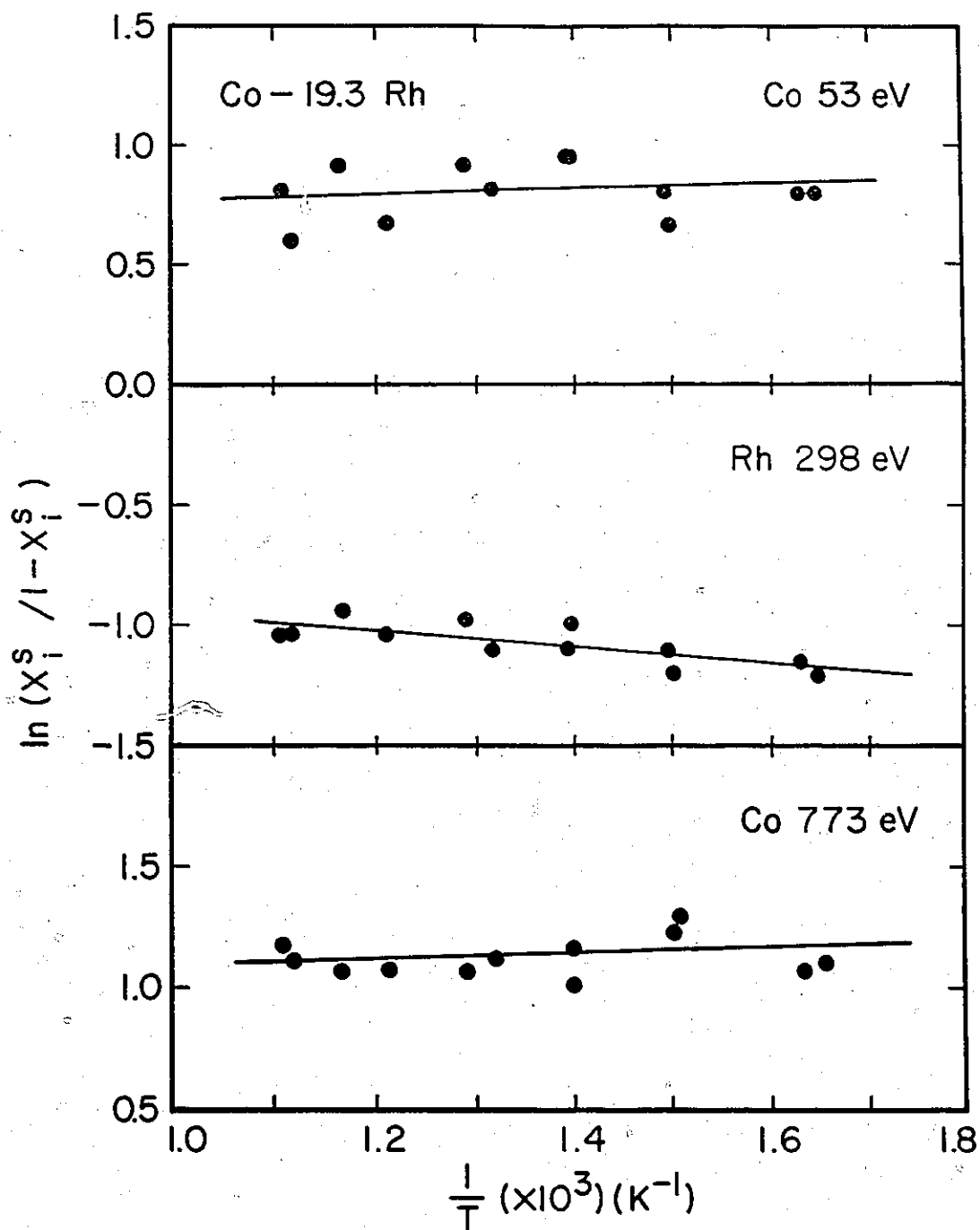


Fig. (5-10)  $\ln(X_i^s / (1 - X_i^s))$  vs.  $1/T$  plots for the 19.3Rh alloy. The data were fit by the least squares fitting of a straight line through the experimental points.

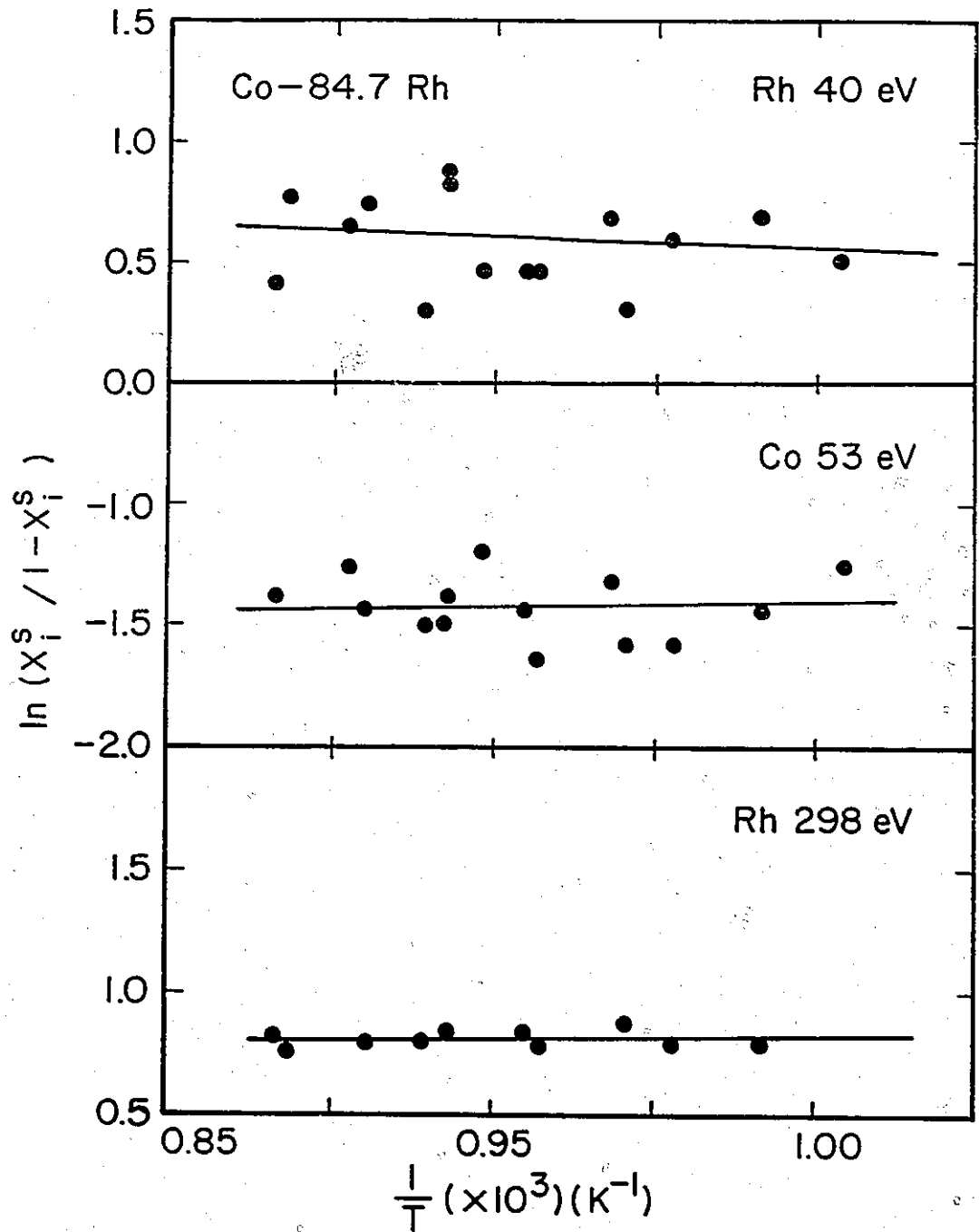


Fig. (5-11)  $\ln(X_s^s / |1 - X_s^s|)$  vs.  $1/T$  plots for the 84.7Rh alloy. The data were fit by the least squares fitting of a straight line through the experimental points.

system. This follows from inspection of eqs. (2-3) and (2-4) where it is clear that the sign of the driving force for segregation does not change with composition. In present case, these models would predict that cobalt (having the smallest binding energy) should segregate to the surface of all the alloys.

The elastic strain energy term,  $E_{el}$ , in equation (2-5) was evaluated using the published data for the Co and Rh elastic constants<sup>(139,140)</sup>. With  $G_{Co} = 6.2 \times 10^{10}$  N/m<sup>2</sup> (at 773 K),  $r_1 = 1.25 \text{ \AA}$  and  $r_2 = 1.34 \text{ \AA}$  a value of  $E_{el} = 7.8$  kJ/mole was obtained for the Co-19.3Rh alloy.

The available surface tension data for Co and Rh is summarized in Table (5-3). This data is confined to the liquid state for Rh, but a few measurements of solid surface tension are available for Co. The lack of data for solid elements has led a number of authors to seek correlations of this property with other physical properties<sup>(142-144)</sup>. Using the data of Mezey and Giber<sup>(142)</sup>, eq. (2-4) estimates a heat of segregation for Co-Rh of -3.7 to -4.1 kJ/mole favouring Co enrichment. Hence using both the bond breaking and lattice strain theories together predict a value of  $\Delta H_{seg} = 3.7-4.1$  kJ/mole favouring Rh enrichment for Co based alloys. This value is approximately a factor of three higher than the average  $\Delta H_{seg}$  value shown in Table (5-2). If the values of Miedema<sup>(143)</sup> or Tyson<sup>(144)</sup> had been used, the surface energy term would be approximately -7.2 kJ/mole or -10.5 kJ/mole, respectively and would almost exactly cancel the strain energy term. Together with the elastic strain energy term, the various calculated values of solid surface tensions therefore predict that the heat of segregation will be zero or slightly positive. The small positive heat of segregation measured for the 19.3Rh alloy is in reasonable agreement with this prediction.

Interestingly enough, the same cannot be said if eq. (2-3) is used with pure element vapourization energies listed by Hultgren and coworkers<sup>(145)</sup>. In this



case  $\Delta H_{\text{seg}}$  is found to be  $-32$  kJ/mole favouring cobalt segregation for a (0001) face, which would significantly overestimate the segregation behaviour of this system. In fact at 923 K such a high enthalpy would predict an almost complete monolayer of Co at the surface and even higher segregation for other low index planes. The failure of this approximation in this case is a clear indication that the surface relaxations, whether electronic or geometrical, which are explicitly taken into account using Eq. (2-3), represent significant contributions to the lowering of the free energy.

For Rh-based alloys, if the elastic energy contribution is ignored (as has been suggested by other authors<sup>(146-148)</sup> when the smaller atom is the solute) then the values of  $\Delta H_{\text{seg}}$  obtained from the Rh 40 eV and Co 53 eV peaks shown for the 84.7Rh alloy are again within the range of values predicted by Eq. (2-4). The Rh 298 eV peak gives a value close to zero. The reason for this is not clear, however it should be noted again that the low energy peaks are more surface sensitive and therefore more likely to yield correct results for the surface composition. In the three above investigations concerned with the case of the smaller atom as the solute, the authors justified the neglect of the elastic strain energy term by noting that the effect is very small in comparison to the bond energy model and is overestimated if one utilizes Eq. (2-5) ( $E_{\text{el}} = -13.4$  kJ/mole favouring Co segregation for the Co-84.7Rh alloy).

Finally, it is interesting to note the very large entropies associated with the segregation in both the 19.3Rh and 83.7Rh alloys. While there is considerable uncertainty in these values, they are considerably in excess of the  $\Delta S_{\text{seg}}$  arising from mixing. It is interesting to note that in each case the change in surface compositions bring the samples into approximately an  $AB_3$  ratio where B is the solvent atom type. In light of this it is tempting to suggest that the large entropy

changes may be associated with the development of ordered surface phases. It would be interesting to attempt to do small spot LEED on these surfaces to see if any long range ordering exists.

Turning to the theory of Abraham and Brundle<sup>(8)</sup> it is very evident from Figure (2-1) that the alloys with Co as solute lie in the lower left quadrant of the  $\gamma^* - \sigma^*$  plane, where both the size ratio and the bond strength favour Co enrichment. This prediction is confirmed by the measurements on the 84.7Rh alloy, where Co enrichment was observed. The alloys with Rh as solute lie in the upper right quadrant where the bond strength ratio still favours Co enrichment (no solute segregation if above the  $\Delta Q_\psi = 0$  curve). However, the size ratio of this alloy now moves the theoretical point to the right, just under the  $\Delta Q_\psi = 0$  curve to where solute enrichment is again predicted. This changeover of the segregating species was observed to occur on the 19.3Rh alloy. It is also interesting to note that the predicted points lie very close to the  $\Delta Q_\psi = 0$  curve, indicating that Co-Rh alloys should be close to ideal and exhibit little segregation by comparison to other systems. For example, the Cu-Ni alloy system shows very pronounced segregation of copper for all alloy compositions with a heat of segregation of approximately -19 kJ/mole<sup>(7, 2)</sup>. The theoretical points for this alloy system are also shown in Figure (2-1) and lie well away from the  $\Delta Q_\psi = 0$  curve. Using these simple arguments, one then expects very small heats of segregation for the Co-Rh system, which is the observed experimental behaviour.

Table (5-3)

Experimental and calculated surface tension values for Co and Rh. (R) indicates that the reference source is a review of literature data. Where calculated values are given, the physical property used for the correlation with other (experimental) surface tension data is indicated in brackets.

Element	Temp. $T_0$ (K)	Surface Energy $\gamma_0$ (mJ/m <sup>2</sup> )	$d\gamma/dT$ * (mJ/m <sup>2</sup> K)	Comments	Ref.
Co(l)	1766(mp)	1873	-0.49	Expt.(R)	(141)
Rh(l)	2239(mp)	2000	-0.30	Expt.(R)	
Co(l)	1766	1846	-0.41	Expt.	(40)
Rh(l)	2239	1915	-0.664	Expt.	
$\alpha$ Co(hcp)	298	2709	-0.48	Calc.	(142)
$\beta$ Co(fcc)	1766	2003		( $\Delta H_{sub}$ )	
Rh(fcc)	298	2828	-0.37		
Rh	2239	2116			
$\alpha$ Co	0	2550	-0.20	Calc. ( $\gamma_{liquid}$ )	(143)
Rh	0	2750	-0.16	Calc. ( $\Delta H_{vap}$ )	
$\alpha$ Co	623	2100	-0.13	Expt.(R)	(144)
$\beta$ Co	1623	1900	(average	Expt.(R)	
$\alpha$ Co	0	2210	value for	Calc.(cohesive	
$\beta$ Co	0	2180	solids)	energy)	
Rh	0	2490			

\*  $\gamma = \gamma_0 + (d\gamma/dT)(T - T_0)$

## CHAPTER 6

### RESULTS AND DISCUSSION II

#### OXIDATION PROPERTIES OF NICKEL-COBALT ALLOYS BETWEEN 673K AND 1073K

##### 6.1 Introduction

The following chapter is concerned with the oxidation properties of nickel-cobalt alloys at temperatures in the range from 673–1073 K. Nickel-cobalt alloys were used as a model binary system in this investigation since they may form a single phase oxide product which has a relatively simple defect structure. A review of the literature has shown that there are no extensive experimental data for the growth of oxides on nickel-cobalt alloys in this temperature range. There are, however, independent thermodynamic and diffusional data for this system which may be used to test the validity of a phenomenological diffusion model which has been applied to these oxidation processes.

The oxidation experiments were completed using Ni-3.86Co (110) single crystal and Ni-4.0Co polycrystalline alloys. The methods of surface preparation and oxidation procedures are described fully in Chapter 4. The (110) orientation was chosen for this work since previous investigations on Ni had shown this surface to form an essentially polycrystalline oxide containing mainly incoherent grain boundaries<sup>(127)</sup>. Films on (100) and (111) Ni have been characterized as having

a fiber texture containing a large number of coherent twin boundaries. The available measurements of grain boundary diffusion in NiO correspond to boundaries of the former type.

In addition to the orientation dependence, experiments showed that different surface pretreatments and methods of exposure of nickel-cobalt to a reactive atmosphere led to changes in scale growth rates and oxide morphologies. For this reason the experimental results are subdivided into three sections. The first two are devoted to the experiments on single crystal alloys which were exposed using two methods: "hot-bare" and "furnace-raised". These methods are similar to those employed by Graham and co-workers<sup>(74)</sup> in experiments which involved oxidation of pure nickel. "Hot-bare" refers to the process whereby samples were annealed at 973 K and a pressure of  $10^{-9}$  Torr to remove any residual oxide film, followed immediately by exposure to oxygen with the sample at the desired temperature. "Furnace-raised" experiments were performed on samples which were cooled to room temperature following the annealing cycle, but prior to exposure to the reactive gas. Once oxygen was admitted to the system, the sample temperature was raised manually to the desired level over a period of 2-3 minutes. The third section of experimental results describes work on the polycrystalline alloys which were not annealed, but which were exposed by raising the sample temperature with oxygen in the system.

The growth kinetics for the different orientations and exposure methods are presented, along with the structures observed by SEM and TEM. In addition, analysis of the oxide compositions was performed using Auger spectroscopy, with SIMS as a secondary technique in a limited number of cases.

Measured differences in oxidation rates for the different experimental conditions are discussed on the basis of structural changes observed for the various

oxide products. In this temperature range the transport of reactants via short-circuit paths is a dominating effect, so that orientation and surface pretreatment have a marked influence on the oxidation process. A semi-quantitative analysis of the kinetic and compositional data is made by using the Wagner model, reviewed in Chapter 2, which has been modified to include the effects of these alternative transport mechanisms.

## 6.2 Oxidation of the Ni-3.86Co (110) Alloy: Hot Bare Exposure

Oxidation of the Ni-3.86Co (110) alloys at  $5.10^{-3}$  Torr was performed by the hot-bare exposure technique at 673, 723 and 773 K for times of up to 50 hours. Oxidation kinetics for these experiments are shown in Figure (6-1) in parabolic form. In each case the rate of oxygen uptake changed little with time. However, since the reactions did not obey an exact parabolic rate law, instantaneous parabolic rate constants ( $k_p(\text{eff}) = (\mu\text{g}/\text{cm}^2)^2/\text{sec}$ ) were obtained by taking limiting tangents to the curves. These data are presented in Table (6-2), pp. 144,145.

Some typical SEM micrographs of the surface of the hot-bare specimens are shown in Figures (6-2) and (6-3). These images show that the oxide layers were not completely dense and uniform in thickness, instead displaying a ridge or coral-like morphology. The early stages of the development of these structures can be seen in the series of samples oxidized at 673 K, Figure (6-2). After only 8 minutes these ridges have dimensions on the order of several hundreds of Ångströms and are separated by regions where the oxide appears to be much thinner and of relatively uniform thickness. Due to the convoluted shapes and irregular sizes of the ridges it is difficult to estimate their spacing at this stage of growth. At longer exposures these ridges appear to swell and merge, yet after 50 hours the structure still appears quite open and porous.

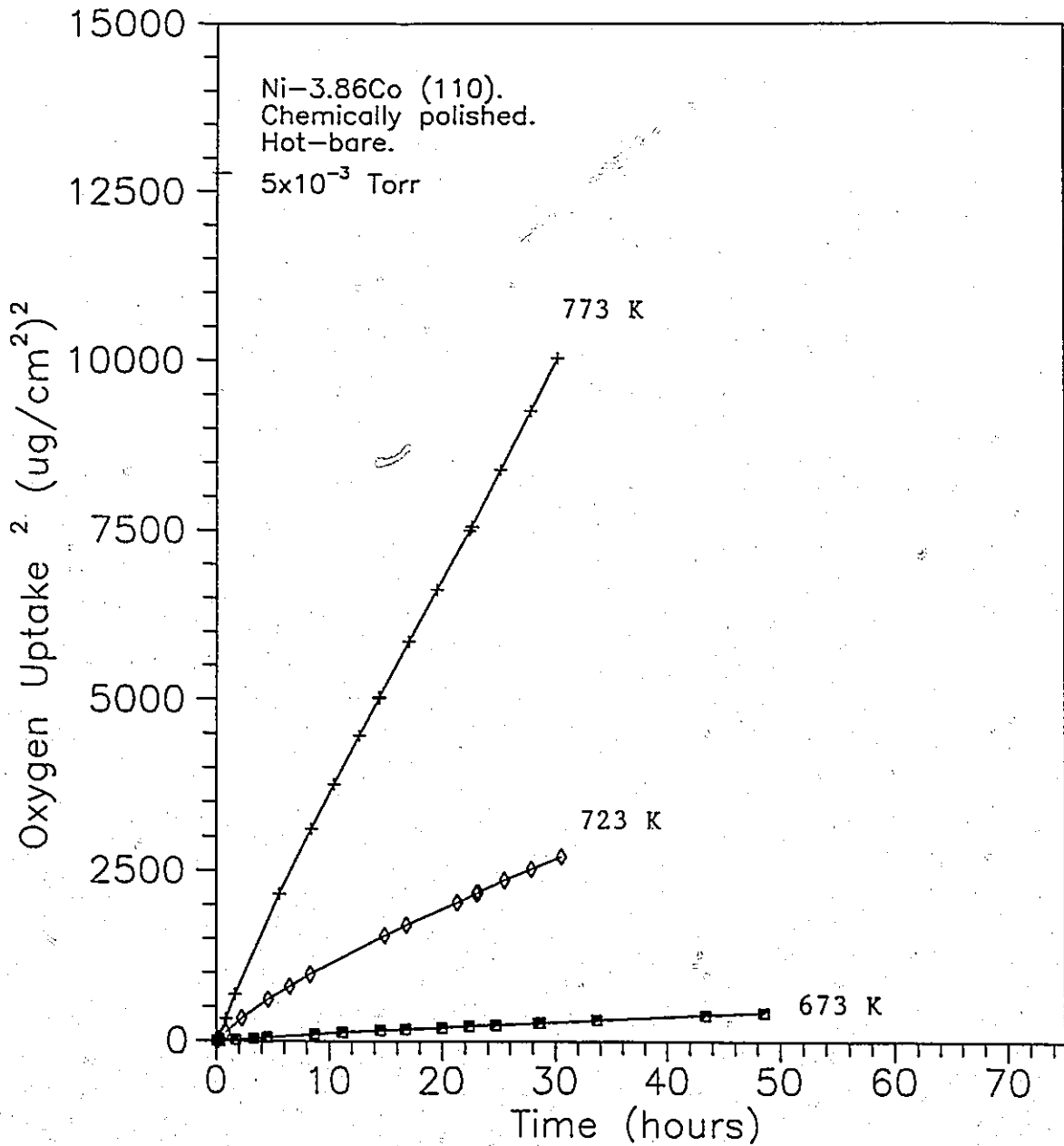


Figure (6-1)

Parabolic plots of oxygen uptake by Ni-3.86Co (110) exposed by the hot-bare technique.



Figure (6-2) Secondary electron images of Ni-3.86Co (110) specimens oxidized by the hot-bare technique at 673 K,  $5 \times 10^{-3}$  Torr  $O_2$ .  
(a) 8 min. exposure:  $1.0 \mu\text{g } O_2/\text{cm}^2$ , (b) 5.8 hr. exposure:  $7.5 \mu\text{g } O_2/\text{cm}^2$  and (c) 48.5 hr exposure:  $20.5 \mu\text{g } O_2/\text{cm}^2$ .

Figure (6-3)

Secondary electron images of Ni-3.86Co (110) specimens oxidized by the hot-bare technique at  $5 \times 10^{-3}$  Torr.

(a) 723 K, 31 hr.,  $53 \mu\text{g O}_2/\text{cm}^2$  and (b) 773 K, 30 hr.,  $100 \mu\text{g O}_2/\text{cm}^2$ .

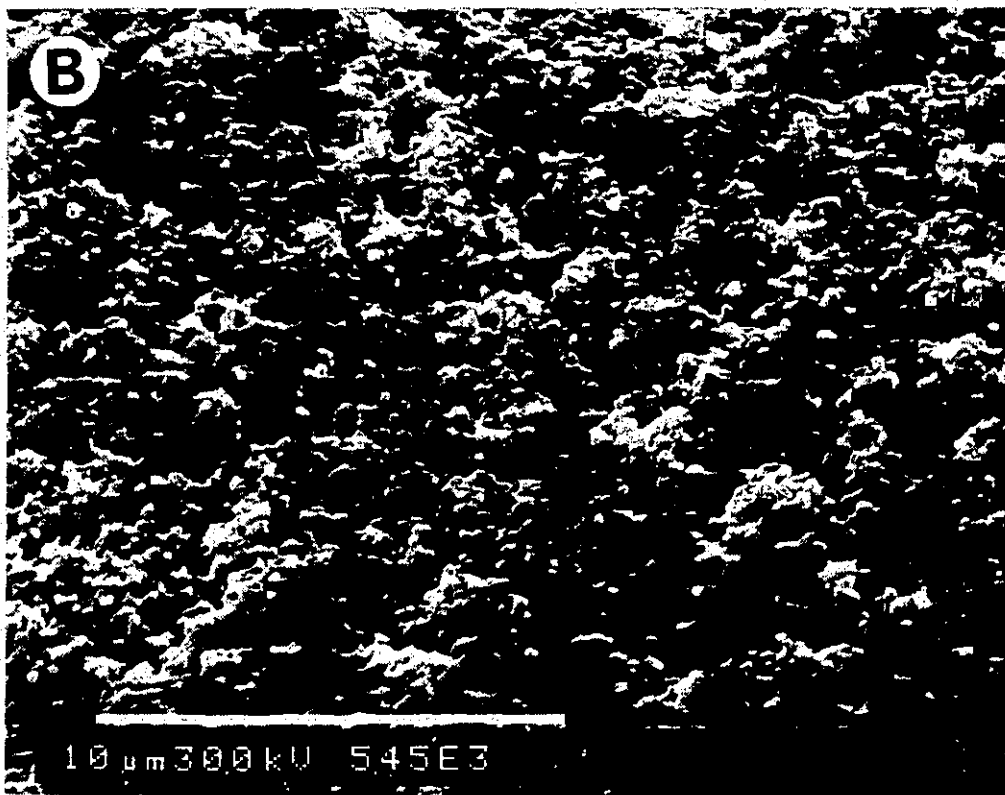
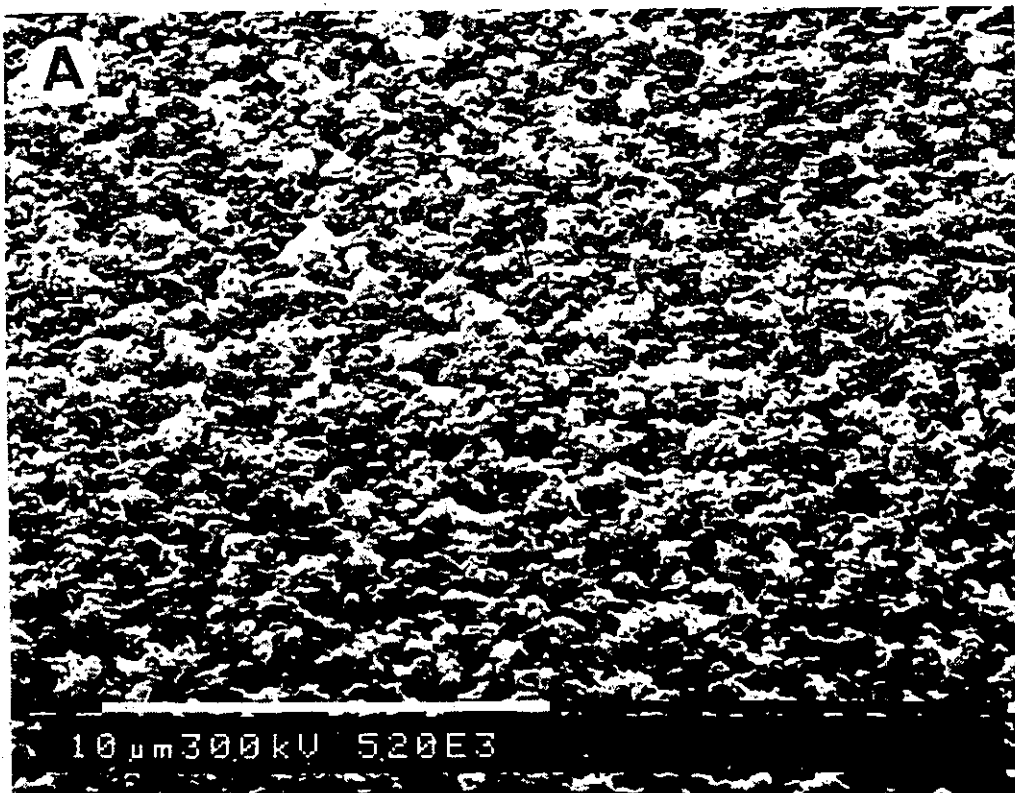


Fig.(6-3)

The composition of the thin oxides grown by the hot-bare technique was determined using Auger and SIMS. The oxides grown for 8 min., 5.8 and 48.5 hrs. at 673 K were depth profiled using SIMS. These results are shown in Figure (6-4). The emission yields of  $^{58}\text{Ni}^+$  and  $^{59}\text{Co}^+$  decreased continuously as the oxide was removed from each specimen by sputtering. Final steady state levels were reached once all oxide was removed from the surface analysis area. A comparison of the ratio of the two species ( $^{59}\text{Co}^+ / ^{58}\text{Ni}^+$ ) vs. sputter time for these three specimens showed that cobalt was always enriched (by a factor of approximately 3x) near the outer oxide surface relative to the underlying oxide near the alloy-oxide interface.

The specimen oxidized for 31 hours at 773 K was sputter depth profiled in conjunction with Auger analysis, as shown in Figure (6-5). The oxygen KLL and overlapping Co and Ni LMM peaks in the range 630-725 eV were collected as a function of sputter time and are represented as maximum to minimum peak-to-peak intensities in this energy window after a numerical differentiation of the data. To convert these overlapping nickel and cobalt peaks into composition in the oxide and alloy substrate, the least squares fitting program was used to simulate observed spectra using elemental standards. The relative contributions assigned to each of the standards by the fitting program were normalized by the ratio of background counts at 725 eV and then used to determine the composition of cobalt at each step in the profile. For the sample in question, the cobalt profile again showed enrichment near the outer oxide surface and decreased rapidly to near the alloy composition after removal of all oxygen.

The oxides produced at 673 K were stripped for TEM analysis and examined in the bright field (BF), dark field (DF) and selected area diffraction (SAD) modes. Figure (6-6) shows a series of images for the three samples. Examination of the BF images revealed that the oxides were polycrystalline with sizes ranging from tens to

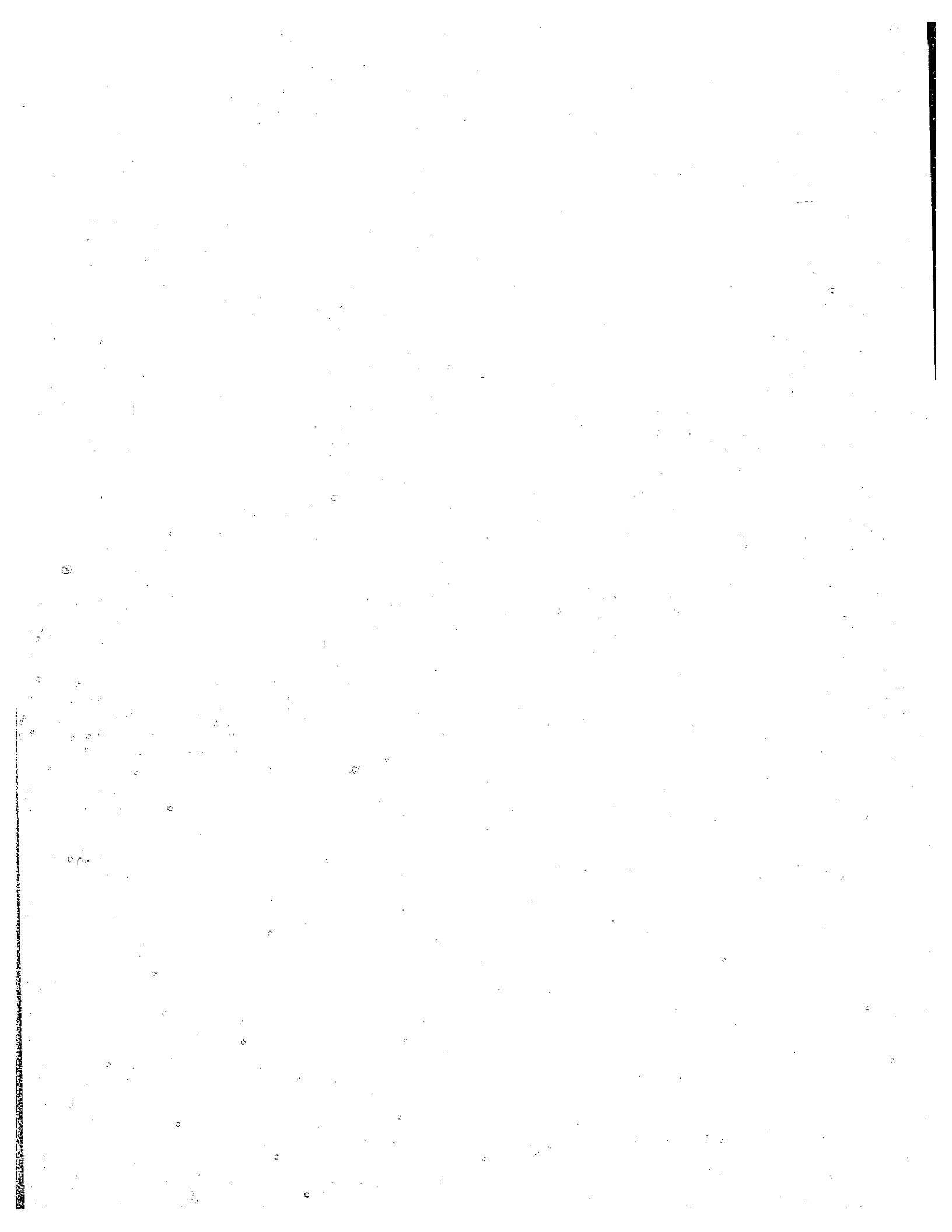


Figure (6-4)

SIMS depth profiles of Ni-3.86Co (110) after oxidation by the hot-bare technique at 673 K,  $5 \times 10^{-3}$  Torr for (a) 8 min., (b) 5.8 hr. and (c) 48.5 hr. The symbols representing  $^{58}\text{Ni}$  and  $^{59}\text{Co}$  correspond to the LHS axis. The ratio of counts,  $^{59}\text{Co}/^{58}\text{Ni}$ , corresponds to the RHS axis.

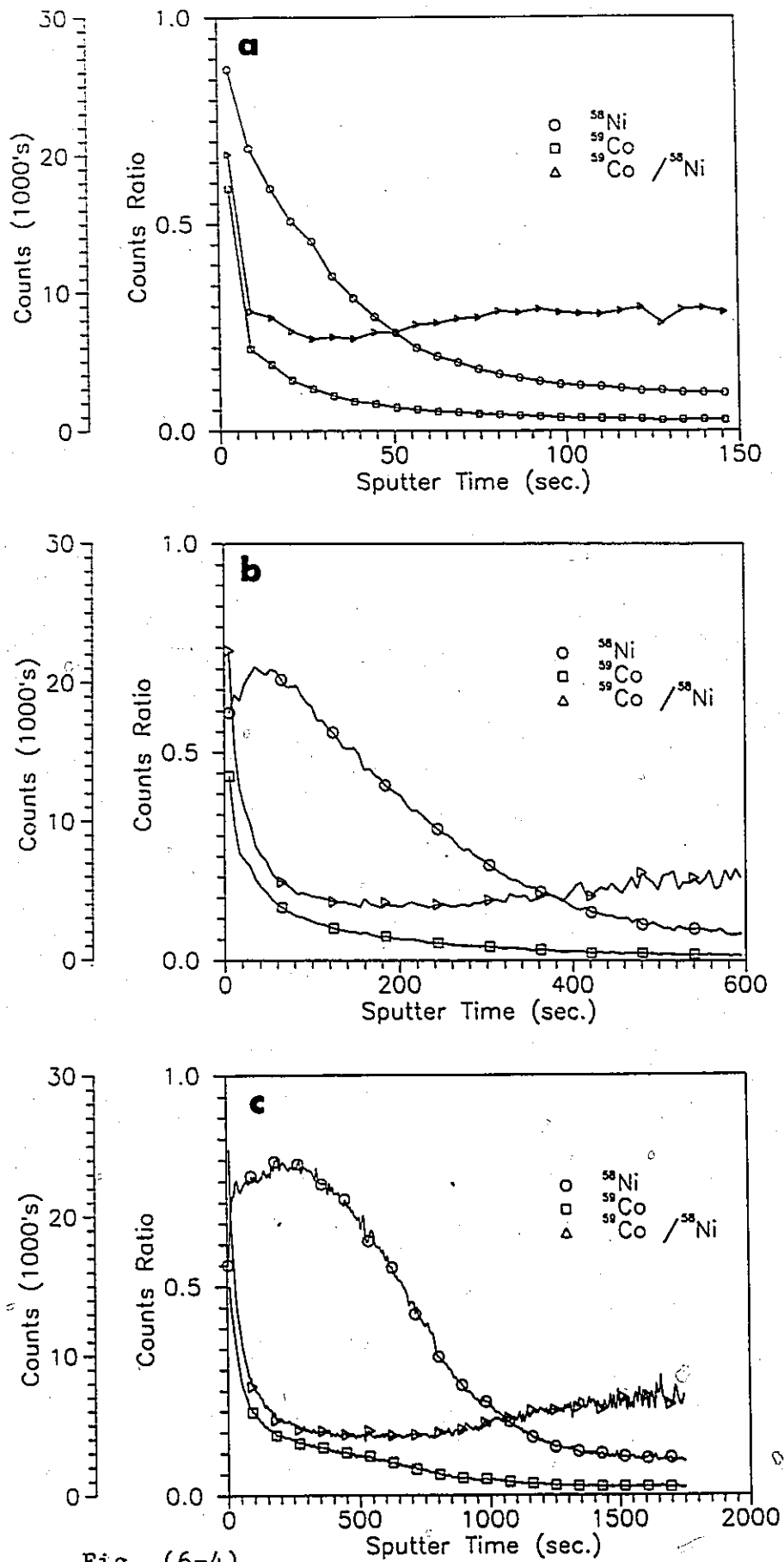


Fig. (6-4)

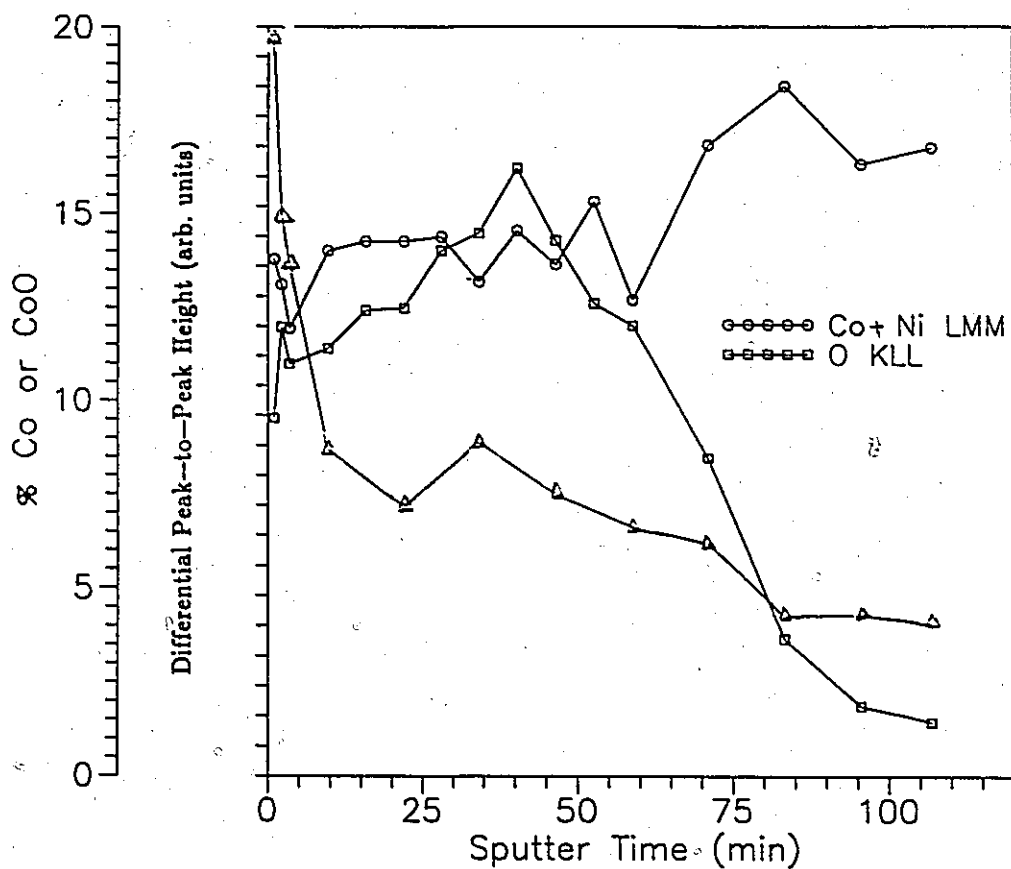


Figure (6-5)

Auger depth profile corresponding to the (110) Ni-3.86Co sample oxidized at 773°K for 31 hr. by the hot-bare technique. Oxygen,  $\square$ , and overlapping Co+Ni,  $\circ$ , differential peak-to-peak heights are shown, corresponding to the RHS axis. The cobalt concentration,  $\Delta$ , determined by a deconvolution of the metal peaks, corresponds to the LHS axis.

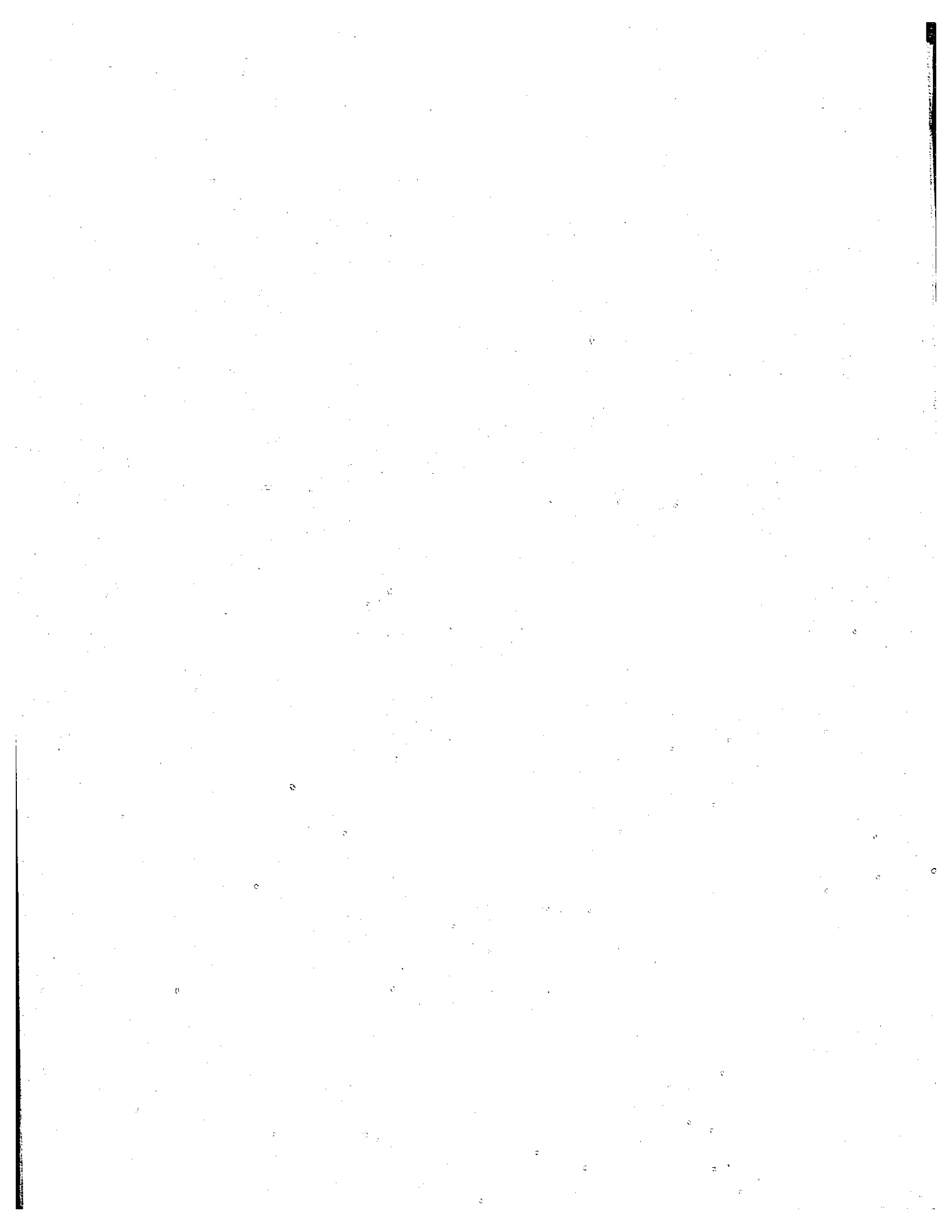


Figure (6-6)

Transmission electron micrographs of oxide films stripped from Ni-3.86Co (110) alloys oxidized by the hot-bare technique: (a) BF, (b) DF 8 min. exposure,  $1 \mu\text{g O}_2/\text{cm}^2$ ; (c) BF, (d) DF 5.8 hr. exposure,  $7.5 \mu\text{g O}_2/\text{cm}^2$ ; (e) BF and (f) after sputtering 10 min, 5 KeV  $\text{Ar}^+$ ,  $1 \mu\text{A}$ , 48.5 hr. exposure,  $20.5 \mu\text{g O}_2/\text{cm}^2$ .

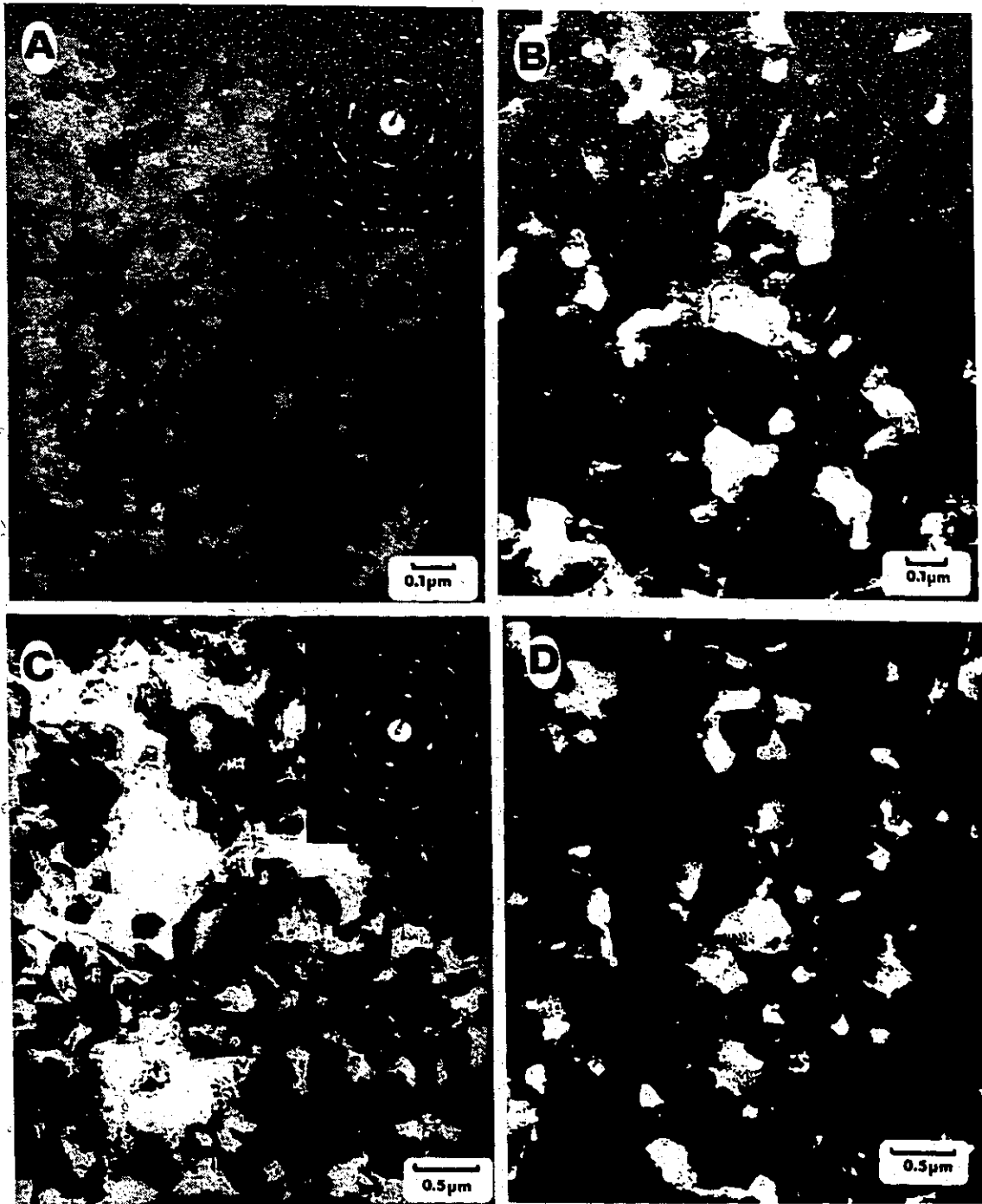


Fig.(6-6)



Fig. (6-6)

hundreds of Ångstroms. Individual grains were most easily observed from a section of the oxide formed after 48.5 hours which was thinned using 4 keV  $\text{Ar}^+$  ions, Figure (6-6)(f).

The SAD patterns for these films were used to identify crystal phases and orientation relationships parallel to the alloy surface. The faint diffraction rings indicated that some crystallites were randomly oriented, but the intense maxima superimposed on these rings was evidence of preferred orientation between the oxide and the (110) alloy surface. The oxide from all three samples was identified as having a single phase fcc structure with interplanar spacings which closely matched those of NiO. The main orientations were determined by superimposing single crystal diffraction patterns to find the closest match to the observed patterns. The orientations which have been identified are shown in Figure (6-6). These orientations are (100),  $2x(310)$ , (311)  $(\text{NiCo})\text{O} \parallel (110) \text{Ni-3.86Co}$ .

### 6.3 Oxidation of the Ni-3.86Co (110) Alloy: Furnace-Raised Technique

Furnace-raised oxidation runs at  $5 \times 10^{-3}$  Torr were performed at 673, 773, 873, 973 and 1073 K. Kinetic measurements for these experiments are shown in Figure (6-7). The effective parabolic constants were again measured by taking limiting tangents to the data in parabolic form and are given in Table (6-2), pp.144,145, for various times.

At 673 K there was little difference in the oxidation kinetics for the samples oxidized by this method and the hot-bare technique. SEM images of this oxide, Figure (6-8)(a), also did not appear to be significantly different from those exposed by the former technique.

The specimens exposed at 773 and 873 K were not as reproducible as those at the three other temperatures studied. At 773 K two different oxide morphologies

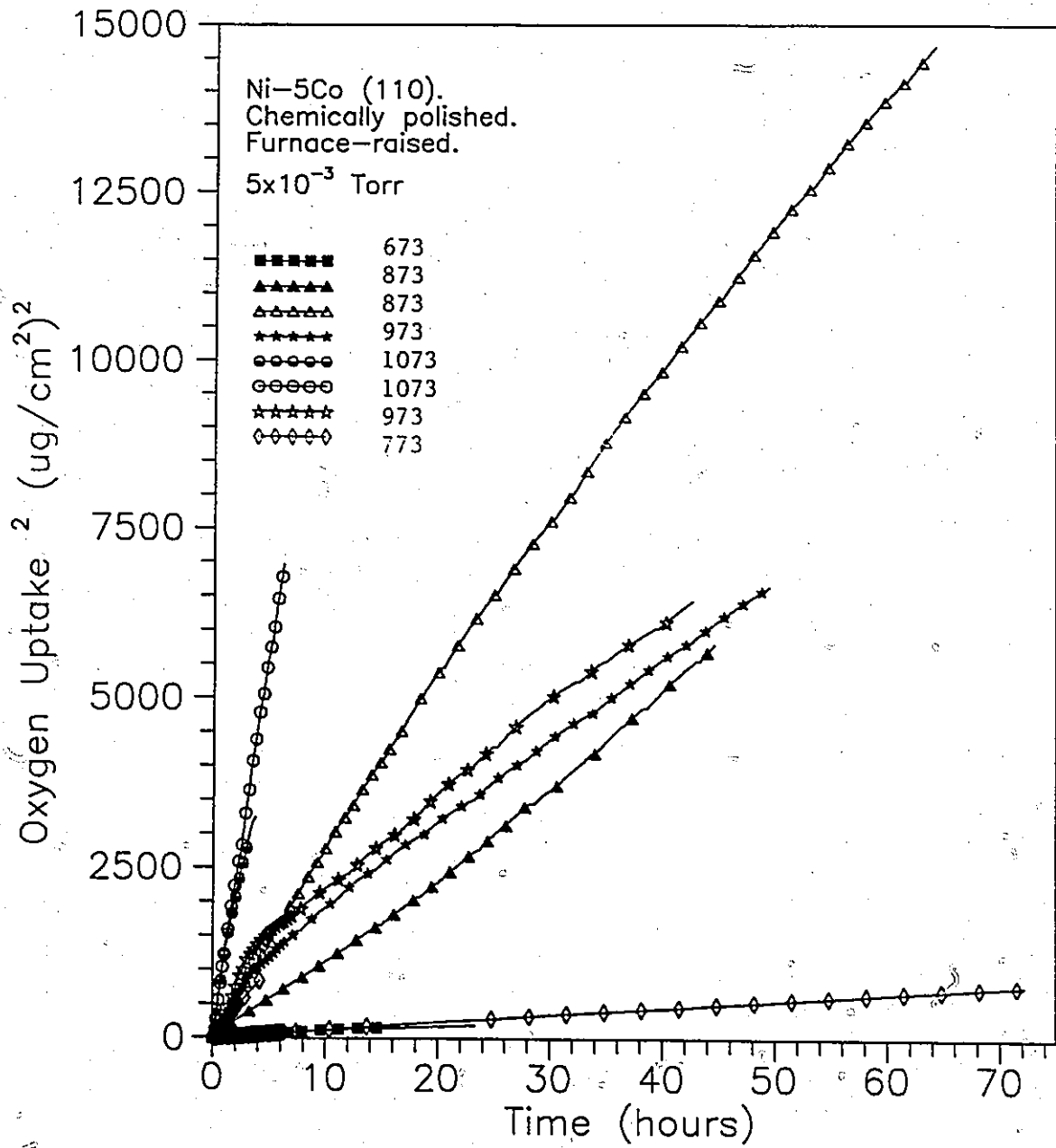


Figure (6-7)

Parabolic plots of kinetic data from the oxidation of Ni-3.86Co (110) alloys by the furnace-raised exposure technique.

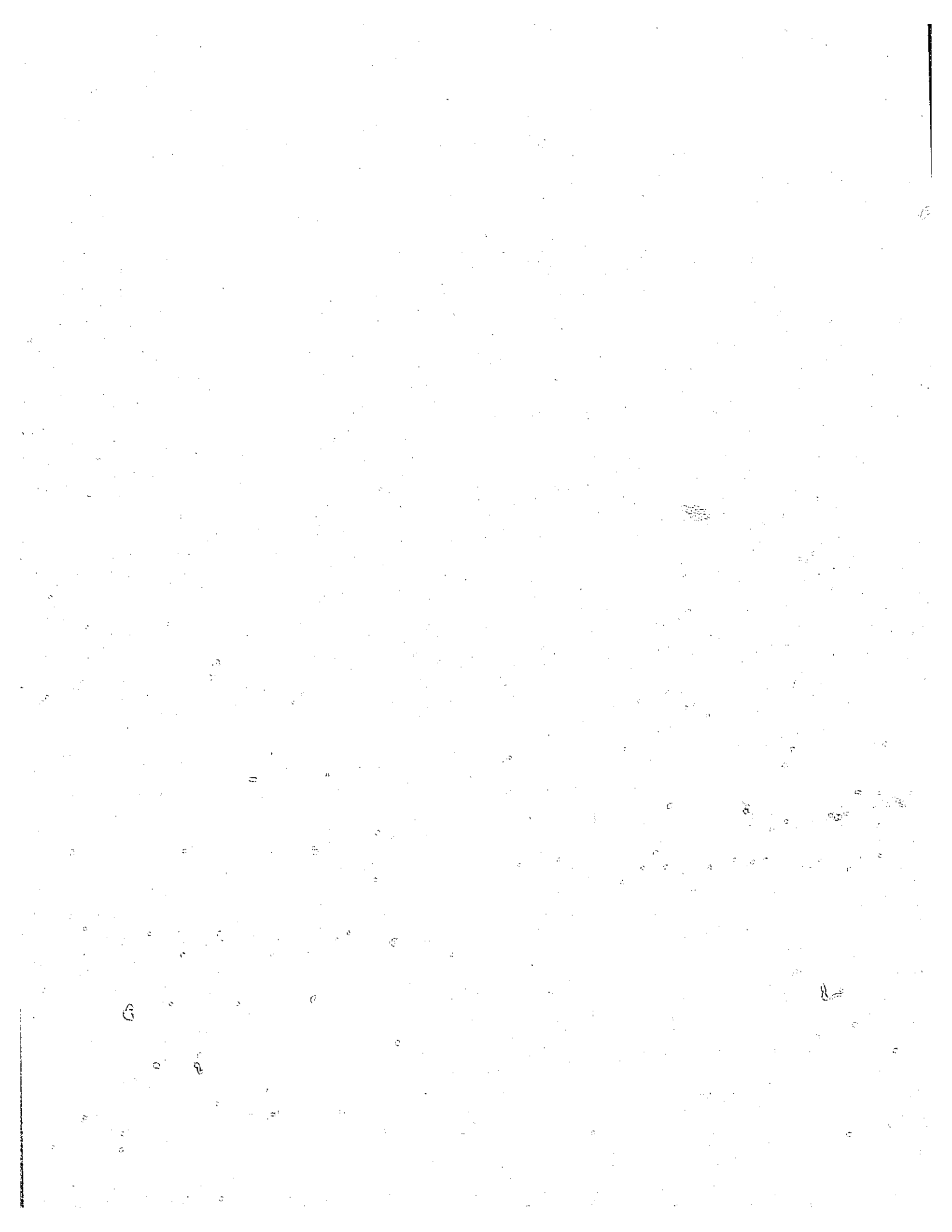


Figure (6-8)

Secondary electron micrographs of Ni-3.86Co (110) specimens oxidized by the furnace-raised technique at  $5 \times 10^{-3}$  Torr.

(a) 673 K, 24 hr.,  $14.0 \mu\text{g O}_2/\text{cm}^2$ , (b) 773 K, 72 hr.,

$27.9 \mu\text{g O}_2/\text{cm}^2$ , (c) 873 K, 44.5 hr.,  $76.2 \mu\text{g O}_2/\text{cm}^2$ ,

(d) 973 K, 49.4 hr.,  $81.5 \mu\text{g O}_2/\text{cm}^2$ , (e) 1073 K, 6.1 hr.,

$83.4 \mu\text{g O}_2/\text{cm}^2$ , (f) 773 K, 4 hr.,  $29.0 \mu\text{g O}_2/\text{cm}^2$  and

(g) 873 K, 64.2 hr.,  $121.0 \mu\text{g O}_2/\text{cm}^2$ .

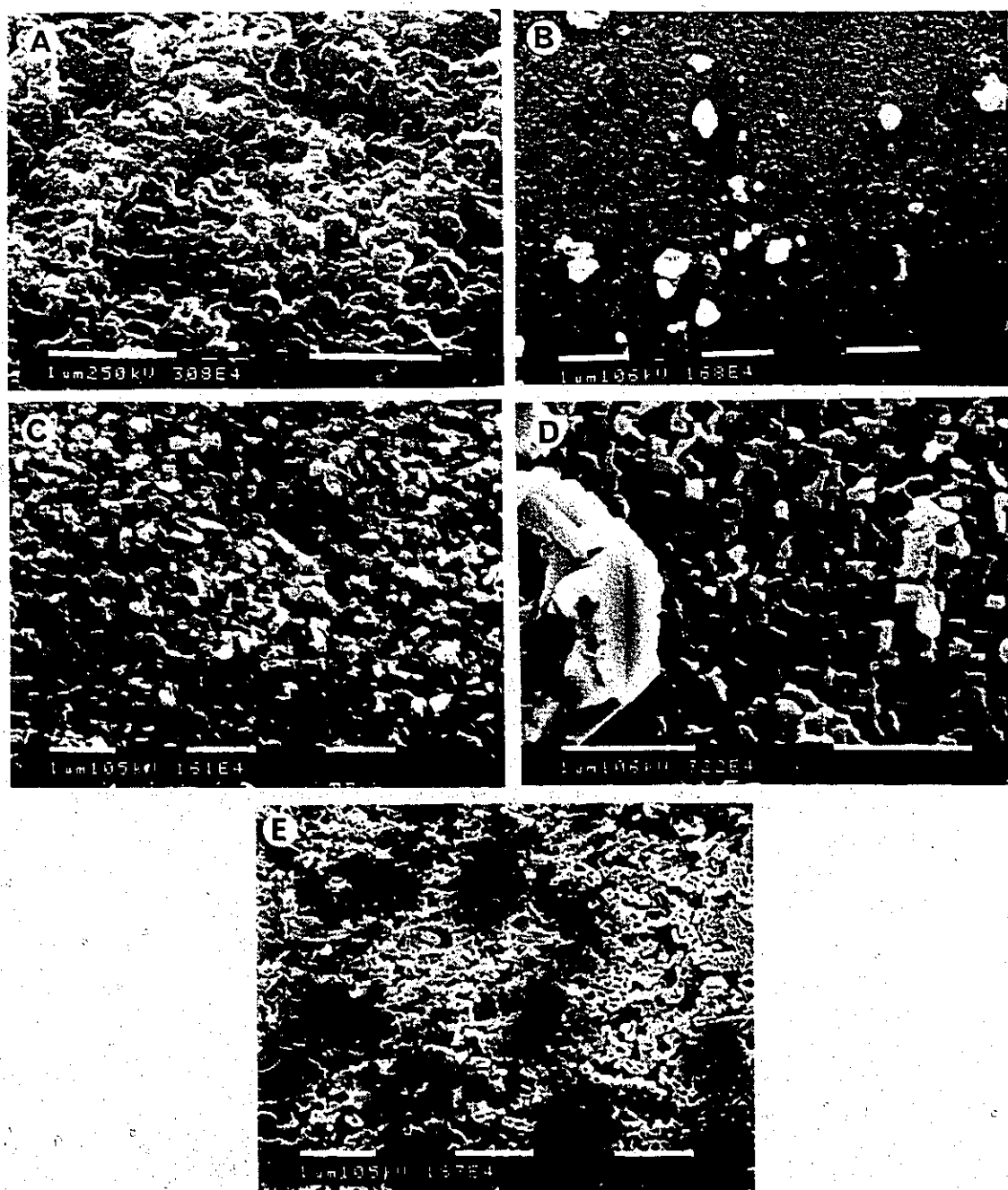


Fig.(6-8)



Fig.(6-8)

developed. The first is shown in Figure (6-8)(b). A very dense and compact layer of oxide was observed through, or on top of which, larger-grained oxide clusters had formed. The second structure corresponds to Figure (6-8)(f) and was composed of a more uniformly distributed scale having a particle size larger than the underlying oxide of the first specimen.

At 873 K variations in morphological development were again observed. One specimen, Figure (6-8)(g), also showed the presence of an underlying compact, oxide with larger-grained clusters on the surface. However, at this temperature, the clusters were more densely packed than the specimen at 773 K. The other type of structure was, as before, composed of larger, uniformly distributed grains, Figure (6-8)(c).

At 973 and 1073 K similar reaction rates and scale morphologies were obtained in separate experiments. The morphology at 973 K consisted of the two oxide structures described above, Figure (6-8)(d), but the clusters were not as closely spaced as those observed at 873 K. At 1073 K the surface appeared much more uniform, without the presence of the outgrowths seen at lower temperatures. This oxide was still not completely dense, but appeared to have a high degree of open porosity as seen in Figure (6-8)(e).

Transmission electron micrographs and associated diffraction patterns for the oxides grown by the furnace-raised technique on (110) Ni-3.86Co are shown in Figure (6-9). BF images and corresponding SAD patterns of specimens exposed at 773 (a,b) and 873 K (c,d) showed clear structural differences between the thin areas of oxide and the larger oxide clusters. The thin areas were highly textured with the (100) (NiCo)O  $\parallel$  (110) NiCo orientation. High magnification BF images of these regions showed distinct mosaic structures. SAD patterns from broader areas of the films which included the large grained clusters showed the presence of faint

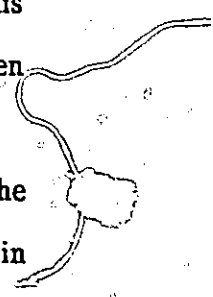


Figure (6-9)

TEM micrographs of oxides stripped from furnace-raised samples: (a,b) 773 K, 72 hr.,  $27.9 \mu\text{g O}_2/\text{cm}^2$ ; (c,d) 873 K, 64.2 hr.,  $121.0 \mu\text{g O}_2/\text{cm}^2$ ; (e,f) 973 K, 49.4 hr.,  $81.5 \mu\text{g O}_2/\text{cm}^2$ ; (g,h) 1073 K, 6.1 hr.,  $83.4 \mu\text{g O}_2/\text{cm}^2$ .

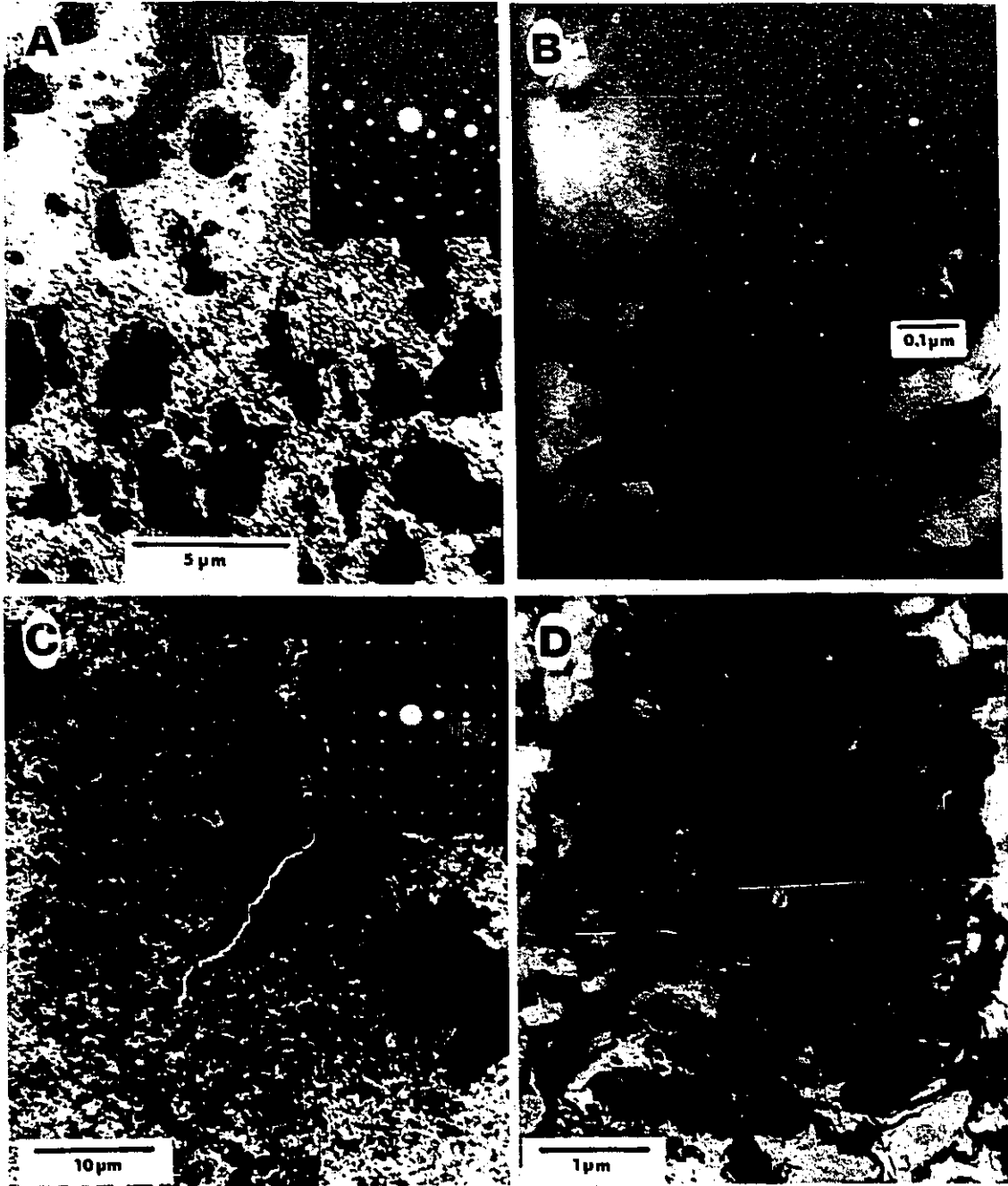


Fig.(6-9)

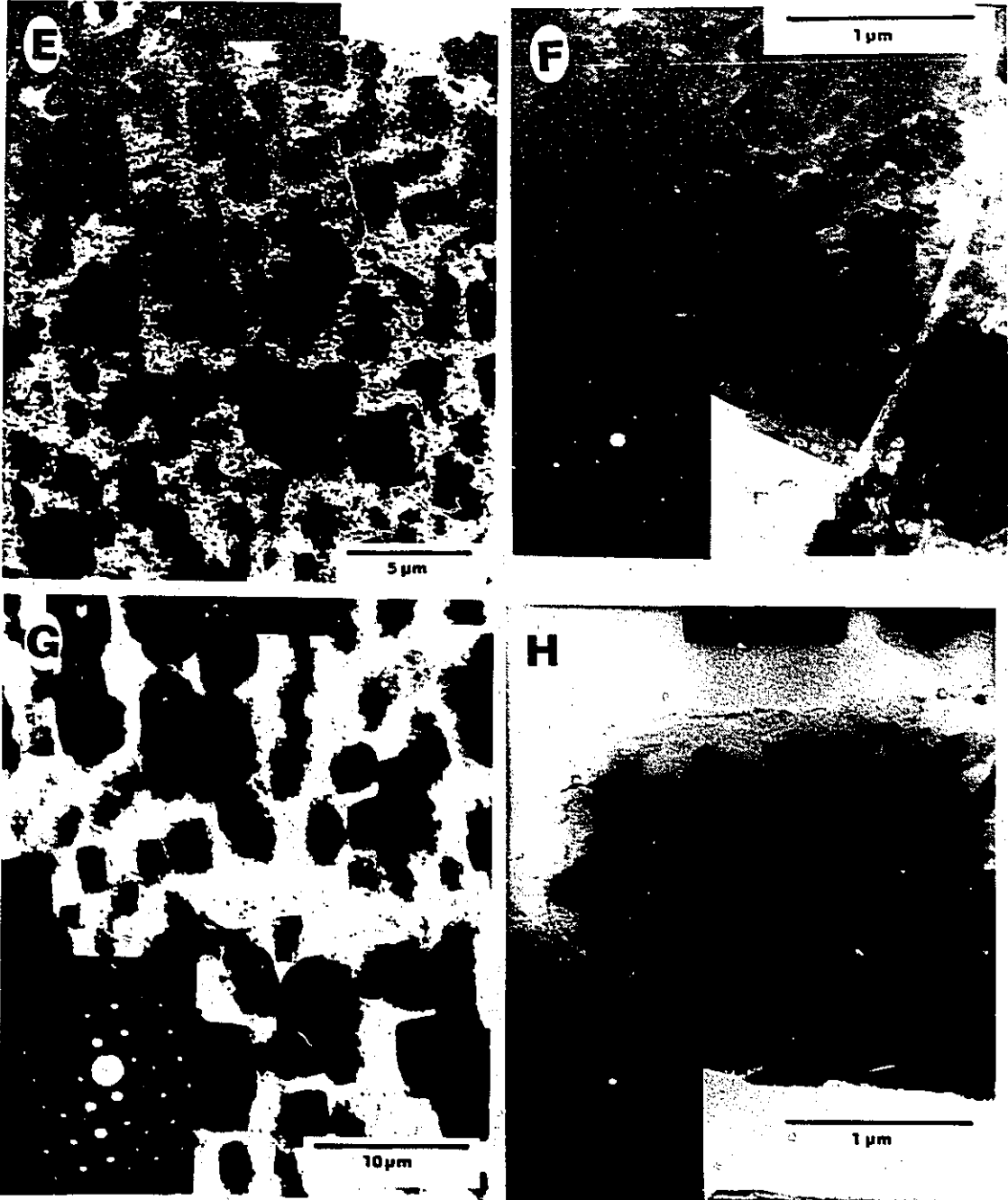


Fig.(6-9)

polycrystalline diffraction rings superimposed on the (100) single crystal pattern.

At 973 K the thin regions were also found to be well oriented with (100) (NiCo)O  $\parallel$  (110) NiCo. However, the large oxide clusters were too thick to allow structural details or diffraction information to be obtained. The thin regions again possessed a mosaic block structure as seen in Figure (6-9)(f).

The oxide stripped from the 1073 K specimen was initially too thick for TEM observations. This specimen was therefore ion milled from the direction of the original oxide-gas interface (4 KeV Ar<sup>+</sup>, 1 $\mu$ A, 15<sup>o</sup> incidence, 45 min.) to produce the thinned section shown in Figure (6-9)(g,h). Remnants of a thin oxide layer were visible between the large elongated structures previously seen in the SEM micrographs, Figure(6-8)(e). The large features were found to have the (100) (NiCo)O  $\parallel$  (110) NiCo orientation and appeared to be single crystals of oxide, Figure (6-9)(h).

Auger composition profiles were obtained from the samples discussed above and are shown in Figure (6-10). The samples analyzed correspond to the surfaces shown in Figure (6-8)[(a)-(f)]. Profiles (b) and (d) were obtained by placing the electron beam between the large periodic oxide outgrowths, and thus correspond to the thin film regions only. Cobalt enrichment was found at the outer oxide surface in all cases. This enrichment varied from approximately 20% for samples oxidized at 873, 973 and 1073 K to 12-18% for the 773 K specimen and 11-12% for the 673 K specimen. In all profiles the cobalt concentration decreased continuously to a level approximately equal to that in the alloy phase.

#### 6.4 Oxidation of the Ni-4.0Co Polycrystalline Alloy

Polycrystalline Ni-4.0Co samples were exposed at 773 , 873 and 1073 K by the furnace-raised technique at  $5 \times 10^{-3}$  Torr. The surfaces of these specimens were

Figure (6-10)

Auger depth profiles of specimens oxidized by the furnace-raised technique at  $5 \times 10^{-3}$  Torr. (a) 673 K, 24 hr.,  $14.0 \mu\text{g O}_2/\text{cm}^2$ , (b) 773 K, 72 hr.,  $27.9 \mu\text{g O}_2/\text{cm}^2$ , (c) 873 K, 44.5 hr.,  $76.2 \mu\text{g O}_2/\text{cm}^2$ , (d) 973 K, 49.4 hr.,  $81.5 \mu\text{g O}_2/\text{cm}^2$ , (e) 1073 K, 6.1 hr.,  $83.4 \mu\text{g O}_2/\text{cm}^2$ , (f) 773 K, 4 hr.,  $29.0 \mu\text{g O}_2/\text{cm}^2$ . Composition analyses were obtained by the computer spectrum simulation method and are given by the triangular symbols.

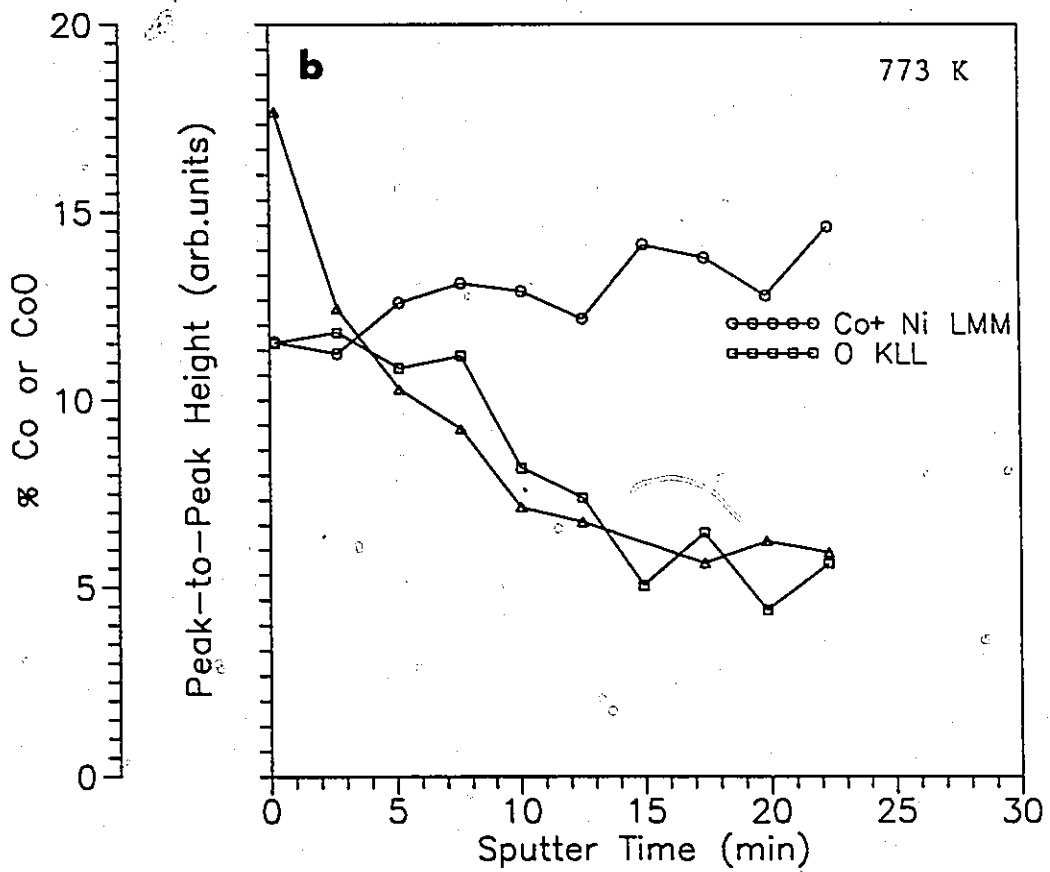
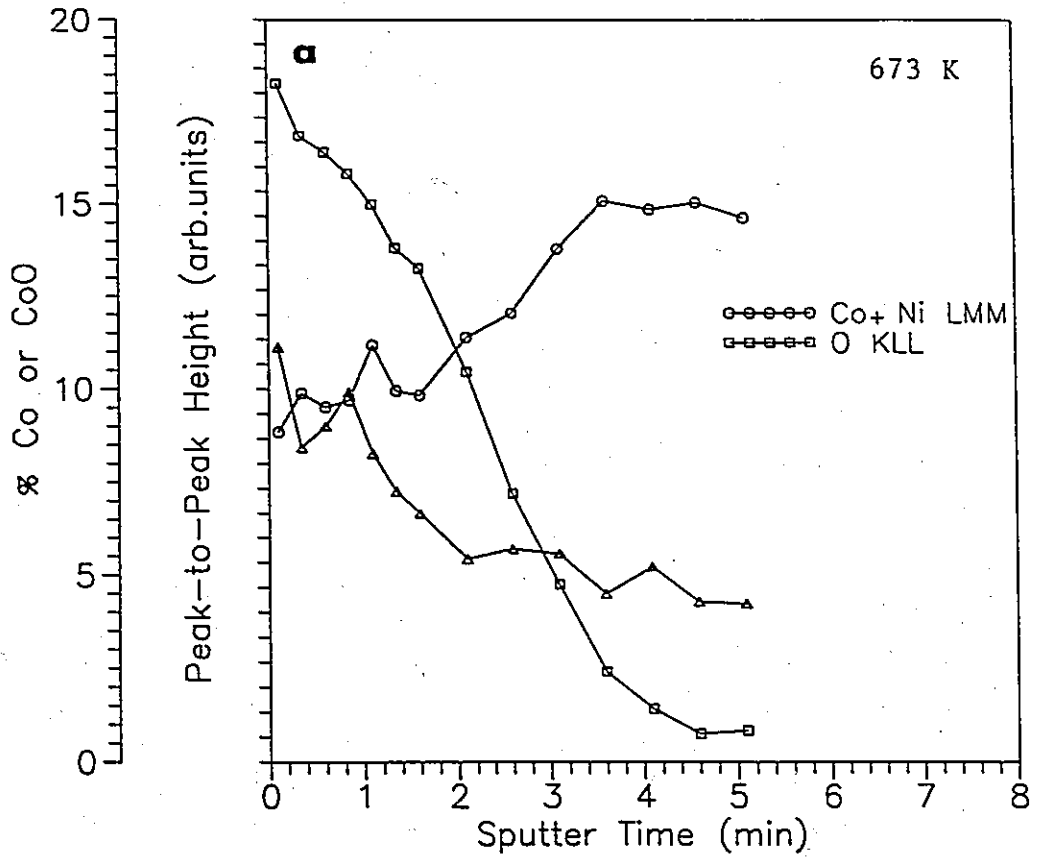


Fig. (6-10)

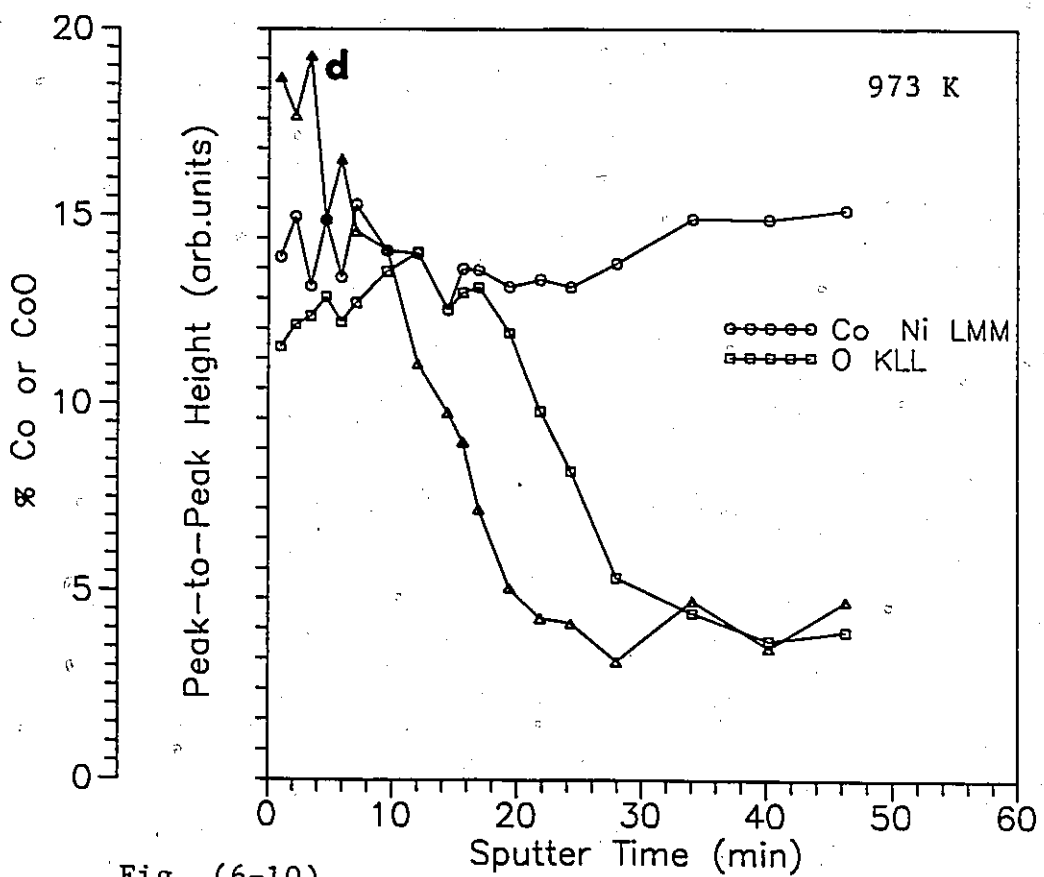
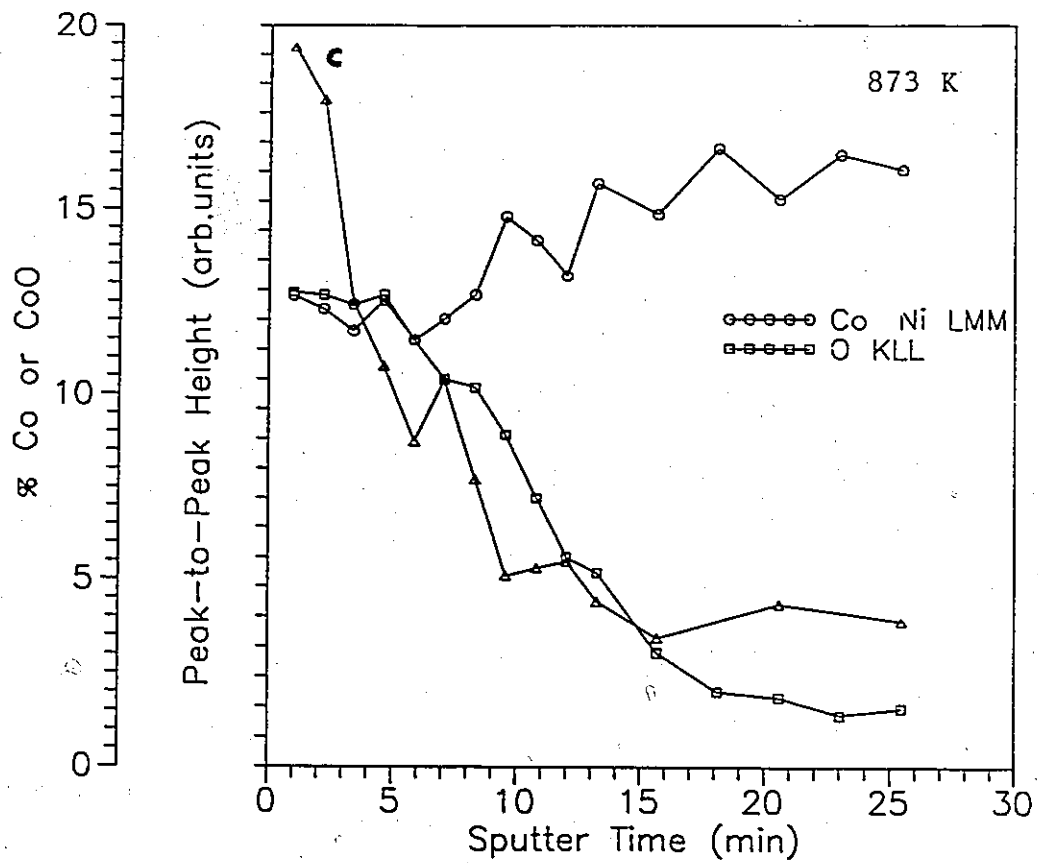


Fig. (6-10)

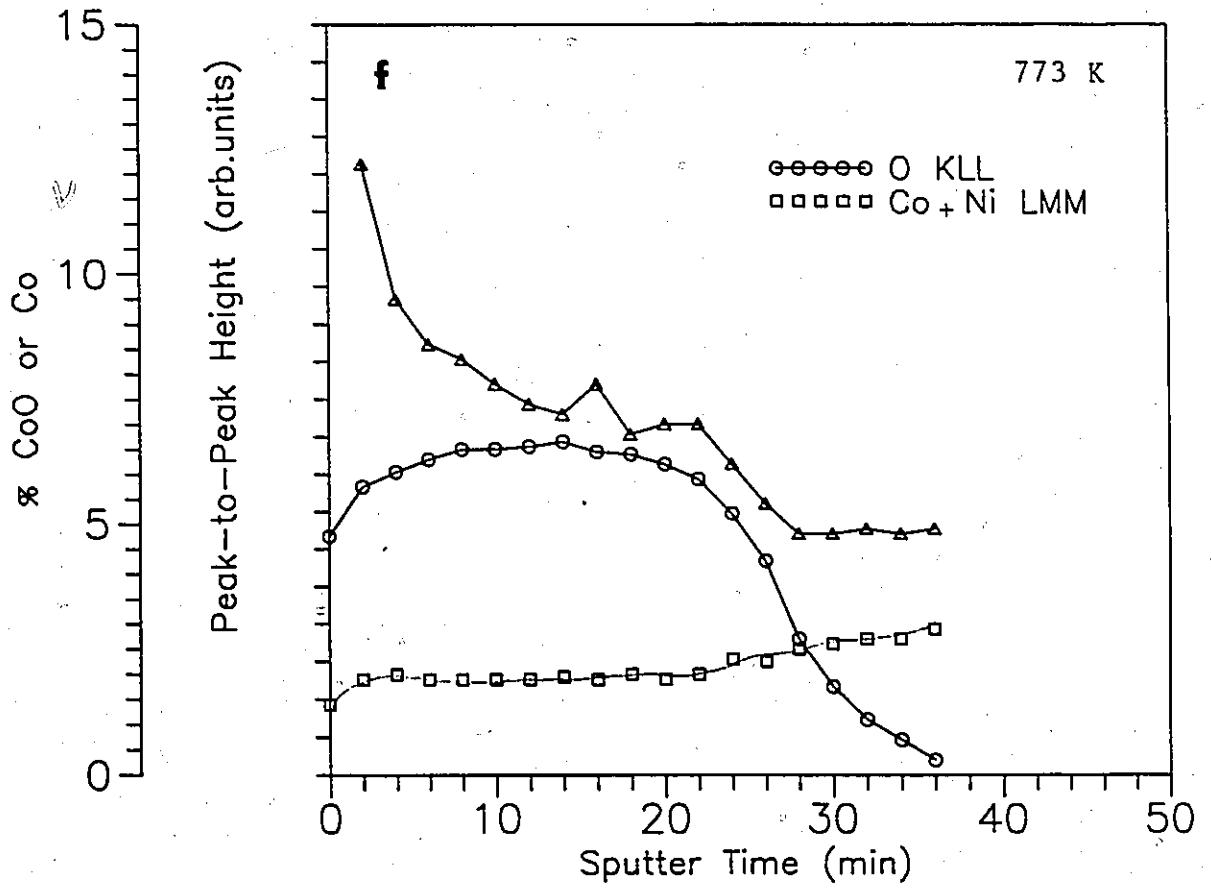
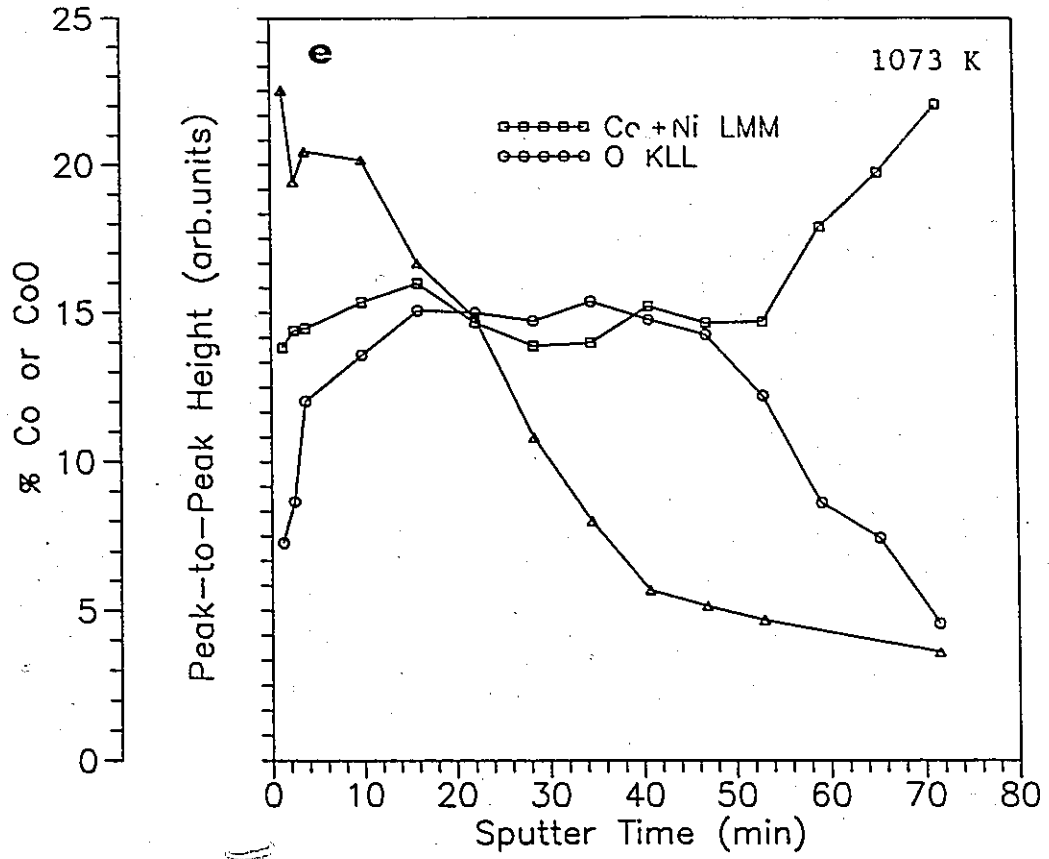


Fig. (6-10)

prepared using  $1\mu\text{m}$  diamond paste as the final polishing step. Kinetic curves are shown in Figure (6-11). The instantaneous parabolic rate constants are shown as a function of oxidation time in Table (6-2). At 1073 K the oxidation rate constant decreased by almost one order of magnitude during the short exposure period of 2 hours. In contrast, the specimen exposed at 773 K oxidized with an unchanging parabolic constant over the 5 hour run.

Examination of these specimens by SEM revealed a distinctly different microstructure from the previous experiments using single crystal surfaces. These oxides were composed of evenly distributed and faceted crystals, as shown in Figure (6-12). The oxides prepared at 773 and 873 K were relatively adherent, however the film on the 1073 K specimen spalled in several places during handling after removal from the oxidation apparatus.

Examination by TEM was possible without ion thinning for the oxides stripped from the 773 and 873 K samples. These results are shown in Figure (6-13)[(a)-(d)]. Regions near the edge of the films were used to image clusters of oxide particles for grain size determination. SAD patterns showed that these oxides were more randomly oriented than those which formed on any of the single crystal surfaces. The oxide from the specimen exposed at 1073 K was thinned to allow observation of individual features within the film, Figure (6-13)(e,f). The approximate grain size for each of these films (measured as the two-dimensional projected height) was determined from a random sampling of the individual crystallites. These results are shown in Table (6-1), p. 143.

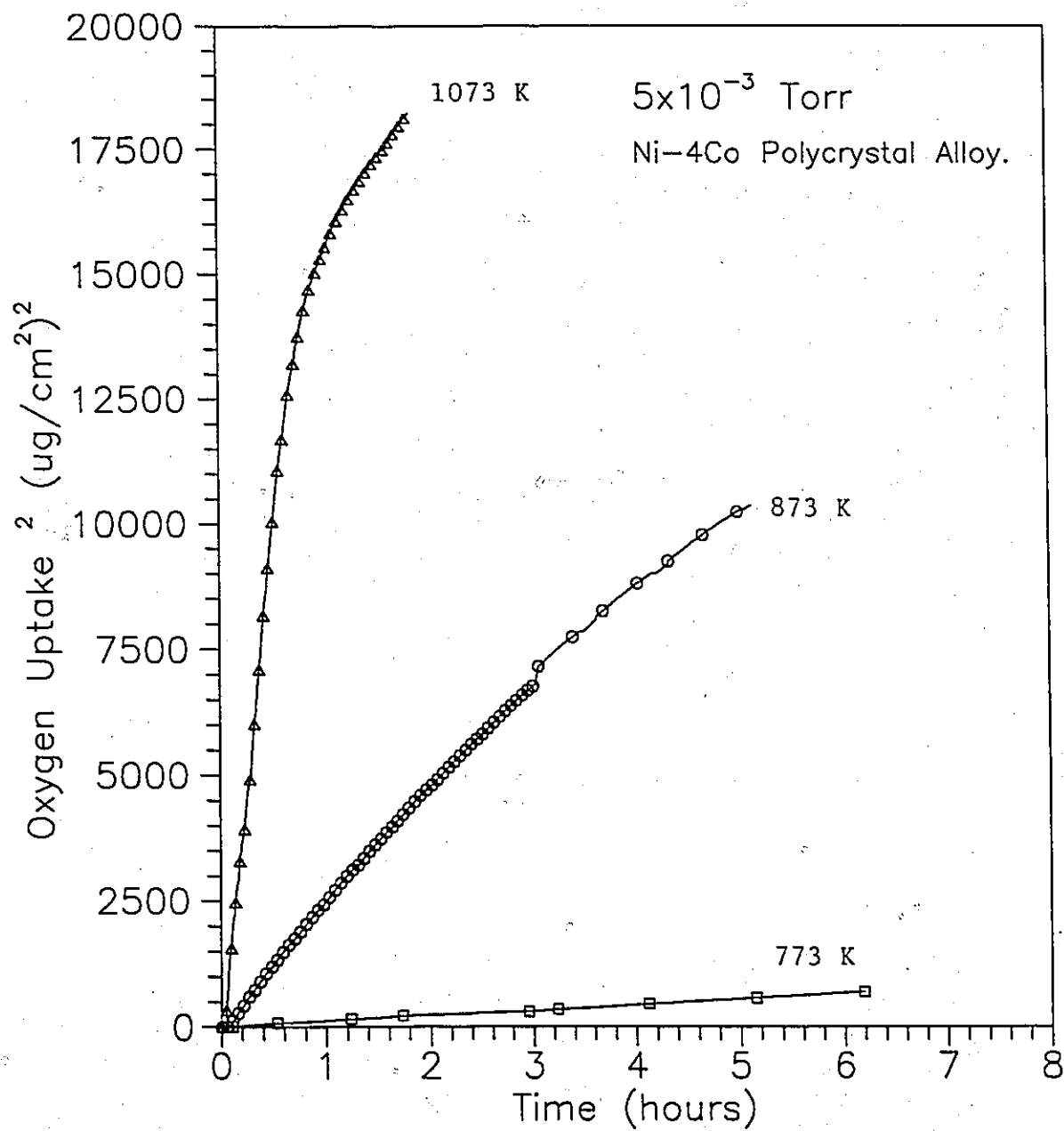


Figure (6-11)

Parabolic plots of kinetic data from the oxidation of Ni-4.0Co polycrystalline alloys by the furnace-raised technique.

Figure (6-12)

Secondary electron micrographs of Ni-4.0Co polycrystalline alloy surfaces after exposure to  $5 \times 10^{-3}$  Torr  $O_2$  at (a) 773 K, 6.2 hr.,  $26.2 \mu\text{g } O_2/\text{cm}^2$ , (b) 873 K, 5.1 hr.,  $102.7 \mu\text{g } O_2/\text{cm}^2$  and (c) 1073 K, 1.8 hr.,  $135.2 \mu\text{g } O_2/\text{cm}^2$ .

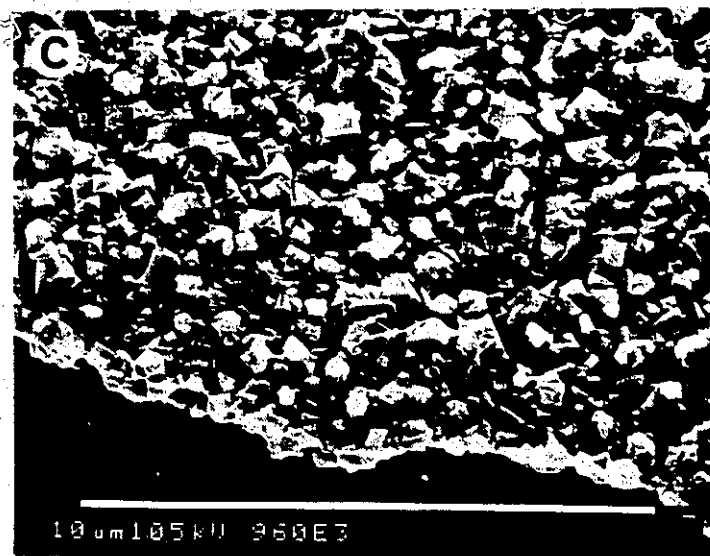
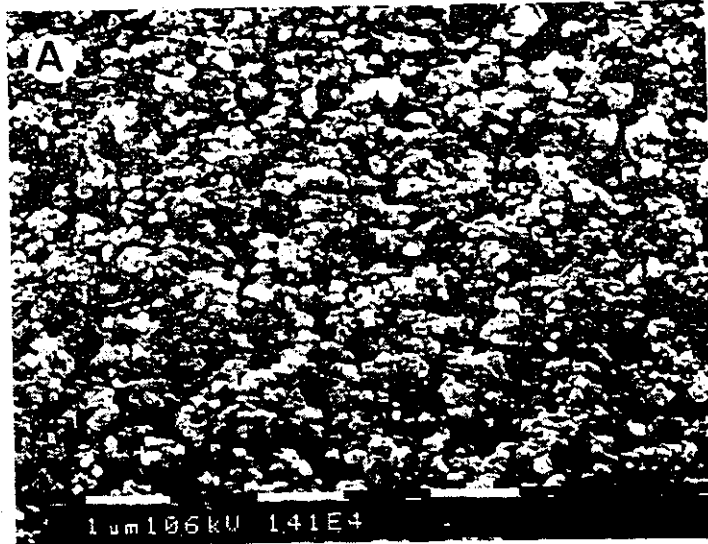
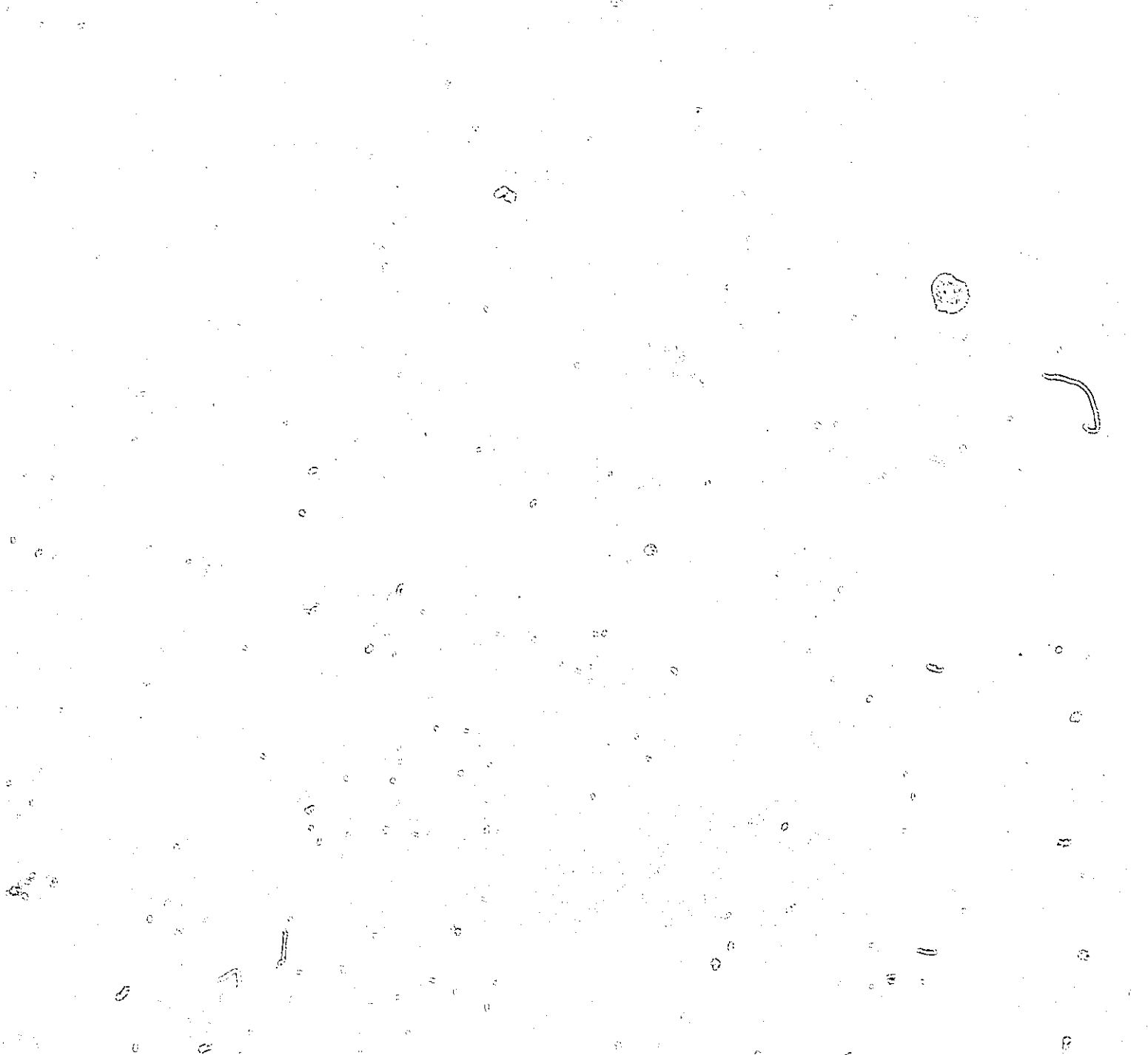


Fig.(6-12)

Figure (6-13)

Bright field transmission electron micrographs of oxide films stripped from Ni-4.0Co polycrystalline alloys exposed at (a,b) 773 K, 6.2 hr.,  $26.2 \mu\text{g O}_2/\text{cm}^2$ , (c,d) 873 K, 5.1 hr.,  $102.7 \mu\text{g O}_2/\text{cm}^2$  and (e,f) 1073 K, 1.8 hr.,  $135.2 \mu\text{g O}_2/\text{cm}^2$ . The latter specimen was thinned from the direction of the oxide-gas interface using 4 KeV  $\text{Ar}^+$  ions with a beam current of  $1 \mu\text{A}$  at an incidence angle of  $15^\circ$ .



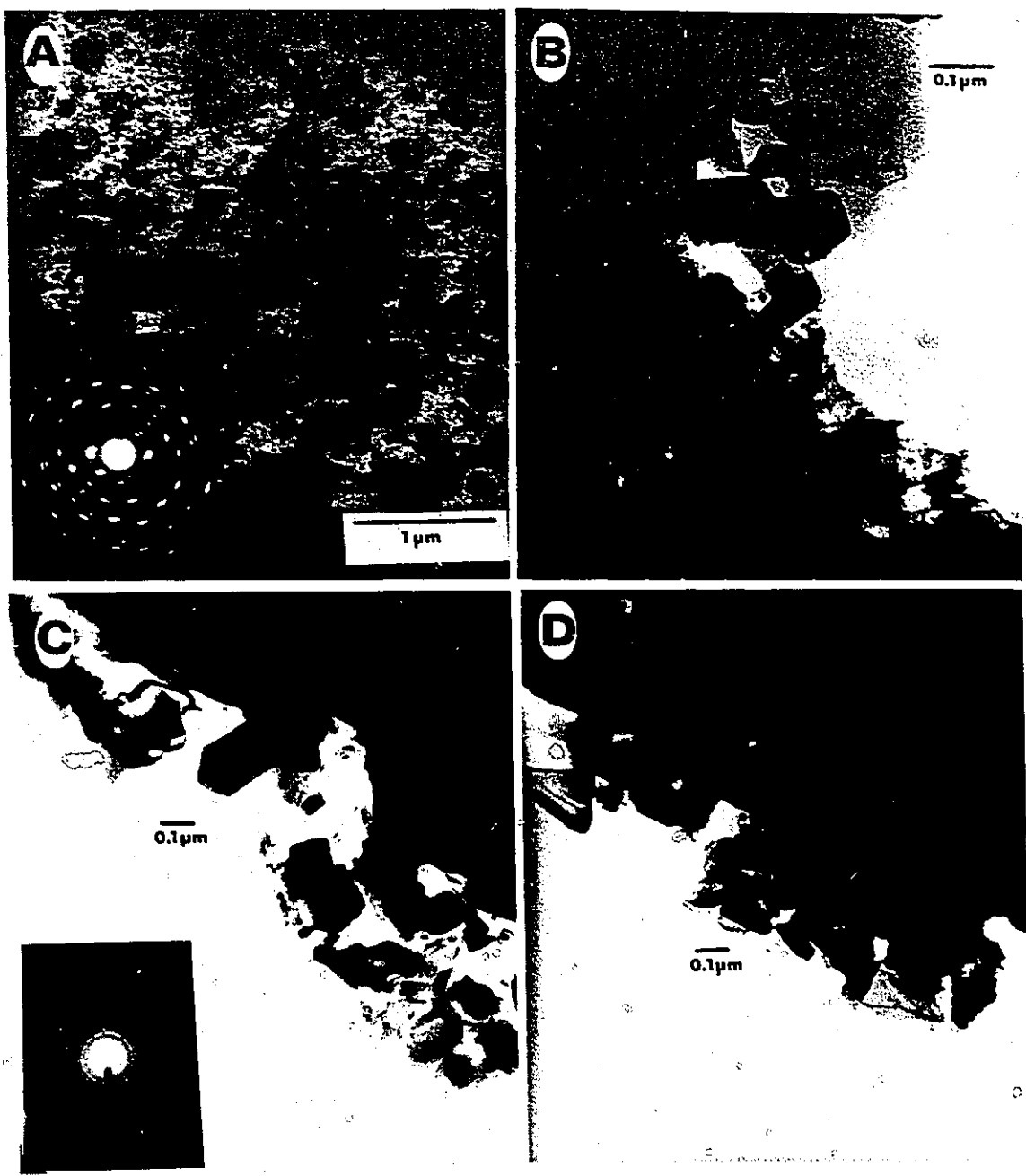


Fig. (6-13)

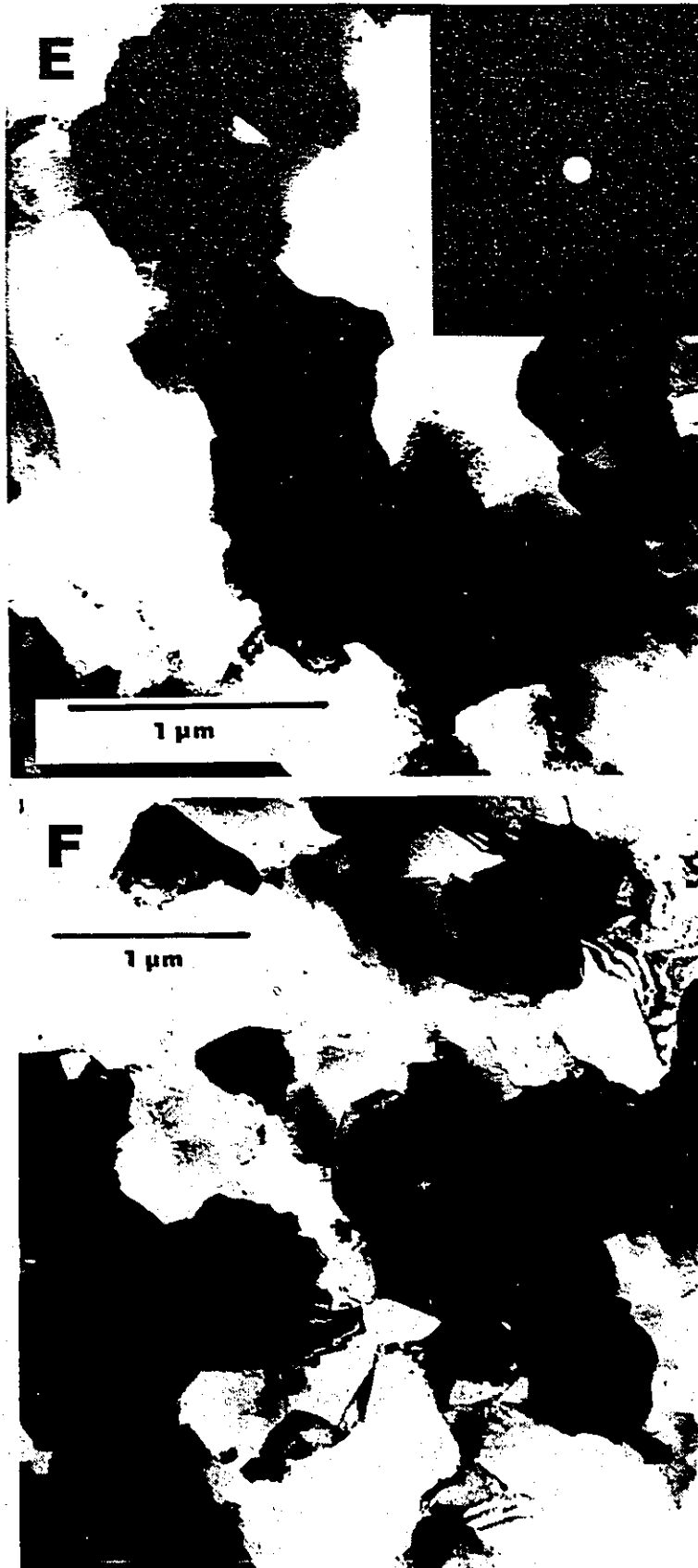


Fig. (6-13)

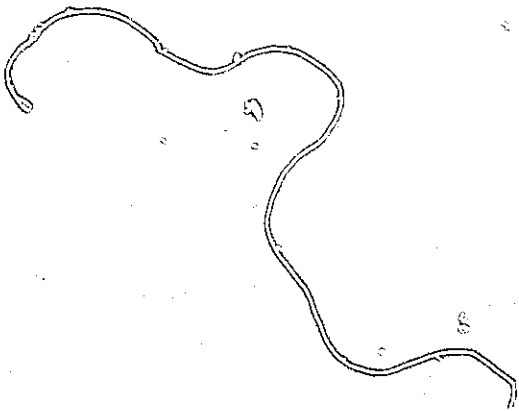


Figure (6-14)

Auger depth profiles through oxides produced on Ni-4.0Co specimens at  $5 \times 10^{-3}$  Torr  $O_2$ . (a) 773 K, (b) 873 K and (c) 1073 K. The sputtering rate for profile (c) was increased relative to (a) and (b) by reducing the area rastered by the ion beam while maintaining a constant beam current. Composition analyses were obtained by the computer spectrum simulation method and are given by the triangular symbols

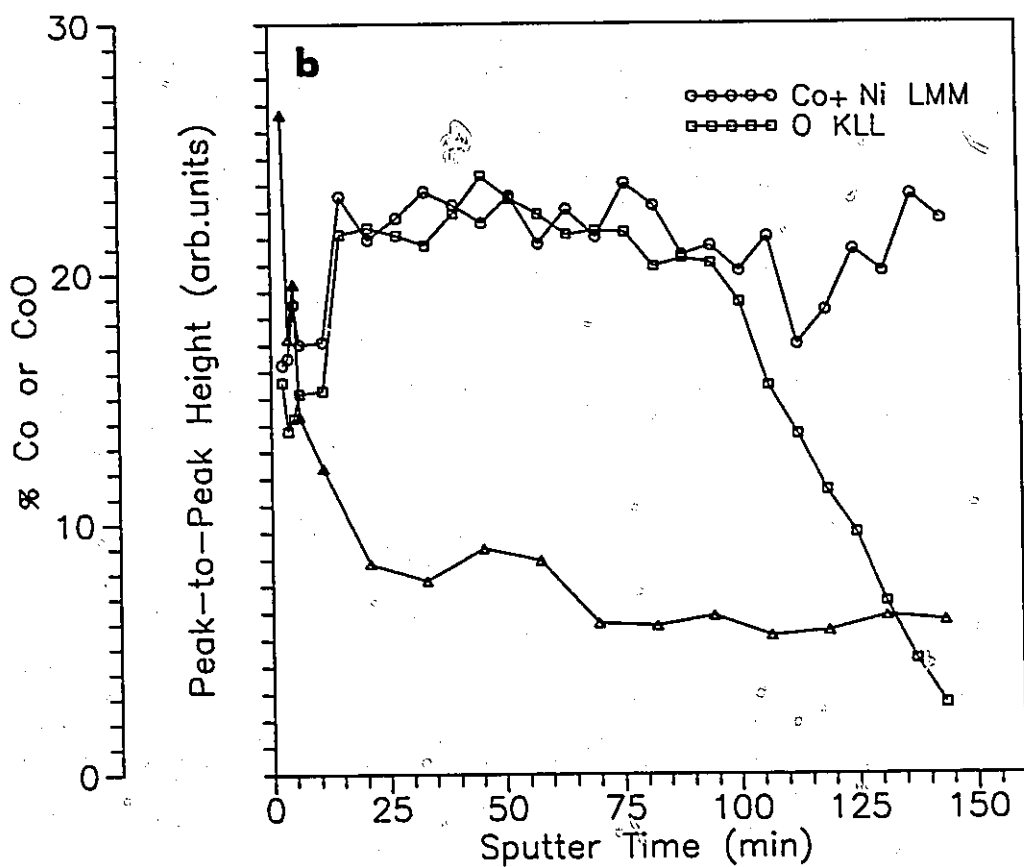
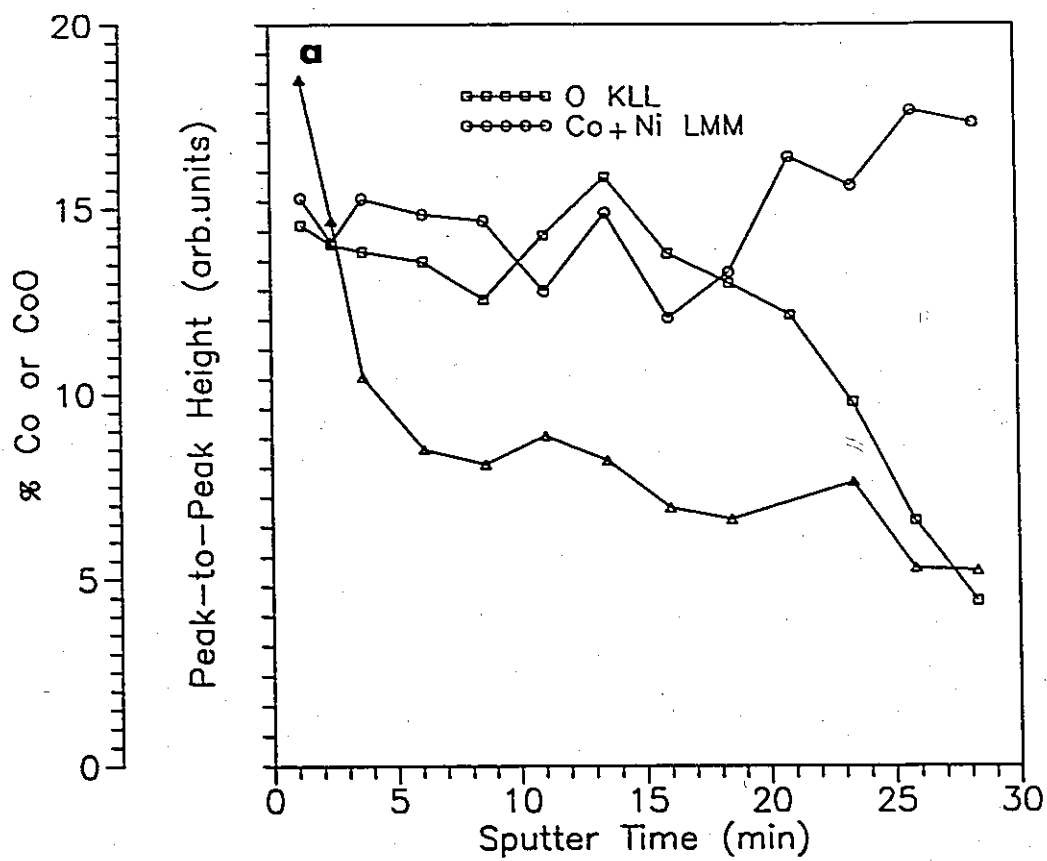


Fig. (6-14)

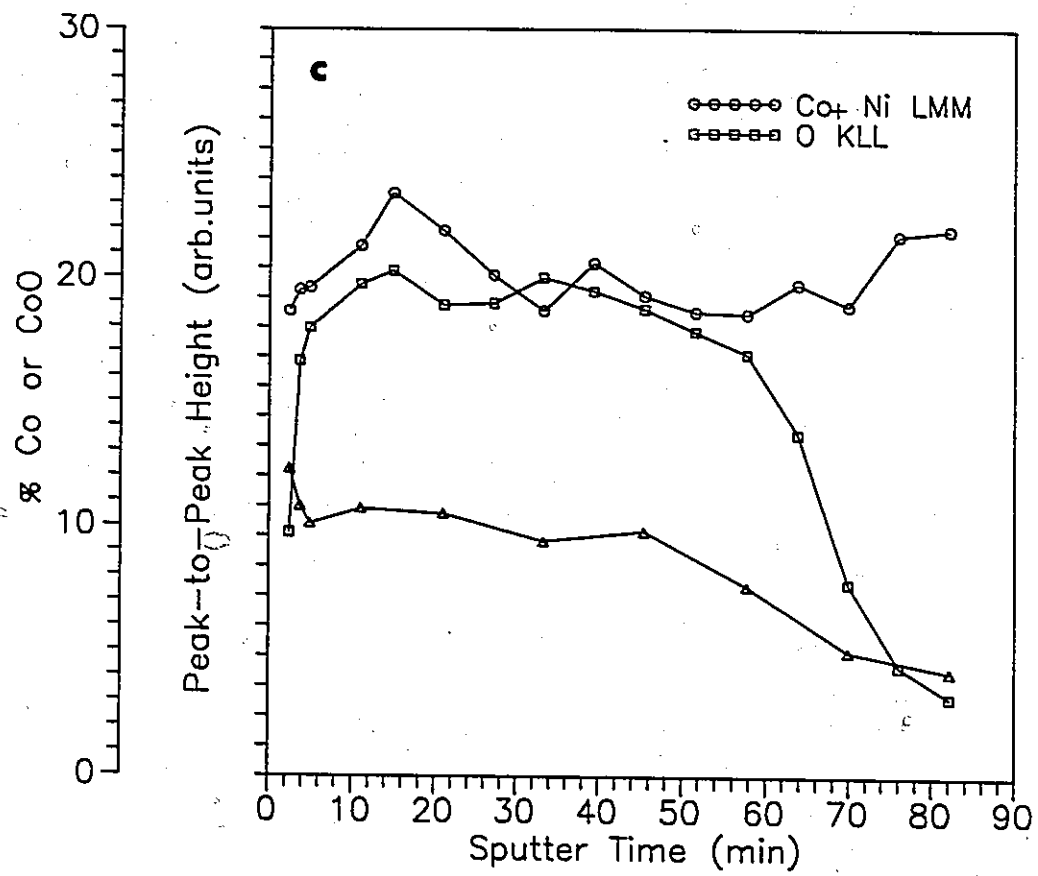


Fig. (6-14)

Table (6-1)  
Average grain diameters of stripped oxide films from polycrystalline  
Ni-4.0Co alloys measured from TEM BF images.

T, K	Avg. Dia.(Å)	Std. Dev.(Å)
773	236	124
873	1005	388
1073	6467	1125

Auger depth profiles through the same oxide structures are given in Figure (6-14). Deconvolution of the (Co+Ni) LMM peaks again indicated an enrichment of cobalt near the oxide-gas interface.

### 6.5 Discussion

The results given in the preceding sections have shown that the oxide products and corresponding reaction rates depend strongly on substrate orientation and methods of surface pretreatment. A semi-quantitative comparison of the measured reaction rates with those predicted from diffusional theory will be given later in this discussion. It will be shown that transport of nickel and cobalt ions in the growing oxide films was occurring by a combination of both lattice and boundary diffusion. On this basis, variations in the observed reaction rates for the three experimental conditions may be rationalized according to the differences in the number and type of boundaries which developed in each case.

Direct comparisons of the instantaneous parabolic growth rates may be made by referring to Table (6-2). These measurements show that, in general, the slowest rates of oxygen uptake were associated with the (110) Ni-3.86Co single crystals oxidized by the furnace-raised technique. Films produced by this experimental condition contained extensive areas of oxide which was highly oriented to the

Table (6-2)  
 Instantaneous parabolic rate constants for oxidation of (110)Ni-3.86Co and Ni-4.0Co  
 polycrystalline alloys at  $5 \times 10^{-3}$  Torr

		Time (hrs)										
		0.5	1	2	4	5	10	20	30	50	70	
T, K		Parabolic rate constant, $\text{gO}^2 \text{cm}^{-4} \text{sec}^{-1}$										
673												
SC, HB	$2.5 \times 10^{-15}$						$2.4 \times 10^{-15}$		$2.3 \times 10^{-15}$			
SC, FR	$3.2 \times 10^{-15}$											$3.2 \times 10^{-15}$
723												
SC, HB	$4.0 \times 10^{-14}$						$2.4 \times 10^{-14}$	$2.1 \times 10^{-14}$	$2.0 \times 10^{-14}$			
773												
SC, HB	$1.2 \times 10^{-13}$						$8.9 \times 10^{-14}$		$8.9 \times 10^{-14}$			
SC, FR	$3.4 \times 10^{-15}$						$2.8 \times 10^{-15}$					$2.4 \times 10^{-15}$
SC, FR	$5.6 \times 10^{-14}$				$5.6 \times 10^{-14}$							
PC, FR	$3.0 \times 10^{-14}$											
873												
SC, FR	$2.9 \times 10^{-14}$			$3.8 \times 10^{-14}$	$2.9 \times 10^{-14}$		$3.4 \times 10^{-14}$	$2.6 \times 10^{-14}$	$3.4 \times 10^{-14}$	$3.0 \times 10^{-14}$		
SC, FR	$7.5 \times 10^{-14}$							$5.6 \times 10^{-14}$	$4.9 \times 10^{-14}$	$5.0 \times 10^{-14}$		
PC, FR	$7.5 \times 10^{-13}$			$6.5 \times 10^{-13}$	$5.5 \times 10^{-13}$							

(continued...)

Table (6-2), continued

T, K	Time(hrs)									
	0.5	1	2	4	5	10	20	30	50	70
973	Parabolic rate constant, $\text{gO}^2 \text{cm}^{-4} \text{sec}^{-1}$									
SC,FR	$6.0 \times 10^{-14}$	$8.6 \times 10^{-14}$	.....	.....	$4.1 \times 10^{-14}$	$3.2 \times 10^{-14}$	$3.4 \times 10^{-14}$	$3.4 \times 10^{-14}$	$3.4 \times 10^{-14}$	$3.4 \times 10^{-14}$
SC,FR	$6.8 \times 10^{-14}$	$8.6 \times 10^{-14}$	$1.5 \times 10^{-13}$	.....	$3.8 \times 10^{-14}$	$3.0 \times 10^{-14}$	$4.1 \times 10^{-14}$	$4.1 \times 10^{-14}$	$3.2 \times 10^{-14}$	$3.2 \times 10^{-14}$
1073										
SC,FR	$4.1 \times 10^{-13}$	$3.6 \times 10^{-13}$	$3.2 \times 10^{-13}$	.....	.....	.....	.....	.....	$2.2 \times 10^{-13}$	.....
SC,FR	$3.4 \times 10^{-13}$	$3.0 \times 10^{-13}$	$2.1 \times 10^{-13}$	.....	.....	.....	.....	.....	.....	.....
PC,FR	$5.5 \times 10^{-12}$	$1.5 \times 10^{-12}$	$7.0 \times 10^{-13}$	.....	.....	.....	.....	.....	.....	.....

Notes: SC,HB: Ni-3.86Co (110), annealed, hot-bare  
 SC,FR: Ni-3.86Co (110), annealed, furnace-raised  
 PC,FR: Ni-4.0Co polycrystal, 1/4m diamond polish, not annealed, furnace-raised

substrate, having a mosaic block structure. The degree of orientation mismatch between adjacent blocks, as determined from the angular rotation or streaking of the SAD spot patterns, was within only a few degrees. In addition to the mosaic structure, a faster growing and less dense type of oxide was observed in some of the furnace-raised experiments. Limited SAD information obtained from these structures showed that they were polycrystalline with random orientations.

These observations suggest that for oxidation reactions which are controlled by boundary diffusion, it is both the number, and perhaps more importantly, the type of boundaries which determine the oxidation rate. The thin mosaic oxide had crystal blocks with sizes on the order of hundreds to thousands of Ångstroms which were clearly visible in the TEM images. That is to say that the regions which appeared to be single crystal from the SAD patterns really contained a large number of internal boundaries — far from being perfect crystals. Due to the thickness of the coarser oxide, it was not possible to estimate grain sizes in these areas by TEM. However, the SEM images indicated that this oxide had a grain size with an upper limit of at least the same range. Having established that the density of low and high angle boundaries within the different areas of these layers did not differ greatly, it may be reasoned that transport rates within the low angle boundaries were significantly slower than for the high angle ones. In addition, the overall rates of oxide growth depends on the relative amounts of the different oxide orientations present. This later observation arises from the variation in reaction rates measured in repeat experiments under similar reaction conditions.

Oxidation of (110) Ni-3.86Co by the hot-bare technique resulted in films having, in general, a higher rate of oxidation than specimens exposed by the furnace-raised technique. These oxides also displayed a higher number of preferred

orientations between the oxide and alloy. For any given film, within a selected area on the order of one micron, there was little variation in the number of orientations from one region to another. It appeared from the SEM images that these films were growing as a network of ridges. These ridges grew at a much faster rate than the relatively thin oxide which separated them. TEM observations confirmed that these areas were much thicker than the surrounding oxide and revealed them to be composed of crystallites whose dimensions were smaller than the ridge features. The enlargement or swelling of the ridges at successively longer oxidation times was therefore presumably due to outward transport of cations along internal boundaries.

It has yet to be determined why these two exposure techniques produced such different morphologies on (110) Ni-3.86Co. A review of the literature has shown that there are few studies of the oxidation of NiCo alloys in this temperature range. There are, however, experimental data for the oxidation of pure nickel which may provide some basis for interpretation of the present results. These studies have been conducted in the regimes of nucleation and growth of two- and three-dimensional oxides by surface analytical techniques, and also in the range of thin films extending up to 5000 Ångstroms in thickness by gravimetric and X-ray diffraction techniques.

The studies of thin film (25-5000 Å) NiO growth on (110) Ni have previously been shown to produce a large number of oxide orientations. Cathcart and co-workers<sup>(82)</sup> used electropolished nickel single crystals which were annealed in hydrogen for 10-15 min at temperatures from 673-873 K prior to oxidation. These samples were then maintained at the same temperatures while the hydrogen was pumped out, followed by exposure to oxygen at slightly less than 1 atm. total pressure. This procedure yielded textured films on (111), (100) and (311) Ni, but produced a polycrystalline oxide on (110) Ni for thicknesses up to 500 Å.

Khoi and coworkers<sup>(77)</sup> identified eleven NiO orientations parallel to (110) Ni

upon exposure to 400 Torr oxygen at temperatures within the range 773–1073 K. These surfaces were also prepared by electropolishing followed by vacuum annealing at  $3 \times 10^{-6}$  Torr at 1073 K for 18 hours. After cooling in vacuum to room temperature the surfaces were exposed to oxygen and then the temperature was increased to the desired level. Total oxide thicknesses in these experiments were up to 5000 Å. Gradual changes in orientation occurred as the scales thickened with a tendency to form (100) NiO parallel to (110) Ni.

With regard to the very early stages of oxidation, there are several papers dealing with the stages of chemisorption, nucleation and spreading of NiO on (110) Ni at room temperature<sup>(84–87)</sup>. These studies were conducted using low energy electron diffraction (LEED) and reflection high energy electron diffraction (RHEED) on starting surfaces which were "atomically" clean, produced in UHV environments. Cleaning was by various techniques, including hydrogen reduction, ion bombardment and vacuum annealing. The first formed two-dimensional oxide structures have been identified as (2X1) and (3X1). This is followed by transformation to a (9X4) structure, which upon further exposure to oxygen, transforms into a three-dimensional oxide with (100) NiO || (110) Ni. Mitchell and coworkers<sup>(85)</sup> estimate that this latter change occurs at oxygen doses greater than  $0.015 \mu\text{g}/\text{cm}^2$ . Exposures beyond  $0.06 \mu\text{g}/\text{cm}^2$  corresponded in the latter study to a further transformation to a (117) NiO || (110) Ni epitaxial relationship.

The present results appear to fall between these two extremes. When (110) Ni–3.86Co samples were exposed to oxygen at room temperature after the UHV annealing cycle (furnace-raised) the resulting oxide exhibited a strong tendency to form (110) (NiCo)O || (110) Ni–3.86Co. It is not clear why or how the additional polycrystalline oxide formed in some experiments. It is possible that slight differences in surface misorientation away from the (110) direction due to the

method of sample preparation could have resulted in nucleation of other, more random orientations at room temperature. Upon heating, these orientations could have grown at a faster rate due to a higher rate of diffusion in the more randomly oriented boundaries. This mechanism would account for the sample-to-sample structural variations in the films.

Exposure of clean (110) Ni-3.86Co surfaces to oxygen at elevated temperatures (hot-bare) resulted in the formation of a greater number of orientations. Presumably this was due to the greater amount of thermal energy available for nucleation of less energetically favorable structures. The effects of misorientation of the alloy surface did not appear to be as significant in this series of experiments; there was a relatively uniform distribution of the different oxide orientations across the surface of each sample. It appeared that the effect of surface structural defects in lowering the activation energy for nucleation was balanced by the additional thermal energy available for nucleation on the remainder of the alloy surface.

The results for the oxidation of the Ni-4Co polycrystalline specimens indicated that these oxides developed in a more uniform or homogeneous way. This was interpreted as being due to the nucleation of mainly random oxide crystallites across the surfaces of these specimens. Such an effect may be expected for cold-worked surfaces which were subsequently exposed to the laboratory atmosphere prior to the oxidation tests; oxide formation on these surfaces would have been almost instantaneous. Further exposure to oxygen and heating in the experimental chamber would merely have resulted in the continued growth of these films, aided by a high density of randomly oriented oxide grain boundaries.

## 6.6 A Diffusion Model for The Growth of (NiCo)O Solid Solution Oxides by Combined Short Circuit Grain Boundary and Lattice Diffusion

In the following section, the results of the present experimental work have been compared to the Wagner model for oxidation of binary alloys which form external solid solution scales. It must be emphasized that this was not an attempt to obtain model predictions which exactly matched the experimentally determined composition profiles and scaling rates. Rather, the approach was to try to demonstrate consistency with and/or highlight the differences between the oxidation model and these lower temperature data. Due to the limited thermodynamic and diffusional data available in this temperature range, certain approximations have been made which in any case would make exact correlations of questionable merit. The most that can be expected therefore, is that general trends in the data may emerge which will give additional insight into the oxidation mechanisms at work over the range of conditions examined in these experiments.

An important feature in the Wagner model was that the oxide layer should be single phase, uniform in thickness and free of any defects such as voids, cracks and other internal boundaries. Obviously in the present case, it is reasonable to alter this model to include grain boundaries and allow for transport of reactants within these structures. This type of transport was accounted for in the oxidation of metals by the use of an effective diffusion coefficient, as introduced in Eq.(3-15). The same approach will be used to describe the flux of cations A and B in a polycrystalline oxide. This leads to expressions for the effective diffusion

coefficients of A and B:

$$D_{A,\text{eff}} = (1-\phi)D_A^l + \phi D_A^b \quad (6-1)$$

$$D_{B,\text{eff}} = (1-\phi)D_B^l + \phi D_B^b \quad (6-2)$$

Here,  $\phi$  is the fraction of grain boundary sites, while  $D_A^l$ ,  $D_B^l$ ,  $D_A^b$  and  $D_B^b$  are the lattice and grain boundary diffusion coefficients of A and B in the solid solution scales. In order to treat the problem on a macroscopic scale, the oxide may again be approximated to be a parallel plate of uniform density and thickness. Such an approximation is obviously very crude in view of the complex morphologies observed for the different experimental procedures. It will, however, facilitate the calculations and the consequences of a non-uniform oxide morphology are left for discussion at the end of this section.

Wagner's coupled transport equations describing the growth of a solid solution scale are now modified to include these diffusion coefficients. The first expression which describes the flux of the two cations in the oxide normalized to a fractional thickness,  $y$ , in terms of an effective parabolic rate constant,  $k_{\text{eff}}$ , and the metal gradient in the film,  $\frac{d\xi}{dy}$ , was introduced as Eq.(2-15) and now takes the form

$$D_{A,\text{eff}}(1-\xi) \left[ \frac{-\partial \ln a_{AO}}{\partial \xi} \frac{d\xi}{dy} + \frac{Z_A}{Z_O} \frac{d \ln a_O}{dy} \right] + D_{B,\text{eff}}\xi \left[ \frac{-\partial \ln a_{BO}}{\partial \xi} \frac{d\xi}{dy} + \frac{Z_B}{Z_O} \frac{d \ln a_O}{dy} \right] = k_{\text{eff}} \quad (6-3)$$

In this expression,  $a$  is an activity and  $\xi$  is the mole fraction of BO in the oxide.  $Z_A$ ,  $Z_B$  and  $Z_O$  are the valences of A, B and O, respectively. The second related transport equation (2-16) arising from the consideration of mass balances within the oxide becomes

$$y k_{\text{eff}} \frac{d\xi}{dy} = - \frac{d}{dy} \left[ D_{B,\text{eff}}\xi \left[ \frac{\partial \ln a_{BO}}{\partial \xi} \frac{d\xi}{dy} - \frac{Z_B}{Z_O} \frac{d \ln a_O}{dy} \right] \right] \quad (6-4)$$

These equations may be simplified further by incorporating suitable

approximations for the solution thermodynamics and diffusion coefficients in the solid solution oxide scales. (29-34)

The ideal solution approximation leads to the following relationships between activity and composition in the alloy and oxide:

$$\frac{\partial \ln a_{AO}}{\partial \xi} = -1/(1-\xi) \quad (6-5)$$

$$\text{and } \frac{\partial \ln a_{BO}}{\partial \xi} = 1/\xi \quad (6-6)$$

Furthermore, at the alloy-scale interface

$$N_B' = \frac{\xi'}{\gamma(1-\xi') + \xi'} \quad (6-7)$$

$$\text{and } a_O' = \left[ \frac{1}{\gamma(1-\xi') + \xi'} \right] \exp(\Delta G_{CoO}^0/RT) \quad (6-8)$$

$$\text{where } \gamma = \exp[(\Delta G_{NiO}^0 - \Delta G_{CoO}^0)/RT] \quad (6-9)$$

in these expressions,  $\Delta G_i^0$  is the free energy of formation of pure oxide  $i$  at the temperature of interest.

Cation diffusion coefficients in the oxide will be functions of the total vacancy concentration. These concentrations depend on both the scale composition and anion activity. The combined dependence may be expressed as follows:

$$D_{Ni}^* = D_{Ni}^{*o} \cdot \left[ \frac{[V_M](NiCo)O}{[V_{Ni}]_{NiO}} \right] \quad (6-10)$$

and

$$D_{Co}^* = D_{Co}^{*o} \cdot \left[ \frac{[V_M](NiCo)O}{[V_{Ni}]_{NiO}} \right] \quad (6-11)$$

where  $D_i^{*o}$  and  $[V_{Ni}]_{NiO}$  are respectively the tracer diffusion coefficient (grain boundary or lattice) of element  $i$  and the vacancy mole fraction (at the grain boundary or in the lattice) in NiO at  $p_{O_2} = 1$  atm.  $[V_M](NiCo)O$  is the vacancy concentration in the solid solution at a given temperature, pressure and

composition. The difficulty in the use of equations (6-10) and (6-11) for the grain boundary case arises from the fact that there are no quantitative measurements of the vacancy concentrations near NiO grain boundaries either as a function of temperature, pressure or orientation. As discussed in Chapter 3, high resolution electron microscopy and computer simulations of grain boundaries in NiO have shown that these concentrations are higher than the bulk values, possibly due to intrinsically reduced formation energies or through interactions with solutes segregated near the grain boundaries. A simple approximation for the variation of the grain boundary vacancy concentration is then to assume that under some given conditions of temperature, oxide composition, boundary structure, and oxygen activity, an equilibrium distribution of defects between the grain boundary and the bulk phase exists. The vacancy mole fraction at grain boundaries will thus be proportional to the lattice vacancy concentration for both NiO or the solid solution. The limited data which shows that the cation grain boundary diffusivity in NiO varies with approximately a  $p_{O_2}^{1/6}$  dependence, as is the case for lattice vacancy concentrations, is consistent with this hypothesis. The term in brackets in Equations (6-10) and (6-11) for the grain boundary case will therefore be replaced by the equivalent term for the lattice vacancy concentrations in the diffusion model.

An approximation for the vacancy mole fraction in (NiCo)O solid solutions was given by Wagner<sup>(29)</sup>, based on the observed quasi-exponential decrease of the vacancy concentration with additions of NiO:

$$\log [V_M]_{(NiCo)O} = \log [V_{Ni}]_{NiO} + \xi \log \frac{[V_{Co}]_{CoO}}{[V_{Ni}]_{NiO}} + \log a_O^{1/\nu} \quad (6-12)$$

The various self-diffusion coefficients may then expressed as

$$D_{Co}^1 = D_{Co}^{01} \beta_a^{\xi} 1/\nu \quad (6-13)$$

$$D_{Ni}^1 = D_{Ni}^{01} \beta_a^{\xi} 1/\nu \quad (6-14)$$

$$D_{\text{Co}}^b \delta = D_{\text{Co}}^{ob} \delta \beta^{\xi} a_{\text{O}}^{1/\nu} \quad (6-15)$$

and

$$D_{\text{Ni}}^b \delta = D_{\text{Ni}}^{ob} \delta \beta^{\xi} a_{\text{O}}^{1/\nu} \quad (6-16)$$

where  $\beta = [V_{\text{Co}}]_{\text{CoO}}/[V_{\text{Ni}}]_{\text{NiO}}$ . The oxygen activity dependence arises from the vacancy formation reactions similar to those which were introduced in section 3.4.1 for NiO. The term  $\nu$  is derived from the pressure dependence for the formation of the predominating vacancy species. If the predominant excess relative charge on cation vacancies is +2, then  $\nu = 3$ , while for a charge of +1,  $\nu = 2$ . A value of  $\nu = 3$  was used in the numerical calculations, based on the observed pressure dependence of the cation grain boundary diffusion coefficients and parabolic rate constants for NiO in previous investigations<sup>(61,74)</sup>. When incorporated into Eqs.(6-1) and (6-2), the effective diffusion coefficients for nickel and cobalt then become

$$D_{\text{Ni,eff}} = \{(1-\phi)D_{\text{Ni}}^{ol} + \phi D_{\text{Ni}}^{ob}\} \beta^{\xi} a_{\text{O}}^{1/\nu} \quad (6-17)$$

and

$$D_{\text{Co,eff}} = \{(1-\phi)D_{\text{Co}}^{ol} + \phi D_{\text{Co}}^{ob}\} \beta^{\xi} a_{\text{O}}^{1/\nu} \quad (6-18)$$

In these final expressions, the grain boundary terms were divided by an assumed value of  $\delta$  (10 Å was used in the numerical calculations).

Equations (6-3) and (6-4) are then simplified by introducing (6-5), (6-6), (6-17) and (6-18) to give the following coupled differential equations:

$$[p-(p-1)\xi] \frac{d \ln a_{\text{O}}}{dy} = \frac{k_{\text{eff}}^*}{\beta^{\xi} a_{\text{O}}^{1/\nu}} - (p-1) \frac{d\xi}{dy} \quad (6-19)$$

and

$$[p-(p-1)\xi] \frac{d^2 \xi}{dy^2} + [(1-1/\nu)(p-1) + \{p-(p-1)\xi\} \ln \beta] \left[ \frac{d\xi}{dy} \right]^2 - \frac{k_{\text{eff}}^*}{\beta^{\xi} a_{\text{O}}^{1/\nu}} \left\{ (1-1/\nu) - \frac{y[p-(p-1)\xi]^2}{p} \right\} \frac{d\xi}{dy} = 0 \quad (6-20)$$

where  $k_{\text{eff}}^*$  is equal to  $k_{\text{eff}}$  divided by the term in brackets in Eq.(6-18). In this notation,  $p$  is the ratio of diffusion coefficients,  $D_{\text{Ni,eff}}/D_{\text{Co,eff}}$ . Boundary conditions required for the solution of these two equations are the same as those used in earlier solutions<sup>(29-34)</sup>: one uses the average content of B in the film,  $\xi_{\text{av}}$ , the gas phase oxygen activity,  $a_{\text{O}}''$ , a relationship between the composition of the film at the alloy-oxide interface,  $\xi'$ , and the corresponding oxygen activity for the alloy-oxide equilibrium. The latter relationship is provided by equations (6-8) and (6-9).

In section 2.3.5 it was shown that  $\xi_{\text{av}}$  may be regarded as being equal to the bulk alloy composition,  $N_{\text{B}}^{\text{O}}$  under the assumption that diffusion in the alloy is much slower than in the oxide. If diffusion in the alloy is not insignificant, then an overall enrichment of the more stable oxide component, CoO, is expected to occur, so that  $\xi_{\text{av}} > N_{\text{B}}^{\text{O}}$ . The Auger profiles reported in the previous section indicate that the latter relationship generally holds true for the experimental conditions tested in this investigation. This finding is significant, since all previous high temperature work on the oxidation of Ni-Co alloys has shown that diffusion in the alloy was negligible compared with transport rates in the oxide layer;  $\xi_{\text{av}} = N_{\text{B}}^{\text{O}}$ . The average composition data obtained from the Auger profiles and experimental parabolic scaling rates have therefore been used in the Wagner analysis to estimate the alloy interdiffusion coefficients.

Equation (2-5) gives a relationship between  $\xi_{\text{av}}$ ,  $\xi'$ ,  $N_{\text{B}}^{\text{O}}$  and  $F(\varphi)$ . Recall that the function  $F(\varphi)$  is a parameter in the solution of the equation for diffusion in the alloy phase (2-17), where  $\varphi = (\alpha/2\bar{D}_{\text{all}})^{1/2}$ . To obtain an estimate of  $\bar{D}_{\text{all}}$ , experimental values of  $\xi_{\text{av}}$  and  $\xi'$  were determined from the Auger composition profiles. In each profile, the position of the alloy-oxide interface was estimated to be the sputter depth at which the O KLL differential peak-to-peak height

Table (6-3)  
 Calculated values of  $\bar{D}_{all}^{(a)}$  and  $\rho$  based on analysis of experimental composition profiles  
 in (NiCo)O films. See text for a description of the calculations.

T, K	$\xi_{av}$	$\xi$	$N_B'$	$F(\varphi)$	$\varphi$	$\frac{k_{eff}}{\bar{D}_{all}}$	$\bar{D}_{all}$	$\bar{D}_{all}^{-1}$ (42) <sup>(b)</sup>	$D_{Ni,dial}$ (141)	$\phi$	$\rho(\text{cm}^{-2})^{(c)}$
(110) Ni-3.86Co, furnace-raised											
673	0.083	0.054	0.025	0.231	0.16	0.15	$3.7 \times 10^{-15}$	$3.3 \times 10^{-21}$	$2.2 \times 10^{-11}$	$1.7 \times 10^{-4}$	$1.7 \times 10^{11}$
773	0.106	0.067	0.028	0.136	0.08	0.04	$1.2 \times 10^{-14}$	$1.4 \times 10^{-18}$	$7.9 \times 10^{-10}$	$1.5 \times 10^{-5}$	$1.5 \times 10^{10}$
773	0.076	0.048	0.020	0.338	0.24	0.34	$4.0 \times 10^{-14}$			$5.0 \times 10^{-6}$	$5.0 \times 10^{10}$
873	0.109	0.053	0.020	0.211	0.14	0.11	$8.9 \times 10^{-14}$	$1.5 \times 10^{-16}$	$1.22 \times 10^{-8}$	$7.3 \times 10^{-6}$	$7.3 \times 10^9$
973	0.119	0.041	0.014	0.233	0.16	0.15	$5.4 \times 10^{-14}$	$5.9 \times 10^{-15}$	$1.1 \times 10^{-7}$	$4.5 \times 10^{-7}$	$4.5 \times 10^8$
1073	0.112	0.047	0.015	0.243	0.16	0.15	$3.6 \times 10^{-13}$	$1.2 \times 10^{-13}$	$6.4 \times 10^{-7}$	$3.8 \times 10^{-7}$	$3.8 \times 10^8$
Ni-4.0Co polycrystalline alloy, furnace-raised											
773	0.094	0.076	0.032	0.133	0.08	0.04	$1.8 \times 10^{-13}$			$2.3 \times 10^{-4}$	$2.3 \times 10^{11}$
873	0.087	0.057	0.021	0.243	0.16	0.15	$6.6 \times 10^{-13}$			$5.4 \times 10^{-5}$	$5.4 \times 10^{10}$
1073	0.091	0.050	0.016	0.320	0.23	0.31	$5.5 \times 10^{-13}$			$6.8 \times 10^{-7}$	$6.8 \times 10^8$

Notes: (a) all D values are in units of  $\text{cm}^2/\text{sec}$ . (b)  $\bar{D}_{all}^{-1} = X_{Ni} D_{Co} + X_{Co} D_{Ni}$  where  $D_{Co}$  and  $D_{Ni}$  are the self diffusion coefficients for a Ni-4.3Co alloy. (c) assuming  $10^{15}$  atom sites/ $\text{cm}^2$

decreased to a value midway between its maximum and minimum levels. The values of  $\xi_{2v}$  obtained in this way are given in the second column of Table (6-3). The third column lists values of  $\xi'$ . This data was used to calculate  $N_B'$  from equations (6-7) and (6-9). Finally,  $F(\varphi)$  was determined from equation (2-35). Function  $F(\varphi)$  was also defined in equation (2-31). Values of  $F(\varphi)$  from (2-31) were thus compared with those generated in Table (6-3), to obtain  $\varphi$  corresponding to the experimental  $F(\varphi)$ . These appear in column six of Table (6-3). The final experimental values of  $k_p$  have been used in the relationship  $\alpha = k_p (V_{\text{all}}/V_{\text{ox}})^{1/2}$ , where  $V_{\text{all}}$  and  $V_{\text{ox}}$  are the molar volumes of the alloy and oxide, respectively. Approximate values of 6.6 and 11.3 cm<sup>3</sup>/mol were obtained from a linear interpolation of the pure metal and oxide data at 4% Co. This leads finally to the values of  $\bar{D}_{\text{all}}$  listed in column eight of Table (6-3).

The experimentally derived data for  $\bar{D}_{\text{all}}$  are to be compared with the literature data shown in Table (6-3). It may be seen that the present values deviate from the reported lattice data for a Ni-4.3Co alloy by up to six orders of magnitude at 673 K. This difference is reduced as the temperature increases, up to approximately 1073 K where there is no significant variation.

Such large discrepancies may have been due to the presence of a significant concentration of short circuit diffusion paths, in the form of dislocations, beneath the growing oxide layers. The presence of these defects could have contributed to an overall enhancement of the alloy interdiffusion coefficient. Data for the diffusion of nickel along dislocation pipes in nickel crystals have been reported<sup>(141)</sup>, and are also shown in Table (6-3). The values in column eight are seen to be lower than the data for dislocation pipe diffusion, which suggests that a combination of lattice

and dislocation diffusion in the alloy could account for the present results. By using the expression for an effective diffusion coefficient which was given in equation (3-15), the fractional number of short circuit diffusion sites per unit area may be derived, which in this case is related to the dislocation density. This has been done, with the data appearing in the final two columns of Table (6-3).

It may be seen from this analysis that dislocation densities of between  $10^{11}$   $\text{cm}^{-2}$  at 673 K and  $10^8$   $\text{cm}^{-2}$  at 1073 K are obtained. A typical dislocation density in a well annealed nickel single crystal is of the order of  $10^8$   $\text{cm}^{-2}$ . It therefore appears that the presence of the growing oxide layer in these experiments resulted in an increase in the dislocation density, possibly in a localized zone, beneath the oxide films. Such an effect has recently been proposed by Pieraggi and Rapp<sup>(149)</sup> to account for stress generation and vacancy annihilation in oxide scales growing by cation-vacancy diffusion. These authors note that even in polycrystalline oxide layers, the innermost grains of the scale, which are in contact with the underlying alloy, maintain close epitaxial relationships with the alloy substrate. They have therefore proposed a model describing the metal-scale interface in terms of an arrangement of misfit dislocations. Vacancy annihilation is presumed to occur by climb of a certain fraction of these dislocations into the metal, which generates elastic compression in the scale and tension in the metal. When the stresses are of sufficient magnitude, it is postulated that they are accommodated by plastic deformation on both sides of the interface due to dislocation glide, which resupplies dislocations at the interface.

Further analysis of the experimental results by the modified Wagner model has been made examining parabolic rate constants and cation concentration profiles. A first estimate of the parabolic rate constant may be obtained from equation (6-19)

by taking  $d\xi/dy=0$  at  $y=0$  and approximating  $\xi$ ,  $\nu$  and  $p$  to be average values  $\xi_{av}$ ,  $\nu_{av}$  and  $p_{av}$ . Upon integration and incorporation of the above approximations

$$k_{est}^* = \nu_{av} \beta \xi_{av} \left\{ p_{av} + (1-p_{av}) \xi_{av} \right\} \left\{ (a_O'')^{1/\nu_{av}} - (a_O')^{1/\nu_{av}} \right\} \quad (6-21)$$

Here, superscript prime and double-prime refer to the alloy-oxide and oxide-gas interfaces, respectively. In order to make comparisons between equation (6-21) and the measured values of  $k_{p,eff}$  the Auger profile data were again used as inputs of  $\xi_{av}$ . Furthermore, the value of  $a_O''$  was known from the experimental test condition, while  $a_O'$  was determined using equations (6-8) and (6-9). The value of  $p_{av}$  was shown to be less than unity in the present study, based on the fact that cobalt is always enriched near the outer oxide surface. This was also the case in tracer diffusion measurements of Co and Ni in NiO and (NiCo)O solid solutions<sup>(102,103)</sup>, where  $0.2 < p < 0.33$ . For grain boundary diffusion in NiO,  $p \approx 0.33$ <sup>(105)</sup>.  $\nu_{av}$  was not determined in the present experiments, however, as indicated in Chapter 3, previous oxidation and tracer diffusion measurements on NiO have shown that to a first approximation,  $\nu \approx 3$  for grain boundary as well as lattice diffusion.

Finally, the parameter  $\beta$  has not been determined for the case of grain boundaries or lattice point defects over the present range of temperatures. At 1273 K the value of  $\beta$  is approximately 125<sup>(150,151)</sup>. In order to obtain an order of magnitude estimate of  $\beta$  at these lower temperatures, a combination of both experimental and independently determined diffusion data were again used. In the case of the Ni-4.0Co polycrystalline alloys, the uniform distribution of randomly oriented oxide boundaries was expected to most closely correspond to the tracer diffusion data which have been reported for Ni and Co in NiO. Thus, these diffusion

data have been used, along with the measured average oxide grain sizes and parabolic rate constants to calculate values of  $k_{p,eff}^*$ . At the same time, equation (6-21) was used with the above parameters of  $\xi_{av}$ ,  $\nu_{av}$  and  $p_{av}$  to generate  $k_{p,eff}^*$  values for different  $\beta$ . These data are listed in Table (6-4), and indicate that  $\beta$  may vary over a range from approximately one to ten.

The calculation of cation profiles in the solid solution oxide scales involved the simultaneous solution of equations (6-19) and (6-20). This procedure was accomplished in the present work using a numerical relaxation method. Equations (6-19) and (6-20) were reduced to a set of three first order differential equations and further written in finite difference form. Starting with an initial guess of the profile shape between specified boundary conditions, the trial solution was iteratively improved using a Newton-Raphson method, until a final solution was obtained, based on specified error criteria. Fortran subroutines for the relaxation technique were obtained from a standard text<sup>(152)</sup>.

The fixed boundary conditions used to calculate the profiles were the two interfacial oxygen activity values, and the value of  $\xi$ . The latter parameter was derived in each case from the experimentally determined values of  $\xi_{av}$ , obtained from the Auger analysis, along with equation (2-23). For each profile calculation fixed values of  $\beta = 10$  and  $\nu = 3$  were used. A trial solution was established on a mesh of 51 points in  $y$  space, which corresponds to the normalized distance inside the oxide layer. Calculations were started by using an estimated value of  $k_{p,eff}^*$  from equation (6-21). Iterations on the trial solution proceeded until the corrections at each mesh point became vanishingly small. The measure for the size of the corrections at which this condition was met was an average error, summed over all mesh points, weighted by a scale factor typical of the size of each type of variable. The correctness of the final solution was checked by comparing the

Table (6-4)  
 An evaluation of the parameter  $\beta$  for polycrystalline (NiCo)O oxides based on a comparison of experimental and calculated  $k_{p,eff}$  values. See text for a discussion of the calculation.

T, K	$k_{p,eff}$ (a) (cm <sup>2</sup> /sec)	Avg.oxide dia.(Å)	$\{(1-\phi)D_{Co}^{o1} + \phi D_{Co}^{ob}\}$ (cm <sup>2</sup> /sec)	$k_{p,eff}^*$ (expt.)	$k_{p,eff}$ from Eq.(6-21)
773	$7.4 \times 10^{-15}$	236	$5 \times 10^{-13}$	0.015	0.161
873	$9.8 \times 10^{-14}$	1005	$9 \times 10^{-13}$	0.109	0.162
1073	$1.7 \times 10^{-13}$	6467	$3 \times 10^{-12}$	0.057	0.159
				0.1	1.0
					3
					10
					100
					$2.0 \times 10^{-2}$
					$2.0 \times 10^{-2}$
					$1.9 \times 10^{-2}$
					$2.4 \times 10^{-3}$

Notes: (a) final experimental values:  $k_p$  (gO<sup>2</sup>/cm sec)<sup>4</sup>  $\approx 4.07 \times 10^{-4}$  (cm<sup>2</sup>/sec) for a Ni-4Co alloy.

average concentration of CoO in the oxide with the experimental value of  $\xi_{av}$ . The solution was accepted as being correct when the difference between the profile and experimental values obeyed the criteria

$$|[\xi_{av}(\text{calculated}) - \xi_{av}(\text{experimental})] / \xi_{av}(\text{calculated})| \leq 0.2$$

If this final criteria was not met, the trial value of  $k_{p,eff}^*$  was adjusted by a small increment and the iteration continued by varying  $k_{p,eff}^*$  until the final average composition of the oxide was within the designated limit.

The calculated parabolic constants and composition profiles are shown in Figures (6-15) to (6-16) along with the experimental data determined by Auger analysis. Several values of  $p$  ranging from between 0.2 and 1.0 were evaluated for each set of data, in order to indicate the effect that this value has on the cation profile shape.

A comparison of the profiles for the single crystal and polycrystalline alloys revealed some interesting differences. The profiles in Figure (6-15) were obtained from the oxide films on (110) Ni-3.86Co exposed by the furnace-raised technique. TEM analysis revealed that certain of these films displayed very thin, highly oriented and compact oxide layers. These correspond to profiles (c,d,e and f) of Figure (6-15). These experimental profiles showed the greatest variation in CoO mole fraction from the inner to the outer oxide surfaces.  $p$  values of between 0.2 and 0.5 appeared to account for the spread in experimental values for these specimens. In addition, the shape of the experimental profiles was matched reasonably well by the calculated curves.

The former profiles were compared to the data for the more polycrystalline oxides on (110) Ni-3.86Co, Figure (6-15) (a,b) and polycrystalline Ni-4.0Co,

Figure (6-15)

Calculated and experimental oxide composition profiles of specimens oxidized by the furnace-raised technique at  $5 \times 10^{-3}$  Torr. (a) 673 K, 24 hr.,  $14.0 \mu\text{g O}_2/\text{cm}^2$ , (b) 773 K, 4 hr.,  $29.0 \mu\text{g O}_2/\text{cm}^2$ , (c) 773 K, 72 hr.,  $27.9 \mu\text{g O}_2/\text{cm}^2$ , (d) 873 K, 44.5 hr.,  $76.2 \mu\text{g O}_2/\text{cm}^2$ , (e) 973 K, 49.4 hr.,  $81.5 \mu\text{g O}_2/\text{cm}^2$ , (f) 1073 K, 6.1 hr.,  $83.4 \mu\text{g O}_2/\text{cm}^2$ . Several values of the parameter  $p$  were evaluated in the calculations and are indicated on the curves.

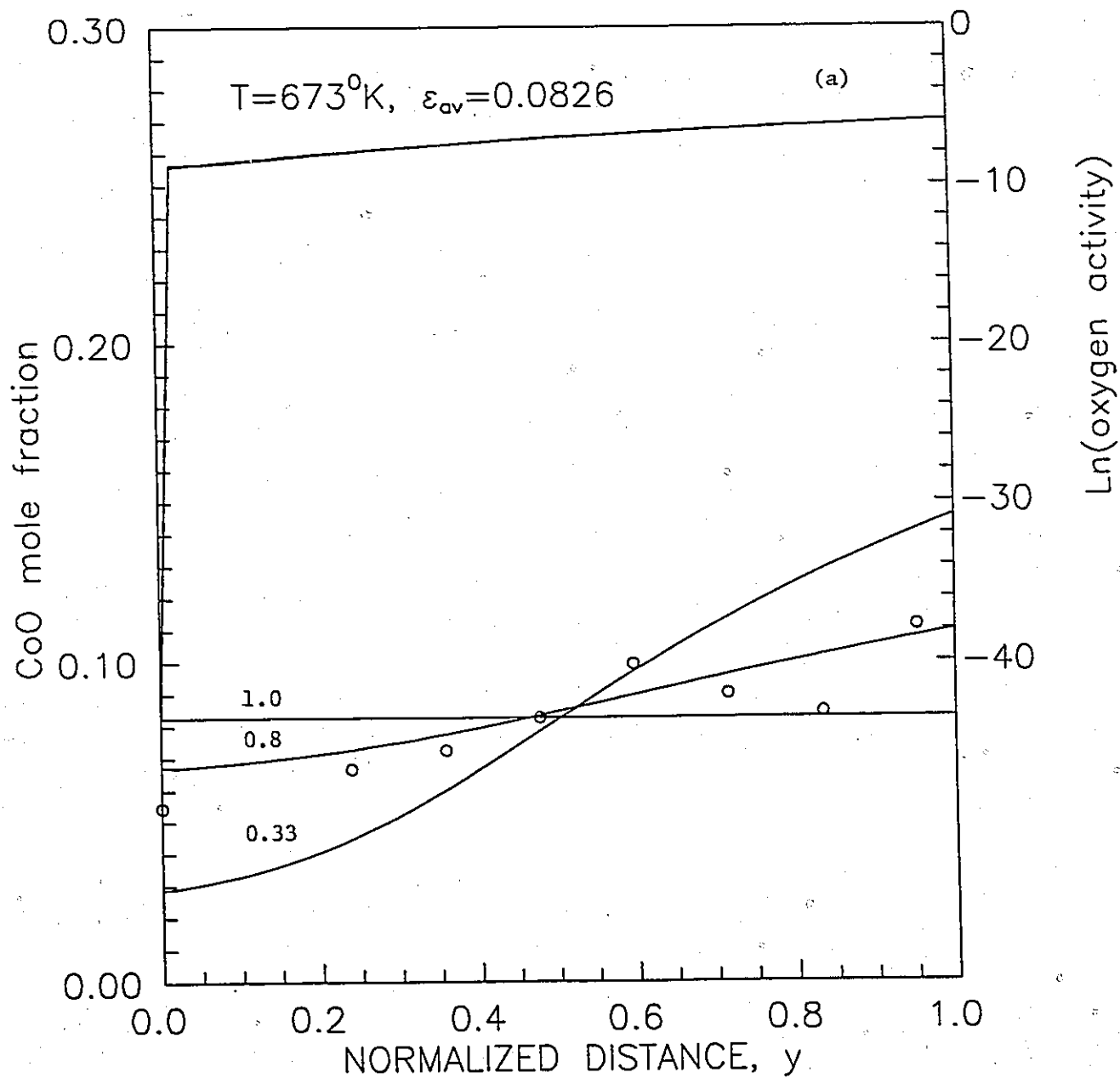


Fig. (6-15)

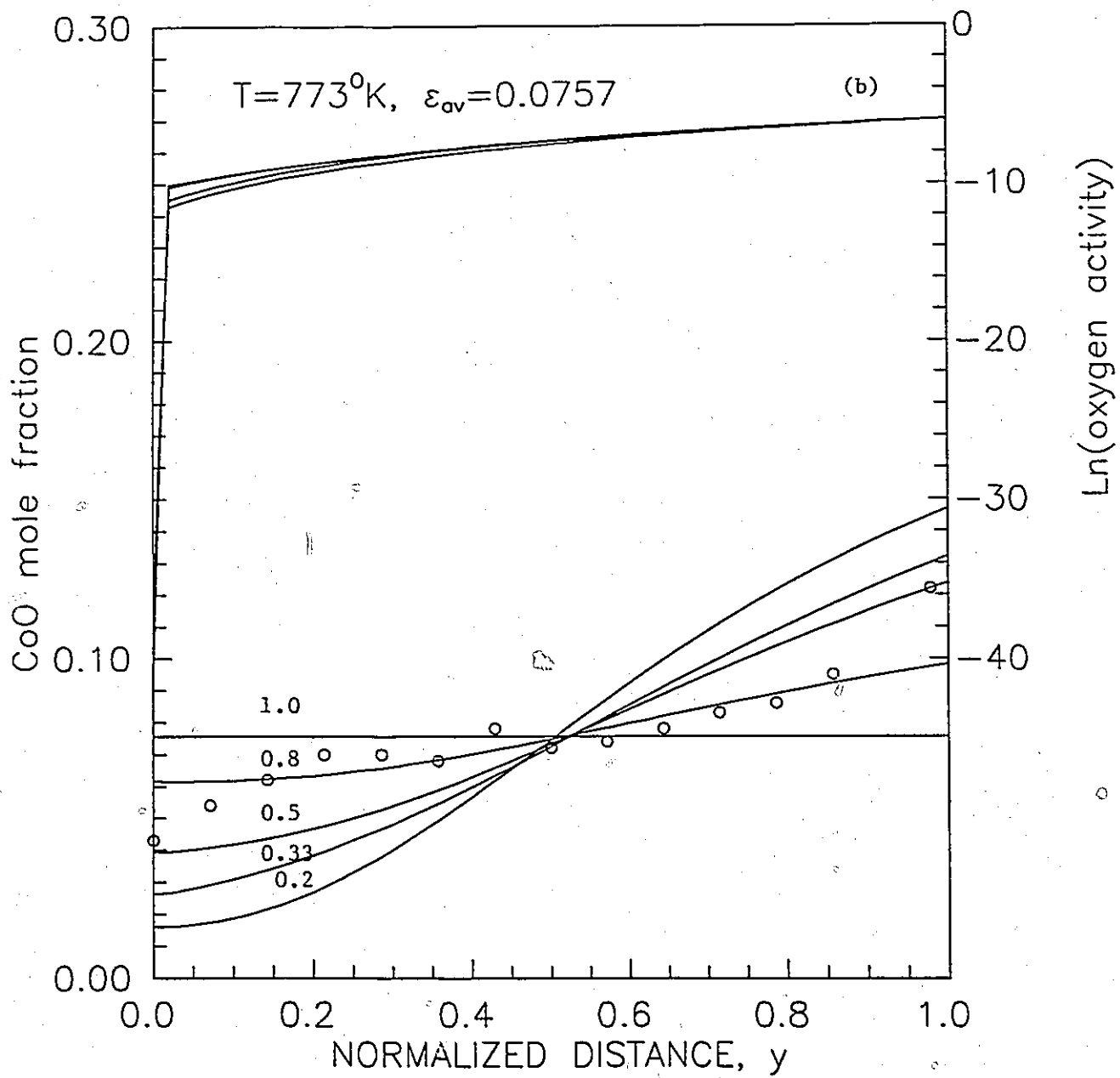


Fig. (6-15)

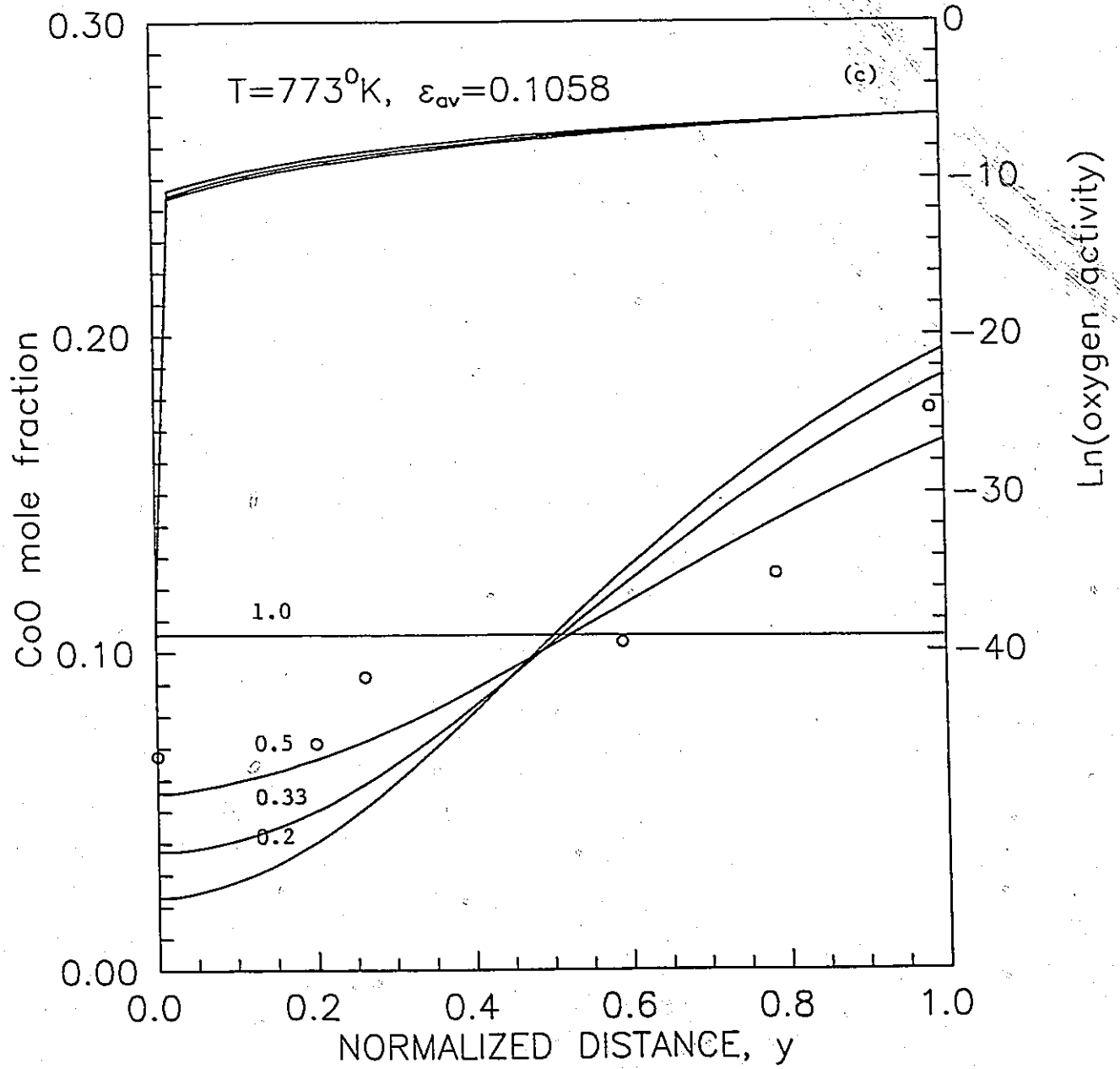


Fig. (6-15)

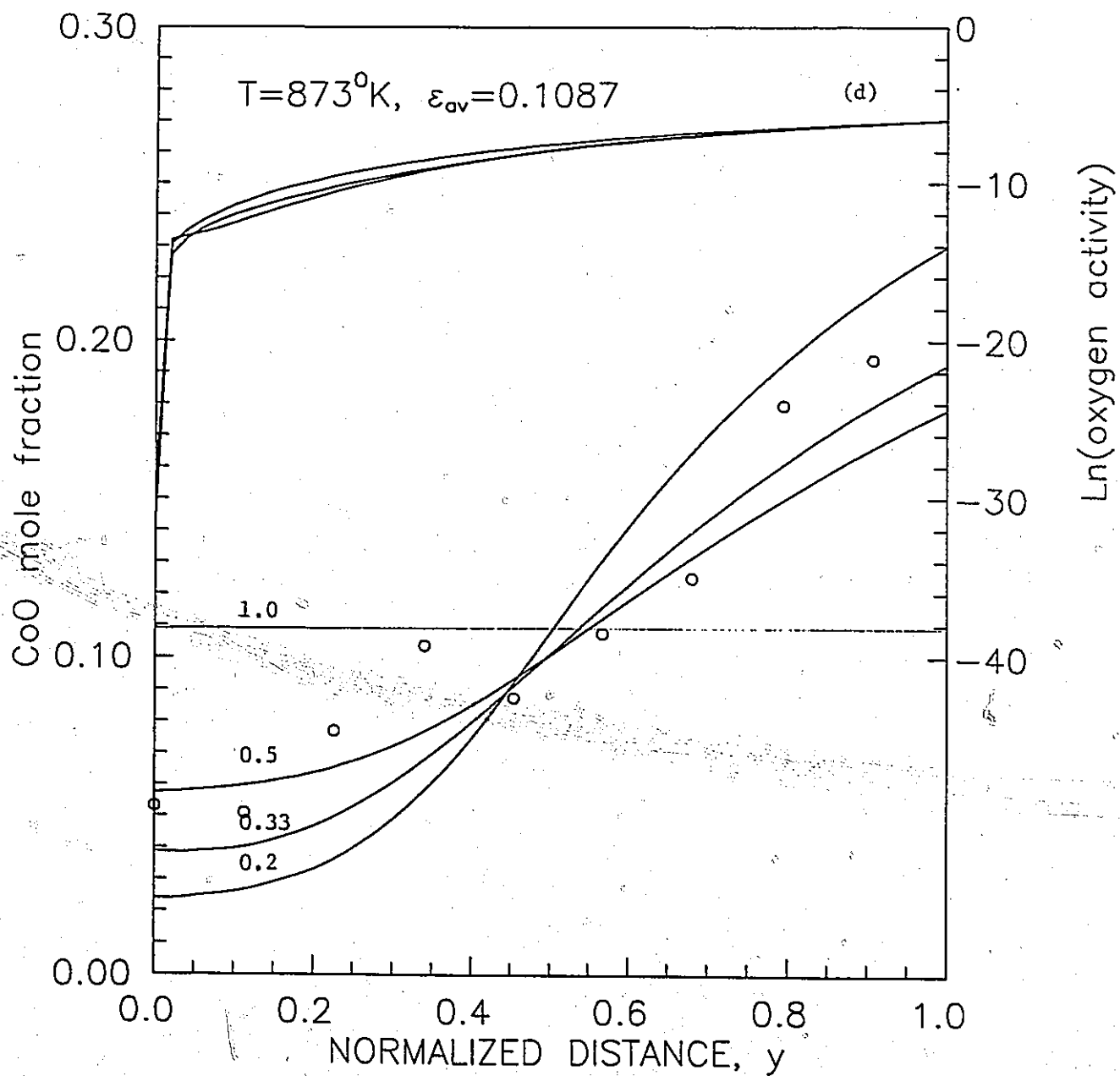


Fig. (6-15)

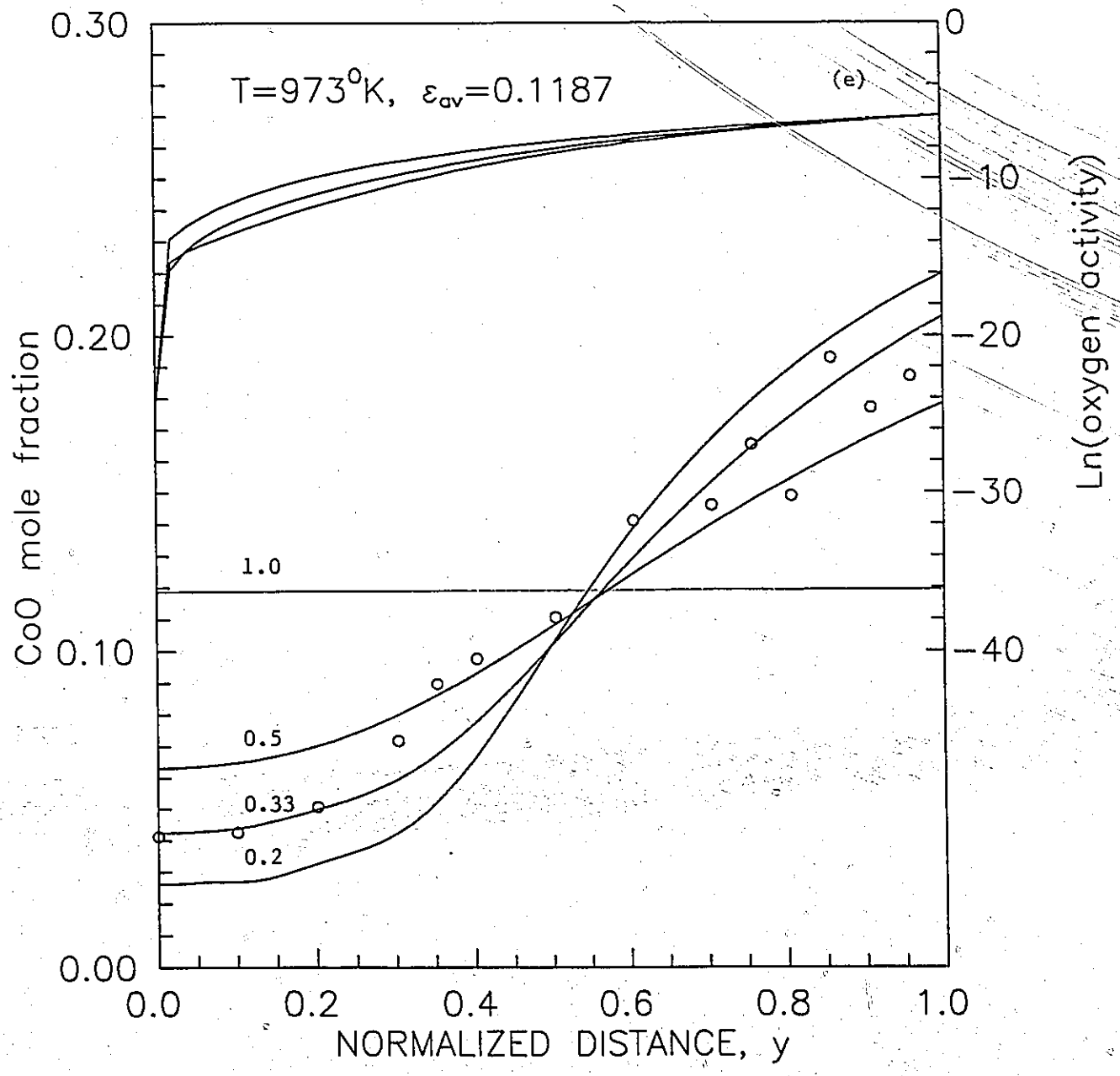


Fig. (6-15)

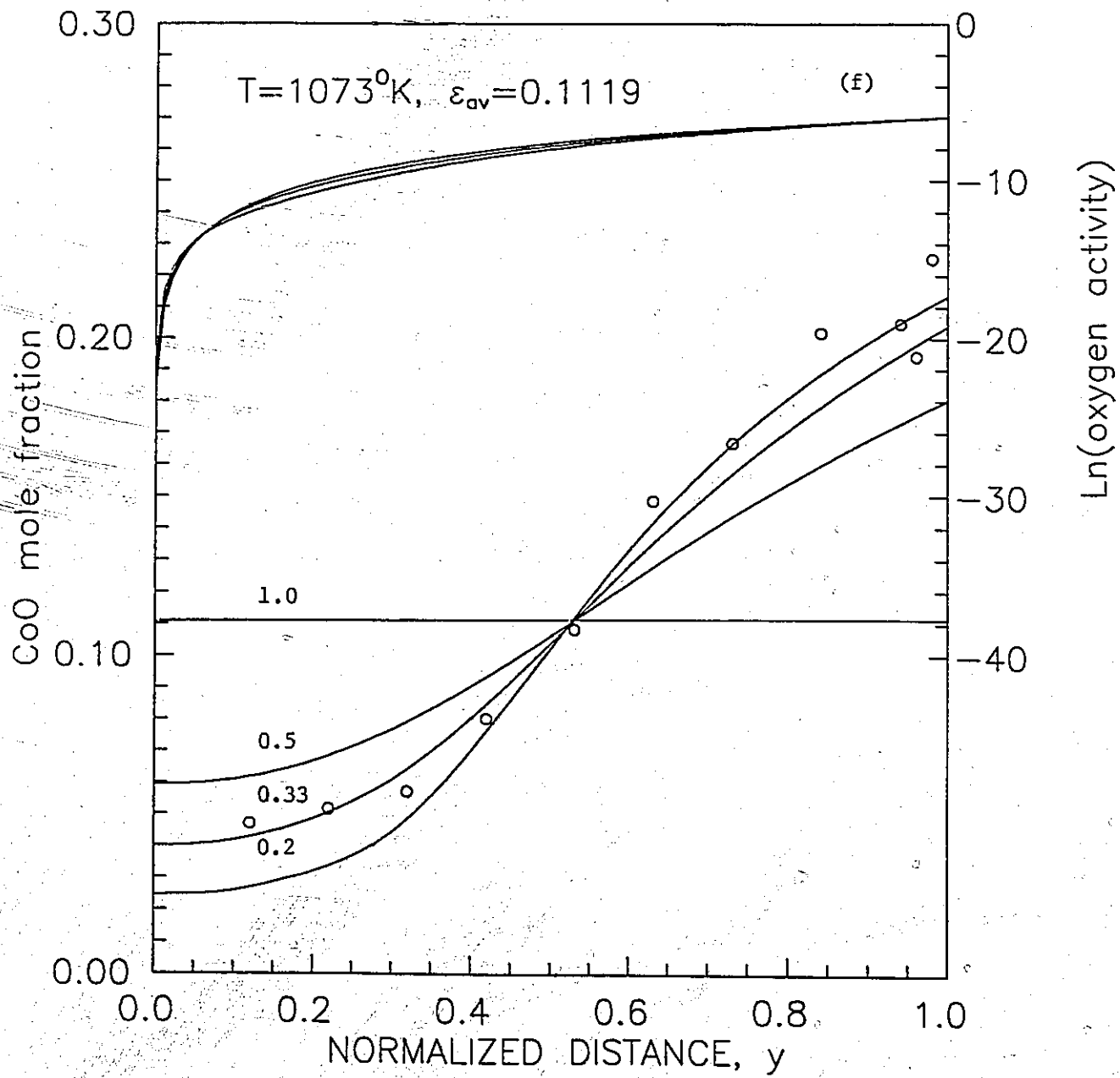


Fig. (6-15)

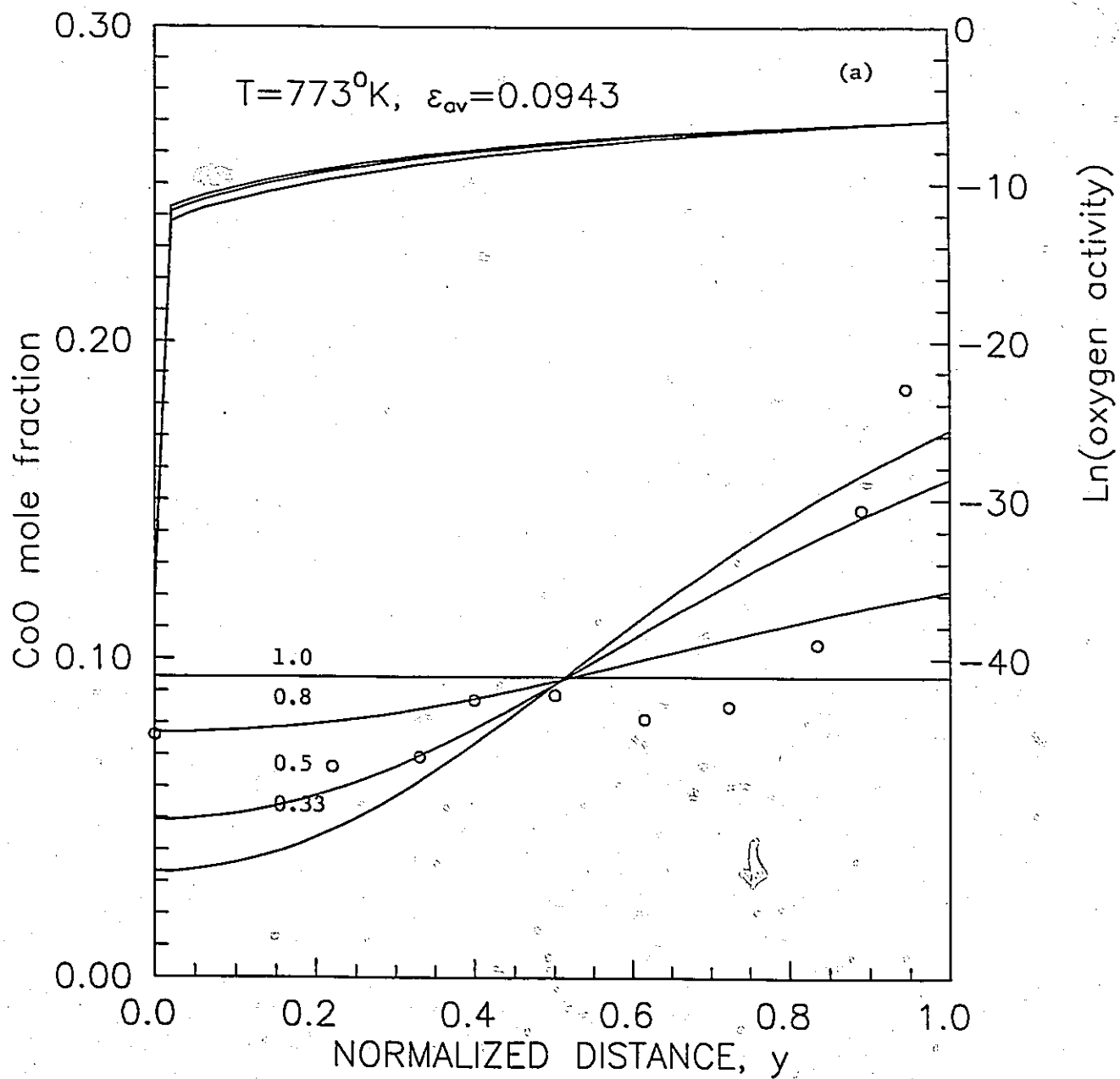


Fig. (6-16)

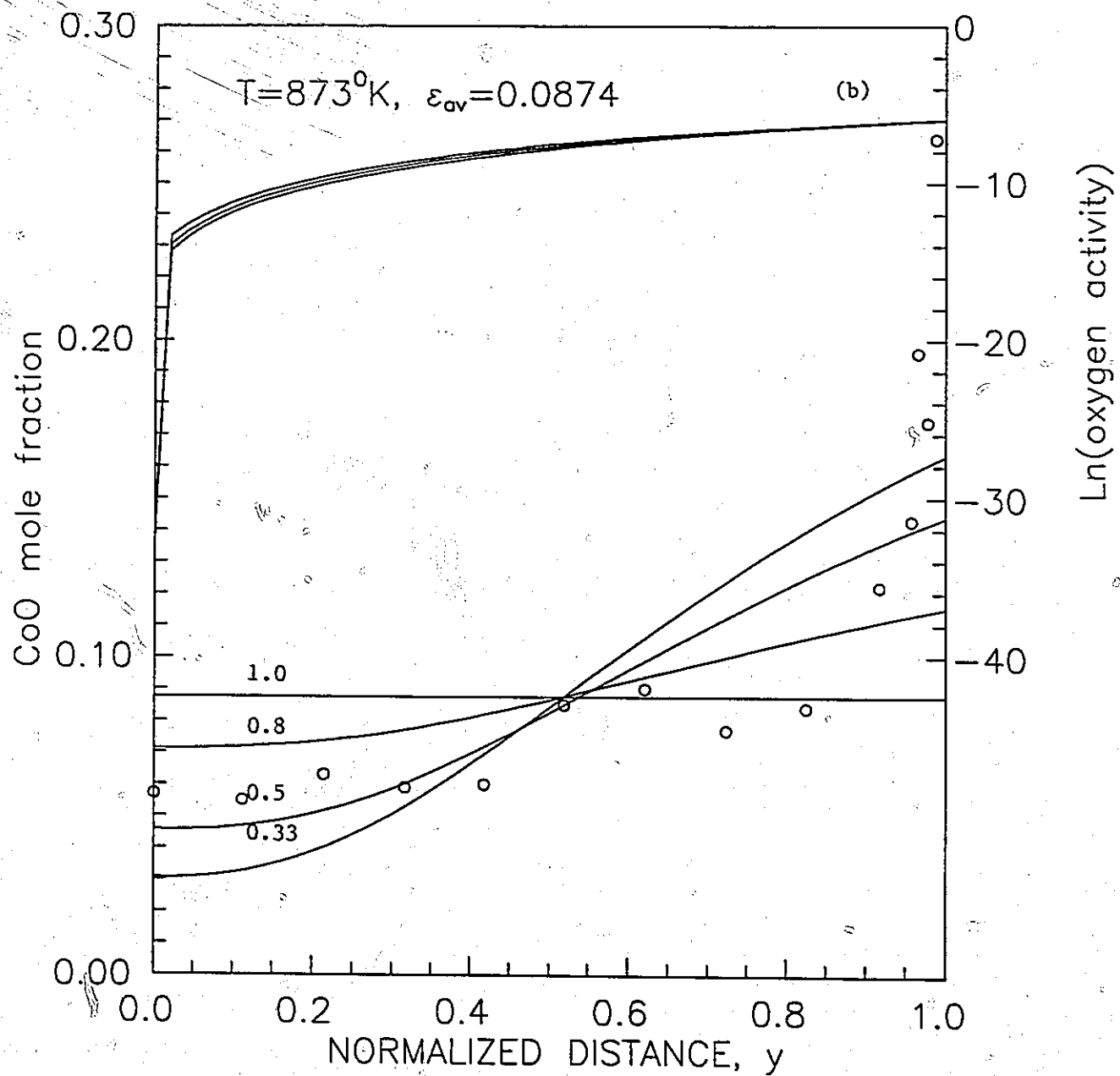


Fig. (6-16)

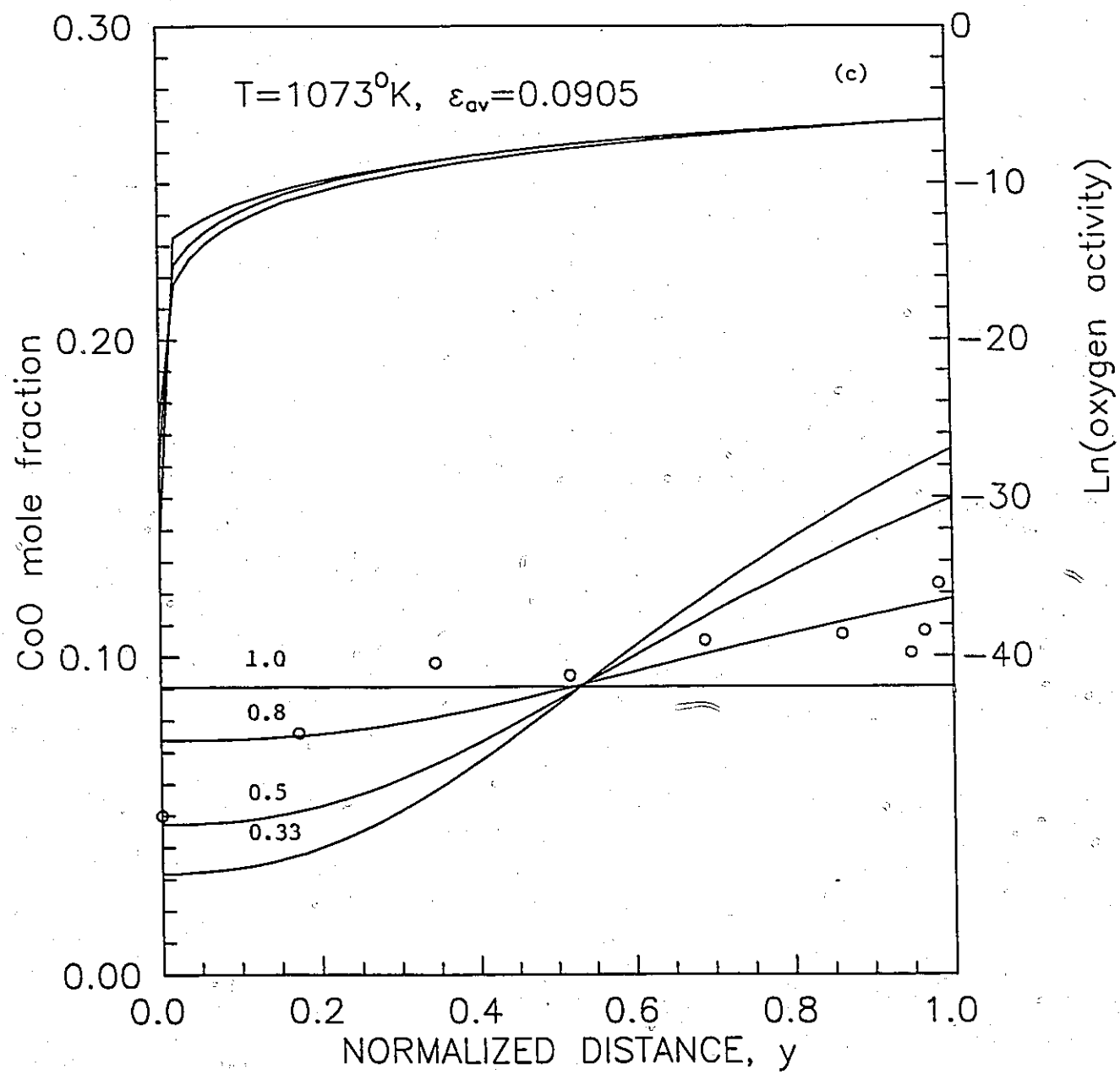


Fig. (6-16)

Figure (6-16). In these examples, the experimental profiles were relatively flat, except near the the outer oxide surface of the polycrystalline Ni-4.0Co samples oxidized at 773 and 873 K.  $p$  values of between 0.5 and 1.0 resulted in calculated profiles which gave a reasonable approximation to the experimental data over most of the oxide thickness. The shapes of the experimental profiles, however, were never as closely followed as for the thin compact films discussed above.

The relative transport rates of nickel and cobalt were therefore seen to depend on the structures formed during growth of these oxides. The high degree of disorder in the random boundaries which were associated with the faster growing polycrystalline oxide films appeared to reduce the difference in transport rates for nickel and cobalt cations in (NiCo)O. Conversely, films which were composed of mainly mosaic structures, having highly oriented adjacent blocks, maintained a higher level of discrimination between cobalt and nickel cations for specific jump sequences.

The experimental values of  $k_{p,eff}^*$  were divided by the the final  $k_{p,eff}^*$  values obtained from the profile calculations in order to estimate the effective diffusion coefficients for cobalt and nickel in the oxide films. The values for cobalt are shown in Figure (6-17) and were calculated using the parameters  $\beta=10$ ,  $\nu=3$  and  $p=.33$ . Also shown for comparison are lattice and grain boundary diffusivities of cobalt in NiO obtained from the Arrhenius expressions reviewed in Chapter 3. All of the experimentally derived diffusion coefficients were higher than those expected solely on the basis of lattice transport, but less than the values for purely grain boundary diffusion. At 673 K the experimental value of  $D_{Co,eff}$  was approximately six orders of magnitude higher than the lattice diffusion rate. This difference was reduced to approximately one order of magnitude at a temperature of 1073 K. It was also

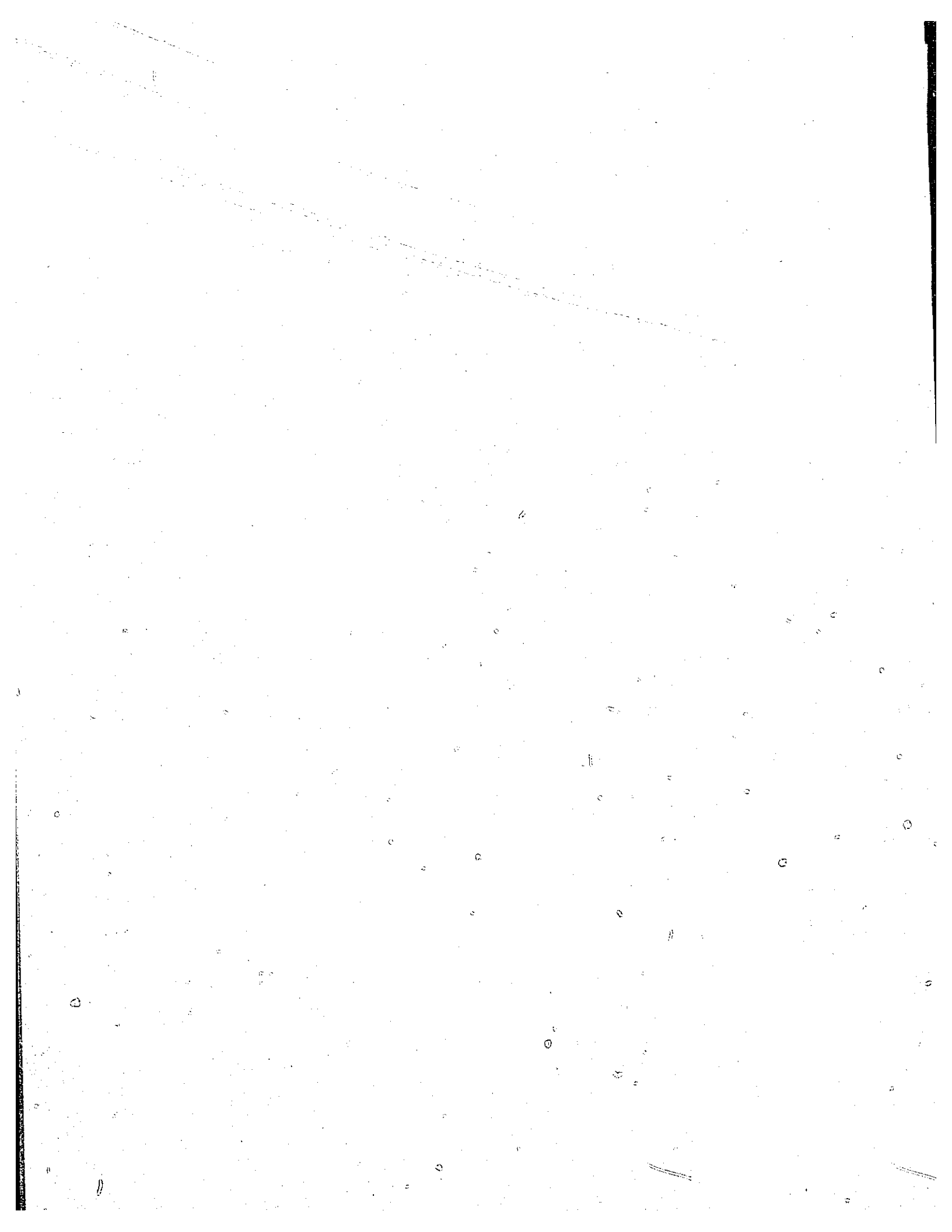


Figure (6-17)

Values of  $D_{\text{Co,eff}}$  derived from the experimental  $k_{\text{p,eff}}$  and calculated  $k_{\text{p,eff}}^*$  data, normalized to pure NiO at one atmosphere oxygen pressure. Open circles represent polycrystalline Ni-4.0Co alloys, while triangles correspond to (110) Ni-3.86Co furnace-raised specimens. For comparison, the literature data for lattice (extrapolated, solid line) and grain boundary (dashed line) diffusion of cobalt in NiO are indicated.

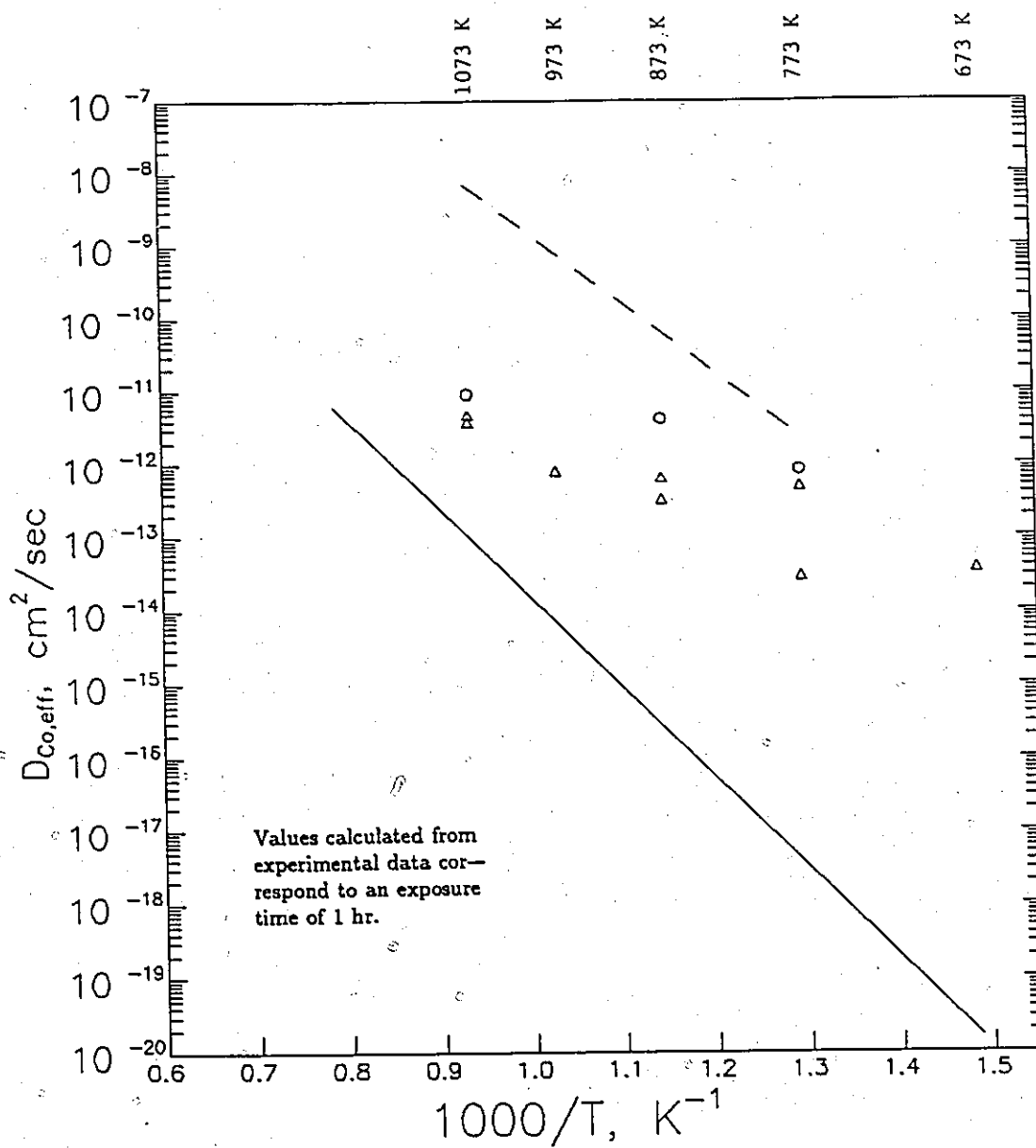


Fig. (6-17)

observed that the oxides which possessed the greatest amounts of polycrystalline oxide had correspondingly higher values of  $D_{Co,eff}$ . This observation supports the argument that the types of boundaries which are formed during oxidation are most influential in determining the rate of scale growth.

The Wagner model for solid solution scale growth on a binary alloy is therefore seen to have limited application to the formation of oxide scales at intermediate temperatures. Over the range of conditions examined in this investigation, short circuit diffusion of reactants along internal boundaries in the oxide has been shown to have a significant effect on scale growth kinetics.

The model does not appear to be adequate in those cases where there was significant variation in the types of boundaries which formed on a single sample. In such cases, differing rates of transport in different boundary structures led to the formation of the oxide layers which were non-uniform in thickness and morphology. The overall growth rates depended on the relative amounts of the various boundaries present in each case.

Furthermore, the relative rates of transport of cobalt and nickel appeared to be dependent on boundary structure. In very compact oxide layers which displayed a high degree of epitaxy with the alloy substrate, the boundaries between adjacent crystal blocks showed the same tendency for the enhanced diffusion of cobalt as has been demonstrated in the high temperature oxidation of Ni-Co alloys.  $p$  values in the range 0.2 to 0.5 resulted in profiles similar to the ones obtained experimentally. In very disordered or random boundaries, the rates of nickel and cobalt diffusion were found to be almost equal. Very flat experimental profiles corresponded to  $p$  values in the range 0.5 to 1.0 and in general, the profile shapes were not accurately reproduced in the calculated curves.

In every experiment, there was an overall enrichment of CoO, the less noble alloying element, in the oxide scale. The Wagner model was used to interpret this phenomenon in terms of enhanced transport in the alloy substrate. Order of magnitude calculations gave predicted dislocation densities in the alloy phase beneath the growing oxide which were consistent with observations and models of the interfacial structure of cation diffusing scales.

## CHAPTER 7

### CONCLUSIONS

#### 7.1 Surface segregation on Co-Rh Alloys

1. Preferential sputtering of cobalt occurred on five Co-Rh alloys ranging in composition from 19.3 to 84.7 at% Rh when irradiated by 4 KeV Ar<sup>+</sup> ions. The enhanced removal of Co by this process is due to the weaker binding energy and smaller mass of Co relative to Rh.
2. Surface segregation measurements were completed for three Co-Rh alloys (19.3, 47.8 and 84.7 at% Rh) in the temperature range 623 to 1123 K under ultra-high vacuum conditions. A 5 to 10 percent increase in the rhodium surface concentration relative to that of the bulk was found for the 19.3Rh alloy, while a 10 to 20 percent increase in cobalt concentration was measured on the 84.7Rh alloy. No conclusive segregation of either component was found on the 47.8Rh alloy.
3. The variation of surface concentration with temperature indicated enthalpy values of  $1 \pm 1 \text{ kJ mol}^{-1}$  and  $-3 \pm 7 \text{ kJ mol}^{-1}$  for the 19.3Rh and 84.7Rh alloys, respectively.

4. These experiments were compared to combined bond breaking and lattice strain theories of segregation. The use of elemental sublimation enthalpies as an estimate of surface bond energy predicted a heat of segregation of  $-35 \text{ kJ mol}^{-1}$  favoring Co enrichment for all compositions in this system. This was much larger than the present experimental values. A closer agreement was found when solid surface tension data were used, giving enthalpies in the range  $-4$  to  $-7 \text{ kJ mol}^{-1}$ .
5. The elastic strain energy contribution to the heat of segregation was estimated for rhodium atoms in a cobalt matrix to be approximately  $7.8 \text{ kJ mol}^{-1}$ . When this value is added to the bond breaking contribution estimated from surface tension data, a positive heat of segregation of between 1 and  $4 \text{ kJ mol}^{-1}$  is expected, now favoring Rh enrichment. The experimental values from the 19.3Rh alloy compare reasonably well to these values.

## 7.2 Oxidation of Ni-Co Alloys in the Temperature Range 673–1073 K

1. (110) Ni-3.86Co and polycrystalline Ni-4.0Co alloys were oxidized at  $5 \times 10^{-3}$  Torr at temperatures from 673 to 1073 K. The oxide morphologies and growth kinetics were shown to be dependent on the methods of surface preparation and exposure of the samples to the reactive atmosphere. The oxide formed on chemically polished and vacuum annealed (110) single crystal surfaces displayed a preferred (100) (NiCo)O  $\parallel$  (110) Ni-3.86Co orientation when samples were initially exposed to oxygen at room temperature and subsequently heated to higher temperatures. The same method of surface pretreatment, but with initial exposure to oxygen at temperatures from 673 to 773 K led to the formation of additional oxide orientations parallel to the alloy surface. Mechanically polished, polycrystalline Ni-4.0Co surfaces which were exposed to oxygen at room

temperature without prior annealing and subsequently raised to the reaction temperature formed essentially polycrystalline (randomly oriented) oxide films.

2. The oxide films having the largest area fractions of the highly oriented (100) (NiCo)O on (110) Ni-3.86Co had the slowest rates of oxygen uptake. This phenomenon was believed to be due to slower rates of transport of cations through low index grain boundaries separating the oxide subgrains or mosaic blocks. The oxides having mainly polycrystalline orientations were associated with the highest rates of transport by grain boundary mechanisms.

3. Auger composition vs. depth profiles revealed that the average concentrations of CoO in the (NiCo)O films was greater than the bulk alloy value in all samples produced in these experiments. These composition profiles were analyzed according to the Wagner<sup>(6)</sup> model for solid solution oxide scale growth and were shown to be consistent with enhanced transport of cobalt in the alloy beneath the growing films. This enhancement was possibly due to the presence of interfacial dislocation networks which may accommodate vacancy annihilation and localized plastic deformation in cation conducting scales.

4. The cobalt oxide concentrations were shown to increase from the alloy-oxide to the oxide-gas interfaces. In general, these increases were related to enhanced rates of diffusion of cobalt cations, relative to nickel, in the growing oxides. More specifically, a correlation was established between the levels of enrichment and oxide structure; the (100) (NiCo)O || (110) Ni-3.86Co oriented layers showed a greater cobalt oxide enrichment effect than for those oxides which were more randomly oriented. This difference was thought to be due to higher levels of discrimination between cobalt and nickel cations for specific jump sequences in low angle oxide boundaries.

## REFERENCES

1. J.W.Gibbs, Collected Works, Longmans, N.Y. (1928).
2. E.E.Hajcsar, P.T.Dawson and W.W.Smeltzer, Surf. Interface Anal., 10, 343 (1987).
3. E.E.Hajcsar, P.R.Underhill, W.W.Smeltzer and P.T.Dawson, Surf. Sci., 191, 249 (1987).
4. D.P.Whittle, High Temperature Corrosion, ed. R.A.Rapp, NACE 6, 171 (1981).
5. W.W.Smeltzer, Oxidation of Metals and Associated Mass Transport, eds. M.A.Dayanada, S.J.Rothman and W.E.King, TMS-AIME (1986).
6. C.Wagner, Corros. Sci., 9, 91 (1969).
7. M.J.Kelley and V.Ponec, Prog. Surf. Sci., 11, 139 (1981).
8. F.F.Abraham and C.R.Brundle, J. Vac. Sci. Technol., 18, 506 (1981).
9. P.Wynblatt and R.C.Ku, Surf. Sci., 65, 511 (1977).
10. O.Kubaschewski and B.E.Hopkins, Oxidation of Metals and Alloys, Butterworths, London (1962).
11. K.Hauffe, Oxidation of Metals, Plenum Press, N.Y. (1965).
12. P.Kofstad, High Temperature Corrosion, Elsevier Applied Science, London (1988).
13. P.Kofstad, High Temperature Oxidation of Metals, Wiley, N.Y. (1966).

14. U.R.Evans, The Corrosion and Oxidation of Metals, Edwin Arnold, London (1960), Supplement (1968).
15. J.D.Eshelby, *Solid State Physics.*, 3, 79 (1956).
16. V.S.Sundaram and P.W.Wynblatt, *Surf. Sci.*, 52, 569 (1975).
17. R.G.Donnely and T.S.King, *Surf. Sci.*, 74, 89 (1978).
18. T.S.King and R.G.Donnely, *Surf. Sci.*, 141, 417 (1984).
19. G.Kerker, J.L.Moran-Lopez and K.H.Bennermann, *Phys. Rev. B*, 15, 638 (1977).
20. R.N.Barnett, U.Landman and C.L.Cleveland, *Phys. Rev. B*, 28, 6647 (1983).
21. C.Wagner, *Z. Phys. Chem.*, B21, 25 (1933); *ibid*, Atom Movements, ASM Ohio, 153 (1951).
22. B.D.Bastow, G.C.Wood and D.P.Whittle, *Oxid. Met.*, 16, 1 (1981).
23. F.N.Rhines, *Trans. AIME*, 137, 246 (1940).
24. J.S.Kirkaldy and L.C.Brown, *Can. Met. Quart.*, 2, 89 (1962).
25. A.D.Dalvi and D.E.Coates, *Oxid. Met.*, 5, 113 (1972).
26. C.Wagner, *Corros. Sci.*, 8, 889 (1968).
27. W.W.Smeltzer and D.P.Whittle, *J. Electrochem. Soc.*, 125, 116 (1978).
28. D.P.Whittle, B.D.Bastow and G.C.Wood, *Oxid. Met.*, 9, 215 (1975).
29. D.E.Coates and A.D.Dalvi, *Oxid. Met.*, 2, 331 (1970).
30. D.J.Young, F.Viani and F.Gesmundo, *Oxid. Met.*, 30, 391, (1988).
31. W.W.Smeltzer, Defects and Transport in Oxides, eds. M.S.Seltzer and R.Jaffee, Plenum Press, New York, 495 (1975).
32. K.Nishida, High Temperature Corrosion, ed. R.A.Rapp, NACE 6, 184 (1981).
33. B.D.Bastow, G.C.Wood and D.P.Whittle, *Corros. Sci.*, 25, 253 (1985).

34. T.Narita, K.Nishida and W.W.Smeltzer, *J. Electrochem. Soc.*, 129, 209 (1982).
35. J.Frenkel, *Kinetic Theory of Liquids*, Oxford University Press, New York (1946).
36. A.Atkinson, *Rev. Mod. Phys.*, 57, 437 (1985).
37. W.Koster and E.Horn, *Z.Metallkunde*, 43, 444 (1952).
38. M.Hansen, *Constitution of Binary Alloys*, McGraw-Hill, New York (1958).
39. H.E.N.Stone, *J. Mater. Sci. Letters*, 11, 1162 (1976).
40. M.M.Mit'ko, E.L.Dubin, A.I.Timofeev and A.I.Chegodaev, *Izv. V. U. Z. Tsuetn. Metall.*, 3, 84 (1978).
41. T.Nishizawa and K.Ishida, *Bulletin of Alloy Phase Diagrams*, 4, 390 (1983).
42. J.Askill, *Tracer Diffusion Data For Metals, Alloys and Simple Oxides*, Plenum, New York (1970).
43. E.E.Hajcsar, Ph.D. Thesis, McMaster University (1988).
44. P.R.Underhill, *Surf. Sci.*, 195, 557 (1988).
45. D.J.Young and F.Gesmundo, *Proc. Vith Intern. Conf. on High Temperature and Energy-Related Materials*, Rome (1987).
46. F.A.Kroger and H.J.Vink, *Sol. State. Phys.*, 3, 307 (1956).
47. S.P.Mitoff, *J. Chem. Phys.*, 35, 882 (1961).
48. Y.D.Tretyakov and R.A.Rapp, *Trans. AIME*, 245, 1235 (1969).
49. W.C.Tripp and N.M.Tallan, *J. Am. Cer. Soc.*, 53, 531 (1970).
50. H.G.Sockel and H.Schmalzried, *Ber. Bunsenges Physik. Chemie*, 72, 745 (1968).
51. C.M.Osburn and R.W.Vest, *J. Phys. Chem. Solids*, 32, 1331 (1971).

52. C.M.Osburn and R.W.Vest, *J. Phys. Chem. Solids*, 32, 1343 (1971).
53. P.Kofstad, *Nonstoichiometry, Diffusion and Electrical Conductivity in Binary Metal Oxides*, Robert E. Krieger Publishing Company, Malabar (1983).
54. J.Deren and S.Mrowec, *J. Mater. Sci.*, 8, 545 (1973).
55. R.Linder and A.Akersrom, *Disc. Farad. Soc.*, 23, 133 (1957).
56. M.T.Shim and W.J.Moore, *J. Chem. Phys.*, 26, 802 (1957).
57. J.S.Choi and W.J.Moore, *J. Phys. Chem.*, 66, 1308 (1962).
58. S.M.Klotsman, A.N.Timofeyev and I.Sh.Trakhtenberg, *Fiz. Metal. Metalloved.*, 14, 428 (1962).
59. M.L.Volpe and J.Reddy, *J. Chem. Phys.*, 53, 1117 (1970).
60. A.Atkinson and R.I.Taylor, *Phil. Mag.*, A39, 581 (1979).
61. A.Atkinson and R.I.Taylor, *Phil. Mag.*, A43, 979 (1981).
62. C.Dubois, C.Monty and J.Philibert, *Phil. Mag.*, A46, 419 (1982).
63. C.Dubois, C.Monty and J.Philibert, *Solid State Ionics*, 12, 75 (1984).
64. A.Atkinson, F.C.W.Pummery and C.Monty, in *Transport in Non-stoichiometric Compounds*, edited by G.Simkovich and V.S.Stubican, Plenum Press, New York (1985).
65. D.M.Duffy and P.W.Tasker, *Phil. Mag.*, A47, 817 (1983).
66. D.M.Duffy and P.W.Tasker, *Phil. Mag.*, A50, 155 (1984).
67. K.L.Merkle and D.J.Smith, *Phys. Rev. Letters*, 59, 2887 (1987).
68. K.L.Merkle, J.F.Reddy and C.L.Wiley, *J. Phys. (Paris), Colloq.*, 46, C4-95 (1985).
69. F.A.Elrefaie, A.Manolescu and W.W.Smeltzer, *J. Electrochem. Soc.*, 132, 2489 (1985).
70. K.Fueki and J.B.Wagner,Jr., *J. Electrochem. Soc.*, 112, 384 (1965).

71. F.N.Rhines, R.G.Connell and M.S.Choi, *J. Electrochem. Soc.*, 126, 1061 (1979).
72. L.Berry and J.Paidassi, *C. R. Acad. Sci. Paris*, 262, C-1353 (1966).
73. D.Caplan, M.J.Graham and M.Cohen, *J. Electrochem. Soc.*, 119, 1205 (1972).
74. M.J.Graham, G.I.Sproule, D.Caplan and M.Cohen, *J. Electrochem. Soc.*, 119, 883 (1972).
75. M.J.Graham, R.J.Hussey and M.Cohen, *J. Electrochem. Soc.*, 120, 1523 (1973).
76. R.Herchl, N.N.Khoi, T.Homma and W.W.Smeltzer, *Oxid. Met.*, 4, 35 (1972).
77. N.N.Khoi, W.W.Smeltzer and J.D.Embury, *J. Electrochem. Soc.*, 122, 1495 (1975).
78. F.N.Rhines and J.S.Wolf, *Metall. Trans.*, 1, 1701 (1970).
79. F.N.Rhines and R.G.Connell, *J. Electrochem. Soc.*, 124, 1122 (1977).
80. J.M.Perrow, W.W.Smeltzer and J.D.Embury, *Acta Met.*, 16, 1209 (1968).
81. A.Atkinson, R.I.Taylor and A.E.Hughes, *Phil. Mag.*, A45, 823 (1982).
82. J.V.Cathcart, G.F.Peterson and C.J.Sparks, Jr., *J. Electrochem. Soc.*, 116, 664 (1969).
83. W.W.Smeltzer, R.R.Haering and J.S.Kirkaldy, *Acta Met.*, 9, 880 (1960).
84. D.F.Mitchell, P.B.Sewell and M.Cohen, *Surf. Sci.*, 61, 335 (1976).
85. D.F.Mitchell, P.B.Sewell and M.Cohen, *Surf. Sci.*, 69, 310 (1977).
86. D.F.Mitchell and M.J.Graham, *Surf. Sci.*, 114, 546 (1982).
87. H.-T.Liu, A.F.Armitage and D.P.Woodruff, *Surf. Sci.*, 114, 431 (1982).

88. M.J.Graham and M.Cohen, J. Electrochem. Soc., 119, 879 (1972).
89. J.Robin, Ann. Chimie XII, 10, 389 (1955).
90. K.Przybylski and W.W.Smeltzer, J. Electrochem. Soc., 128, 897 (1981).
91. R.Diekmann, Z. Phys. Chem. N.F., 107, 189 (1977).
92. R.E.Carter and F.D.Richardson, Trans. AIME, 200, 1244 (1954); 203, 336 (1955).
93. A. Atkinson, Rev. Mod. Phys., 57, 437 (1985).
94. S.Mrowec and K.Przybylsky, Oxid. Met., 11, 365 (1977).
95. F.Gesmundo and F.Viani, J. Electrochem. Soc., 128, 460 (1981).
96. B.Bergman and J.Agren, J. Am. Cer. Soc., 69, C-248 (1986).
97. B.Kaufman and H.Nestor, CALPHAD, 2, 81 (1978).
98. K.Torkar and R.Schneider, J. Solid State Chem., 18, 89 (1976).
99. M.Kinoshita, W.D.Kingery and H.K.Bowen, J. Am. Cer. Soc., 56, 398 (1973).
100. G.Zintl, Z. Phys. Chem. N. F., 48, 340 (1966).
101. G.Zintl, Z. Phys. Chem. N. F., 54, 110 (1967).
102. W.K.Chen and N.L.Peterson, J. Phys. Chem. Solids, 34, 1093 (1973).
103. W.K.Chen and N.L.Peterson, J. Phys. Chem. Solids, 33, 881 (1972).
104. W.K.Chen and N.L.Peterson, J. Am. Cer. Soc., 63, 566 (1980).
105. A.Atkinson and R.I.Taylor, Phil. Mag. A., 45, 583 (1982).
106. N.Tabet and C.Monty, Proceedings of the 9th International Symposium on the Reactivity of Solids, Cracow (1980).
107. A.Preece and G.Lucas, J. Inst. Metals, 20, 219 (1952).
108. S.F.Frederick and I.Cornet, J. Electrochem. Soc., 102, 285 (1955).
109. W.W.Smeltzer, Acta Met., 7, 191 (1959).
110. G.C.Wood and J.M.Ferguson, Nature, 208, 369 (1965).

111. K.Nishida, T.Narita, N.Ohya and T.Yamauchi, Trans JIM, 16, 755 (1975).
112. I.Ishikawa and T.Homma, Annual Meeting of the Japan Institute of Metals, April (1976).
113. T.Homma, K.Ishiguro and M.Matsunaga, Seisan Kenkyu, 30, 452 (1978).
114. M.Takemori, A.Tanaka and T.Homma, Seisan Kenkyu, 34, 72 (1982).
115. D.Majumdar, R.G.Spahn and J.S.Gau, J. Electrochem. Soc., 134, 1825 (1987).
116. E.E.Hajcsar, Z.Z.He, P.R.Underhill and W.W.Smeltzer, J. Vac. Sci. Technol., A6, 3006 (1988).
117. J.J.Burton, C.R.Helms and R.S.Polizzotti, J. Vac. Sci. Technol., 13, 204 (1976).
118. P.V.Shigolev, Electrolytic and Chemical Polishing of Metals, 2nd. ed., Freund, , 147 (1974).
119. W.J.McG.Tegart, The Electrolytic and Chemical Polishing of Metals in Research and Industry, 2nd. ed., Pergamon, London (1959).
120. A.Tanaka, M.Takemori and T.Homma, J. Electron Spectrosc. Relat. Phenom., 32, 277 (1983).
121. L.P.Fox, U. S. Patent No. 2,680,678, June 8, 1954.
122. D.C.Joy, D.E.Newbury and D.L.Davidson, J. Appl. Phys., 53, R81 (1982).
123. P.B.Hirsch, A.Howie, R.B.Nicholson, D.W.Pashley and M.J.Whelan, Electron Microscopy of Thin Crystals, Butterworths, London (1965).
124. Bauman et al, J. Microscop., 122, 181 (1981).

125. High Accuracy Pressure Measurements, MKS Instruments, Inc., Andover, MA.
126. Operating and Maintenance Instructions for High Accuracy 170 Series Sensor Heads, MKS Instruments, Inc., Andover, MD.
127. N.N.Khoi, Ph.D. Thesis, McMaster University (1972).
128. P.R.Underhill, Surf. Int. Anal., 8, 21 (1986).
129. N.Q.Lam, H.A.Hoff, H.Wiedersich and L.E.Rehn, Surf. Sci., 149, 517 (1985).
130. T.G.Dye, A Fursey, G.O.Lloyd and M.Robson, J. Sci. Instrum. (J. Phys. E.) 1, 463 (1968).
131. M.P.Seah and W.A.Dench, Surf. Int. Anal., 1, 2 (1979).
132. H.E.Bishop, Scanning Electron Microsc., Part II, 259 (1983).
133. M.P.Seah, Scanning Electron Microsc., Part II, 521 (1983).
134. J.P.Langeron, L.Minel, J.L.Vignes, S.Bouquet, F. Pellerin, G.Lorang, P.Ailloud and J. Le Hericy, Surf. Sci., 138, 610 (1984).
135. W.Farber, G.Betz and P.Braun, Nucl. Instrum. Meth., 132, 351 (1976).
136. G.Betz, Surf. Sci., 92, 283 (1980).
137. R.Kelly, Nucl. Instrum. Meth., 149, 553 (1978).
138. L.C.Feldman and J.W.Mayer, Fundamentals of Surface and Thin Film Analysis, North Holland, New York (1986).
139. Staff, Centre D'Information Du Cobalt, Cobalt Monograph, CIC, Belgium (1960).
140. A.S.Darling, Intern. Met. Rev., 18, 91 (1973).
141. Metals Reference Book, 5th Edn., ed. by C.J.Smithells, Butterworths London (1976).

142. L.Z.Mezey and J.Giber, Jpn. J. Appl. Phys., 21, 1569 (1982).
143. A.R.Miedema, Z. Metallik., 69, 287 (1978).
144. W.R.Tyson, Can. Met. Quart., 14, 307 (1975).
145. R.Hultgren, P.D.Desai, D.T.Hawkins, M.Gleiser, K.K.Kelley and D.D.Wagman, Selected Values of the Thermodynamic Properties of The Elements, Am. Soc. Metals, Metals Park, OH (1973).
146. N.H.Tsai, G.M.Pound and F.F.Abraham, J. Catalysis, 50, 200 (1977).
147. W.M.H.Sachtler and R.A.van Santen, Appl. Surf. Sci., 3, 121 (1979).
148. M.P.Seah, J.Catalysis, 57, 450 (1979).
149. B.Pieraggi and R.A.Rapp, Acta Metall., 36, 1281 (1988).
150. W.B.Crow, Diffusion of Cobalt, Nickel and Iron in Cobalt Oxide and Nickel Oxide, Report ARL-70-0090, Project No. 7921 (June 1970), USAF, Ohio.
151. J.J.Stiglich, J.B.Cohen and D.H.Whitmore, J. Am. Ceram. Soc., 56, 119 (1973).
152. W.H.Press, B.P.Flannery, S.A.Teukolsky and W.T.Vetterling, Numerical Recipes: The Art of Scientific Computing, Cambridge University Press, Cambridge (1986).